Metal Oxides for Hydrogen Activation and Sustainable Chemical Conversions

by

Evan V. Miu

B.S. in Chemical Engineering, Bucknell University, 2016

Submitted to the Graduate Faculty of

the Swanson School of Engineering in partial fulfillment

of the requirements for the degree of

Doctor of Philosophy

University of Pittsburgh

2023

UNIVERSITY OF PITTSBURGH

SWANSON SCHOOL OF ENGINEERING

This dissertation was presented

by

Evan V. Miu

It was defended on

June 13, 2023

and approved by

Götz Veser, PhD, Chemical & Petroleum Engineering

John A. Keith, PhD, Chemical & Petroleum Engineering

Leanne M. Gilbertson, PhD, Civil & Environmental Engineering

Co-advisor, James R. McKone, PhD, Chemical & Petroleum Engineering

Co-advisor, Giannis Mpourmpakis, PhD, Chemical & Petroleum Engineering

Metal Oxides for Hydrogen Activation and Sustainable Chemical Conversions

Evan V. Miu, PhD

University of Pittsburgh, 2023

Our green, renewable future remains an unsatisfyingly distant reality. Although we are taking actions to suppress anthropogenic harm to the natural world, there is scientific consensus that radical changes are needed today to avoid significant ecological and climate damage. In this direction, a hydrogen-based economy has been proposed as a sustainable alternative to a fossil-based economy. Hydrogen is receiving such attention because it has the potential to be carbon-free, producing only water when used as a fuel. However, the production of hydrogen is currently tightly linked to fossil fuels, and fossil-free methods remain under-developed. Sourcing hydrogen from water and renewable electricity has been proposed as a significant opportunity for making positive steps towards a more sustainable future.

This dissertation focuses on the development of catalytic schemes that combine water electrolysis and hydrogenation chemistries through mediated hydrogen transfers. The specific approach uses metal oxide hydrogen bronzes to electrocatalytically activate hydrogen from water and then supply it for general hydrogenation chemistries. It is worth noting that the chemical industry is the leading consumer of hydrogen, and it will remain so for many decades. This work is driven by the hypothesis that these bronzes offer fine control over the activity of hydrogen and can be tuned to accommodate specific hydrogenations. Research herein includes fundamental studies of the thermodynamics, transport phenomena, and kinetics of hydrogen intercalation into metal oxides. Additionally, a mediated hydrogenation using tungsten oxide is demonstrated. Overall, this research offers foundational knowledge of bronze-mediated hydrogenations and presents a means for environmentally benign hydrogen utilization, bringing us closer to a sustainable chemical industry.

Table of Contents

List of Tables

List of Figures

Preface

To my parents: you taught me to “think” — so, I thought really hard.

James McKone and Giannis Mpourmpakis, these brief words do not adequately express the depth of gratitude I have for each of you. James, you helped me choose Pittsburgh as the place to spend my graduate years and shaped the course of my life and career. You have taught me to think critically, communicate logically, and to put people before projects. You are a role model who’s example I will always try to follow, both as a genuinely good person and as an inquisitive scientist. Yanni, you have taught me to never forget my values and have constantly encouraged me to pursue my dreams. You have inspired me to always go beyond my comfort zone, to push further and deeper, and to incessantly improve. You have set examples of excellence in technical and emotional intelligence that I will forever be chasing. Thank you both for being incredible advisors and phenomenal friends.

Götz Veser, John Keith, and Leanne Gilbertson, you have been wonderfully engaging, supportive, and critical at every step of my graduate school process. Each of you have stimulated me to be a more well-rounded thinker and scientist, and I will always value the moments of time we have spent together.

Members of the McKone and Mpourmpakis labs, you have given me the joy of working with bright colleagues and friends. You have continuously pushed me to be better, and I will miss our opportunities to spontaneously jump onto a whiteboard...or into a beer.

Kat, Yoko, Jo, Ken, and Ema Wakabayashi, you have always encouraged me and given me the confidence to chase difficult things. You remind me to enjoy the journey, appreciate the small details of life, and to smile. Thank you for guiding me and for always being there.

Marcus and Cassie, you have been a second family to me in Pittsburgh. You’ve been supportive in a way that I never knew was possible. Thank you for keeping me balanced.

Christian, Alex, Matthew, and Kate, you have remained my closest friends even though we’ve been separated by new jobs, extra degrees, and hundreds of miles. I have cherished the moments we’ve been able to sneak in together these last few years, they most certainly kept me going. Thank you for keeping me happy.

1.0 A Perspective on What Sustainable Hydrogen Could Look Like in Chemical Manufacturing

The International Panel on Climate Change (IPCC) reported in April 2022 that global surface temperatures are likely to rise at least 1.5 °C in the 21st century.[1] The report projected this minimum temperature increase as a best case scenario, considering maximum CO_2 and greenhouse gas (GHG) emissions occurring between the years of 2020-2025. Preventing larger surges in temperature immediately requires "rapid and deep reductions in GHG emissions," with net-zero CO_2 emissions necessary by 2050. These reductions amount to an average of 7.6% of GHG emissions per year—in comparison, the global halt in trade precipitated by the COVID-19 pandemic reduced GHG emissions in 2020 by only 6.7% for the full year versus 2019.[2, 3] If current policies and practices are maintained with no change, then temperature increases are projected to exceed 3 °C by 2100 and will continue to rise thereafter. The findings of the IPCC communicate a clear and urgent message: changes in the operation of the world's economies and industries are needed today, or else significant climate damage is inevitable.

In pursuit of limiting GHG emissions, hydrogen has long been proposed as a carbon-free alternative to petroleum-derived fuels and materials.[4] The great promise of hydrogen is that, once burned or oxidized for energy, it produces only water as a byproduct. This clean energy source can be used as a fuel for vehicles or for heating homes. It can also be used as an accessible source of hydrogen atoms in the chemical industry, allowing for the sustainable production of valuable materials and compounds. Nearly all of the current demand for hydrogen is attributable to the manufacturing and chemical industries, and not to fuel applications.[5] Continuing through 2030, this hydrogen demand will sink to just above 50% in the IEA's Net Zero Emissions by 2050 scenario, with cases such as transportation and energy making up the other use streams. While H_2 would be a clean resource, 99% of hydrogen is currently produced from fossil fuels.[6, 7] In the US, 95% of hydrogen is produced via steam methane reforming (SMR), which is an energy intensive process that converts methane and steam to hydrogen and carbon monoxide. To increase hydrogen output, water gas shift

(WGS) is performed in conjunction with SMR, converting CO to CO_2. A recent study[8] has shown that SMR with WGS emits approximately 20% more GHGs per unit energy than the direct burning of methane when the produced H_2 is used as a fuel. Furthermore, SMR produces 13 kg of CO_2 per 1 kg of H_2, resulting in ~900 Mt of global CO_2 emissions per year.[9] Although the use of hydrogen is carbon-free, its synthesis and production is highly polluting.

Acknowledging the carbon intensity of fossil-based hydrogen, carbon capture, utilization, and storage (CCUS) has been proposed as a way of reducing CO_2 emissions.[10] CCUS implementations are added to (or modify) SMR processes, adsorbing, separating, or converting CO_2 to inhibit its emission. Hydrogen produced via SMR and CCUS is termed "blue" hydrogen, and is being pursued as a clean fossil-based hydrogen. Although a promising approach, carbon capture is notoriously difficult to implement, limited by poor return on investment that is inadequately offset by carbon credit programs or political incentives.[11] CCUS also only offsets the carbon emission issue, necessitating either storage or use of the captured CO_2. It is not currently clear what a sustainable long-term CCUS solution will look like. Recognizing the difficulties of CCUS implementation, there is growing evidence of a need for fossil-free hydrogen.[12]

This need has motivated decades of research into electrochemical water splitting. In general, water splitting (also electrolysis) generates H_2 and O_2 from water, constituting what is known as "green hydrogen" when the input is renewable electricity. Today, green hydrogen represents about 1% of the H_2 that is produced, increasing to only 25% by the year 2050 in net-zero scenarios.[13] Part of the reason water electrolysis is difficult to use more frequently is because it remains a more expensive source of hydrogen than methods such as SMR. Depending on natural gas prices, the highest performing electrolyzers can approach cost equivalence with SMR, however, most implementations can only produce H_2 that is twice as expensive.[7] More specifically, H_2 derived from fossil resources (coal, natural gas, etc.) currently carries a levelized cost of 0.5-2 USD/kg. By contrast, hydrogen from renewable source (including "green hydrogen") has a levelized cost of 3-8 USD/kg.[14] The high cost of electrolysis therefore limits the proliferation of green hydrogen, even if the approach represents a carbon-free (in terms of chemistry to produce H_2) source of H_2.

The proposition of a hydrogen economy supported by "green hydrogen" from electrolysis carries yet another intrinsic cost associated with H_2. This concept is visualized in Figure 1. In water splitting, H_2 is generated in conjunction with the oxidation of water to O_2, requiring a thermodynamic minimum input of 1.23 V defined by the positions of the O_2/H_2O (+1.23 V vs. RHE) and H^+/H_2 (0 V vs. RHE) redox couples. These couples are shown by vertical lines in the top section of Figure 1. Building an industry around H_2 as a hydrogen carrier therefore embeds this +1.23 V energy expenditure into every hydrogen unit. This dissertation asks the following question: is making H_2 from water the best way to provide reactive hydrogen for chemical manufacturing?

It is important to note that the chemical industry needs hydrogen for platform high-volume chemistries such as ammonia and methanol synthesis. With SMR as our main means of producing hydrogen, industrial chemical transformations have traditionally relied on H_2 as a hydrogen source. Prototypical climate scenarios propose "green" H_2 as a 1-to-1 swap for SMR H_2 in order to take advantage of existing chemical processes. In this approach, the main hydrogenation inputs would not be different, only the progeny of the H_2 would change.

We note that there only exists a small range of chemistries (Figure 1, highlighted in pink) in which H_2 is a practical hydrogen carrier. The bounds of this region are $1\text{x}10^{-9}$ atm (accessible vacuum) to 1000 atm (high pressure reactors). If "green hydrogen" were to be a go to hydrogen input, then only hydrogenations which can be performed in this range are feasible. Many important processes do operate in this range, however, Figure 1 communicates three opportunities in moving away from H_2:

1. Easily accessible electrochemical potentials correspond to entirely intractable H_2 fugacities (green region)
2. Electrolyzing H_2O to H_2 could be intrinsically wasteful, depending on the desired hydrogenation (blue region)
3. For certain hydrogenations, H_2O can thermodynamically behave as a hydrogen source (orange region)

Using H_2 as a hydrogen input to chemical processes limits the range of accessible hydrogenation chemistries and the efficiency by which we can perform them. The bottom panel

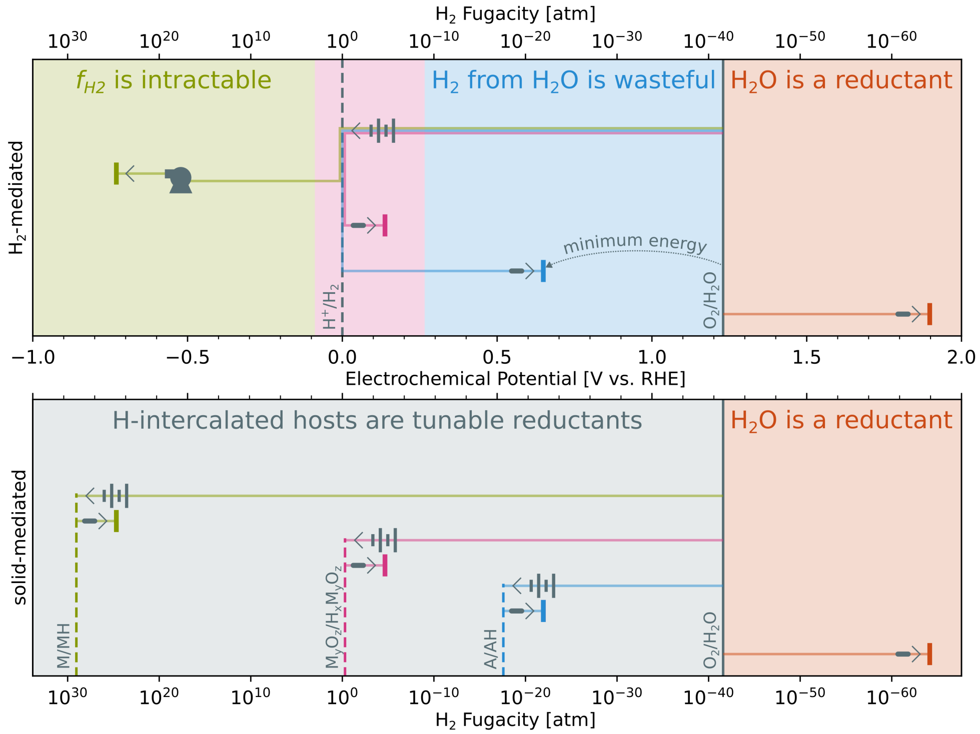

Figure 1: Fugacity–potential duality of hydrogen transfers. The x-axes are shared and equivalent, as defined by the Nernst equation. The top panel shows two vertical lines, one at 0.0 V vs. RHE representing the H^+/H_2 couples and one at +1.23 V vs. RHE corresponding to the O_2/H_2O redox couple. The horizontal lines represent potential reactions, for example electrochemical water splitting moving from O_2/H_2O to H^+/H_2. The small vertical lines are example fictitious hydrogenations which lie in four different regions. The green region requires fugacities of H_2 which are physically unattainable in industry. The pink region, spanning from 1000 atm to 1E-9 atm, is the space of fugacities which could be accessible when using H_2 as a hydrogen source. The blue region, between about +0.25 V vs. RHE to 1.23 V vs. RHE is the hydrogen activity space in which using H_2 as a hydrogen donor is energetically wasteful. The orange region contains chemistries in which H_2O could thermodynamically be considered as a direct hydrogen donor. The bottom panel shows how H-mediators, the dashed vertical lines, could be used as reductants in place of H_2. Electrolysis could be performed such that the product is H attached to some mediator instead of producing H_2.

of Figure 1 illustrates an alternative paradigm of hydrogenations in which H_2O is used as a process input and a hydrogen source in place of H_2. In this manner, renewable electricity and water are inputs to intensified reactor schemes: instead of making H_2, protons and electrons are attached to some active intermediate that has a reduction potential *different* than 0.0 V vs. RHE. A suitably designed intermediate would exhibit a 1 H^+ / 1 e^- reduction potential that is just negative of the desired hydrogenation target, which allows the intermediate to then donate its hydrogen equivalents. Importantly, this scheme requires active materials which can both selectively uptake hydrogen from water and intentionally deliver hydrogen to another molecule. Specific examples are discussed later in this chapter. Here, we discuss several relevant reports in literature which help frame this alternative approach to chemical hydrogenations.

1.1 Interpreting Hydrogenation Chemistries Through the Lens of Proton-Coupled Electron Transfers

We begin by emphasizing that hydrogen transfers are not restricted to the exchange of an atomic H unit. The hydrogen atom is comprised of a proton and an electron—these constituents are allowed to transfer sequentially and can also come from and go to different locations. These steps are shown schematically in Figure 2, which is a square scheme for proton-coupled electron transfer (PCET).[15] This image represents the conversion of some substrate X (top left) to a hydrogenated product XH (bottom right). The diagonal line shows a single H atom transfer, or a concerted proton-electron transfer. Horizontal lines show proton transfers and vertical lines show electron transfers. Either is able to occur first. These various mechanistic pathways can result in exotic reactivity and importantly provide different handles for tuning reaction behavior, such as pH and applied electrochemical potentials. Addition of a hydrogen atom to X can be written according to Equation 1.1.1.

$$\mathrm{X} + \frac{\mathrm{n}}{2} \cdot \mathrm{H_2} \rightleftharpoons \mathrm{XH_n} \tag{1.1.1}$$

In Equation 1.1.1, X is a substrate, H_2 is the dihydrogen molecule, and XH_n is a hydro-

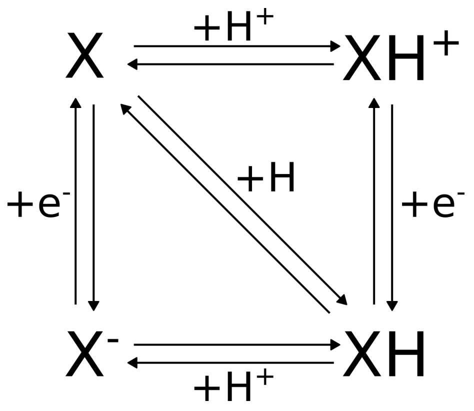

Figure 2: Proton-coupled electron transfer square scheme for unit proton and unit electron transfer, highlighting multiple mechanistic explanations for a general hydrogenation. A hydrogen atom can react with some reactant A to form AH, following the diagonal line in the center of the square. Also possible is the transfer of a proton (horizontal line) followed by an electron (vertical line) and vice versa. The same mechanisms are feasible in the reverse direction of dehydrogenation.

genated product. A total of n hydrogen atoms are added to X. As written, Equation 1.1.1 communicates that the underlying chemistry constitutes the transfer of atomic H units. We can relax this by considering the following equilibrium:

$$H^+ + e^- \rightleftharpoons \frac{1}{2} \cdot H_2 \tag{1.1.2}$$

Combining Equations 1.1.1 and 1.1.2 gives:

$$X + H^+ + e^- \rightleftharpoons XH \tag{1.1.3}$$

As written, Equation 1.1.3 communicates the possibility of decoupled proton and electron transfers. From a thermodynamic perspective, Equation 1.1.1 and Equation 1.1.3 are equivalent. This same logic is the basis of the computational hydrogen electrode model, which revolutionized the theoretical analysis of electrochemical catalysis.[16] We continue by noting that Equation 1.1.3 looks like an electrochemical half reaction. As such, it has some equilibrium reduction potential (or free energy of hydrogenation). If we wanted to select a suitable hydrogen donor according to the scheme shown in Figure 4, then we could consider a similar half reaction which describes the hydrogen insertion equilibrium for a mediator.

$$\mathrm{M} + \mathrm{H}^+ + \mathrm{e}^- \rightleftharpoons \mathrm{MH} \tag{1.1.4}$$

In Equation 1.1.4, M is a mediator and MH is its hydrogen carrying analog. Combining with Equation 1.1.3 gives the following expression for a mediated net hydrogenation.

$$\mathrm{X} + \mathrm{MH} \rightleftharpoons \mathrm{XH} + \mathrm{M} \tag{1.1.5}$$

There has been increasing evidence in the last few years that net hydrogenations can be viewed as these coupled electrochemical half reactions.[17, 18, 19] This is schematized in Figure 3a, where some catalyst S mediates the redox coupled hydrogenation of X to XH. From the perspective of S, hydrogen uptake constitutes a reduction, and delivery of hydrogen to X is an oxidation. Together, these half reactions comprise a full net hydrogenation of X.

One well-studied example of redox coupling is the thermochemical reduction of oxygen to water and hydrogen peroxide. It has been shown to operate as coupled H_2 oxidation and O_2 reduction when using H_2 as a thermochemical reductant, rationalized by mixed potential theory[17] These ties have been further evidenced by the same group of authors as they have used analytical electrochemical techniques to successfully screen for active thermochemical catalysts.[18] The identification of a paired redox mechanism for peroxide synthesis from H_2 and O_2 suggests that protons and electrons are exchanged through the course of reaction, rather than individual H atoms. Individual catalyst particles can therefore be viewed as short-circuited electrodes that are responsible for shuttling electrons between active sites. Charge balancing protons are then free to independently diffuse across the surface of the catalyst, or even exchange with a proton-conducting medium that is in contact with the particle.

More recent work has investigated thermochemical nitrate reduction.[19] Here, nitrate reduction to ammonia on bimetallic catalysts was shown to also proceed according to a coupled electrochemical mechanism. The authors were able to demonstrate that the half reactions were independently and uniquely catalyzed by the two metals (Pd, Cu) in their catalyst. Using voltammetry, they were able to identify a potential at which HOR (on Pd)

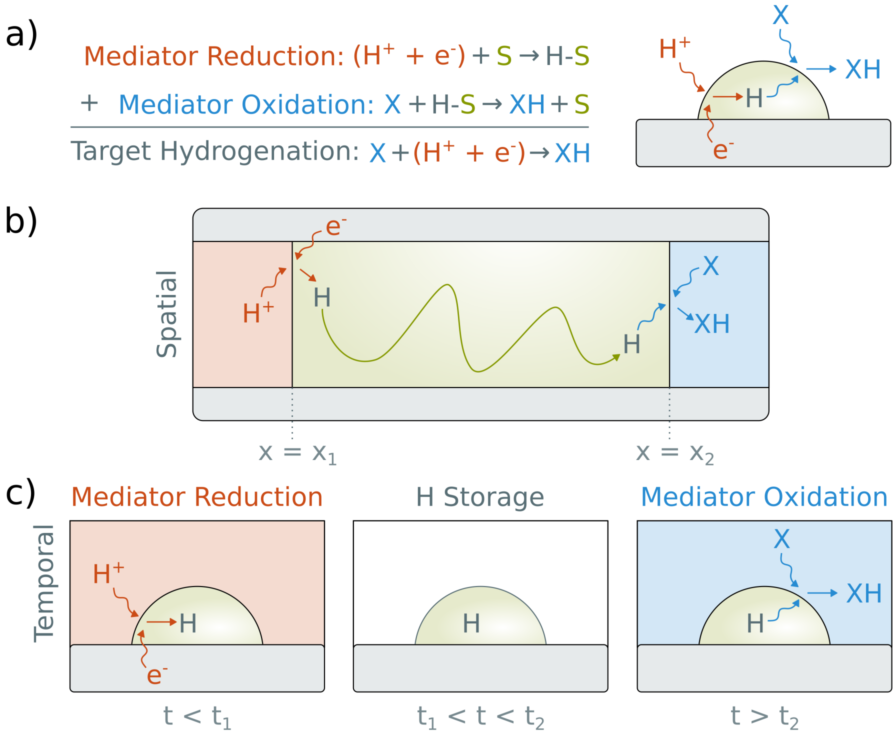

Figure 3: Mechanistic consequences of a proton-coupled electron transfer interpretation of hydrogenations. a) Illustration of how a single catalytic site could be responsible for a net hydrogenation by combining a reduction event and an oxidation event. b) Depiction of the spatial separation of the reduction and oxidation event, a “spatially decoupled” hydrogenation. c) Example of a hydrogen activation step that is followed at a later time by a hydrogen transfer step, a “temporally decoupled” hydrogenation.

and nitrate reduction (on Cu) occurred in equal, but opposite, rates. Under thermochemical conditions, the authors observed a nearly identical open circuit potential, indicating that H_2 and NO_3^- chemically polarized the bimetallic catalyst. The authors term this phenomena galvanic coupling.

These two examples are exergonic thermochemical reactions and simultaneously occur at a single catalyst particle. They both used H_2 as a reductant, which afforded a sufficient chemical potential to hydrogenate the respective reactants. In the direction of net hydrogenation, the initial oxidation to provide H^+ and e^- is exergonic, as is subsequent hydrogenation of the target substrate. Coupled half reactions in this scenario operate analogously to fuel cells, where these spontaneous chemical reactions shuttle electrons through short-circuited active sites instead of an external power load to accomplish redox transformations. Considering our interest in using H_2O as a hydrogen source, it is important to recognize that activating H from H_2O requires an energy input. So, if the same galvanic coupling mechanism is to be leveraged to use H_2O as a hydrogen source, then there needs to be energy added to these reacting systems. This energy input has been achieved both electrochemically and photochemically.

Practically, energizing these reactions has been accommmplished through the spatial and temporal separation of redox events, shown in Figure 3b and Figure 3c, respectively. In the case of spatially separating the galvanically coupled redox events, one could imagine using a suitable active material to physically separate, but chemically connect, two completely different reaction environments. This mode of operation is exemplified by palladium membrane reactors.[20, 21, 22, 23] As shown in Figure 3b, the left compartment (orange) could be an aqueous electrochemical environment and the right compartment (blue) could contain an organic molecule. As long as the active material (green) can transport protons and electrons at an adequate rate, protons from the left side of the system could be supplied as reactive hydrogen to the right side.

Photochemical methods have also been used to supply this energy input to pull protons and electrons from H-containing materials (typically alcohols instead of water). This scheme is shown in Figure 3c, and has mostly been achieved in a temporally decoupled sense. UV irradiation was shown to reduce ZnO and TiO_2 nanoparticles, with the injected electrons accompanied by protons.[24] Ethanol was implicated as an electron hole scavenger and proton source.[25] The injected protons and electrons were then removed by reacting with 2,4,6-tri-*tert*-butylphenoxyl and 2,2,6,6-tetramethyl-piperidin-1-yl-oxyl radicals, as well as other targets.[26] These studies make it clear that endergonic H activation from organic molecules (i.e. PCET to some metal oxide nanoparticle) can be achieved photochemically, and the activated H can be reacted with a range of oxidants.

Interpreting hydrogenations as PCET reactions provides unique opportunities for the design of mediated hydrogenations. When using water as a terminal hydrogen source in a hydrogenation reactor, there must be an input of energy in order to activate H equivalents. This energy can be provided electrochemically or photochemically, and can also be supplied in spatially or temporally decoupled manners. With the growing availability of cheap renewable electricity, we are particularly interested in exploring further electrochemically driven hydrogenations.

Beyond specific process designs, mediated hydrogenations require certain active materials. There are several material types which can be considered as hydrogen mediators in electrochemical schemes. At a high level, these mediators come in two major classes: homogeneous and heterogeneous. Homogeneous mediators are co-dispersed in the same medium as the hydrogenation target, and therefore require separation after reaction. Although they are highly active and selective,[27] the separation requirement makes homogeneous mediators economically difficult to implement. Accordingly, we focus our attention on heterogeneous hydrogen mediators.

Candidate heterogeneous H mediators must satisfy a particular set of minimal requirements. Mediators should reversibly uptake hydrogen without substantial changes in chemical identity upon H activation or transfer (i.e. adequate materials will be catalytic). Materials must also be able to conduct both protons and electrons. This differentiates solid H mediators from proton conductors such as Nafion, which are commonly employed in proton-conducting electrolyzers and stack architectures. Candidates should be solid and/or be able to form macroscopic, rigid objects. This is especially the case when designing spatially separated hydrogenations, since the mediator has the additional function of separating different reaction environments. It is worth noting that these requirements are satisfied by essentially all electrode materials which are usable as electrodes in proton batteries.

As a specific example, metal hydrides are one of the most explored classes of materials for mediating H transfers. Out of all hydrides, palladium has received the most attention with respect to mediated hydrogenations.[21, 20, 28, 29, 30] Other metal hydrides are known to form (Ti, Ni, etc.) and are of interest because they are cheaper than Pd and also provide H at wide range of chemical potentials.[31, 32] Numerous metal hydrides have also seen use as an electrode in rechargeable nickel-metal hydride batteries. Examples include mixtures of cerium, neodymium, titanium, or vanadium with nickel, cobalt, iron, chromium, or manganese. Alkali and alkaline earth metals also form hydrides.

Metal oxides are also a promising group of materials. As specific examples, V_2O_5, VO_2, TiO_2, MoO_3, and WO_3 have all been explored as proton intercalation battery electrodes.[33, 34, 35, 36, 37, 38, 39, 40, 41, 42] WO_3 is perhaps the most studied example from the group of metal oxide hydrogen bronzes,[43] which are metal oxides that are known to intercalate hydrogen into their bulk lattices. Hydrogen in these bronzes has been shown to thermochemically hydrogenate organic oxidants,[44] further supporting observations made in the oxide nanoparticle work discussed above.

Although bronzes have been shown to engage in reversible H uptake, it is still not clear which metal oxides are appropriate for which chemical reactions. While there have been extensive investigations into the functionality of tungsten oxide bronzes, there have been a dramatically smaller number of studies on other bronzes, such as molybdenum, vanadium, titanium, etc.[45, 46, 47] A large portion of the work in this dissertation therefore aimed to answer the question of what drives hydrogen intercalation in metal oxides, such that they can be sufficiently paired to particular hydrogenations.

In this dissertation, we are specifically interested in oxides because they are cheaper than complementary metal hydrides (such as Pd). They also exhibit a huge accessible design space, owing to possibilities of doping, crystal structure engineering, and polymorph expression. The insertion of hydrogen into these bronzes occurs in both electrochemical and thermochemical environments[48, 49, 50] and is a reversible process. Hydrogen typically bonds to the lattice oxygens of the bronzes, and results in dramatic changes in electronic structure, optical properties, and catalytic function of the host metal oxide, offering a potential means of tuning material properties.

The majority of research described herein therefore examines fundamental aspects of how hydrogen interacts with metal oxides. Chapter 2 investigates what characteristics of the metal oxides influence hydrogen intercalation. Intercalation is a reversible redox reaction, and so these studies are relevant both hydrogen insertion and hydrogen removal from bulk oxides. Chapter 3 studies the transport of hydrogen in tungsten oxide thin films under both thermochemical and electrochemical conditions. It both quantifies the diffusion of H equivalents and provides an example of the fugacity–potential duality outlined above. Chapter 4 considers how hydrogen intercalation influences the kinetics of the hydrogen evolution reaction on tungsten oxide. Observations made in Chapter 4 have broad implications for catalysis on metal oxides under reducing conditions in both electrochemical and thermochemical settings. With these fundamental studies complete, Chapter 5 demonstrates the full cycle of electrochemical hydrogen activation from water and delivery to a model hydrogen acceptor through the use of a tungsten oxide mediator. Chapter 6 then summarizes and connects each of these individual efforts while making recommendations for future research that could build on this body of work.

2.0 Factors Influencing the Thermodynamics of Hydrogen Uptake by Metal Oxides

The first part of this chapter is reproduced from “Predicting the energetics of hydrogen intercalation in metal oxides using acid–base properties,” which was published in ACS Applied Materials & Interfaces.[51] The second part is taken from “Global and local connectivities describe hydrogen intercalation in metal oxides,” which is currently under review at Physical Review Letters.

2.1 Context

This Chapter investigates the thermodynamics of hydrogen intercalation and de-intercalation in metal oxides. These thermodynamics define the driving forces for hydrogen transfers and can differ between unique metal oxide types. The work in this Chapter frames the thermodynamics of H intercalation in metal oxides through two complementary perspectives: electronic structure and geometric structure. Understanding the interplay between electronic structure, geometry, and hydrogen insertion enables the targeted design of metal oxides for H uptake. Accordingly, this Chapter presents the conceptual grounding necessary for the implementation of the thermodynamic scheme presented in Figure 1 of Chapter 1.

2.2 Investigating Electronic Structure as the Driver of Hydrogen Intercalation in Metal Oxides

2.2.1 Introduction

The ability to predict intercalation energetics from first principles is attractive for identifying candidate materials for energy storage, chemical sensing, and catalysis. In this work, we introduce a computational framework that can be used to predict the thermodynamics of hydrogen intercalation in tungsten trioxide (WO_3) Specifically, using density functional theory (DFT), we investigated intercalation energetics as a function of adsorption site and hydrogen stoichiometry. Site-specific acid-base properties determined using DFT were used to develop linear structure screening models that informed a kernel ridge energy prediction model. These regressions provided a series of hydrogen binding energy predictions across stoichiometries ranging from WO_3 to $H_{0.625}WO_3$, which were then converted to equilibrium potentials for hydrogen intercalation. Experimental validation using cyclic voltammetry (CV) measurements yielded good agreement with the predicted intercalation potentials. This methodology enables fast exploration of a large geometric configuration space and reveals an intuitive physical relationship between acidity, basicity, and the thermodynamics of hydrogen intercalation. Furthermore, the combination of theoretical and experimental results suggests $H_{0.500}WO_3$ as a maximum stable stoichiometry for the bronzes that arises from competition with hydrogen evolution rather than the inability of WO_3 to accommodate additional hydrogen. Our experimental results further indicate hydrogen insertion in WO_3 is highly irreversible for low H-stoichiometries, which we propose to be a consequence of the semiconductor-to-metal transition that occurs upon initial H-intercalation. Overall, the agreement between theory and experiment suggests that local acid-base characteristics govern hydrogen intercalation in tungsten trioxide, and this insight can aid the accelerated discovery of redox-active metal oxides for catalytic hydrogenations.

Intercalation is a process where a host material accepts a guest atom into its lattice, subsequently inducing a significant change in material properties. This process is the basis of numerous chemical technologies, including electrochromic devices,[52, 53] sensors,[54, 55] battery materials,[56, 57] and redox catalysis.[58, 59, 60, 61, 62] Tungsten trioxide (WO_3) is of particular interest as an intercalation host for its ability to form stable tungsten trioxide bronzes (M_xWO_3) (where M is a metal or hydrogen).[48, 44, 63] Our specific interest in WO_3 revolves around its use in redox catalysis, where it has been employed both as a catalyst and a catalyst support. For example, methanol oxidation[58, 59] and CO_2 reduction[61, 62] have been shown to benefit from the use of WO_3 or a closely related compound. At their core, these reactions involve the net transfer of protons and electrons (i.e., hydrogen equivalents), which implies that the ability of WO_3 to intercalate hydrogen to form hydrogen tungsten bronze (H_xWO_3 where $0 \leq x \leq 0.5$) may be a critical factor in its catalytic properties.

Tungsten oxide bronzes have also been explored for energy storage applications. Aside from hydrogen, WO_3 is also known to intercalate lithium, sodium, and potassium ions upon the application of an electrochemical potential.[64, 65, 66] The process of electrochemical intercalation involves coupled cation-electron charge transfer, where electrons are injected into the WO_3 along with charge-compensating cation under an appropriately negative electrochemical potential. The reverse de-intercalation process proceeds upon application of a positive potential. The rate of H_xWO_3 formation has been shown to be significantly enhanced upon the inclusion of structural water, and $WO_3 \cdot xH_2O$ can also exhibit both battery-like and pseudocapacitive behaviors.[67, 68] This behavior indicates that WO_3 exhibits complex intercalation mechanisms that depend on its precise composition, microstruture, and chemical environment.

We recently reported that the classical picture of hydrogen spillover—the catalytic hydrogenation of a transition metal oxide—to crystalline WO_3 is mechanistically congruent to electrochemical intercalation, where both can be treated as heterogeneous proton-coupled electron transfer (PCET) reactions.[69] Other work has also demonstrated the ability of WO_3 to engage in simultaneous, spatially separated thermal and electrochemical catalysis, which could confer significant benefits on activity, selectivity, or stability.[70] Together, these results point toward a unified thermodynamic description of the reactivity of hydrogen within metal-oxide hydrogen bronzes like H_xWO_3, which depends on the equilibrium chemical potentials of protons and electrons within the oxide phase.[71]

Considering the inter-relationships between thermochemical and electrochemical reactivity in these systems, the ability to computationally predict the equilibrium potential, U_{eq}, for a wide range of H-intercalation reactions would be valuable for enabling the design of new metal-oxide based hydrogenation catalysts. In this context, hydrogen binding and diffusion in WO_3 has been extensively studied using density functional theory (DFT).[72, 73, 74, 75, 76] Much of this work, however, has focused on narrow ranges of H stoichiometries or has not considered the effects of multiple possible atomic configurations of hydrogen within the H_xWO_3 lattice. To build a complete energetic description of hydrogen insertion and uptake, both denser sampling of compositions and specific examination of the bronze configuration space are needed.

Computational methods for predicting the intercalation thermodynamics of metal oxide materials have also been extensively developed in the context of energy storage materials. A common approach involves constructing a convex energy hull by using DFT calculations.[77, 78, 79] In this method, multiple structural configurations are investigated for a given stoichiometry, where the lowest-energy state is expected to be representative of the experimentally-observed structure. This process is repeated for incremental changes in composition, and all resulting formation energies are placed in the energy-composition plane. A geometric convex hull is then drawn around the array of points, the vertices of which give the stable compositions and the most thermodynamically plausible pathway for the intercalation reaction. Herein, we describe the prediction of proton intercalation in H_xWO_3 by combining DFT calculations with linear and kernel ridge regression techniques to decrease the overall computational expense that would normally be required to sample a wide variety of atomic configurations. We have further coupled the computational results with experimental measurements of the H-intercalation potentials for monoclinic WO_3 in aqueous sulfuric acid solution. This combined computational-experimental approach significantly accelerates the process of predicting H-intercalation potentials and provides additional physical insights regarding how the acid-base and redox chemistries of oxide bronze materials are related.

2.2.2 Computational Methods

Spin-polarized density functional theory calculations were performed using the Vienna Ab-Initio Simulation Package (VASP)[80] and all visualizations were performed using VESTA.[81] The projector augmented wave method was used to model the electronic wavefunctions and the Perdew-Burke-Ernzerhof functional[82] was used to approximate the exchange-correlation energy. Grimme's D3 correction[83] with Becke-Johnson damping[84] was included to account for dispersion effects. The combination of PBE with the D3 correction has been shown to improve the prediction of tungsten oxide bronze formation energies[85] and metal oxide lattice parameters[86] with respect to uncorrected PBE. Integration of the

Brillouin zone was performed using the tetrahedron method with Blöchl corrections.[87] A kinetic energy cutoff of 520 eV was used to construct the plane wave basis set. During geometry relaxations, k-space was sampled using a 3 x 3 x 3 k-point mesh. Electronic energies were converged to variations of less than 1E-6 eV and relaxations were conducted using the conjugate gradient algorithm until all forces were smaller than 0.01 eV/Å.

Periodic calculations were performed using unit cells of WO_3 that contained 8 W atoms, 24 O atoms, and the stoichiometrically relevant number of H atoms. Experimentally determined lattice parameters of monoclinic tungsten trioxide[88] were used to generate the initial, non-intercalated metal oxide structure. Cell shape, volume, and ionic positions in the bare WO_3 were relaxed to find the initial structure for subsequent hydrogen intercalations. Table 4 in Appendix A contains the experimental and DFT relaxed lattice parameters. During structural optimizations of the intercalated H_xWO_3 configurations, cell shape and volume were kept fixed, whereas all atomic positions were allowed to relax. Bader charge analysis was performed using the Henkelman method.[89] Local and projected electronic density of states were generated for each optimized structure using a 5 x 5 x 5 k-point mesh. The occupied and unoccupied electronic band centers were determined from the relevant local, projected density of states.[90]

The binding energies (BE) of hydrogen within the H_xWO_3 lattice were calculated using the following relationship:

$$\Delta E_{j,bind} = E_{j,H_xWO_3} - E_{WO_3} - 4x \cdot E_{H_2} \tag{2.2.1}$$

where E_{j,H_xWO_3} refers to the electronic energy of the bronze formed by binding a hydrogen at oxygen atom j, and x is the ratio of H:W atoms included in the unit cell. E_{H_2} is the energy of a single diatomic hydrogen molecule. These binding energies were used in conjunction with physicochemical descriptors to train the acid-base models.

All regression methods were performed using the `scikit-learn` package[91] implemented in Python. The structural search models were built around multiple linear regressions. Data were generated from random atomic configurations (i.e., positions of the H atoms within the unit cell) at each investigated H-stoichiometry. Twelve data points were used for training and four were used for validation.

For $H_{0.125}WO_3$, the bare WO_3 lattice has 24 possible intercalation configurations, as given by the 24 O atoms in the unit cell. The lowest energy $H_{0.125}WO_3$ configuration was used as the base geometry for $H_{0.250}WO_3$ calculations; hence, all investigated $H_{0.250}WO_3$ geometries shared the same $H_{0.125}WO_3$ starting configuration. This procedure was continued for higher H-stoichiometries, resulting in a linear model for each investigated level of x in H_xWO_3. More rigorous energy predictions were then generated using a kernel ridge regression (KRR) model. A Laplacian kernel with a width of 2.0 was used as the weighting function for the KRR model and the L_2 regularization strength was set to 0.03. Model performance was assessed through mean absolute error (MAE) of validation data computed using 10-fold cross-validation repeated 200 times. We define MAE as $\frac{1}{n} \cdot \sum_i |y_i - x_i|$, where y_i is the model-predicted energy, x_i is the DFT calculated energy, and n is the number of samples.

The site-specific energies predicted using the KRR model were converted to expectation values by weighting and averaging according to the Boltzmann distribution:

$$p_j = \frac{e^{\frac{-\Delta E_{j,pred}}{k_b \cdot T}}}{\sum_k e^{\frac{-\Delta E_{k,pred}}{k_b \cdot T}}} \tag{2.2.2}$$

$$\Delta E_{exp} = \sum_j p_j \cdot \Delta E_{j,pred} \tag{2.2.3}$$

Confidence intervals on the predicted energies were also computed according to these Boltzmann weightings. The full canonical partition function at each stoichiometry was approximated using the $k = 24$ model-predicted energies that resulted from intercalation of the lowest energy configuration from the previous stoichiometry. Model-predicted BE and associated confidence intervals were converted to equilibrium electrochemical potentials for H-intercalation by applying the computational hydrogen electrode model (CHE)[92] to the potential-dependent formation energies of two contiguous stoichiometries:

$$\Delta E_{int} = \Delta E_{H_{x+\Delta x}WO_3,expected} - \Delta E_{H_xWO_3,expected} - 8\Delta x \cdot eU \tag{2.2.4}$$

where e is the charge of the electron and U is the applied electric potential. The equilibrium electrochemical hydrogen intercalation potential, U_{eq}, is the value of U that drives ΔE_{int} to zero. This potential can be directly compared to the empirically observed equilibrium potential versus the reversible hydrogen electrode (RHE). This formulation is mathematically identical to that used in the determination of equilibrium voltage via convex hulls.[77] The full algorithm implementing linear screening models and kernel ridge predictions is outlined in Figure 4.

2.2.3 Experimental Methods

Nanoparticulate WO_3 was prepared using a previously reported ion exchange method.[69] All electrochemical characterization was performed using a Gamry Interface 1000 potentiostat in a three-electrode configuration. Counter and reference electrodes were graphite (Electron Microscopy Sciences 0.25 in. diameter, Spectro-Grade) and Ag/Ag^+ (CH Instruments CHI111P), respectively. The working electrode was WO_3 supported on glassy carbon (GC, CH Instruments CHI104P). In a representative deposition of WO_3 onto GC, 0.085 g of Nafion dispersion (Ion Power, 1100 EW @ 20 wt% in IPA) was mixed with an equivalent weight of synthesized WO_3 powder and 100 μL of deionized water (>18 MΩ-cm, Millipore Advantage A10). The slurry was sonicated for 20 minutes, and then 4 μL were deposited onto the glassy carbon electrode. An infrared heat lamp was used to dry the sample for 10 minutes.

After cooling to room temperature, the sample was immersed in 0.5 M H_2SO_4(aq) electrolyte for electrochemical characterization. The test cell was constructed of borosilicate glass fitted with a custom teflon cap. A nitrogen purge was used to clear the electrolyte of oxygen before testing, and was left running through the duration of each experiment. Cyclic voltammetry experiments were conducted at a scan rate of 1 mV/s and all scans reported herein were the first cycle observed, unless otherwise indicated. The working electrode was thoroughly cleaned and coated with a fresh film after each voltammogram was recorded. Electrochemical impedance spectroscopy (EIS) was performed in an identical cell setup. Measurements were taken at DC potentials of +0.45, +0.30, +0.15, and 0.00 V vs. RHE with an AC modulation of ± 10 mV. Each sample was pre-polarized at the relevant DC potential for 5 minutes prior to the start of EIS data collection. The investigated frequency range was 10 mHz to 100 kHz, moving from high to low frequencies. Data were fit in the complex plane using a Randles circuit that included a Warburg impedance unit in series

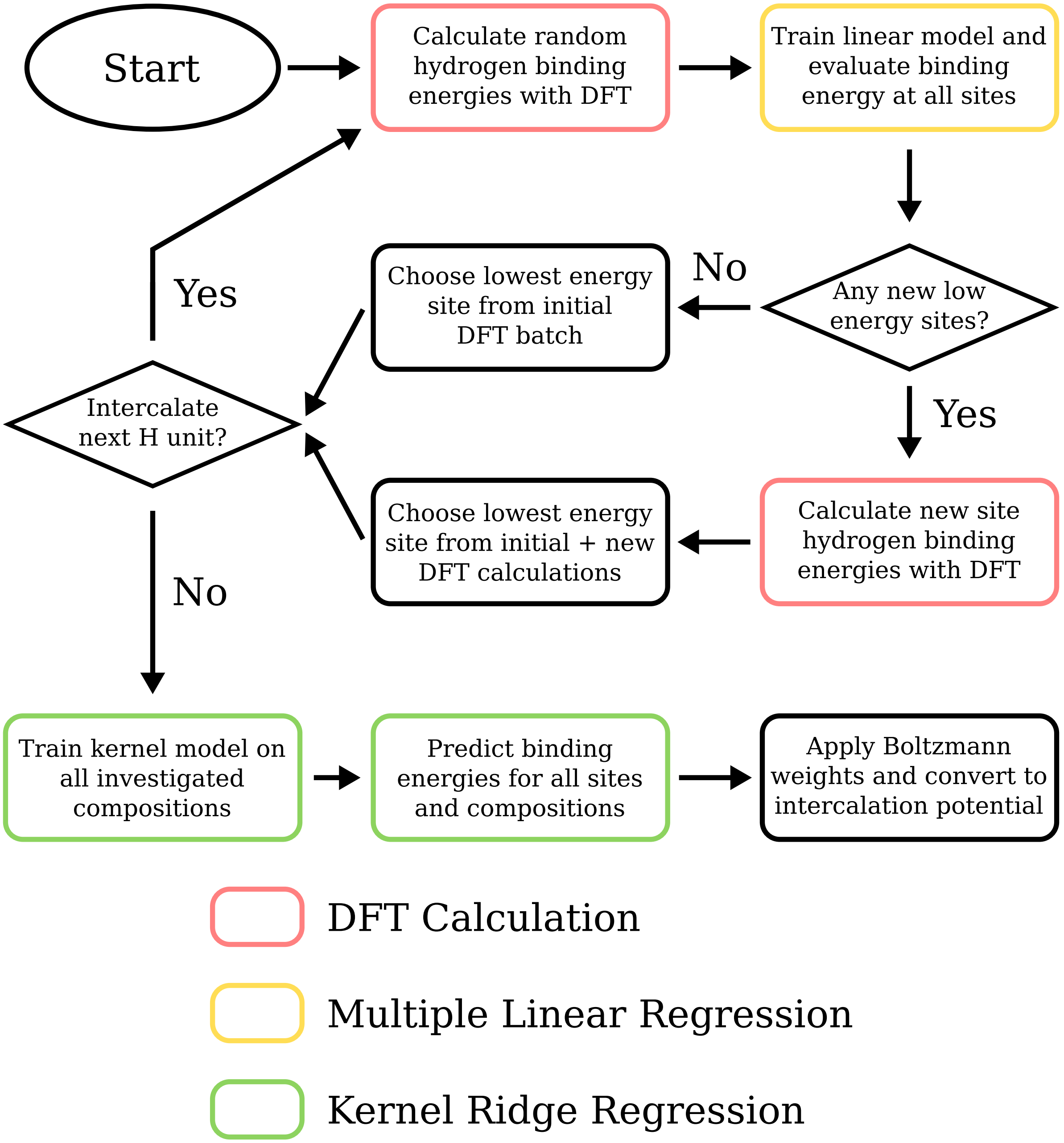

Figure 4: Screening and prediction algorithm used in this work. The goal was to restrict energy predictions to the kernel ridge prediction (green) section, avoiding the expensive DFT (red) sections. This was achieved by accelerating site selection using the linear models (yellow).

with a charge-transfer resistance.

2.2.4 Results and Discussion

Prior reports of hydrogen intercalation into tungsten trioxide have resulted in widely variable observations and interpretations.[67, 68, 93, 94, 95, 96] Crystal structure, particle morphology, substrate, and electrolyte composition all influence the characteristics of resulting voltammetry measurements. We focused on the monoclinic crystal structure because it is thermodynamically stable at ambient conditions and the most commonly observed polymorph. The ion-exchange synthesis method employed here produces a disk-shaped nanomaterial that we previously characterized in detail using XRD, SEM, and HR-TEM.[69] The high aspect ratio of these disks helps to minimize the distance over which H-equivalents diffuse in the bulk, resulting in improved resolution of intercalation features in CV. Figure 43 of Appendix A further demonstrates the benefit of using nanoparticulate WO_3 rather than dense WO_3 prepared by thermal oxidation of W foils.

Figure 5 shows isometric and (001) zone-axis views of the bulk WO_3 model used in this work. $H_{0.500}WO_3$ is also shown to demonstrate the binding locations of hydrogen atoms as well as the associated lattice distortion. The depicted H positions reflect the most exothermic H binding sites, as discussed in detail below.

In principle, generating a rigorous convex energy hull requires the evaluation of every possible atomic configuration for a given composition. Within the framework of DFT, this approach would pose a prohibitive computational cost if attempted for every configuration. For example, Figure 5a shows that a single unit cell of WO_3 has 8 W atoms and 24 O atoms. Even when considering that hydrogen would be expected to bind to the lattice oxygens to form hydroxyl groups;[76, 74, 97] a single H atom insertion into the unit cell has at least 24 possible configurations. Accordingly, not considering symmetries or degeneracies, the number of potential configurations is generally described by the combination 24–choose–x (${}_{24}C_x$), where x is the number of H atoms in a unit cell of W. This rapidly grows to an intractable problem for direct computation via DFT: for the stoichiometry of $H_{0.500}WO_3$, there exist up to ${}_{24}C_4$ (10,626) possible atomic configurations within the unit cell.

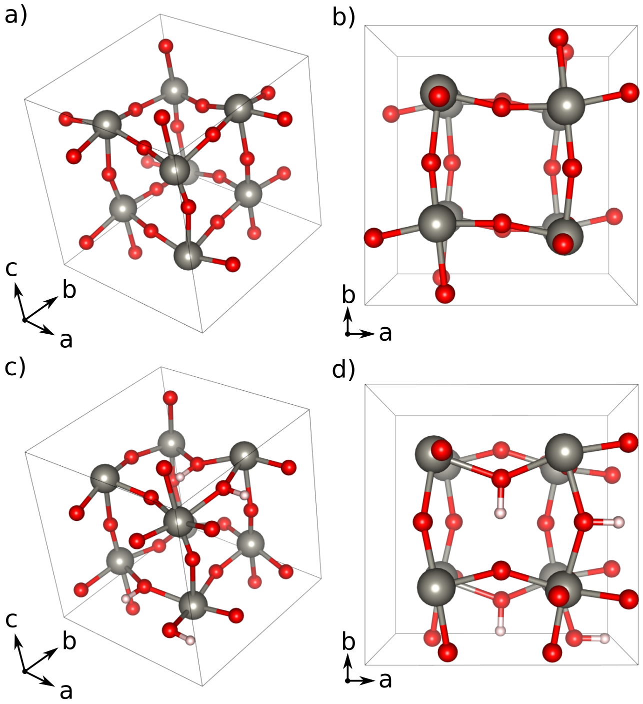

Figure 5: Representative schematics of H_xWO_3 at two different degrees of H intercalation: a) isometric view and b) (001) zone axis view of the WO_3 unit cell; c) isometric and d) (001) zone axis view of the lowest energy configuration of the $H_{0.500}WO_3$ unit cell.

This issue is commonly remedied by employing the cluster expansion method to approximate the energies for viable configurations of the intercalated material.[98, 99] DFT calculations are used to fit the expansion and find the effective cluster interactions, which further enable the determination of relevant thermodynamic quantities using Monte Carlo simulations. Cluster expansion highlights the geometric effects of bulk intercalation on system energy; however, it provides limited information about the relationship between chemical properties and system energy. In an effort to elucidate the relationship between intuitive chemical properties and intercalation energies, we instead applied regression methods commonly used in data science.[100] By doing so, we accelerated the configurational-space search similarly to cluster expansion, while also retaining the ability to describe the underlying physics of the H-intercalation process in WO_3.

Constructing such a model from DFT calculations requires first selecting appropriate descriptors—readily calculable properties of the associated compounds that can then be used to estimate the property of interest via regression models. We chose to use descriptors of the acid-base character of metal oxides, which are widely understood to influence their catalytic activity[101, 102, 103, 104, 105, 106] and also bear strongly on the thermochemistry of PCET processes.[107] Consequently, we expected the intercalation of hydrogen into bulk WO_3 to exhibit a strong relationship between local acid-base character and site-specific hydrogen BE. Mathematically, we represent this relationship as follows:

$$\Delta E_{j,est} = \beta_0 + \sum_i \beta_i x_i \tag{2.2.5}$$

In Equation 2.2.5, the features, x_i, quantify the acidity or basicity of an individual site and the coefficients, β_i, are a series of parameters that can be fit to training data using linear regression.

This formulation describes the screening portion of our approach, where we investigated the candidate descriptors listed in Table 1. These metrics represent various interpretations of local acidity and basicity. Each quantity was calculated for a given site, j. Items labeled “before” were calculated before intercalation, and those labeled “after” were calculated after intercalation occurs at that site. Bader charges were referenced to the number of valence electrons considered for each atom type. The p-band centers were computed for occupied

Table 1: All acid-base properties explored as model features in this work.

Bader Charges	**Projected Band Centers**
$O_{j,before}$	$\epsilon_{p,j,before}$
$O_{j,after}$	$\epsilon_{p,j,after}$
$W_{j,before}$	$\epsilon_{d,j,before}$
$W_{j,after}$	$\epsilon_{d,j,after}$
σ $O_{j,after}$	σ $\epsilon_{p,j,after}$
σ $W_{j,after}$	σ $\epsilon_{d,j,after}$

states, and d-band centers were computed for unoccupied states. Standard deviations (σ) for charges and centers were determined from all 24 site quantities resulting from intercalation at site j. These screening models were constructed individually for each level of stoichiometry to guide the search for the most exothermic configuration. This lowest energy binding site was then used as the starting geometry for the binding of additional hydrogen to iteratively generate the next stoichiometric unit, and ultimately to outline the convex energy hull for H_xWO_3.

Two classes of acid-base quantities were investigated—the first was Bader charge (O_j and W_j in Table 1). The Bader charge directly accounts for electron populations, making it a potential descriptor for Lewis acidity and basicity. Considering intercalation on a generic lattice oxygen site, O_j, the first two descriptors in the first column of Table 1 correspond to the Bader charge of O_j before and after intercalation. Those O sites are also coordinated by two lattice W atoms; the W contributions were therefore computed as the average Bader charge of these neighboring atoms. Finally, perturbations in electron density caused by the introduction of hydrogen were quantified through the standard deviation, σ, of the Bader charges for all O or W atoms in the unit cell. Lower values correspond to a more homogeneous distribution of charge, whereas higher values indicate more heterogeneity. Only the post-intercalation σ was considered because σ is a statistic describing all individual sites; hence, a given configuration has only one σ. The value of σ, however, did change depending on the specific site(s) at which hydrogen binds, since each hydrogen perturbs the oxide electronic structure differently at each site.

The relationship between DFT calculated hydrogen BE and the values of σ for the resulting oxides are shown in Figure 44 of Appendix A. We observed the general trend that more heterogeneous (larger σ) systems have less exothermic BE, suggesting that more homogeneous (smaller σ) systems are more stable. Therefore, the degree of homogeneity can be viewed as a proxy for bulk material stability, with more homogeneous materials being more stable and vice-versa due to increased symmetry.

The second class of descriptors we used comprise the local, projected electronic density of states (DOS). Specifically, the projected band centers (ϵ) were used to quantify the energetic positioning of the electrons involved in bonding. Whereas Bader charge tracks the charge density at each site, the electronic DOS gives information on the propensity for a site to engage in an electron transfer, similar to molecular orbital or hard-soft acid base theory.[108, 109, 110] For example, occupied oxygen p-band centers and unoccupied aluminum s-band centers have previously been shown to correlate with acidity and dissociative hydrogen binding on γ-alumina surfaces.[90] We similarly examined the occupied p-band centers, ϵ_p, of the oxygen atoms. Higher values of ϵ_p are closer to the Fermi level, E_f, and more likely to donate electrons; therefore, they can be considered more basic.

To characterize DOS contributions from tungsten, we examined the unoccupied d-band centers, ϵ_d, of the W atoms coordinating the O sites of interest. This selection was motivated by results shown in Figure 45, where decomposing the total DOS for a representative W atom revealed that low-lying unoccupied states have nearly 100% d-band character. Lower values of ϵ_d are closer to E_f and more likely to accept electrons; accordingly, they can be considered more acidic. Similarly to our treatment of Bader charges, ϵ_p and ϵ_d were determined for an adsorption site before and after intercalation, and standard deviations of the band centers in the resulting oxide were also calculated to evaluate homogeneity of the bulk cell bands.

To further illustrate the use of acid-base descriptors to determine the energetic consequences of H-intercalation in H_xWO_3, Figure 6 visualizes the DOS metrics used to quantify O site acidity and basicity. Figures 6a and 6b demonstrate the positioning of representative projected O p-band and W d-band centers with respect to the Fermi level; these quantify basicity and acidity, respectively. Manual inspection of the results of these calculations

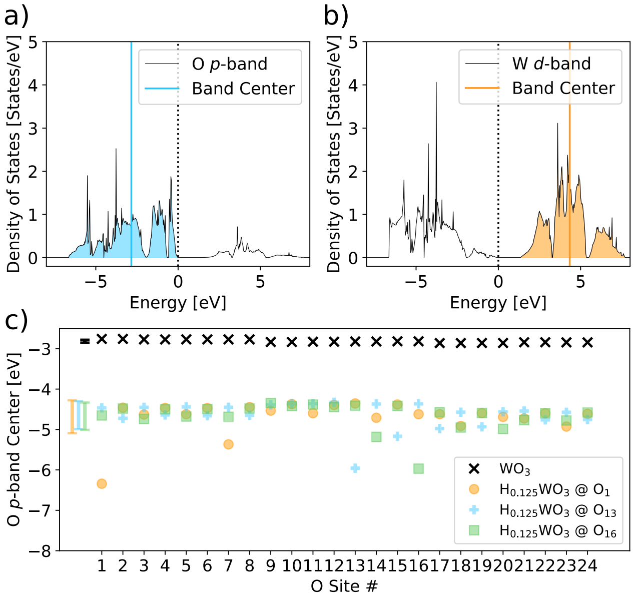

Figure 6: Representative data compiling calculations associated with electronic density of states: a) calculated oxygen p-band centers associated with site basicity; b) calculated tungsten d-band centers associated with site acidity; c) variation in the oxygen p-band center across all the oxygen atoms in the unit cell of WO_3 and three $H_{0.125}WO_3$ examples that vary based on the position of a single H atom in the unit cell. Vertical error bars near the left axis show $\pm 1\ \sigma$ for each group, centered around the respective means.

showed that although the hydrogen atom bonds to oxygen in WO_3, the resulting electron redistribution affects the W d-band. Figure 46 demonstrates how intercalation to $H_{0.125}WO_3$ causes the unoccupied d-states for a representative W atom to shift down and resemble a degenerate semiconductor. With the proton binding to lattice oxygen and the associated electron populating the d-band, both the oxygen and tungsten contributions to adsorption sites are relevant to binding energetics.

We note that GGA exchange-correlation functionals are typically under-performing at predicting the electronic structure of semiconducting materials, with a significant underestimation of electronic band gap. Improved results can be attained from the use of a Hubbard U correction or moving to higher levels of theory, such as using hybrid functionals. Figure 46 further compares the W d-projected DOS between PBE-D3 and the hybrid HSE06[111] functional to examine the potential deviations of the GGA approach. In the context of this work, it is important to note the absolute values of the predicted band centers and Bader charges are not quantitatively significant to the resulting energy predictions. What remains critical to the generation of an accurate model is the gradient of the relationship between the descriptor and the prediction target. This is because the regression models employ a free floating intercept that can correct for constant offsets in the underlying data. Figure 46 clearly shows that the major difference between PBE-D3 and HSE06 electronic structures is a constant offset in band positions, whereas the shape of the DOS does not change very much between functionals. As a result, PBE-D3 seems to be sufficient in capturing the general character of the electronic bands. Considering also the accurate energies returned by PBE-D3 for the WO_3 system[85, 86], we conclude the selected GGA level of theory is acceptable for building the training and validation data sets.

Figure 6c shows the effects of inserting the first unit of hydrogen into the unit cell of WO_3. Prior to intercalation, the p-band centers of O atom sites are essentially indistinguishable from one another, which reflects the homogeneity and symmetry of the bare oxide. The results of binding hydrogen to three different sites—thereby generating three $H_{0.125}WO_3$ polymorphs designated O_1, O_{13}, and O_{16}—are also shown. After hydrogen uptake, all of the O p-band centers within the oxide are shifted more negative, indicating decreased site basicities. These bands are stabilized with respect to the initial empty lattice and become less reactive. This behavior in a bulk solid is directly analogous to the acid-base rules put forth by Metiu et al. for oxide surfaces,[102] where basic (acidic) surfaces become less basic (acidic) upon adsorption of an acid (base). Varying the H-adsorption location results in significantly different energetic perturbations to the locations of O *p*-band centers across the full oxide. Furthermore, due to the adsorption of hydrogen, the site of intercalation always becomes the least basic. Finally, the overall heterogeneity in band center energies also changes depending on the site of intercalation, as illustrated by standard deviations depicted as error bars in the left-hand-side of Figure 6c. Similarly distinctive behavior was observed for the W *d*-band centers, O Bader charges, and W Bader charges, and can be determined for representative configurations across all stoichiometries of H_xWO_3.

The results shown in Figure 6 illustrate that even a modest number of complete electronic structure calculations provides a wealth of information about the site-specific acid-base properties of H_xWO_3 with a given H stoichiometry. We leveraged the availability of this information to examine the extent to which these properties correlate with DFT-calculated hydrogen BE. Figure 7 details descriptor correlation and linear screening model performance. The data shown are for the conversion of $H_{0.125}WO_3$ to $H_{0.250}WO_3$.

The correlation matrix shown in Figure 7a compiles the pair-wise Pearson correlation coefficients (PCC) for all twelve acid-base metrics and the DFT-calculated BE. This type of coefficient ranges from -1 to 1 and indicates the linearity of the correlation between the paired quantities. A value of zero indicates an absence of a linear correlation, while a value of -1 or 1 corresponds to exact linearity. It is important to note that while the sign of the coefficient indicates the direction of correlation, the magnitude only indicates the degree of linearity and not the constant of proportionality.

As an illustrative example, the first column of the matrix in Figure 7a gives the correlations for the DFT BE with each candidate descriptor. The averaged neighboring W atoms' *d*-band centers are negatively correlated with energy: as they become more positive (less acidic), hydrogen binding becomes more preferable. The O *p*-band centers are also negatively correlated with energy: as the centers become more positive (more basic), hydrogen binding becomes more exothermic. These relationships suggests that the hydrogen prefers sites that are more basic overall, which is analogous to the observed relationship between

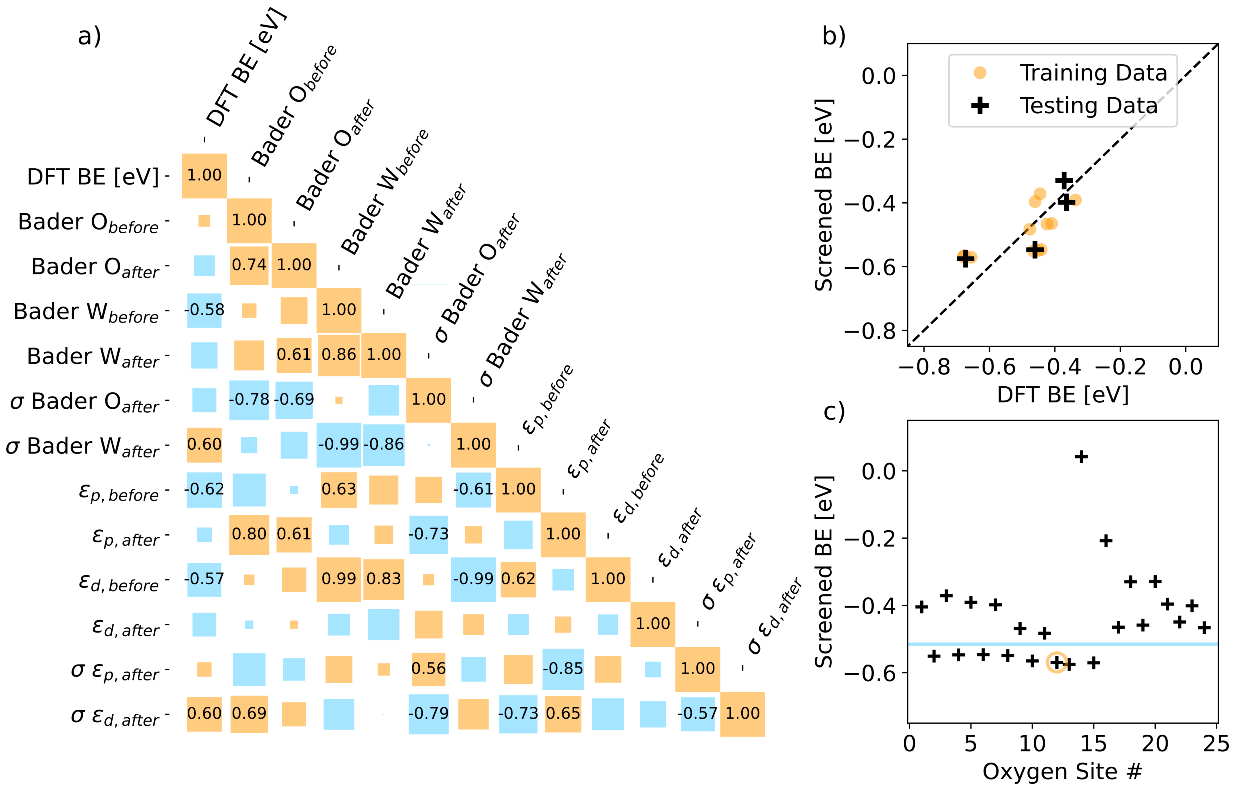

Figure 7: Data used to construct and evaluate linear relationships between acid-base properties and hydrogen BE, shown here for formation of $H_{0.250}WO_3$. a) Pearson correlation coefficient matrix for pairings of acid-base features and BE, with coefficient values only shown for those considered significant (> 0.55 or < -0.55). b) Parity plot showing the linear screening model performance after training on data from DFT calculations. c) Model-predicted BE for each site in the $H_{0.125}WO_3$ lattice for hydrogen BE. The solid line indicates the threshold for conducting an additional explicit DFT calculation to confirm site BE. Although the linear model predictions do not directly identify the most exothermic site according to DFT calculations (circled), they do help accelerate its identification.

Table 2: Linear model coefficients for each change in H:W ratio.

Parameter	**Descriptor**	$\mathbf{H_{0.125}WO_3}$	$\mathbf{H_{0.250}WO_3}$	$\mathbf{H_{0.375}WO_3}$	$\mathbf{H_{0.500}WO_3}$	$\mathbf{H_{0.625}WO_3}$
β_0	Intercept	-117.204	7.751	7.784	-15.682	-14.288
β_1	$\epsilon_{p,j,before}$	0.577	-0.333	-0.487	-0.402	0.054
β_2	$\epsilon_{d,j,before}$	-0.577	0.322	2.639	3.204	5.005
β_3	$W_{j,before}$	44.743	-3.997	-6.801	1.744	0.290

d-band occupancies and adsorbate BE on pure metal surfaces.[112] Revisiting Figure 6, then, it is apparent that a single O atom most likely binds only one H atom, as the adsorption site then becomes significantly less basic than other sites in the oxide.

While the correlations shown in Figure 7 contain dense information about the physical implications of hydrogen uptake, our primary interest was in using them to select appropriate descriptors for the linear screening models. As can be seen, only five of the descriptors exhibit significant ($|\text{PCC}| > 0.55$) linear relationships with the DFT BE. Of these, we selected only the three "before" descriptors to help accelerate screening. This is because using the "after" intercalation descriptors would require DFT calculations to be performed to collect parameters for the model, thereby erasing the computational cost savings when using this data-driven approach. Accordingly, the three features we used were O *p*-band centers, W *d*-band centers, and W Bader charges, all before intercalation. These three were used in all screening models. Table 2 details the coefficients and intercepts determined for each H-stoichiometry in H_xWO_3.

Moving across the rows in Table 2, the magnitudes and signs of the β_i values vary significantly, indicating the relationship between hydrogen BE and each individual feature varies with composition. Rather than fit our acid-base model to the global dataset, splitting according to composition allowed for localization of each model. This local approach has been shown to improve the prediction accuracy of models trained on imbalanced data sets[113] and was employed here to capture the effect of composition on each β_i. Furthermore, this local approach helps avoid a reversal paradox[114] encountered in evaluating energy vs. composition data for intercalating systems. Figure 47 in Appendix A compares the efficacy of using global vs. local data for model training.

The performance of the $H_{0.250}WO_3$ model is depicted in Figure 7b. Importantly, the general trend in energies is captured well by the screening model, highlighting its ability to identify the most exothermic H binding sites. Figure 7c shows the model-predicted hydrogen BE at each oxygen site. Intercalation at the site of the previous H adsorption, O_{14}, is predicted to be endothermic by the model, recapitulating the prior observation that binding multiple units of H to a single site is thermodynamically unfavorable. Binding energies at every other site are predicted to be exothermic and fall within a range of -0.6 to -0.2 eV. The orange circle shows the most exothermic site according to DFT. The cyan line shows the cutoff point for a follow-up DFT analysis: for sites below the cutoff line that had not been previously subjected to a DFT calculation (i.e., they did not appear in the testing or training data), an additional, explicit calculation was performed.

As noted previously, when hydrogen intercalates into WO_3, there are many sites (O atoms) where the H can reside. Figure 8 shows the most exothermic configurations for the H:W ratios of 0.125, 0.250, 0.375, and 0.500. Interestingly, our data suggest that H intercalation in H_xWO_3 follows a staging process akin to lithium intercalation in carbon-based battery materials.[115] When viewing along the (001) zone axis, hydrogen atoms first fill the right-most channel, then the center channel. Viewed along the (100) axis, the atoms populate the cell alternating between the lower and center channels. Thus, it is apparent that hydrogen tends to intercalate in WO_3 in an ordered manner, as revealed through the most exothermic configurations identified by our linear models.

While the linear screening models were successful at identifying trends in hydrogen BE, they did not achieve sufficient accuracy for comparison to experimental results. To improve the accuracy of the predicted H intercalation energies, we constructed a second statistical model using kernel ridge regression (KRR). This model took the most stable configuration at each stoichiometry (identified by the linear models) as an input and predicted the BE for the next unit of hydrogen at every O site. Figure 9 shows the performance of the KRR model as a parity plot that compares the associated predictions with the DFT-calculated BE. Hyperparameter tuning for the KRR model is further discussed in Appendix A and shown in Figure 48.

The KRR model includes the same three descriptors used in the screening stage as well as the initial O Bader charge and the H-stoichiometry itself. Repeated 10-fold cross

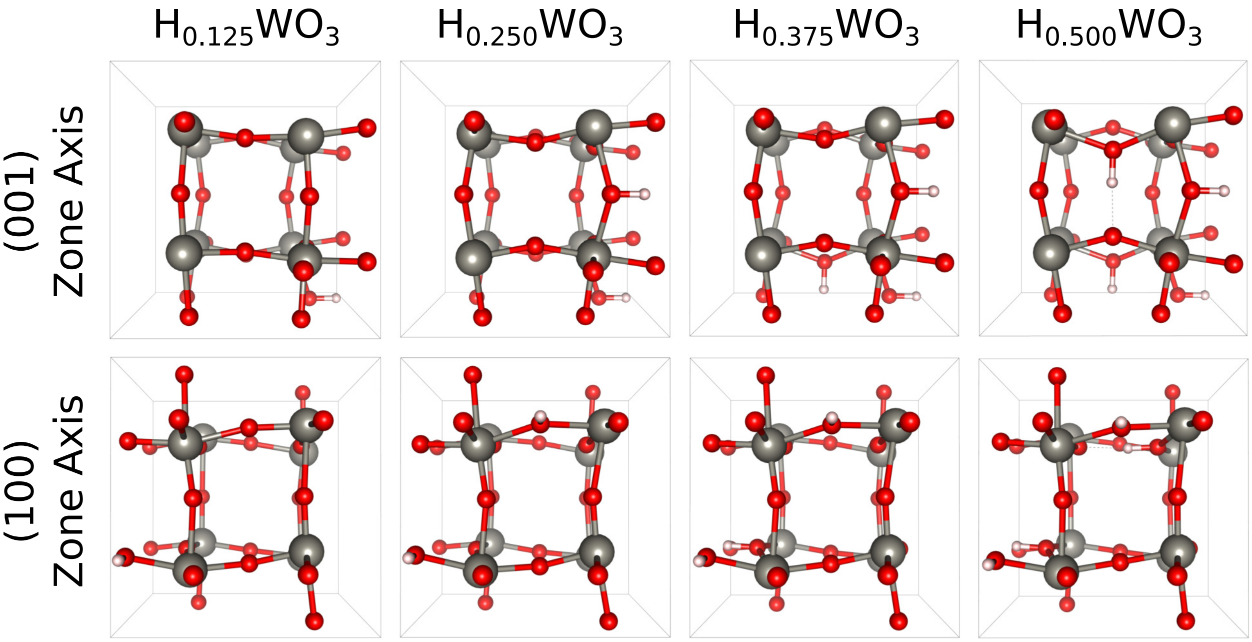

Figure 8: Most exothermic configurations for x = 0.125, 0.250, 0.375, and 0.500 in H_xWO_3 unit cells, increasing from left to right. The first row shows the (001) zone axis, and the second row shows the (100) zone axis. The ordering observed in the (001) axis suggests hydrogen intercalation occurs via staging.

validation showed an average model MAE of 0.063 eV, illustrated by the inset of Figure 9. 94% of all models exhibited an MAE lower than 0.10 eV, therefore we can say that the parameterized KRR model is accurate to 0.10 eV with a p-value of 0.06. One of the biggest differences between the linear models and this KRR model is the local vs. global approach. The global analysis here performs well because KRR is not restricted to linear correlations, but can effectively capture non-linear behavior. Regularization also helps limit the variance in predictions by the KRR model, where the linear models are not regularized.

KRR model results for H_xWO_3 at all of the modeled stoichiometries are compiled in Table 3. The most exothermic DFT-calculated BE (DFT BE) and most exothermic KRR model-predicted BE (KRR BE) for each stoichiometry are shown, along with the expectation energies calculated via Boltzmann weighting of all O site KRR predictions (Expectation BE). DFT intercalation potentials (DFT Potential) were then calculated from the most exothermic BEs per the convex hull formulation, whereas the KRR model-predicted intercalation

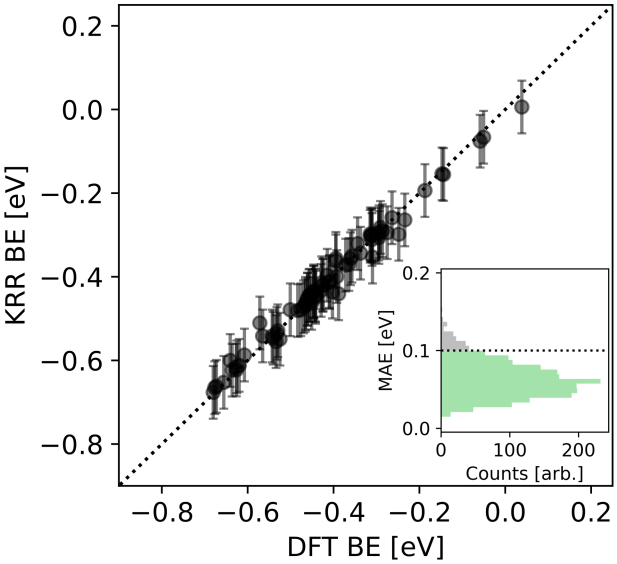

Figure 9: Parity plot demonstrating performance of the acid-base kernel ridge regression model. Error bars are drawn as ±0.063 eV, which was the average MAE resulting from repeated 10-fold cross-validation. The inset is the null distribution of MAE values formed from each model created during cross-validation, with the dotted line demarcating a nominal accuracy limit of 0.10 eV. 94% of all models generated in cross-validation exhibited MAEs lower than this threshold.

Table 3: KRR model predictions compared to DFT calculated values, all in eV.

Energy Type	$\mathbf{H_{0.125}WO_3}$	$\mathbf{H_{0.250}WO_3}$	$\mathbf{H_{0.375}WO_3}$	$\mathbf{H_{0.500}WO_3}$	$\mathbf{H_{0.625}WO_3}$
DFT BE	-0.457	-0.680	-0.641	-0.608	-0.427
KRR BE	-0.445	-0.676	-0.623	-0.587	-0.414
Expectation BE	-0.437	-0.667	-0.610	-0.569	-0.395
DFT Potential	0.457	0.223	-0.040	-0.033	-0.180
KRR Potential	0.437	0.229	-0.057	-0.040	-0.175

potentials (KRR Potential) were calculated from the Expectation BE. Notably, the deviations between the DFT and KRR BE do not exceed 0.021 eV, again demonstrating the ability of KRR to capture the relationship between acidity, basicity, and hydrogen BE.

Figure 10 depicts the complete set of hydrogen BE predictions that resulted from the KRR model. The convex energy hull (solid black line in Figure 10a) considers only the lowest energy configurations. However, this approach does not consider that a system with finite thermal energy may access energy states that are above the minimum, and will likely do so according to a Boltzmann distribution. This can be addressed by using the full KRR dataset to generate expectation values according to Eqs. 2.2.2 and 2.2.3 (orange dots in Figure 10a), which results in predicted hydrogen BE that are slightly higher (less negative) than the most exothermic case. Further application of Boltzmann probabilities enables a confidence interval to be assigned to the expectation value (shaded area in Figure 10a).

These energy vs. composition curves can be interpreted as reaction coordinate diagrams, where the transition from one composition to the next corresponds to a PCET reaction for a unit cell of H_xWO_3 intercalating an additional unit of hydrogen. Accordingly, applying the computational hydrogen electrode formulation enables us to account for the influence of applied potential, as shown in Figure 10b. The equilibrium potential for a given reaction step can be found by varying the applied potential until the step of interest becomes thermoneutral, as indicated by the black brackets. For example, these data predict that the initial transition from WO_3 to $H_{0.125}WO_3$ has an equilibrium reduction potential of 0.44 V vs. RHE.

Interestingly, our calculations show that $H_{0.250}WO_3$, $H_{0.375}WO_3$, and $H_{0.500}WO_3$ are equally stable at an applied potential of -0.04 V vs. RHE. This suggests that $H_{0.250}WO_3$ can

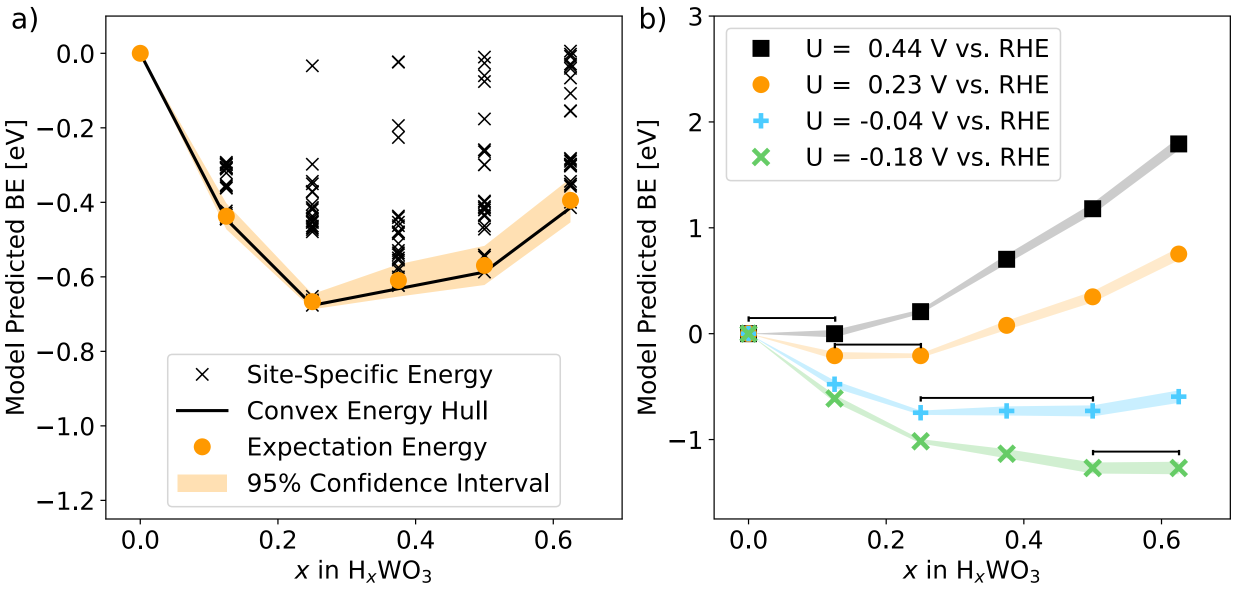

Figure 10: a) Hydrogen BE predictions for 24 configurations of each stoichiometry. Both the lowest energy convex hull and expectation energy interpretations of the data are shown. The shaded area constitutes the 95% confidence interval on the Expectation BE. b) The effect of applying a potential on H_xWO_3. Equilibrium intercalation potentials were taken as the value of U that causes a given increase in stoichiometry to be thermoneutral. The black brackets indicate the neutral step at each applied potential.

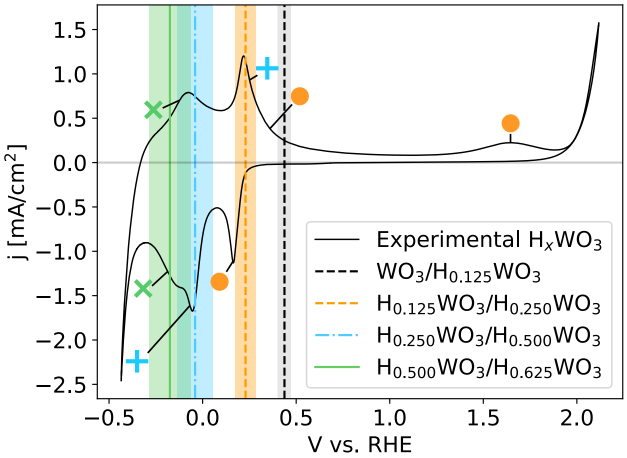

Figure 11: Experimental cyclic voltammogram of H_xWO_3 in 0.5 M H_2SO_4 electrolyte compared to predicted intercalation potentials. The vertical lines show the KRR-predicted intercalation potentials, with the shaded areas showing associated 95% confidence intervals. The symbols further demarcate pairwise assignments of redox features corresponding to H-intercalation and de-intercalation. This scan was performed at a 1 mV/s sweep rate.

be directly reduced to $H_{0.500}WO_3$ without forming the intermediate $H_{0.375}WO_3$ as a thermodynamically stable compound. Furthermore, a large number of $H_{0.125}WO_3$ states are situated only slightly above the convex hull. Accordingly, if H-intercalation via the minimum-energy path exhibits a significant activation energy, it is plausible that WO_3 forms $H_{0.250}WO_3$ with no stable $H_{0.125}WO_3$ phase by passing through these higher energy states. As noted above, hydrogen staging in H_xWO_3 also occurs in increments of 2 H atoms per channel in the unit cell, corresponding to a stoichiometric increment of 0.250. These observations suggest hydrogen population in WO_3 may follow a compositional pathway of WO_3 to $H_{0.250}WO_3$ to $H_{0.500}WO_3$ to $H_{0.625}WO_3$, which is consistent with the experimental observations discussed below.

With computational predictions of equilibrium electrochemical potentials in hand, it is possible to compare theory to experiment. Figure 11 shows a representative cyclic voltammogram of WO_3 in N_2-saturated 0.5 M H_2SO_4(aq) overlaid with the predicted equilibrium potentials shown in Figure 10b. Several redox features were observed in the potential range from −0.5 to 2.2 V vs. RHE. These negative and positive limits were dictated respectively by the hydrogen evolution reaction (HER) and the oxygen evolution reaction (OER), both of which can be accessed by H_xWO_3 without irreversible degradation. The voltammetric features related to H-intercalation and de-intercalation are labeled with colored symbols, along with the Nernst equilibrium potentials predicted by the KRR model.

We observed at least three distinct H-intercalation events in the voltammograms, and each of these exhibited nonzero peak-to-peak separation at scan rates as low as 1 mV/s. This is consistent with kinetic and/or mass transfer limitations, which are known for anhydrous H_xWO_3.[68] Nonetheless, the equilibrium potential for the associated intercalation/de-intercalation reactions must be located between the respective positive and negative peak currents. Accordingly, the predicted equilibrium potential ranges (i.e., expectation values ± 95 % confidence intervals) for each redox couple—$WO_3/H_{0.250}WO_3$, $H_{0.250}WO_3/H_{0.500}WO_3$, and $H_{0.500}WO_3/H_{0.625}WO_3$— agree with the observed features.

The peak assignments are further justified by UV-vis measurements shown in Figure 49. These data show increased absorption across the optical spectrum, confirming the darkening of the film expected with the electrochromism of bronze formation. Tauc plots of the films polarized to various degrees of intercalation also show a loss of semiconducting character, in line with the EIS measurements shown below. Hydrogen insertion also perturbs the crystal structure of the WO_3, as evidenced by XRD results in Figure 50 that indicate a progressive increase in crystal symmetry.

The equilibrium potential for the $WO_3/H_{0.125}WO_3$ redox couple is noticeably unpaired with any features observed in the CV. This observation further supports the notion that $H_{0.125}WO_3$ formation is kinetically sluggish, resulting in the direct formation of $H_{0.250}WO_3$ from WO_3. Beyond the low-lying metastable states that may offer a direct path from WO_3 to $H_{0.250}WO_3$, it is possible that the limited electronic conductivity in bare WO_3 also hinders the rate of electron transfer. Consequently, high overpotentials are needed to drive the WO_3 to $H_{0.125}WO_3$, and it is plausible that they are high enough to overlap with the onset of $H_{0.250}WO_3$ formation. Intercalation onset overpotentials in this case could also be attributable not to reaction kinetics, but instead to the least negative potential that is required to raise the Fermi level of the WO_3 above the conduction band minimum (i.e., to place the semiconductor into strong forward bias).

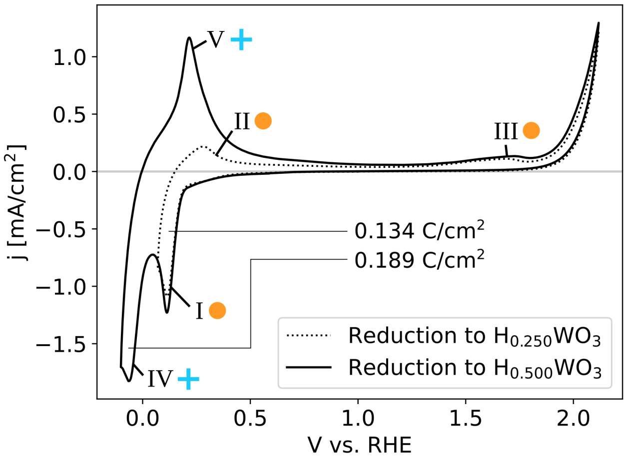

Figure 12: Window-opening CV over the first and second intercalation events showing the irreversible charge-discharge behavior of low H-content H_xWO_3 and the corresponding oxidation feature at ∼1.7 V vs. RHE. These scans were performed at 1 mV/s.

These data also provide a plausible explanation for why $H_{0.500}WO_3$ is frequently observed as the maximum H-stoichiometry in laboratory experiments.[44] The equilibrium potential for the $H_{0.250}WO_3/H_{0.500}WO_3$ couple is modestly negative of 0 V vs. RHE, which means that increasingly negative applied potentials increase the driving force for the hydrogen evolution reaction. Hence, hydrogen evolution likely competes directly with the formation of higher bronze stoichiometries. Specifically, we speculate that $H_{0.625}WO_3$ is unstable toward decomposition via hydrogen evolution, where the reaction product is $H_{0.500}WO_3$, as has been suggested previously.[43]

Figure 12 presents a set of "window-opening" experiments over the potential range encompassing only the initial H-intercalation events. Considering the positions of the redox features and the composition vs. energy profile shown in Figure 7, peaks I and IV apparently correspond to the formation of $H_{0.250}WO_3$ and $H_{0.500}WO_3$, respectively. The expected ratio of IV:I integrated areas is thus 1:1. We observe a slightly larger ratio of 1.41:1 that nonetheless supports the assignments made in Figure 11. The extra charge could perhaps result from overlap between $H_{0.625}WO_3$ reduction and peak IV, which might contribute charge injection beyond the $x = 0.500$ composition. Peak IV also occurs negative of 0.0 V vs. RHE, and so we also cannot rule out additional charge from background hydrogen evolution.

In another intriguing observation, we identified two oxidation features that could be paired with the $WO_3/H_{0.250}WO_3$ redox couple: one at ∼0.25 V vs. RHE and another at a much more positive potential of ∼1.7 V vs. RHE. Peak I corresponds to the initial H-intercalation event; reversing the voltammetric scan at 0.07 V vs. RHE results in two oxidation features, labeled II and III. The control experiment shown in Figure 51, where the CV was initiated as a positive-going sweep starting with no intercalated hydrogen, suggests that peak III is not due to the electrode substrate or adventitious contaminants. Moreover, peak II is not large enough to constitute full removal of H from $H_{0.250}WO_3$, and we observed that the distinctive blue coloration of H_xWO_3 was only fully converted back to the initial pale yellow/green upon cycling to large positive potentials or allowing the sample to stand in air for at least several minutes. Hence, although a small overpotential is required to initiate de-intercalation of hydrogen from $H_{0.250}WO_3$, a much larger positive bias is required to fully de-intercalate the bronze.

We postulate that the irreversibility of intercalation is not primarily attributable to classical electron-transfer kinetics, but instead to the distinct difference in electronic conductivity between WO_3 and H_xWO_3. It is well established that H-intercalation in WO_3 induces a semiconductor-to-metal transition;[116] accordingly, de-intercalation leads to a transition from a metallic state to a semiconducting one. This may give rise to the situation schematized in Figure 13a, where the final units of hydrogen in H_xWO_3 ($x < 0.250$) become isolated from the substrate by a layer of semiconducting WO_3. This “stranded” hydrogen would only then be removed from the bronze upon application of a sufficiently large overvoltage to induce electromigration of the remaining H units and/or dielectric breakdown of the oxide layer. Similar observations of irreversibility have been previously made for lithium ion trapping in WO_3.[117]

The irreversible coloration of the film could also be due to loss of lattice oxygen and formation of substoichiometric WO_{3-x}.[118] Although this is plausible, we observe a full return to the yellow-green color of the original oxide if samples are left in ambient air. Because gain or loss of lattice oxygen involves multiple electron transfers, we do not expect ambient oxygen to convert WO_{3-x} to WO_3 at an appreciable rate; we therefore conclude that the trapping of hydrogen equivalents is responsible for the irreversibility of film coloration.

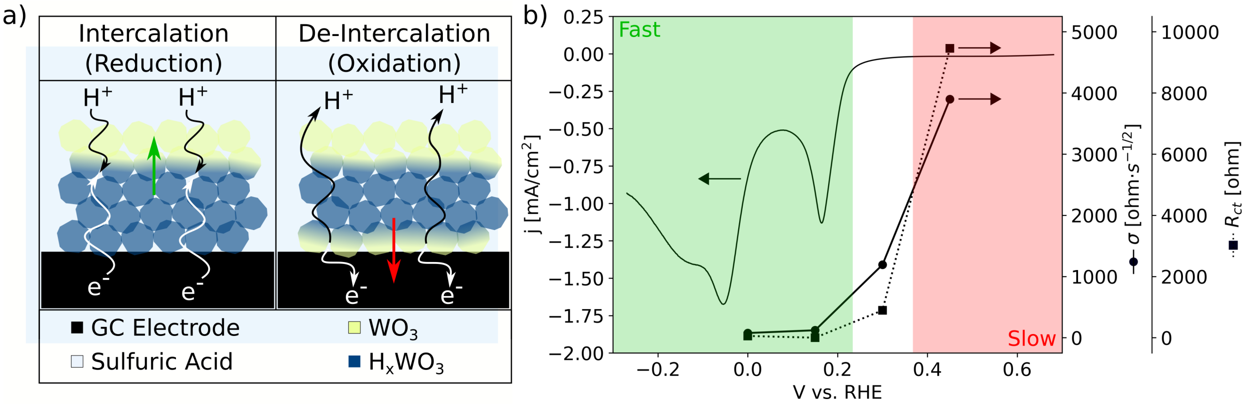

Figure 13: a) Illustration of the stranding effect that may result from the metal-to-semiconductor transition in H_xWO_3 (x < 0.250) upon hydrogen removal and b) EIS fit parameters demonstrating significant mass and charge-transfer limitations for non-intercalated bronze.

Further studies to understand this effect are warranted, as this type of irreversibility presents a challenge when using WO_3 in energy storage, optoelectronics, or redox catalysis.

Figure 13b shows the results of fitting a Randles circuit to impedance data taken at various potentials. The raw data and fits are shown in Figure 52 of Appendix A. It is clear that the parent WO_3 exhibits a large charge-transfer resistance (R_{ct}) and appreciable mass transfer limitations for charge transfer (Warburg coefficient, σ). Polarization to potentials that coincide with H-intercalation results in a drastic reduction in both of these parameters, suggesting charge transfer is much faster in bronzes than in the pure oxide. Interestingly, the reduction in σ and R_{ct} begins even positive of the initial intercalation (peak I in Figure 12) at ∼0.30 V vs. RHE. We also observed an initial small cathodic current upon polarization of the sample at 0.3 V vs. RHE prior to collecting impedance data. This leads us to believe that the improved charge-transfer rate is related to either a small amount of charge accumulation at the nanoparticle-electrolyte interface or near-surface proton reduction. Regardless, the EIS data clearly show that WO_3 and H_xWO_3 are characterized by vastly different charge-transfer dynamics.

2.2.5 Conclusions

We have introduced a computational framework to predict and rationalize hydrogen intercalation thermodynamics in H_xWO_3 using acid-base properties that can be readily calculated with computationally inexpensive DFT methods. Pair-wise correlations between hydrogen BE, density of states, and Bader charges revealed an intimate relationship between acidity, basicity, and hydrogen intercalation energies that is broadly indicative of the reaction as proton-coupled electron transfer. By applying data science methods, we predicted the most stable atomic configurations and the associated hydrogen BE in H_xWO_3 using an accelerated scheme that replaces large-scale DFT calculations with targeted ones based on statistical regression. The additional application of Boltzmann statistics to each of these predicted intercalation configurations enabled us to calculate expectation values and physically meaningful confidence intervals for the equilibrium potentials of H-intercalation reactions. The resulting predictions agreed with experiments, both in terms of the total number of distinct redox events and their onset potentials. Electrochemical measurements on crystalline H_xWO_3 also evidenced significant irreversibility for H-intercalation at low hydrogen stoichiomeries, possibly due to electronic conductivity limitations associated with the known semiconductor-to-metal transition in this hydrogen bronze.

In summary, this work provides valuable insights into factors that influence hydrogen uptake in WO_3 across the full range of experimentally accessible H-stoichiometries. More broadly, we have introduced a computational framework that can be applied to other oxide bronze materials to elucidate the composition-dependent energetics of hydrogen intercalation. Our work outlines a pathway for accelerated computational materials discovery of redox-active metal oxides of interest for applications in catalysis and energy storage.

2.3 Investigating Geometric Structure as the Driver of Hydrogen Intercalation in Metal Oxides

Cation intercalation into metal oxide hosts is critical to many technologies, including energy storage [119], optoelectronics [120], and catalysis [121]. Numerous experimental and computational techniques have been used to understand this phenomenon, including analytical electrochemistry [122], X-ray techniques [123], infrared measurements [124], and density functional theory (DFT) calculations [125]. These methods are regularly applied in concert [126] and provide multi-faceted views of how a material engages in intercalation. However, these approaches can be costly and/or time-consuming, inhibiting the development of application-specific intercalation materials. This limitation is not restricted to cation intercalation and is generally relevant to processes involving the formation or breakage of chemical bonds.

Structure-based descriptors [127] have been employed to accelerate the characterization of bonding interactions in materials. These descriptors have been shown to correlate with difficult-to-obtain performance indicators, such as reaction rates and adsorption energies [128]. The simplest example is the local coordination number (LCN), which is an integer giving the number of bonds that connect a specific atom to its neighbors [129]. Notable extensions of the LCN are the generalized coordination number (for sites on metal nanoparticles) [130] and the adjusted coordination number (for sites on metal oxides) [131]. A further adaptation of the LCN is the orbitalwise coordination number [132], which incorporates additional information about electron structure. Although each are powerful descriptors of chemical interactions, calculating these LCNs requires material-specific parameterization or the use of costly quantum chemical methods, limiting their ability to drive exploratory materials design.

In pursuit of increased generality and rapid prediction of bonding thermodynamics, more modern descriptors of structure venture beyond scalar LCNs to higher dimensional constructs that encode a given material as a graph [133]. While LCNs describe the local environment in which a chemical reaction occurs, graph descriptors detail the full global structure of a material. The state-of-the-art in machine learning applied to describing chemical bonding

[134, 135] uses graph representations to make exceptional predictions of energetic behavior, suggesting that global connectivity—not just local coordination—could be used to describe and predict the thermodynamics of chemical bonding. It is therefore plausible that multiple scales of connectivity contribute to observable chemical behavior.

This section demonstrates how global and local connectivities can be used together to quantitatively predict the equilibrium energetics of hydrogen intercalation in metal oxides. We have previously investigated hydrogen intercalation in tungsten oxide using acid-base properties as descriptors [39]; however, these properties must be determined via computationally-demanding quantum chemical calculations. This work expands the set of materials under investigation and uses inexpensive, structure-based descriptors to determine the energetics of hydrogen intercalation in oxides. Here, we introduce a mathematical definition of global connectivity, Ω. Importantly, Ω is a single number (not a full graph or matrix) that characterizes the overall connectivity of a structure. It is therefore as interpretable as a LCN and can be used to differentiate between materials based on their distinct geometries. Equations 2.3.1-2.3.4 summarize the definition of Ω for a general atomic structure, and Figure 14 illustrates the calculation of Ω for two contrasting examples of fictitious metal oxides.

$$\mathcal{L}(u,v) = \begin{cases} 1, & \text{if } u = v \\ -\frac{1}{\sqrt{d_u d_v}}, & \text{if } u \neq v \text{ and } u \text{ is adjacent to } v \\ 0, & \text{otherwise} \end{cases} \tag{2.3.1}$$

$$\mathcal{L}X = \boldsymbol{\lambda}X \tag{2.3.2}$$

$$LEL = \sum_k \sqrt{\lambda_k} \tag{2.3.3}$$

$$\Omega = \frac{\sqrt{\lambda_1} + \sqrt{\lambda_\epsilon}}{LEL} \tag{2.3.4}$$

Equation 2.3.1 gives the symmetric normalized Laplacian matrix [136], $\mathcal{L}$, which catalogs a structure's atom-to-atom connections. $\mathcal{L}$ is an NxN matrix, with N being the total number of atoms contained in the molecule, nanoparticle, unit cell, etc. For the oxides in this work,

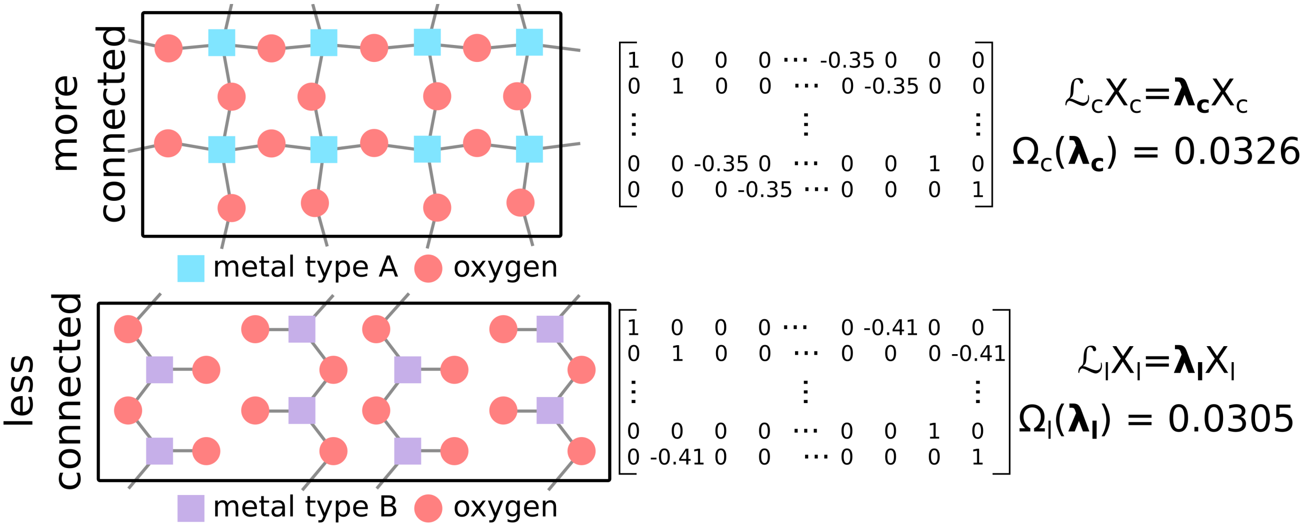

Figure 14: Scheme for calculating Ω for two example oxide systems. The top system is more connected and the bottom system is less connected; atoms in the top system are, on average, bonded to more neighboring atoms than those in the bottom system. Portions of the $\mathcal{L}$ matrices for each system are shown in the center column. Each entry is computed according to Equation 2.3.1. Performing eigenvalue decompositions on $\mathcal{L}_c$ and $\mathcal{L}_l$ yields the full eigenvalue spectra, $\boldsymbol{\lambda_c}$ and $\boldsymbol{\lambda_l}$. Ω_c and Ω_l are computed from these spectra according to Equation 2.3.4. More connected systems have larger Ω values.

N includes all metal, oxygen, and hydrogen atoms present in the unit cell. Therefore, N increases with higher levels of hydrogen insertion. In Equation 2.3.1, u and v are atom indices and d_i is the degree of atom i. Here, the degree is the LCN of an atom, i.e. the number of atoms which are directly bonded to it. Further discussion on $\mathcal{L}$ is included in Appendix A. Notably, $\mathcal{L}$ can be constructed without the use of bond distances and angles. It can be determined for an arbitrary system without any geometry optimization or specific knowledge of spatial arrangement. This is demonstrated in Figure 14, which shows a more connected oxide in the top row and a less connected oxide in the bottom row. More connected systems are those that are more coordinatively saturated and densely bonded. The center column of Figure 14 shows portions of the unique $\mathcal{L}$ representations of each oxide, computed according to Equation 2.3.1.

The spectrum of eigenvalues for a given system, $\boldsymbol{\lambda}$, is determined from $\mathcal{L}$ with Equation 2.3.2. In this eigenvalue decomposition, $\boldsymbol{\lambda}$ is a vector containing N entries and X is the corresponding set of N eigenfunctions. $\boldsymbol{\lambda}$ is invariant to the ordering of rows and columns in $\mathcal{L}$, i.e. the sequence of atom labeling does not impact the resulting spectrum. When ordering from smallest to largest, the first entry, λ_0, is always zero. All remaining entries are strictly positive and lie between zero and 2 because of the normalization of $\mathcal{L}$ [136].

Ω is calculated from three quantities given by $\boldsymbol{\lambda}$: the algebraic connectivity, λ_1 [137], the spectral gap, λ_ϵ [138], and the Laplacian-Energy Like invariant, LEL [139]. The invariance of $\boldsymbol{\lambda}$ asserts that these three values are also insensitive to atom numbering. As a result, they are known as graph invariants. Each holds unique information regarding the structure of the atomic system described by a particular $\mathcal{L}$ matrix.

λ_1 is the second entry of $\boldsymbol{\lambda}$ when the eigenvalues are ordered from smallest to largest. It has been shown to quantify the connectivity of networks represented by $\mathcal{L}$, where smaller values are less connected and larger values are more connected [137]. For example, the more connected oxide in Figure 14 has a λ_1 of 0.134, while the less connected oxide has a λ_1 of 0. A weakness of λ_1 is that it cannot distinguish different systems if they individually contain non-bonded sections: they will each have λ_1 values of 0, even if their geometries are dramatically dissimilar. Including λ_ϵ in the definition of Ω helps alleviate this limitation. λ_ϵ is the smallest non-zero eigenvalue of $\mathcal{L}$ [138]. It quantifies how easy it is to traverse from one point in a graph to another. Smaller values indicate that a structure contains multiple isolated parts which are connected by a small number of bonds. Because λ_ϵ is defined to be non-zero, it can uniquely characterize layered systems that cannot be distinguished via λ_1.

Finally, the LEL invariant is used to scale λ_1 and λ_ϵ to make fair comparisons between systems containing different numbers of atoms. It is computed as the sum of the square roots of all entries in $\boldsymbol{\lambda}$, according to Equation 2.3.3. The LEL invariant is used as a normalization factor to account for effects on global connectivities computed for systems of different sizes.

Equation 2.3.4 defines the global connectivity, Ω, of a chemical system using each of the three graph invariants discussed above. Ω ranges from 0 to 1 and can be interpreted as the fraction of $\boldsymbol{\lambda}$ associated with a system's connectivity. This is illustrated in Figure 14, with the more connected oxide exhibiting a larger Ω than the less connected oxide. With this definition of Ω, we introduce the concept of global connectivity to explore the thermodynamics of hydrogen intercalation in metal oxides. First, we generated a dataset of hydrogen binding energies at various lattice oxygen sites in five bulk metal oxides. These binding energies were computed using DFT. Details are given in Appendix A. The oxides we considered include V_2O_5, MoO_3, WO_3, VO_2, and TiO_2, as described in Section S3. Figure 15 shows how the DFT binding energies of hydrogen atoms in each oxide correlate with the inverse of Ω. As can be seen, oxides with smaller Ω values (less connected systems) exhibit more exothermic H-binding energies. These systems contain a large number of under-coordinated sites which are amenable to bonding with a guest hydrogen atom. Systems with higher Ω values have sites that are more coordinatively saturated, resulting in more endothermic (or less exothermic) binding.

Although Figure 15 suggests a relationship between hydrogen binding energies and Ω, in some cases, single values of Ω returned multiple values of hydrogen binding energies. This is a consequence of the global nature of Ω: a given oxide has a unique Ω value, so that independent site types within its structure can not be differentiated. These multiple site types also present many possible intercalation configurations [39]. The colored symbols in Figure 15 show the energetics of the most stable binding configurations for each investigated oxide stoichiometry, and the black symbols show the unstable configurations. A line of best fit was drawn considering the most stable intercalated systems, since these are the ones with

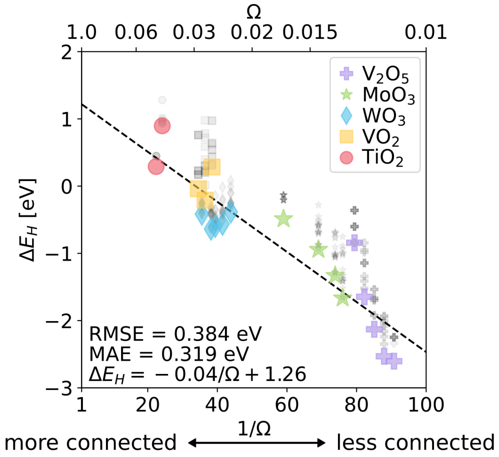

Figure 15: Correlation between hydrogen binding energies in extended metal oxides with the inverse of the global connectivity, Ω. Less connected oxides containing a larger number of under-coordinated sites bind hydrogen atoms more strongly and more connected systems with fully saturated atoms bind hydrogen more weakly. The larger colored symbols represent stable configurations at each stoichiometry, and the black symbols correspond to unstable configurations. A line of best fit is drawn through the set of stable configurations.

the highest probability of contributing to observed intercalation behavior.

Overall, Ω captured the trend of increasing H binding strength across oxides ($TiO_2 < VO_2 < WO_3 < MoO_3 < V_2O_5$), illustrating its ability to describe meaningful structural traits of each metal oxide. However, using Ω alone as a descriptor for hydrogen binding energy gives an uncertainty >0.3 eV, which is too large to quantitatively predict the equilibrium energetics of hydrogen intercalation. The invariability of Ω with atomic configuration also makes it impossible to obtain precise site-specific hydrogen binding energies from Ω alone.

Hydrogen (proton-coupled electron) intercalation into metal oxides can be viewed as two events: 1. binding of a proton to a lattice oxygen and 2. addition of an electron in the diffuse oxide conduction bands. The global nature of Ω could capture information relevant to event 2. However, proton affinity (relevant to event 1.) is dependent on local site coordination [140]. Therefore, we hypothesized that augmenting Ω with a local coordination descriptor could provide superior predictions of hydrogen insertion behavior in metal oxides. To construct an intercalation model capable of explaining site-specific energetics, we included local information through a scaled coordination number, CN_s, defined by Equation 2.3.5:

$$CN_s = \frac{\#\text{ of bonds in neighborhood}}{\#\text{ of bonds in unit cell}} \tag{2.3.5}$$

The numerator is the number of bonds within two nearest-neighbors of the site of interest, demonstrated by Figure 57 of Appendix A. The denominator is the total number of bonds in the unit cell (according to the relevant oxide crystal structure). Hence, CN_s is the fraction of bonds in the unit cell which are associated with a given site. This description of local coordination differentiates each site type and assists Ω in describing hydrogen intercalation energies. Taken together, Ω and CN_s quantify structure at global and local scales.

Figure 6 summarizes the performance of a kernel ridge regression (KRR) model that was used to calculate hydrogen intercalation energies using only Ω and CN_s. This model was trained on DFT-calculated hydrogen binding energies in the investigated metal oxides. Full details on model construction are included in Section S5. Intercalation chemistry is typically analyzed through the use of convex energy hulls, such as those shown in Figure 6a. The x-axis shows the amount of hydrogen contained in the oxide lattice, and the y-axis is the formation energy of a given intercalated oxide. As can be seen, the KRR model reproduced the DFT convex energy hulls with a root mean square error (RMSE) of 0.129 eV and a mean absolute error (MAE) of 0.089 eV (in terms of H-binding energy on a site-specific basis). Accordingly, Figure 6a suggests that Ω and CN_s could be useful descriptors of hydrogen binding in these metal oxides.

While the convex hulls identify stable phases of intercalated oxides, a more practical thermodynamic quantity is the hydrogen intercalation potential, U_H. These potentials can be calculated from the slopes of the convex energy hulls (see Appendix A). Figure 16b compares experimental U_H values to those calculated from the KRR hulls. Each horizontal grouping of data points is a collection of experimentally measured U_H values for a single H-intercalation equilibrium potential. For example, the red circles are the $TiO_2/H_{0.125}TiO_2$ redox couple. The vertical lines on each data point are the error associated with the model prediction, taken as the MAE of the KRR model (±0.089 eV). The filled markers are data extracted from published literature reports [33, 34, 35, 36, 37, 38, 39, 40, 41, 42] and the open markers are from measurements we performed as a part of this work. Methods used to

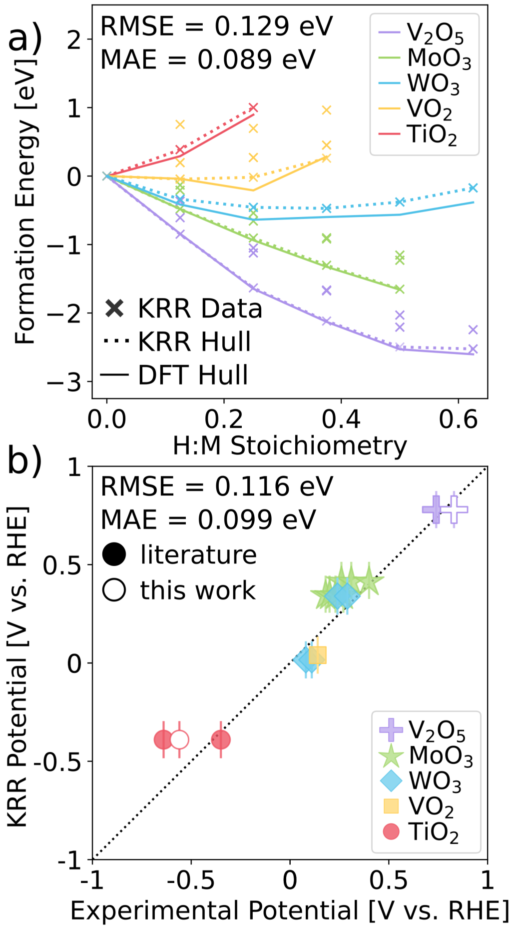

Figure 16: Performance of connectivity–based regression model in evaluating hydrogen intercalation energies and potentials in metal oxides. a) Convex energy hulls for five different oxides, with solid lines representing DFT-computed hulls and dotted lines showing the regression model-predicted hulls. All formation energies are referenced to the non-intercalated oxide and gaseous H_2. b) Comparison between experimental and regression model-predicted intercalation potentials. Vertical lines show ± the KRR model error. Filled symbols are published experimental reports and open symbols are experiments performed in this work.

obtain the experimental data included in Figure 16b are described further in Appendix A.

In general, the KRR model reproduced experimental potentials with an accuracy that would be expected from DFT calculated potentials, giving a RMSE of 0.116 eV. Furthermore, for oxides with data on more than one hydrogen intercalation equilibrium, the structure-based model correctly captured the phenomena of higher stoichiometries having more negative intercalation potentials. The performance of Ω and CN_s versus other metrics of connectivity is provided in Appendix A. We reiterate that determining Ω and CN_s did not require any quantum chemical calculations or other expensive computations other than generating data for developing the model. These features therefore provide a rapid route for determining hydrogen intercalation potentials in metal oxides that is based entirely on the structure of the parent oxides. In principle, the same statistical models could be built using experimental data from one set of metal oxides to predict insertion potentials of another set.

To interrogate the physical relevance of Ω to intercalation, we applied a convolutional neural network (CNN) to the same regression task addressed with the KRR model. The major difference in this approach was that the inputs were taken directly as the $\mathcal{L}$ matrices. During training, this allowed the CNN to auto-embed representations of $\mathcal{L}$ which were significant to hydrogen intercalation. If the CNN emmbeddings correlate with Ω, that would suggest Ω is a meaningful metric of connectivity. The results of this analysis are shown in Figure 17, and full implementation details of the CNN are described in Appendix A.

The axes in Figure 17 are the first and second principal components of the CNN's final hidden layer. Each data point is an intercalated oxide, and the color represents each oxide's global connectivity. There is a clear gradient in color moving from left to right in Figure 17, suggesting that Ω is strongly correlated with the feature space that was generated by the network. The hidden layer node values, and therefore their principal components, are interpretable as features that have been self-generated by the network during training. Hence, without explicitly considering Equations 2.3.1–2.3.4, the CNN arrived at a hidden layer feature space that closely resembled Ω. This interpretation of our model gives further evidence of system-scale, global connectivity as a physically meaningful descriptor of hydrogen intercalation thermodynamics in metal oxides.

In conclusion, this work introduced global connectivity, Ω, as a reactivity descriptor in

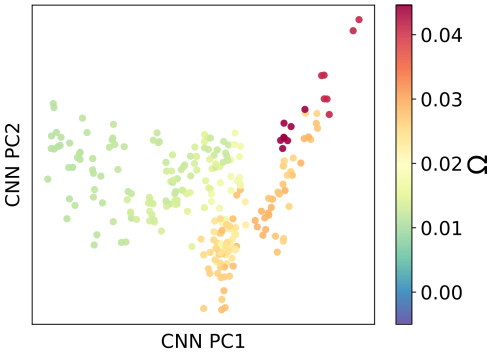

Figure 17: Interrogating symmetric normalized Laplacians with a convolutional neural network. 2D heat map illustrating how Ω strongly correlates with the primary and secondary principal components of the network's final hidden layer embeddings. The gradient in color from left to right suggests that the convolutional network extracted the global connectivity from the input $\mathcal{L}$ matrices, highlighting the importance of Ω in determining the energetics of hydrogen intercalation in metal oxides.

redox-active metal oxides. We first derived an expression for Ω and illustrated its roots in spectral graph theory. Using DFT to calculate hydrogen intercalation energies in a set of five oxides, we showed that Ω captured the general thermodynamic trends of intercalation. Then, we combined Ω with a scaled local coordination, CN_s, to build a regression model that depended only on structural information that is readily obtained from experiment. This structure-based model leveraged both global and local connectivities to accurately capture the trends and values of hydrogen intercalation potentials across all investigated oxides when compared against electrochemical experiments performed in the lab. To further support Ω as a meaningful descriptor of oxide redox reactivity, we applied a convolutional neural network to convert Laplacian matrices directly into hydrogen intercalation energies. We observed a strong correlation between the principal component space of the final hidden layer of the network and Ω, suggesting that the CNN embedded the linear algebra that links $\mathcal{L}$ and Ω. Future work can further develop the concept of global connectivity by incorporating more node- and edge-level information into $\mathcal{L}$. These information-rich Laplacians could then be compared to more sophisticated network models, such as crystal graph convolutional neural networks [133]. Overall, this work introduces Ω as a useful metric for global connectivity and demonstrates how simplified representations of global and local structure can be used together to predict hydrogen binding in metal oxides. Our model has the potential to advance materials design by translating chemical information to local and global connectivity descriptors, aiding both materials discovery acceleration and optimization.

3.0 Hydrogen Transport in Tungsten Oxide Nanoparticle Films

This chapter is reproduced from “Comparisons of WO_3 reduction to H_xWO_3 under thermochemical and electrochemical control,” which was published in the Journal of Materials Chemistry A.[69]

3.1 Context

The work presented here examines the transport of hydrogen in tungsten oxide thin films. Rapid transport of H into, through, and out of an oxide is critical to the practical implementation of the framework shown in Figure 1. Using tungsten oxide as a model material, this Chapter quantifies hydrogen transport under a variety of conditions. The central finding is that bulk H diffusion in tungsten oxide is slow. Rapid H transport only occurs in the presence of an additional proton-conducting medium that facilitates proton-coupled electron transfer. Without the ability to engage in proton-coupled electron transfer, H diffuses only a few 10s of microns over the course of many minutes in bulk tungsten oxide. This suggests that deploying oxides as H mediators will require the targeted enhancement of bulk H transport and guides the reactor-level hydrogenations performed in Chapter 5.

3.2 Introduction

Projections from the US EIA show the industrial sector surpassing the transportation sector in net energy consumption within the next decade.[141] This anticipated transition underscores the need to increase the energy efficiencies of industrial chemical conversions. Moreover, the chemical industry remains broadly dependent on fossil resources both as energy inputs and feedstocks.[142] A massive increase in the availability of renewable electricity is projected to occur alongside the increase in industrial fuel consumption,[141, 143, 144, 145] presenting a unique opportunity to pursue electrification as a means to decrease the environmental impacts of commodity chemical production. [146, 147, 148] With this objective in mind, studying the inter-relationships between thermal and electrochemical catalysis will be integral to the development of advanced technologies for electrification of the commodity chemical industry.

Numerous prior reports have pointed toward interesting opportunities to integrate thermal and electrochemical reactivity to improve catalytic processes. Among the most prominent of these involve the concept of nonfaradaic electrochemical modification of chemical activity (NEMCA; also called electrochemical promotion of catalysis, EPOC).[149, 150, 151, 152, 153, 154, 155, 156, 157, 158] NEMCA effects are seen when fuel-cell-like assemblies are placed within thermochemical reaction environments and then polarized, which accelerates the desired reaction by modulating the coverage of reactive species on catalyst surfaces. Electrochemical potential has also been used to drive Faradaic processes to improve reactor performance, as in recent reports involving the use of electroactive membranes to control product selectivity in methane dehydroaromatization and steam methane reforming. [159, 160] Membrane-based approaches have also been used to generate reactive hydrogen directly via electrolysis, as in Itoh's report of benzene hydrogenation to cyclohexane and Sherbo's demonstration of phenylacetylene hydrogenation to ethylbenzene. [161, 162] Interfacial electron transfer processes have also been implicated as key elementary steps in nominally thermochemical redox reactions. For example, Flaherty and co-workers demonstrated a hydrogen peroxide synthesis pathway where hydrogen oxidation and oxygen reduction proceed simultaneously on a Pd nanocatalyst. [163] These prior results all point toward enormous scientific and practical opportunities for continued study at the disciplinary interface between thermal and electrochemical catalysis.

Tungsten trioxide (WO_3) is an attractive material for comparing thermal and electrochemical phenomena for several reasons. It is a reducible oxide that can take up hydrogen to form hydrogen tungsten bronze, H_xWO_3 (where 0¡x¡0.5), which exhibits mixed proton-electron conductivity at room temperature. [48, 64, 164, 165, 166] This reaction occurs under thermochemical conditions via H-spillover, where H_2 (or another hydrogen donor) dissociatively adsorbs at a catalytic metal (e.g., Pt) and the resulting surface-bound hydrogen then migrates to a WO_3 support. [167, 168, 169, 170, 171, 172] The reverse process has also been shown to occur when Pt/H_xWO_3 is heated in the presence of a hydrogenation target like pent-1-ene or acrolein. [173, 174] This unique reactivity makes WO_3 and related compounds attractive as catalyst promoters and supports for hydrogenation, hydrogenolysis, steam reforming, and several other reactions. [175, 176, 177, 178] H_xWO_3 bronze is also known to form electrochemically via H-intercalation from acidic electrolytes. [179, 180] Thus, tungsten oxides are widely used as electrochromic materials, since H_xWO_3 bronze is deep blue while WO_3 is yellow-green.

The ability to reversibly interconvert between WO_3 and H_xWO_3 under thermal and electrochemical conditions makes tungsten oxides interesting for use in hydrogenation/dehydrogenation schemes where electrochemical steps feed thermal steps or vice versa. For example, a recent report showed that H-spillover at Pt/WO_x interfaces can be used to spatially separate key elementary processes associated with hydrogen oxidation in a fuel cell anode.[181] Nonetheless, it remains unclear whether H-intercalation and H-spillover can be induced under mutually compatible conditions and whether the associated reaction mechanisms are the same or different.

We have worked to address these questions by using time-resolved optical microscopy to directly observe the formation of H_xWO_3 from WO_3 under thermal (H-spillover) and electrochemical (H-intercalation) conditions at room temperature and in the presence of H_2SO_4(aq). Specifically, we placed nanocrystalline WO_3 thin films in contact with either an electrode or a spillover-active composite (WO_3-supported Pt) and imaged the migration of deeply colored H_xWO_3 fronts laterally across the films. We found that the apparent rates of diffusion were comparable for H-spillover and H-intercalation when the applied potential matched the equilibrium potential for the H_2/H^+ redox couple (0 V vs. RHE). Moreover, the H_xWO_3 fronts were found to migrate far too fast to be limited by solid-state diffusion of H^+. Therefore, we propose a unified mechanism in which electrons are injected into the WO_3 film either through Pt-catalyzed H_2 oxidation or an external applied potential, while protons are taken up from the electrolyte.

3.3 Results & Discussion

A method from a prior report[182] was used to synthesize nanoparticulate WO_3, which we modified by eliminating polyethylene glycol as a structure-directing agent to minimize the possibility of contaminants in the final product. A complete description of the synthetic approach has been included in the ESI.† Briefly, aqueous Na_2WO_4 solutions were converted to tungstic acid (H_2WO_4) by elution through a proton exchange resin, and the resulting sols were aged for three days at room temperature prior to being calcined in air at 500 °C for 1 hour.

Fig. 18 compiles electron microscopy and X-ray diffraction data confirming the formation of monoclinic WO_3. SEM images, as in Fig. 18a, show a well-distributed film containing tightly packed nanodisks. The disks had diameters of several hundred nm and thicknesses of a few tens of nm, suggesting crystal growth of the individual disks was inhibited in one lattice direction. HR-TEM micrographs, shown in Fig. 18b, confirm the disk morphology and dimensions seen in SEM. Lattice spacings of 3.73 and 3.85 Å were measured and respectively assigned to the (020) and (002) d-spacings of monoclinic WO_3.[183] These observations suggest the imaging zone-axis was in the (200) direction and insinuate the exposed flat side of the disks mainly comprised (100) crystal facets.

XRD measurements (Fig. 18c) were performed to compare the crystal structures of the as-synthesized material to commercial monoclinic WO_3 powder (Sigma Aldrich, $\leq$100 nm particle size). Diffraction results confirm a monoclinic crystal structure and show increased intensity in the (002) and (020) reflections relative to the commercial monoclinic powder. Thus, we conclude that the as-synthesized WO_3 consists predominantly of monoclinic nanodisks with a large proportion of exposed (100) crystal facets. Further characterization and analysis of disk formation is included in the ESI.†

Fig. 19 compiles data confirming the ability of our WO_3 nanodisks to form H_xWO_3 through H-intercalation and H-spillover. Cyclic voltammetry measurements on thin films of WO_3 showed a cathodic shoulder at $\sim$0.1 V vs. RHE and a cathodic peak at $\sim$-0.1 V vs. RHE. These features are associated with the intercalation of hydrogen equivalents, where protons bind to framework oxygens to form hydroxyls and electrons populate the

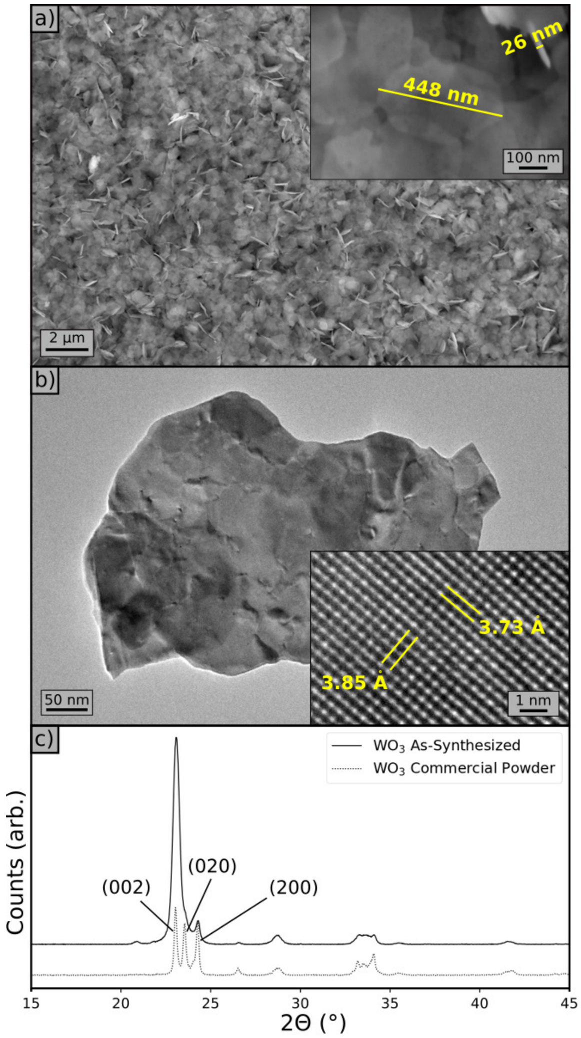

Figure 18: Compiled materials characterization results: (a) scanning electron micrograph of WO$_3$ nanodisks deposited on a glass slide coated with fluorine-doped Sn oxide; b) low- and high-resolution transmission electron micrographs of a single WO$_3$ disk; (c) X-ray diffraction data comparing WO$_3$ nanodisks with commercial WO$_3$ nanopowder.

tungsten *d*-band.[184] More negative potentials resulted in a further exponential onset of cathodic current density, which we attribute to hydrogen evolution at H_xWO_3 and/or the Au substrate. In the positive sweep, the data show a broad anodic feature attributable to proton de-intercalation that peaks in the range from 0.1 to 0.3 V vs. RHE and decays gradually at more positive potentials. All samples exhibited the expected electrochromic behavior (Fig. 19b,c), where constant-potential reduction at -0.2 V vs. RHE coincided with a color change to navy blue within tens of seconds. Similarly, submersion of a Pt/WO_3 composite thin film into 0.5 M H_2SO_4(aq) solution that had been pre-saturated with H_2(aq) at 1 atm resulted in the formation of a deeply colored Pt/H_xWO_3 film within one minute (Fig. 19d,e). Notably, this color change was 10–100 times faster when using aqueous H_2(aq) than H_2(g), which agrees with Boudart's observation that H-spillover is accelerated by water.[168] This further implies that water facilitates the movement of hydrogen equivalents across the metal/oxide boundary by mediating the transfer of protons, electrons, or both.

Cyclic voltammetry of WO_3 films on Au substrates at 100 mV/s resulted in progressively decreasing changes in coloration to yield films that remained light blue after as few as 5 cycles. We attribute this to the fact that WO_3 is a wide band gap semiconductor, whereas H_xWO_3 is a conductor over the full range of x values from 0 to 0.5.[185, 186] Hence, under reductive conditions it is easy to inject electrons from the Au working electrode into H_xWO_3 and reduce the entire film. By contrast, hydrogen de-intercalation results in the formation of nearly insulating WO_3, which could result in "stranded" regions of H_xWO_3 separated from the Au electrode. Hence, the large (>100 mV) potential difference between cathodic and anodic features in the voltammogram, which would normally be attributed to sluggish electron-transfer kinetics, is likely the result of a complex interplay between interfacial electron-transfer kinetics and solid-state proton/electron transport. This also agrees with a recent report discussing slow proton diffusion as a limiting characteristic of WO_3-based pseudocapacitors, particularly those comprised of anhydrous nanomaterials.[187]

The phenomenological similarities between H_xWO_3 formation from WO_3 via electrochemical and H-spillover processes led us to hypothesize that they may proceed via congruent reaction mechanisms. To address this hypothesis, we devised an experiment that would enable observation of both under the same conditions. The approach, which is conceptually

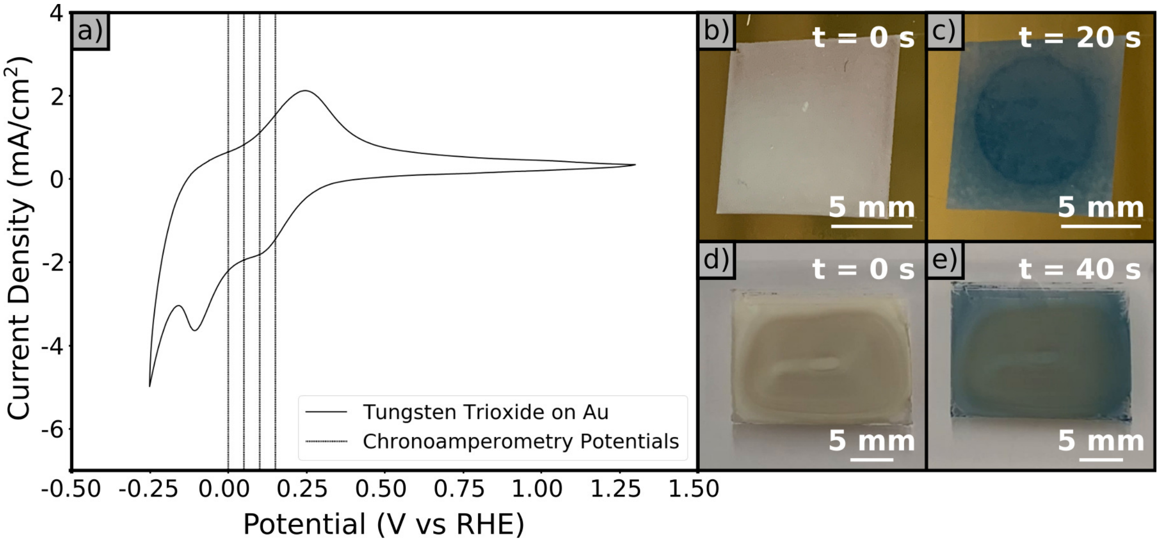

Figure 19: Voltammetric data and visual evidence of film coloration under electrochemical (H-intercalation) and thermochemical (H-spillover) conditions. Panel (a) is a cyclic voltammogram of a WO_3 nanodisk film deposited on Au-coated glass, collected in 0.5 M H_2SO_4(aq) at 100 mV/s. The dashed vertical lines indicate the potentials at which the constant-voltage experiments (schematized in Fig. 20) were conducted. Panels (b) and (c) are optical photographs depicting coloration of a WO_3 film on a Au electrode before and after constant-potential intercalation at -0.2 V vs. RHE. Panels (d) and (e) show the coloration of a platinized WO_3 film before and after H-spillover via submersion in hydrogen-saturated 0.5 M H_2SO_4(aq) for 40 seconds.

similar to the methods that Stevenson used to image Li intercalation in Mo oxides,[188] is schematized in Fig. 20 along with representative data for electrochemical and spillover-based H_xWO_3 formation. Briefly, thin films of WO_3 nanodisks were deposited onto a glass microscope slide that had been pre-coated in a defined region with an electrically addressable Pt or Au thin film or with WO_3-supported Pt nanoparticles. The boundaries between these films were then imaged under an optical microscope and videos were recorded after applying a specified electrochemical potential in 0.5 M H_2SO_4(aq) electrolyte or after submerging the Pt/WO_3+WO_3 in 0.5 M H_2SO_4(aq) that had been pre-saturated with H_2(aq) at 1 atm. These treatments resulted in the progressive migration of a deeply colored H_xWO_3 front across the film. The location of the front was then extracted from the associated video frames to generate time vs. position data. Complete details on video analysis are included in the ESI.†

A key distinction between a conventional picture of H-spillover versus electrochemical intercalation centers on the source of protons and electrons in the system. H-spillover onto an oxide support is generally considered to occur through dissociative adsorption of H_2 followed by migration of H equivalents (either as atomic hydrogen or a proton-electron pair) across the metal/oxide interface. [189] In this picture, protons and electrons both originate at the catalytic metal (Pt in this case) and move across the interface together. In H-intercalation, the metallic electrode merely acts as a source of electrons, which are injected into the conduction band of the oxide as mobile charge carriers. This excess negative charge is compensated by the uptake of a cation (e.g., H^+), which does not need to proceed in the same location as electron transfer from the electrode to WO_3. If both of these pictures are correct, we would expect to see the H_xWO_3 front move slower for H-spillover than for H-intercalation. This is because "spilt over" H equivalents would need to diffuse over mm distances through the solid film, whereas protons could intercalate into the film from the electrolyte local to the growing H_XWO_3 front. Instead, the data in Fig. 20e show that the rate of front migration across the WO_3 thin film is comparable under thermal and electrochemical reaction conditions. This result provides strong evidence of mechanistic congruence between these two processes.

Fig. 21 collects the initial linear migration rates for a set of H_xWO_3 fronts over a range

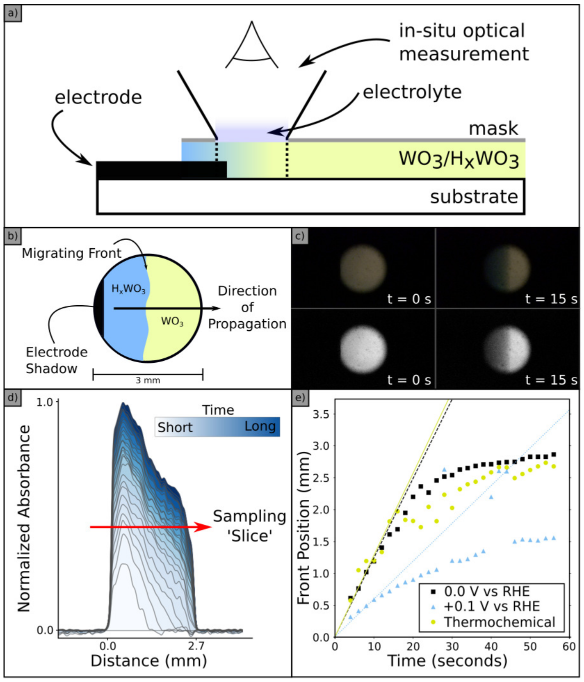

Figure 20: Schematics and representative data used in determining the initial rate of H_xWO_3 front migration. Panel (a) illustrates the general experimental setup employed for *in-situ* optical microscopy measurements. Panel (b) schematizes the imaged area for H-intercalation at an intermediate time point during the experiment. Panel (c) depicts images of the migrating front at two time points before (top) and after (bottom) conversion from RGB color channels to a single transmitted intensity. Panel (d) depicts normalized absorbance data versus linear distance from the electrode as a function of time. Panel (e) compiles front position vs. time data for two H-intercalation experiments at 0 and 0.1 V vs. RHE, respectively and one H-spillover experiment in 0.5 M H_2SO_4(aq) saturated with H_2(aq) at 1 atm.

of applied potentials using Pt and Au electrodes. The data fall in a narrow range of 50–150 μm/s and show a monotonic increase in the initial rate as the applied potential becomes more negative. This weak potential dependence agrees with Surendranath's recent observations, in which rates of electrochemically induced H-reverse spillover were found to increase linearly with applied potential.[181] This potential dependence could be due to an increase in the equilibrium concentration of H in H_xWO_3, thereby increasing the driving force for H migration. A second possibility is that the rate of front propagation is limited by electron-transfer kinetics, which would also result in an increased reaction rate with applied overpotential. The Au data also show slightly greater rates of front propagation as compared to Pt, which we attribute either to a modest systematic error in the rate measurements or differences in charge-transfer resistance at the metal/WO_3 interface.

Fig. 21 also includes H-spillover data, where the film was submerged in 0.5M H_2SO_4(aq) saturated with H_2(aq) at 1 atm. The chemical potential of electrons in the H_2/H^+ redox couple in a solution of this composition is equivalent to an applied potential of 0 V vs. RHE, allowing direct comparison of thermochemical and electrochemical conditions. When treated in this way, the initial rate data show remarkably close agreement between thermochemical and electrochemical reduction using a Pt catalyst/electrode, further supporting mechanistic congruence.

Finally, the data in Figs. 20e and 21 strongly suggest that the rate of H_xWO_3 front migration in this system cannot be limited by solid-state proton diffusion. For example, in the case where 0 V vs. RHE was applied, the front was found to traverse ~2.5 mm in 20 seconds. Based on the simple relation $\delta = \sqrt{4Dt}$, where δ is the diffusion distance and D is the diffusion coefficient, this observation would require a proton diffusion coefficient of ~8×10^{-4} cm^2/s, which is faster than that of protons in water and therefore unrealistically large.[190] Thus, it is highly unlikely that the formation of H_xWO_3 in this system requires the diffusion of protons and electrons together over mm distances, even in the case of H-spillover. Instead, the protons in H_xWO_3 must originate predominantly from the electrolyte, which wets the entire oxide film. As additional evidence to this effect, the ESI† includes experimental results in which the WO_3 film was coated with a layer of polydimethylsiloxane to restrict solution access. This resulted in a distinct change in the shape of the front propagation curve along

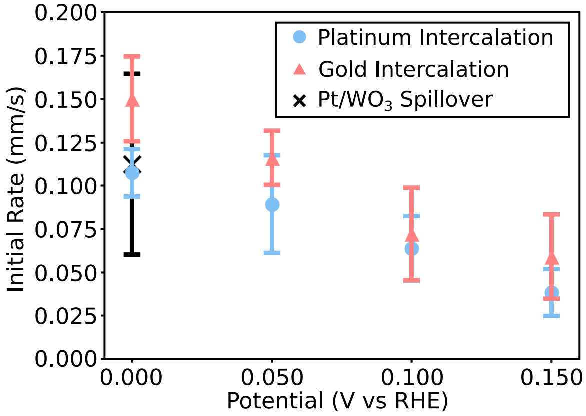

Figure 21: Initial rates of H_xWO_3 front migration versus applied potential, based on the linear fits depicted in Fig. 20e. The data labeled "Pt/WO_3 Spillover" correspond to H-spillover conditions in which the H source was a Pt/WO_3 composite thin film in contact with a 0.5 M H_2SO_4(aq) solution saturated with H_2(aq) at 1 atm, and have therefore been reported at 0 V vs. RHE. Error bars are reported as 1.96 times the standard errors of the mean of three replicates for each experiment, and therefore indicate upper and lower 95% confidence limits on the mean.

with a decrease in the apparent diffusion coefficient to values that are commensurate with prior reports of proton diffusion in porous or hydrous H_xWO_3.[169, 191, 192, 193]

These time-resolved microscopy measurements point to a single reaction mechanism that governs H_xWO_3 formation in the presence of H_2SO_4(aq). This mechanism is illustrated schematically in Fig. 22, where H_xWO_3 formation proceeds through temporally coupled but spatially independent proton and electron transfer. In the case of H-spillover, then, the function of Pt is not as a source of H atoms, but instead as a source of electrons that result from the chemical oxidation of H_2. Hence, the Pt catalyst can be considered in this case as a nanoscale bipolar electrode that drives proton intercalation via simultaneous hydrogen oxidation and WO_3 reduction.

In conclusion, we have directly compared the dynamics of WO_3 reduction to H_xWO_3 under thermochemical and electrochemical conditions. The results indicate these reactions occurs by a congruent mechanism involving electron transfer coupled with proton uptake, where the electron and proton need not come from the same source. Hence, classical H-spillover does

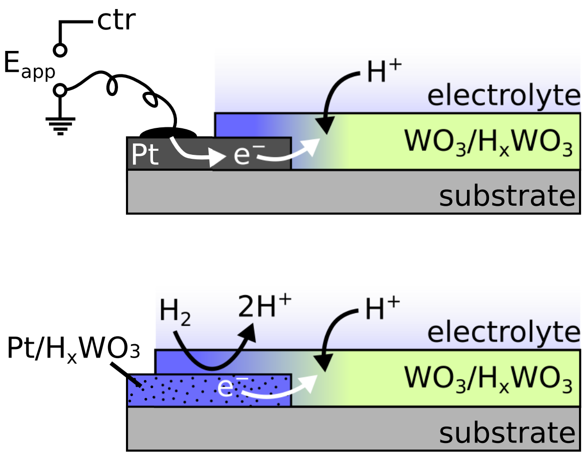

Figure 22: Schematic depicting congruent reaction mechanisms for H-intercalation (above) and H-spillover (below) in the presence of a proton-conducting electrolyte. In both cases, the reduction reaction proceeds via electron transfer through the propagating H_xWO_3 film, while proton transfer occurs from the electrolyte adjacent to the WO_3/H_xWO_3 boundary. For H-intercalation, electrons originate in the electrode, whereas for H-spillover, they are generated from the oxidation of H_2 at H_xWO_3-supported Pt. Note that the dimensions are not shown to scale.

not occur in this system, or it does so at a much slower rate than H-intercalation, even when H_2 is used as the reductant. It is possible that this type of proton-electron transfer predominates in many H-spillover processes, which further implies that thermocatalytic reactions involving H-spillover would benefit from the judicious incorporation of proton-conducting electrolytes.

These results highlight the value of exploring the inter-relationships between thermal and electrochemical phenomena. Additional work remains in understanding the process of H-reverse spillover, which is likely to be complicated by slow electron transport through insulating oxides. We are also interested in considering how H-spillover and intercalation can be integrated into intensified "thermo-electrocatalytic" reaction schemes in which electric potential is used to manipulate the thermodynamics and kinetics of industrially relevant redox reactions.

4.0 Emergent Catalysis on Tungsten Oxide via Hydrogen Intercalation

This chapter is reproduced from “The sensitivity of metal oxide electrocatalysis to bulk hydrogen intercalation: Hydrogen evolution on tungsten oxide,” which was published in the Journal of the American Chemical Society.[121]

4.1 Context

This Chapter studies the kinetics of the hydrogen evolution reaction on tungsten oxide hydrogen bronzes. Experimental and computational observations made in Chapter 2 (and the related Appendix A) imply that hydrogen insertion could dramatically change the catalytic behavior of metal oxides. Crystal structure, UV-Vis absorbance, interfacial charge transfer resistance, and many other properties are altered when H is intercalated into tungsten oxide. These properties are indicative of changes to both geometric and electronic structure, which have been linked to the activity of many different kinds of catalysts. Additionally, Chapter 2 demonstrated that geometric and electronic structure influence an oxide’s interaction with H, so we hypothesized that catalytic behavior of metal oxide bronzes could be a function of H stoichiometry.

The combined computational and experimental observations presented in this Chapter could have broad implications for metal oxide catalysis. These observations stem from the observation that the active catalyst for hydrogen evolution is an intercalated H_xWO_3 and not non-intercalated WO_3. Recalling the feasibility of H insertion under thermochemical and electrochemical conditions presented in Chapter 3, the formation of a hydrogen bronze is conceivable in any environment which is sufficiently reducing. Metal oxide supports–frequently used in gas-phase thermochemical catalysis–may be bronzes under reaction conditions, contributing a yet-to-be considered catalytic competency. Even further, since hydrogen bronze surfaces are characteristically different than their parent oxides, H intercalation could provide a possible means for dynamically controlling catalytic activity.

4.2 Introduction

Metal oxides are tremendously important components of catalytic systems, being used both as supports for active materials and as catalysts themselves[194, 195]. Their widespread application is a result of their diverse chemical properties, offering tunable reactivity as a function of composition and structure. Historically, oxides have been used extensively in thermochemical environments and have seen only a few use cases in electrocatalysis. However, research in recent years has been reinvigorated and extended the application of oxide catalysts to a wider range of electrochemical reactions[196, 197, 198, 199, 200]. With the potential for broad use in electrocatalysis, it is important to recognize that many metal oxides can undergo redox reactions themselves[201, 202]. In an electrochemical environment, this redox reactivity can be instigated by applied potential and interaction with the solvent environment, frequently manifesting in the transfer of ions to/from the oxide catalyst.

One redox reaction that occurs in aqueous environments is hydrogen intercalation, which is the insertion of protons and electrons into the full oxide lattice under sufficiently reducing conditions[203]. Unlike surface processes, such as hydration and poisoning, intercalation is a bulk phenomenon: instead of being adsorbed only to the oxide surface, hydrogen also penetrates deep into the structure of the material. The reaction reduces the formal oxidation state of the metal in the oxide to generate a metal oxide hydrogen bronze[43]. This often results in electrochromism, where electrons populate the metal d-band and enhance photon absorption in the visible and near-infrared regions [204]. Filling the conduction band via bulk intercalation can also induce semiconductor-to-metal transitions in metal oxides[205]. Moreover, empirically observed rates of hydrogen intercalation occur on timescales similar to catalytic turnover[206, 207]. Therefore, the associated changes in electronic structure can also be expected to occur alongside electrocatalytic reactions on oxides.

Tungsten trioxide, WO_3, is a redox-active metal oxide that undergoes bulk hydrogen intercalation to tungsten oxide hydrogen bronze, H_xWO_3[48]. It has also recently been used in a variety of technological applications, including in electronic devices and for enhancing fuel cell electrode stability[208, 209]. The ability of WO_3 to undergo H intercalation is understood to be critical for each of these applications. The changes in optical absorption and electrical conductivity accompanying WO_3 reduction to H_xWO_3 arise from a shift in electronic structure that is describable as a re-positioning of the *d*-band. Considering the *d*-band model that describes trends in catalytic activity for metals, it is reasonable to expect that electronic changes resulting from bulk hydrogen intercalation will also affect the catalytic function of the bronze[210]. In this direction, previous work has shown that pre-modified substoichiometric (high O vacancy) $WO_{3-\delta}$ electrodes exhibit greater HER rates than stoichiometric WO_3[211]. Vacancy formation is understood to alter oxide electronic structure, which results in altered catalytic activity[212, 213]. However, when starting with stoichiometric WO_3, it is unlikely that O vacancies form in significant concentrations in an electrochemical environment at potentials relevant to the HER[214]. Rather, WO_3 readily undergoes bulk hydrogen intercalation in a cathodic electrochemical environment[207, 214, 206, 215]. Since intercalation also alters oxide electronic structure and catalysis is dependent on band positioning, we can expect hydrogen intercalation to influence the catalytic activity of metal oxides like H_xWO_3.

Combined computational and experimental studies of bulk hydrogen intercalation and its influence on cathodic reactions on metal oxides are yet to be performed[216, 217, 211, 218]. However, prior work has demonstrated that hydrogen intercalation has a significant impact on the activity of other catalysts[219, 220]. One example is a recent study on electrochemical hydrogen evolution catalyzed by MoS_2[219]. The authors found that hydrogen intercalation directly impacts both the electrical conductivity and hydrogen adsorption behavior of MoS_2, resulting in enhanced activity and increased robustness in neutral and alkaline pH environments. Another example is a study on Pd-catalyzed electrochemical hydrogen evolution, where the authors observed a steady increase in activity upon cycling applied potentials[220]. They concluded this performance increase was due to a change in H adsorption energetics induced by hydrogen intercalation. These reports further motivate an investigation into the influence of bulk hydrogen intercalation on metal oxides and their catalytic behavior.

In this work, we have combined theory and experiment to demonstrate that bulk hydrogen intercalation precedes hydrogen evolution on WO_3 in aqueous acidic electrolytes. H_2 generation does not occur on WO_3, as might be expected. Instead, applying a potential forms a new catalyst, H_xWO_3, which then allows the HER to occur. This process is reversible, and applying a sufficiently positive potential will eventually lead to removing H from H_xWO_3 to regenerate WO_3.

Hydrogen intercalation fundamentally changes the reactivity of WO_3. Specifically, intercalation drastically alters the electronic structure of the oxide, essentially forming a new catalyst with markedly higher HER activity. With constant-charge (canonical) and constant-potential (grand canonical) DFT calculations, we show that these electronic changes activate surface metal sites for the HER. We further demonstrate that a constant-charge analysis, as is traditionally applied for gas-phase systems and in the computational hydrogen electrode (CHE) approach, does not fully describe the experimentally-measured activities[16]. Rather, a constant-potential DFT (CP-DFT) approach accurately captures the experimentally observed hydrogen intercalation and evolution characteristics of H_xWO_3. Using CP-DFT, we also observe that the elementary reaction energetics for the HER on H_xWO_3 are relatively insensitive to applied overpotential (i.e. individual steps exhibit small charge transfer coefficients). Instead, increasing the applied overpotential increases the equilibrium H content in the bronze, which indirectly increases the rate of HER turnover by altering the catalyst electronic structure and providing a surface that yields lower HER activation barriers. We further illustrate the effect of intercalation on HER catalysis by comparing experimentally measured rates of hydrogen evolution on H_xWO_3 to reaction rates derived from electrochemical microkinetic models of varying degrees of x in H_xWO_3. Critically, the observed HER activity can only be rationalized by considering intercalated states with stoichiometries of $H_{0.500}WO_3$ or greater. Weak electrochemical activation is further evidenced via large apparent Tafel slopes (ranging from 120 to > 400mV/dec) that we observed experimentally and confirmed with first-principles electrochemical microkinetics. This work clearly demonstrates that bulk hydrogen intercalation is an important consideration in cathodic electrocatalysis on metal oxides.

4.3 Materials and Methods

4.3.1 Computational Methods

Spin-polarized DFT calculations were performed using VASP and the projector augmented wave (PAW) method[80]. Atomic visualizations were generated using VESTA[81]. For energy calculations and geometric relaxations, exchange-correlation was modeled using the PBE functional[82]. Dispersion corrections were included using the D3 method with Becke-Johnson damping[83, 84]. The PBE-D3 level of theory has previously been shown to give good energetic and structural results for the metal oxides and hydrogen bronzes explored in this work[85, 86]. Electronic density of states were determined using the hybrid HSE06 exchange-correlation functional in a single-point calculation at the optimized PBE-D3 geometry[111]. In all calculations, PAW pseudopotentials and a plane wave basis with a cutoff of 520 eV were used to model the electronic wavefunctions. Ground state geometries were optimized with an electronic convergence threshold of 1x10^{-6} eV. Electronic convergence was tightened to 1x10^{-7} eV for transition state optimizations. Transition states were located using the climbing image nudged elastic band (CI-NEB) method and further optimized using the improved dimer method (IDM)[221, 222]. Both the ASE and VTST implementations of CI-NEB were used in initial transition state searches, while the IDM was executed as available in the standard VASP distribution[223]. For all states, geometries were relaxed until the largest observed force was less than 0.05 eV/Å. Intermediate ground states and transition states were confirmed via vibrational frequency analysis. Ground states that returned imaginary frequencies, or transition states that gave extra imaginary modes, were further optimized to a minimum with tighter force criteria. Reciprocal space was sampled using a k-point density of 0.3 Å and Gaussian smearing with a width of 0.02 eV was used to smooth the electronic occupancies.

H_xWO_3 surfaces were constructed as 1x1x2 and 2x1x1 supercells for the (001) and (100) facets[224]. The bulk geometries over a range of hydrogen stoichiometries, $x = 0.000, 0.250, 0.500$ and 0.625, were used as starting points. These values of x were chosen to match the compositions that form the discrete redox couples and staging levels observed in H_xWO_3 in prior experimental and computational studies.[225, 215] Moreoever, while we cannot rule out the possibility that other H_xWO_3 phases form under HER conditions, the stoichiometries selected for this work give a progression of x values that allows us to probe the effect of increasing H content in WO_3. Initially, the bulk unit cell for each stoichiometry was optimized with respect to lattice parameters and atomic positions. Volume- and position-optimized bulk cells were then used to create surface models. Including lattice parameters as additional degrees of freedom allowed us to track the effects of structural rearrangement on catalytic activity. The surface structures were further relaxed prior to any adsorbate calculations by including a 15 Å vacuum layer in the direction perpendicular to the surface.

All results shown in this work, unless otherwise mentioned, pertain to the (100) facet of H_xWO_3. Although the most thermodynamically stable facet is (001), we find that adsorption energies of H are more favorable on (100). This is shown in Figure 73 of Appendix C. We also see from SEM images and XRD measurements that there is a sufficient number of exposed (100) facets on the nanoparticles we used in experiments. This is discussed and illustrated in Appendix C.

Electrolyte and solvent effects were included using the VASPsol extension[226]. This approach leverages the linear GLSSA-13 implicit model to describe the solvent, which is water in this case[227]. As such, all calculations were run using a relative permittivity of 78.4. The cavitation energy was not included in the determination of total energy, since this effect is small and its inclusion can cause oscillations and inefficiencies in optimizations[228, 229]. The electrolyte was modeled using a linearized Poisson-Boltzmann equation with a Debye length of 4.3 Å, which corresponds to the 0.5 M H_2SO_4 electrolyte used in the experiments included in this work. In addition to the implicit solvent and electrolyte models, explicit waters were included to better approximate the Helmholtz layer and to provide a hydrogen source in our calculations. Two water molecules and an extra hydrogen atom forming the ${H_5O_2}^+$ Zundel cation were used per surface unit cell (Figure 23), as including more water molecules did not significantly alter energies.

For DFT calculations at constant charge (i.e. no excess electrons), the free energy of a given state was calculated as follows:

$$F = E_{elec} + E_{ZPE} + T \cdot S \tag{4.3.1}$$

In Equation 4.3.1, F is the total canonical free energy of the system, E_{elec} is the electronic DFT energy, E_{ZPE} is the zero point energy, and $T \cdot S$ is the entropic contribution. The zero point energies and entropies were determined from vibrational modes calculated using the harmonic oscillator approximation. All free energies were computed at 298.15 K, to compare calculated results to room-temperature experimental data.

Constant-potential DFT (CP-DFT) calculations were performed by varying the number of excess electrons included in the cell until a desired electrochemical potential was achieved. Our approach and analysis follows that given by the authors of the VASPsol package and is described in detail here[226]. The electrochemical potential on the SHE scale was calculated as:

$$U = -(\epsilon_{fermi} - \phi_{solvent}) - \phi_{SHE} \tag{4.3.2}$$

In Equation 4.3.2, ϕ_{SHE} is the value of the SHE redox couple which was taken to be 4.44 eV, ϵ_{fermi} is the Fermi level of the electrode, and $\phi_{solvent}$ is the electrostatic potential deep in the solvent region[230]. Rather than manually changing the number of excess electrons after individual DFT calculations, an automated script was used to search for a desired potential via a gradient descent algorithm:

$$N_e[i+1] = N_e[i] - a \cdot (U_{target}[i] - U[i]) \tag{4.3.3}$$

Here, N_e is the number of excess electrons at a given image i, U_{target} is the desired electrochemical potential, $U(i)$ is the electrochemical potential of the current configuration, and a is a scaling factor used to control the size of the correction applied to N_e for the next guess. Previous work found an a value of 1.0 V^{-1} to be sufficient, but this caused oscillations around the target potential in our calculations[231]. Reducing a to a value of 0.5 eliminated these oscillations. A tolerance of 0.020 V was used as a convergence criterion for terminating the optimization of electron numbers.

To account for the excess electrons in the systems held at constant potentials, the grand canonical free energy, Ω, was considered instead of the typical canonical free energies[226, 232, 233]. This was achieved through a modification of Equation 4.3.1:

$$\Omega = E_{elec} + E_{ZPE} + T \cdot S - N_e \cdot \phi_{solvent} - N_e \cdot (-\phi_{SHE} - U) \tag{4.3.4}$$

By combining Equations 4.3.1 and 4.3.4, we considered the grand canonical free energy as the canonical free energy with two additional corrections:

$$\Omega = F - N_e \cdot \phi_{solvent} - N_e \cdot (-\phi_{SHE} - U) \tag{4.3.5}$$

The second term on the right-hand side of Equation 4.3.5 is required to account for the excess electrons in the system. The third term on the right-hand side of Equation 4.3.5 arises from the Legendre transform that connects the canonical ensemble to the grand canonical ensemble[226]. Combining these two corrections and considering Equation 4.3.2 results in the following, simplified total grand canonical energy expression:

$$\Omega = F - N_e \cdot \epsilon_{fermi} \tag{4.3.6}$$

Equation 4.3.6 clearly shows how excess electrons influence the total grand canonical energy, where each electron (or fractional electron) makes an energy contribution to the system's Fermi level on an absolute energy scale. Grand canonical free energy differences were then computed by considering Equation 4.3.6 for two unique states at a common electrochemical potential, U. Again, this potential was achieved for each state by varying the excess electrons according to Equation 4.3.3. Details concerning the implementation of the electrochemical microkinetic model are included in Appendix C. The software is available on an open-source basis for use according to the MIT license on Github.

4.3.2 Experimental Methods

Electrochemical measurements were collected using a Gamry Interface 1000 potentiostat in a three electrode setup. Considering the relatively low HER activity of H_xWO_3, contamination of the working electrode or electrolyte by adventitious transition metals would result in false activity measurements. Thus, we did not use any electrode materials containing transition metals with comparatively higher HER activity, such as Pt. The counter electrode in all measurements was a graphite rod (Electron Microscopy Sciences 0.25 in. diameter, Spectro-Grade). The reference electrode for all experiments was Ag/AgCl (CH Instruments CHI111P), and was experimentally calibrated to the RHE scale by measuring the open circuit potential of a platinum electrode (0.5 mm Pt wire, 99.997% metals basis, Alfa Aesar) submerged in fresh H_2 (99.999%, Matheson) saturated 0.5 M H_2SO_4 electrolyte. Applied potentials were further converted to the SHE scale using a small adjustment for solution pH—this facilitates direct comparisons to computational results. Reference electrode calibration was always performed after HER activity measurements of H_xWO_3 in a separate electrochemical cell (using electrolyte transferred from the testing cell), again to minimize the possibility of Pt contamination. Only the graphite counter electrode and the Ag/AgCl reference electrode were used between activity measurements and calibrations. The electrolyte was discarded after the RHE–SHE calibrations so as not to introduce Pt to the testing cell. As further evidence of sample cleanliness, we observed none of the characteristic features of Pt contamination, such as erratic changes in HER activity or steadily increasing activity with time.

Films of WO_3 nanoparticles were deposited by drop casting catalyst ink onto glassy carbon disk electrodes (CH Instruments CHI 104, 3 mm diameter for non-hydrodynamic experiments, or SPI 4181GC-AB, 5 mm diameter for rotating disk electrode experiments). A representative catalyst ink contained 0.05 g of WO_3 nanoparticles, 0.05 g of Nafion dispersion (Ion Power, 1100 EW @ 20 wt% in IPA), and 250 μL of >18.2 MΩ·cm water. The ink was dried using an infrared heat lamp. The WO_3 nanoparticles were synthesized using a modified literature procedure[234]. Our modifications and the effect on particle morphology has been reported previously[206]. Appendix C provides confirmation of the identity and morphology of the synthesized WO_3.

Cyclic voltammetry measurements were performed in a static cell setup, which consisted of a glass beaker with an in-house machined polytetrafluoroethylene (PTFE) cap. All cyclic voltammograms were collected at a scan rate of 1 mV/s. The working electrode for this setup was glassy carbon (CH Instruments CHI 104, 3 mm diameter) on which 1 μL of catalyst ink was deposited. Chronopotentiometry measurements were performed using a rotating disk setup (Pine Research MSR). The working electrode consisted of a glassy carbon disk (SPI 4181GC-AB, 5 mm diameter) polished to a mirror finish. 2 μL of catalyst ink were deposited onto this larger disk. The glassy carbon disk with WO_3 film was inset into a PTFE shroud (Pine Research E4TQ ChangeDisk) and was rotated at 1600 RPM. An argon purge was used to remove dissolved oxygen and other atmospheric contaminants. Voltage responses during the constant-current chronopotentiometry experiments were converted to steady-state potentials by averaging the final two seconds of data after the potential reached a constant value. Constant-current measurements were run between 5 and 60 seconds, depending on the applied potential and the approach to steady state.

Kinetic currents were extracted from the rotating disk measurements by applying the Koutecký-Levich equation[235]:

$$\frac{1}{i_m} = \frac{1}{i_k} + \frac{1}{0.62 n F A D_O^{2/3} \omega^{1/2} \nu^{-1/6} C_O^*}$$

where i_m is the measured current, i_k is the kinetic current (free of mass transfer), n is the number of electrons involved in the reaction, F is Faraday's constant, D_O is the Grotthuss diffusion coefficient of protons, ω is the disk rotation rate, ν is the kinematic viscosity of the electrolyte, and C_O^* is the concentration of protons in the electrolyte. This equation was solved for i_k, which was then converted to the reported current densities by considering the area of the disk electrode.

Solution resistance was measured using electrochemical impedance spectroscopy, wherein a 10 mV AC waveform was applied over a DC potential. The solution resistance ranged from 5 to 6 Ω, which is within the expected range for the cell geometry used in experimental data collection[236]. EIS was performed at both open circuit potential (approximately +0.3 V vs. SHE) and at potentials where significant hydrogen evolution occurred (approximately -0.5 V vs. SHE), and no systematic differences were observed exceeding sample-to-sample variation. The resulting data were then adjusted to account for 100% of the iR drop associated with this solution resistance after experiments were complete.

4.4 Results and Discussion

4.4.1 Influence of Bulk H Intercalation on H Adsorption and Electronic Structure

We first examined the possible reaction pathways to molecular H_2 on the metal oxide surface. We considered HER pathways through three elementary steps[237, 238]:

1. $* + H^+ + \lambda_n \cdot e^- \rightarrow H^*$ (Volmer)
2. $H^* + H^+ + \lambda_n \cdot e^- \rightarrow H_2$ (Heyrovsky, Eley-Rideal)
3. $H^* + H^* \rightarrow H_2$ (Tafel, Langmuir-Hinshelwood)

These are respectively referred to as adsorption, surface-mediated, and water-mediated steps, as shown in Figure 23. Each of these steps may be accompanied by the transfer of protons and/or electrons toward or away from the oxide/solution interface. Although proton transfer is restricted to integer amounts (e.g. 0 or 1), electron transfer can occur in fractional amounts, which we denote as λ_n[239, 240, 241]. This partial electron transfer is tightly tied to electrochemical activation (*vide infra*).

Figure 23a shows a bare oxide surface consisting of only tungsten and oxygen atoms, plus a $H_5O_2{}^+$ cation composed of two water molecules and an extra proton. The first step in H_2 formation is the reductive adsorption of protons from the electrolyte. Figure 23b depicts an example $H_{0.625}WO_3$ surface with three distinct H-binding sites populated: terminal oxygens (O_t), bridging oxygens (O_b), and surface tungsten metal sites (W). Although O atoms behave as basic centers and metals as acidic centers, reduced protons can interact with both site types owing to the amphoteric nature of hydrogen[215]. We emphasize that catalytically relevant atomic configurations may include any combination of the site types illustrated in Figure 23b. A variety of surface configurations can be achieved with respect to the positioning of the adsorbed H units among the three different site types. Further, the stable arrangement of surface H atoms can change depending on the H_xWO_3 bulk hydrogen stoichiometry. Also shown in Figure 23b is a sub-surface hydrogen representative of the bulk intercalated hydrogen, indicated with a circle. The number of these particular hydrogen atoms was varied as required to achieve a certain value of x in H_xWO_3 (see computational methods).

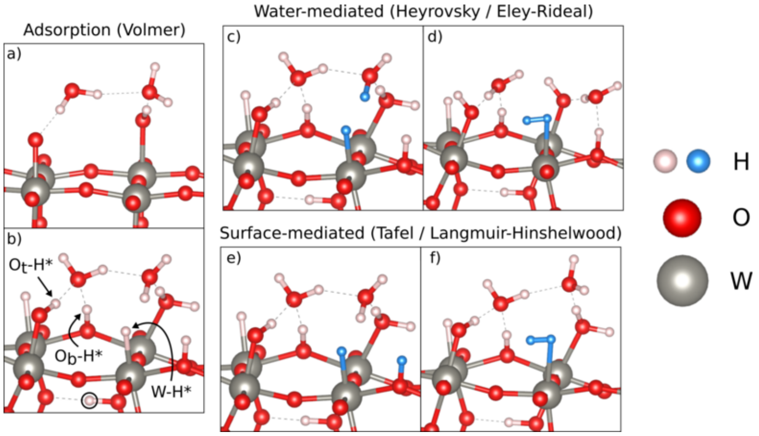

Figure 23: Major reaction steps to form H_2 on WO_3. The blue atoms are hydrogens involved in the formation of molecular H_2. Tungsten atoms are gray, oxygen atoms are red, and spectator hydrogen atoms are white. a) A bare, non-hydrogenated surface with a near-surface explicit $H_5O_2^+$ cation. b) An example of a $H_{0.625}WO_3$ surface demonstrating all possible hydrogen adsorption locations: terminal oxygen, O_t, bridge oxygen, O_b, and tungsten, W. Various combinations of site types are possible and will impact reaction energetics. The bulk intercalated hydrogen is also shown, marked by the circle. H_2-coupling occurs after adsorption through two mechanisms. c) Initial and d) final states for the water-mediated (Heyrovsky, Eley-Rideal) mechanism. e) Initial and f) final states for the surface-mediated (Tafel, Langmuir-Hinshelwood) mechanism.

Following the surface adsorption of hydrogen, H–H coupling must occur to form molecular H_2. This can proceed through the water-mediated or surface-mediated routes. In the water-mediated mechanism, surface H atoms form H_2 by reacting with a proton from the electrolyte. This is demonstrated specifically in Figures 23c and 23d for the $H_{0.625}WO_3$ surface. In the surface-mediated mechanism, two surface H atoms react with one another to generate H_2; this is shown in Figures 23e and 23f for the $H_{0.625}WO_3$ surface.

When considering surface-mediated H_2-coupling, it is important to note that metal oxides differ from metallic surfaces in that active sites of a single type are separated by relatively long distances. For example, the W sites on the WO_3 surface are separated by ~ 5.2 Å, which is too large for surface-mediated H–H coupling to occur. This contrasts with metallic catalysts like Pt, for example, where equivalent surface sites on the FCC (111) facet are separated by only ~ 2.8 Å. This distance can be feasibly traversed by neighboring adsorbed H's, allowing two congruent FCC top sites to support surface-mediated H_2-coupling. Because of the large spacing between sites on the oxide, surface-mediated hydrogen evolution on H_xWO_3 must proceed through the contribution of multiple site types.

As an initial assessment of HER catalytic activity, we calculated hydrogen atom binding energies on (100) H_xWO_3 surfaces with varying levels of bulk hydrogen stoichiometry, x, as presented in Figure 24a. These energies were computed as binding energies referenced to H_2 and the relevant oxide surface. We observed a notable shift in the preferred site for H-adsorption as the value of x in H_xWO_3 was increased. At low H stoichiometries, hydrogen tends to adsorb more strongly to the basic oxygen centers and interaction with W sites is modestly endergonic. The HER on tungsten oxide could therefore be expected to proceed at oxygen centers on the $H_{0.000}WO_3$ surface. However, as bulk H stoichiometry increases, H adsorption at oxygen sites becomes more endergonic and H adsorption at W sites becomes more exergonic. This is noted specifically for W-H^* binding with the red circles in Figure 24a. In fact, the effects of hydrogen intercalation are pronounced enough to cause an inversion in site preference, where for $H_{0.500}WO_3$ and $H_{0.625}WO_3$ the W site is the most energetically feasible location for initial H adsorption. WO_3 and $H_{0.625}WO_3$ therefore interact with hydrogen intermediates in entirely distinct ways, with direct consequences for reaction mechanism and overall turnover.

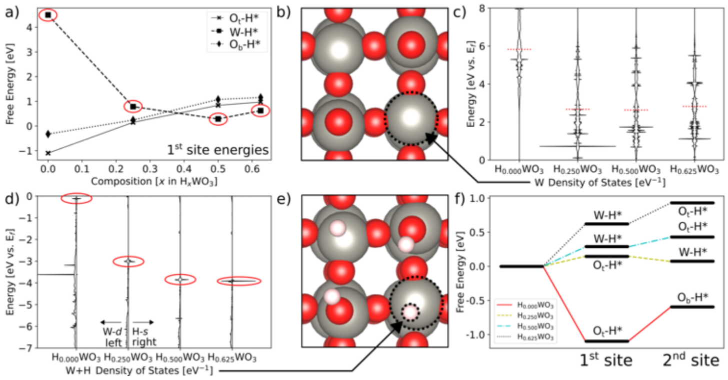

Figure 24: Effect of hydrogen intercalation on hydrogen adsorption free energies and electronic structure of H_xWO_3. a) Free energies of adsorption at the three unique site types on H_xWO_3 as a function of bulk H stoichiometry x. b) Top view of bare oxide surface. c) Unoccupied W d density of states associated with the W atom indicated in b), where the red dashed lines indicate the location of the band centers. d) Occupied local W d- and H s-projected density of states, with the W-H bonding states indicated by the red circles. The states in d) are those corresponding to the atoms indicated in e), which shows the oxide surface with H adsorbed at the W and O_t sites. f) Minimum energy pathways for the consecutive adsorption of H atoms at different sites as a function of H stoichiometry x in H_xWO_3.

We next considered the physical reasons for why bulk hydrogen intercalation changes the behavior of H adsorption on H_xWO_3 surfaces. Figure 24b shows a surface of tungsten oxide and Figure 24c depicts the local *d*-projected density of states for a bare surface W atom with no adsorbed H. We observed that increasing bulk H stoichiometry shifts unoccupied *d*-band centers (dashed red lines) closer to the Fermi level, indicating increased site acidity[105]. Comparing Figures 24a and 24c reveals that the stronger acid sites correspond to more favorable H adsorption energies. In a similar manner, Figure 24d shows the occupied W *d*- and H *s*-projected density of states for the surface atoms outlined in Figure 24e. The red circles in Figure 24d point out energy levels that show high densities of states for both the W *d* and H *s* electrons. These shared energy states imply W-H bonding, and we observed a stabilization of these bonding states as bulk H stoichiometry was increased. As with the increased W site acidities, the stabilized W-H bonding states correlate with more favorable H adsorption free energies.

While W sites are activated due to increased acidity, oxygen centers are deactivated due to decreased basicity. This is shown in Figure 72 of Appendix C. As electrons fill the electronic states of the oxide, the occupied O *p* band is shifted to lower energies and moves further from the Fermi level. This corresponds to less basic sites, which are less reactive toward amphoteric H. Notably, the relationship between reactant binding and acid–base character is well-characterized for oxides, and we have confirmed it for the interaction of hydrogen with the bulk lattice oxygens of WO_3[102].

We further examined the energetics of multiple sequential H adsorption steps at different surface site types, as shown in Figure 24f. Multiple sites were considered because 1) they will together be important for evaluating surface-mediated mechanisms and 2) the water-mediated mechanism may be affected by H atoms that are not bound at the most energetically favorable site. Notably, only non-intercalated WO_3 yields exergonic H adsorption. However, under sufficiently negative applied potentials, it is possible that multiple sites are simultaneously populated. This is evidenced by the observation that for any non-zero level of hydrogen intercalation, the second H site adsorption is less energetically demanding than the first. Together, these results show that the oxide surface may indeed be populated with hydrogen at multiple types of sites. Therefore, the two site configurations shown in Figure

24f were used to evaluate H_2 formation via surface- or water-mediated mechanisms.

For this set of adsorption calculations, explicit waters were not included and solvation was accounted for with an implicit model. This simplification was made to facilitate the screening of all possible site configurations on both (100) and (001) surfaces, which are shown in their entirety in Figure 73 of Appendix C. For a given surface with constant bulk hydrogen stoichiometry, we do not expect the trend in adsorption energies to change in the presence of explicit waters[229]. Therefore, this approach is sufficient for screening and site selection purposes for the individual oxide surfaces as in Figure 24. Trends across different bronze stoichiometries, however, might be affected by the explicit waters owing to changes in surface electronic structure—specifically the semiconductor-to-metal transition and possible changes in surface polarizability. As a result, comparisons across stoichiometries were made with the inclusion of explicit water molecules. Combined implicit/explicit solvation was also employed for kinetic analysis, as detailed in the following sections.

4.4.2 Constant-Charge vs. Constant-Potential Frameworks

What we have shown so far underpins a complex reaction network for the HER on H_xWO_3. Hydrogen intercalation significantly perturbs the acidity and basicity of the metal- and oxygen-based surface sites, leading to emergent reactivity. This highlights different H adsorption characteristics for different stoichiometries of H_xWO_3, branching into distinct reaction pathways that may contribute to the observed HER activity over a range of applied overpotentials. While we have used constant-charge DFT to describe general trends in H adsorption energetics, we found it necessary to apply more realistic modeling techniques to arrive at quantitative reaction energies and barriers for each elementary step to producing molecular H_2.

Since we are operating under electrochemical conditions, our quantum chemical approach must be carefully selected to produce accurate kinetic information. Canonical DFT methods (like those used in the CHE formalism) operate in the NVT ensemble, with the total number of electrons held constant[16]. For the adsorption of hydrogen to a surface site, we can consider the initial state as a proton in solution and the final state as a surface-bound H.

Charge transfer between the surface and the proton occurs with adsorption, and this requires there to be a change in the number of electrons in the simulated catalyst slab. This presents a problem for comparing canonical DFT calculations to electrochemical experiments, since the charge transfer yields a different apparent electrochemical potential for the initial and final reaction states[242]. Note also that this contrasts with thermochemical reactions, where canonical DFT is appropriate because the surface is not connected to an external circuit and the catalyst electrochemical potential can indeed change[70]. Using constant charge DFT for electrochemical reaction energies could therefore result in comparing experimental and theoretical data from different thermodynamic ensembles.

CP-DFT is more relevant to experimental electrochemical conditions, since electrochemical instruments are designed to manipulate the net charge in the working electrode (via transfer to or from the external circuit) to attain the desired electrochemical potential. CP-DFT methods replicate this behavior by shifting the thermodynamic ensemble from NVT to μVT: the number of electrons is treated as an additional variational parameter which drives the electrochemical potential to become a result of the calculation itself. Extensive gains have been made over the last few years to enable constant-potential calculations, and we refer the reader to several prior reports for further explanation of constant-potential methods[226, 231, 232, 233, 243].

Figure 25 compares the CHE and CP-DFT approaches to assess which method is more viable for describing the HER on H_xWO_3. Figure 25a compiles CHE and CP-DFT H adsorption equilibrium potentials on several bronze stoichiometries. The adsorption configurations we modeled correspond to the most endergonic H binding steps in Figure 24f. Notably, the equilibrium potentials returned via CHE and CP-DFT differed by as much as > 1 eV, depending on bulk H content. At $H_{0.000}WO_3$ and $H_{0.250}WO_3$, the CHE returns more negative equilibrium adsorption potentials than CP-DFT. The CHE and CP-DFT approaches agree on the position of equilibrium for $H_{0.500}WO_3$, and CP-DFT predicts a more negative equilibrium potential than the CHE on $H_{0.625}WO_3$. Details on the calculation of equilibrium potentials using each method are given in Appendix C. This disagreement between the CHE and CP-DFT approaches is consistent with prior investigations into the differences in free energies of adsorption for intermediates relevant to CO_2 reduction[243].

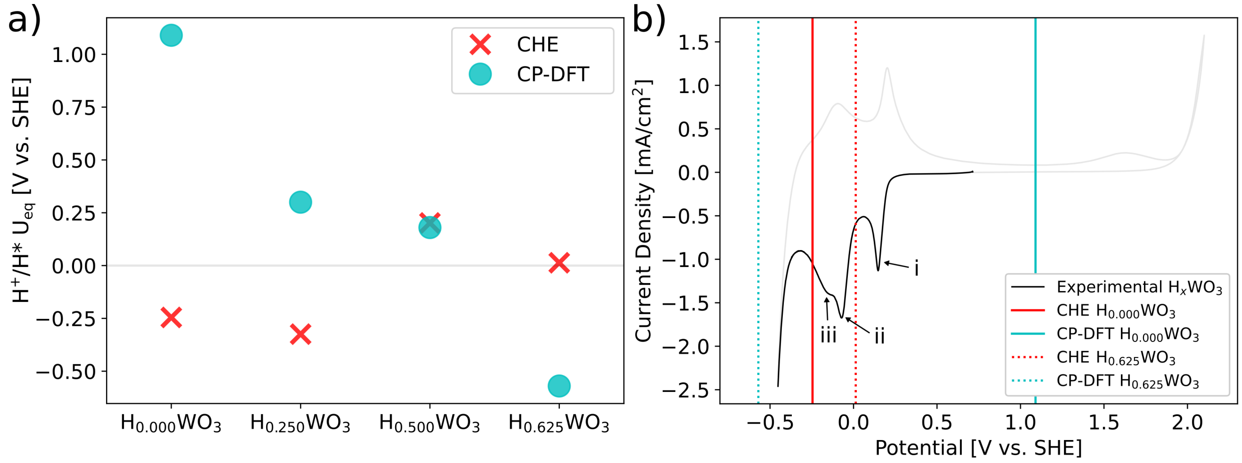

Figure 25: Comparison between constant-charge and constant-potential DFT approaches with experimental cyclic voltammetry. a) Calculated equilibrium potentials for hydrogen adsorption at thermodynamically limiting steps of adsorption, identified in Figure 24f. Potentials determined via CHE and CP-DFT are shown. The CHE potentials here are different from those apparent from Figure 24f because the present calculations include explicit water solvent molecules. b) A selection of equilibrium potentials from (a) overlaid with a representative cyclic voltammogram of WO_3 nanoparticles recorded in 0.5 M H_2SO_4 at a scan rate of 1 mV/s. The reference electrode was Ag/AgCl, the counter electrode was graphite, and an Ar purge was used. The cathodic peaks in the CV are attributable to bulk H intercalation and correspond to i) $WO_3/H_{0.250}WO_3$, ii) $H_{0.250}WO_3/H_{0.500}WO_3$, and ii) $H_{0.500}WO_3/H_{0.625}WO_3$ redox couples. Intercalation is followed by the exponential onset of the HER at ~ -0.4 V vs. SHE.

Figure 25b overlays the equilibrium potentials for H adsorption on WO_3 and $H_{0.625}WO_3$ with an experimental cyclic voltammogram (CV) of WO_3 nanoparticles. The DFT-calculated H^+/H^* equilibrium potentials (vertical lines) are related to the interaction of solvated protons with the H_xWO_3 surface, whereas the peaks seen on the CV are related to bulk hydrogen intercalation[215]. From the experimental CV, it is clear that hydrogen intercalation occurs at potentials positive of the HER onset, and the HER does not achieve an appreciable rate until < -0.4 V vs. SHE. This supports the conclusion that the HER occurs predominantly on the surface of the bronze (i.e., $x > 0$ in H_xWO_3) and not on WO_3.

Another key observation is that the CHE equilibrium potential for H adsorption on $H_{0.000}WO_3$ is negative of the $H_{0.000}WO_3/H_{0.250}WO_3$ reduction. This is inconsistent with the experimental observation of bulk hydrogen intercalation because H intercalation also requires the formation of surface bound H intermediates. Thus, the H^+/H^* equilibrium potentials for a given H stoichiometry must be equal to or positive of the equilibrium potential for intercalation to a higher H stoichiometry, else intercalation would not be able to occur. In fact, the CHE-derived H^+/H^* equilibrium potential for $H_{0.000}WO_3$ is calculated to be at $\sim$ -0.25 V vs. SHE, which occurs negative of all intercalation features in the CV. If this equilibrium potential was valid for H adsorption, then H would not be able to interact with the WO_3 surface in any meaningful way and intercalation would not be observed until potentials negative of $\sim$ -0.25 V vs. SHE. Using CP-DFT, the apparent equilibrium potentials are in much better agreement with experimental observations. Specifically, hydrogen binding on WO_3 occurs at $\sim +1.1$ V vs. SHE, meaning the surface can adsorb hydrogen before an intercalated bulk phase is formed. By contrast, the highly intercalated $H_{0.625}WO_3$ is seen to have an equilibrium potential for H adsorption that is negative of the observed $H_{0.500}WO_3/H_{0.625}WO_3$ intercalation feature in the CV. In fact, this is still consistent with experiment, since we do not see any experimental evidence of intercalation above the $H_{0.625}WO_3$ stoichiometry.

The results shown in Figure 25 suggest that the CP-DFT approach is an improvement over the CHE when describing the dynamics of H adsorption and intercalation on H_xWO_3, and quite possibly other oxides. Indeed, although the CHE has seen widespread success in describing the thermodynamics of numerous electrochemical systems, it makes assumptions that may not accurately describe the kinetics of some electrocatalytic reactions. One important assumption of the CHE is that elementary steps require electrons to transfer in integer multiples. For elementary electrochemical reaction steps, the number of electrons transferred does not have to be an integer value[239, 244]. The possibility of partial electron transfer results from the ability of an electrode to redistribute charge in the near-vicinity of the electrode surface; hence, forming or breaking a bond between a proton and the electrode surface does not always require the transfer of a full electron into or out of the electrode[241]. Since the number of electrons transferred prior to and during the rate-determining step of an electrocatalytic reaction governs the dependence of reaction barriers on applied potential, an accurate kinetic analysis would benefit from the relaxation of the unit electron transfer assumption[245]. Still, the integer electron transfer assumption made by the CHE could be appropriate for fully thermodynamic investigations.

Overall, comparing the CHE equilibrium potentials with experiment suggests that the CP-DFT approach is better suited to describing the interaction of H_xWO_3 with hydrogen under electrochemical conditions. We note, however, that the $H_{0.000}WO_3$ CHE equilibrium potential for H adsorption does match well to the observed HER onset. Prior work has investigated WO_3 and its substoichiometric derivative, $WO_{2.9}$, for HER catalysis[211]. In that work, the limiting potential for hydrogen adsorption on WO_3 was found to occur at around -0.50 V vs. SHE, in rough agreement with our value of -0.25 V vs. SHE. The difference likely arises from our calculations including both explicit and implicit water solvation, whereas the prior results were computed in the gas phase. Notwithstanding that difference, either value is in reasonable agreement with the experimentally observed HER onset at -0.4 V vs. SHE. However, we clearly observe the formation of $H_{0.250}WO_3$ at considerably more positive potentials, and so the H^+/H^* adsorption equilibrium on $H_{0.000}WO_3$ is likely irrelevant in the potential range where we experimentally observe hydrogen evolution. Accordingly, the H adsorption equilibria we calculated with CP-DFT are broadly consistent with the physical picture of H adsorption followed by H insertion, followed by further H adsorption and H_2 evolution on the oxide bronze. For these reasons, we applied CP-DFT to execute more detailed calculations of hydrogen evolution energetics on H_xWO_3.

4.4.3 Partial Electron Transfer Governs the Potential-Dependence of Reaction Energies and Barriers

Using CP-DFT, we calculated from first-principles the dependence of reaction energies and barriers on applied potential. Figure 26a takes the water-mediated H_2-coupling step as an example and shows the change in grand canonical free energy, $\Delta\Omega$, with potential. The surface-mediated energetics are shown in Figure 76, but we found that the water-mediated mechanism is always more feasible. For reduction reactions, we expect a positive slope for $d\Delta\Omega/dU$ and a negative slope for oxidation reactions. Non-electrochemical (thermal) reactions have slopes of zero. For reactions that obey classical mechanisms involving unit proton-electron transfer in each elementary step, we would further expect the magnitude of $d\Delta\Omega/dU$ to be near 0.5 for activation barriers and 1.0 for full elementary steps. Remarkably, we instead observe slopes <0.3 for the water-mediated energies and barriers; that is, each of the elementary steps we modeled depend only weakly on applied potential.

The weak potential dependence is especially clear on $H_{0.000}WO_3$, where the H_2-coupling reaction energy changes by less than 0.25 eV over a span of at least 0.6 volts. Interestingly, we observed a significantly larger change in the same reaction energy, greater than 1.5 eV, by changing from $H_{0.000}WO_3$ to $H_{0.625}WO_3$. This demonstrates that H-intercalation has a more substantial influence on reaction energetics than changes in applied potential for a hypothetically fixed H stoichiometry. Stated more simply, if we considered only the $H_{0.000}WO_3$ surface and were able to prevent bulk H intercalation, then we would expect to need massive overpotentials to achieve appreciable HER turnover. Instead, investigating multiple H_xWO_3 surfaces shows the HER only proceeds at a meaningful rate with $x > 0$. This observation suggests that applied potential only indirectly influences the rate of hydrogen evolution on H_xWO_3—applying an electrochemical potential to the oxide primarily sets the bulk hydrogen stoichiometry, which in turn has a significant effect on reaction energies.

Although DFT calculations allow us to determine potential-dependent reaction energies at constant stoichiometries, the stoichiometry is also a function of applied potential. It is therefore challenging to experimentally measure the independent impacts of composition and overpotential on overall activity. Doing so would require that applied potential be

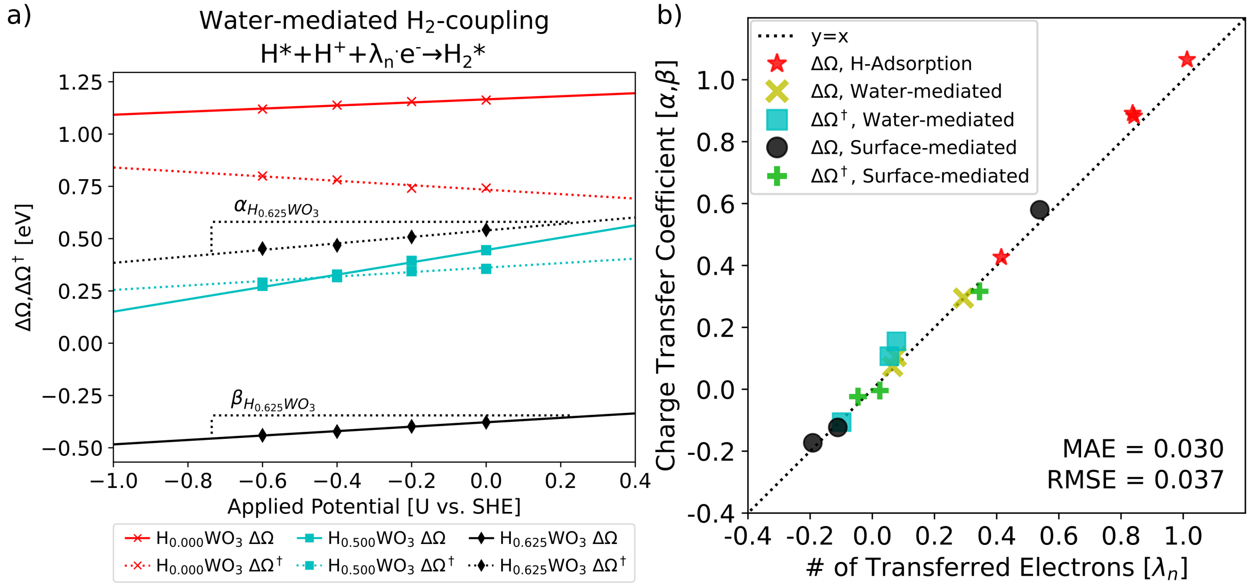

Figure 26: Energies and barriers for the water-mediated H_2-coupling step on H_xWO_3, which was found to be the most favorable pathway for hydrogen evolution. a) Reaction energies and barriers determined at several potentials (markers), with lines of best fit showing the linear dependence on applied potential. Changes in stoichiometry result in larger energy shifts than change in potential. b) Parity plot demonstrating 1:1 correspondence between number of electrons transferred and the apparent charge transfer coefficients.

modulated independently of bulk hydrogen stoichiometry. Since both hydrogen intercalation and hydrogen evolution are dependent on electrochemical potential, transient methods (e.g. electrochemical impedance spectroscopy or open-circuit potential/current decay[246]) could perhaps be used in future studies to more fully map the composition-overpotential-activity space.

We now examine why the energies shown in Figure 26a are such weak functions of applied potential. Figure 26b presents a comparison between two different types of charge transfer coefficients—defined as the slope of the relationship between reaction free energy or activation energy and applied potential—and the number of electrons transferred for each step, λ_n. The determination of these quantities is outlined in Appendix C. The charge transfer coefficients for transition states are labeled with α and the full elementary step reactions with β. We observed an excellent one-to-one agreement between charge transfer coefficients and λ_n, supporting the conclusion that partial electron transfer defines the potential dependence of the grand canonical free energies[244, 245, 240]. This once again highlights the benefit of using CP-DFT vs. the CHE model in our system. For these types of multi-site, multi-step catalytic reactions, charge transfer coefficients can deviate significantly from their expected values, and CP-DFT allows us to determine, from first principles, these unexpected values.

The relationship between charge transfer coefficients and λ_n also offers a means to accelerate the determination of the potential dependence of electrochemical reaction energies and barriers. In Figure 26a, each data point comprises a separate pair of energy calculations (of the initial and transition state configurations or the initial and final state configurations). The charge transfer coefficients for a given step are extracted from the resulting slope across multiple points, and therefore require many individual DFT calculations. We can instead perform a single pair of calculations at one potential and extract the number of electrons transferred between the states of interest. Because λ_n appears to remain virtually constant over modest overpotentials (see Figure 75 in Appendix C), Figure 26b suggests we can treat λ_n directly as the charge transfer coefficient. Doing so would avoid the execution of calculations at multiple potentials, reducing the total cost and increasing the speed of a CP-DFT analysis.

4.4.4 Effect of Bulk Hydrogen Intercalation on Preferred Reaction Pathways and HER Rates

Our computational and experimental data show that the energetics of hydrogen adsorption and of H_2-coupling on H_xWO_3 are both strong functions of bulk hydrogen intercalation. In Figure 27, we summarize what we conclude are the minimum energy pathways for hydrogen evolution, starting from bare H_xWO_3 surfaces and considering both hydrogen intercalation and evolution. The most feasible pathway for the HER is highlighted with the bolded arrows and outlined ellipses. Beginning with a non-intercalated tungsten oxide electrode, applying an increasingly negative bias will first preferentially intercalate hydrogen and form the bronze instead of evolving H_2. Once the bronze is formed, the reaction mechanism for the HER shifts from oxygen-centered surface coupling (top path) to metal-centered water-mediated coupling (bottom path). The top path is the hypothetical minimum energy pathway to H_2 on non-intercalated $H_{0.000}WO_3$. In this path, hydrogen first populates the terminal oxygens and then the bridging oxygens. Next, a water-mediated H adsorption occurs at the bridge oxygen, forming a bridging O-2H* consisting of two individual H atoms bound to O. We consider this step to proceed prior to H–H bond formation because the second incoming proton prefers binding to the O center. These H atoms only subsequently combine to form H_2, which then desorbs. Note, however, that the mechanism on $H_{0.000}WO_3$ should be considered as hypothetical, since it does not likely contribute meaningfully to hydrogen evolution. For the intercalated oxides, adsorption first occurs at the metal site, then at the terminal oxygen, but the latter H* does not participate in catalytic turnover. Instead, a third H adsorption occurs to facilitate the water-mediated formation of H_2 at the metal site, which then desorbs. Although both paths lead to H_2, the bold arrows in Figure 27 outline the practical consequence of applying a potential to WO_3, which is to sequentially intercalate and then evolve hydrogen on an H_xWO_3 surface.

An important takeaway from Figure 27 is the configuration of the catalyst surface prior to initial H adsorption within the catalytic cycle; this configuration is indicated by the yellow ellipses at the end of each pathway. The site of initial hydrogen adsorption does not necessarily dictate this configuration because it may not be consistent with the surface

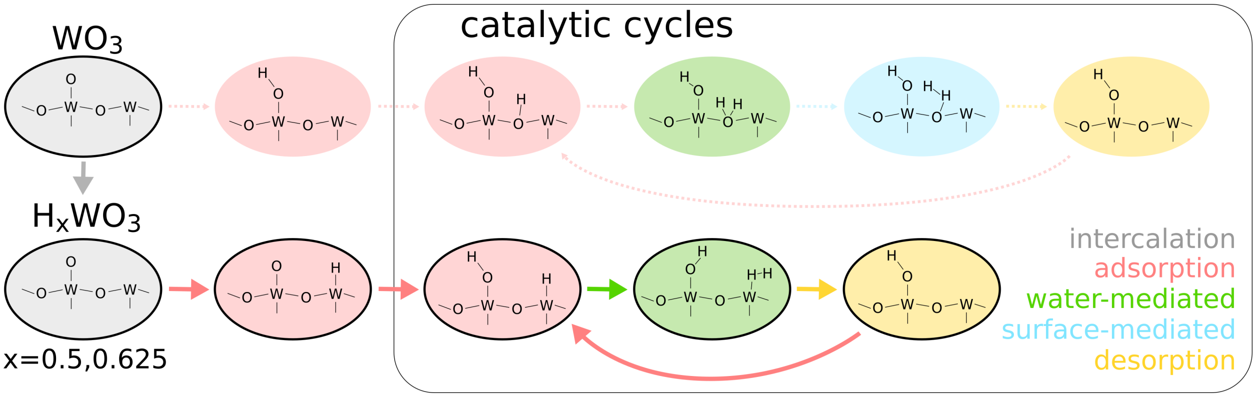

Figure 27: Reaction pathways from bare H_xWO_3 through H_2 formation and the relevant catalytic cycles. As bulk H stoichiometry increases, active sites for the HER shift from O centers to W centers. The bold arrows indicate the practical result of progressively decreasing applied potential, which first induces H-intercalation and then drives the HER.

composition resulting from catalytic turnover. For example, on $H_{0.625}WO_3$ the first H adsorbs to the metal site and the second adsorbs to a terminal O site. The desorption of molecular H_2 at the end of the cycle will expose only a metal site, leaving the terminal O-bound H as a spectator. Therefore, the start of the next catalytic cycle occurs as H adsorbs to an exposed metal site with the terminal oxygen site already populated. This elementary step is different from the initial adsorption of H to W, which occurs without a terminal O-bound H. Hence, the reaction coordinate diagrams shown in Figure 28 and the energies which informed the microkinetic models (*vide infra*) were referenced to the rightmost configurations shown in Figure 27 (i.e., desorbed states within the catalytic cycle).

Figure 28 shows reaction coordinate diagrams for the HER on $H_{0.000}WO_3$, $H_{0.500}WO_3$, and $H_{0.625}WO_3$. The different bronze compositions contrast starkly in apparent activity. $H_{0.000}WO_3$ gives rise to a highly unfavorable pathway to H_2, further supporting the notion that WO_3 cannot be responsible for HER activity. Furthermore, increased intercalation reduces the energy requirement for H_2 formation, thereby resulting in enhanced catalysis. Note that $H_{0.250}WO_3$ is not included in the remainder of this analysis since it is also unlikely to play a significant role at potentials relevant to HER on H_xWO_3. This is apparent from Figure 25b, where significant HER is only seen at potentials negative of the equilibrium potentials for formation of H:W ratios ≥ 0.500.

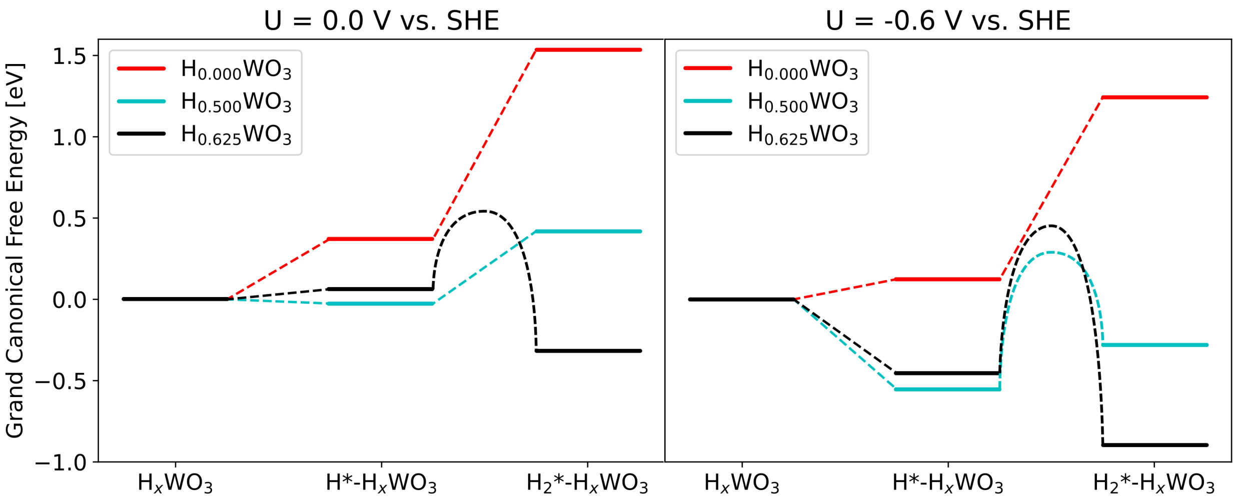

Figure 28: Reaction coordinate diagrams for three selected stoichiometries of tungsten oxide hydrogen bronze. The left panel shows reaction energies at an applied potential of 0.0 V vs. SHE, and the right at -0.6 V vs. SHE. Transition states are indicated via curved lines. Non-activated steps are shown with straight lines. All energies are determined using the PBE-D3 functional in the grand canonical, constant-potential formalism.

The reaction coordinate diagrams shown in Figure 28 further demonstrate the influence of applied potential on hydrogen evolution at H_xWO_3. Each intermediate and transition state energy is evaluated as an independent function of potential, such that the potential dependence of each elementary step can be used as the basis of a full microkinetic model. Figure 28 also shows that composition not only has an outsized effect on the single elementary step shown in Figure 26a, but also for the full HER pathways on H_xWO_3. We reiterate here that the initial states of the catalysts are the desorbed surfaces in Figure 27, with monatomic H adsorption occurring at full coverage of the respective adsorption sites. By constructing the reactions in this way, we can input all CP-DFT reaction energetics into a microkinetic model for the calculation of HER reaction rates and make direct comparisons to experimental HER measurements.

The experimental kinetic current density given by H_xWO_3 is shown in Figure 29a alongside the potential-current density relationships from first-principles-based microkinetic models for WO_3, $H_{0.500}WO_3$, and $H_{0.625}WO_3$. Complete details on construction of the microkinetic models, including discussion of the underlying assumptions, are presented in Appendix

C. Comparing experiment to theory clearly shows that only $H_{0.500}WO_3$ and $H_{0.625}WO_3$ replicate the steady state kinetic current densities observed in constant-current rotating disk electrode experiments. Indeed, the modeled HER rates on pure WO_3 were more than twenty orders of magnitude lower than the experimentally observed rates. In fact, as discussed in Appendix C, the calculated current densities specifically for WO_3 are an upper bound on the actual values. This motivates the conclusion that $H_{0.000}WO_3$ is irrelevant to the HER and should not be considered as an active catalyst. Instead, only the intercalated oxides provide sufficiently reactive sites for H_2 formation.

When first comparing the reaction coordinate diagrams in Figure 28 and the computed rates in Figure 29a, it seems unexpected that the $H_{0.500}WO_3$ gives lower activity than the $H_{0.625}WO_3$ surface. $H_{0.500}WO_3$ has a slightly lower barrier to H_2 than $H_{0.625}WO_3$ and would be expected to give faster turnover. However, the $H_{0.625}WO_3$ surface has a more favorable equilibrium balance between the H^* and $H_2{}^*$ species, as can be seen by the relatively exergonic energy change in forming $H_2{}^*$. Because the $H_{0.500}WO_3$ surface results in an endergonic energy change for this step, the equilibrium position favors the H^* state, thereby inhibiting H_2 evolution.

As a further check on activity, we examined the Tafel slopes and their dependence on potential. We chose not to fit a single straight line through the data, as there is some evidence of curvature even after correcting for 100% of uncompensated resistance. Moreover, the non-classical values of the charge transfer coefficients encountered through CP-DFT would be expected to cause Tafel slopes to deviate from cardinal values (e.g. 30, 40, 120), and we did not want to introduce modeling bias[238, 247]. However, with the experimental data points occurring at relatively large gaps in potential increments, using discrete differences as Tafel slopes is also not ideal. To address the uncertainty in fitting the data and associated inaccuracies, we opted to apply Gaussian process regression. This approach allowed us to fit and interpolate the experimental data, resulting in more accurate estimates of the (potential-dependent) Tafel slopes. Details on the regression methods are included in Appendix C.

Figure 29b compares potential-dependent Tafel slopes from the first-principles-based microkinetic models with the Tafel slope relationship derived from Gaussian process regression of the experimental measurements shown in Figure 29a. The experimental Tafel slope begins

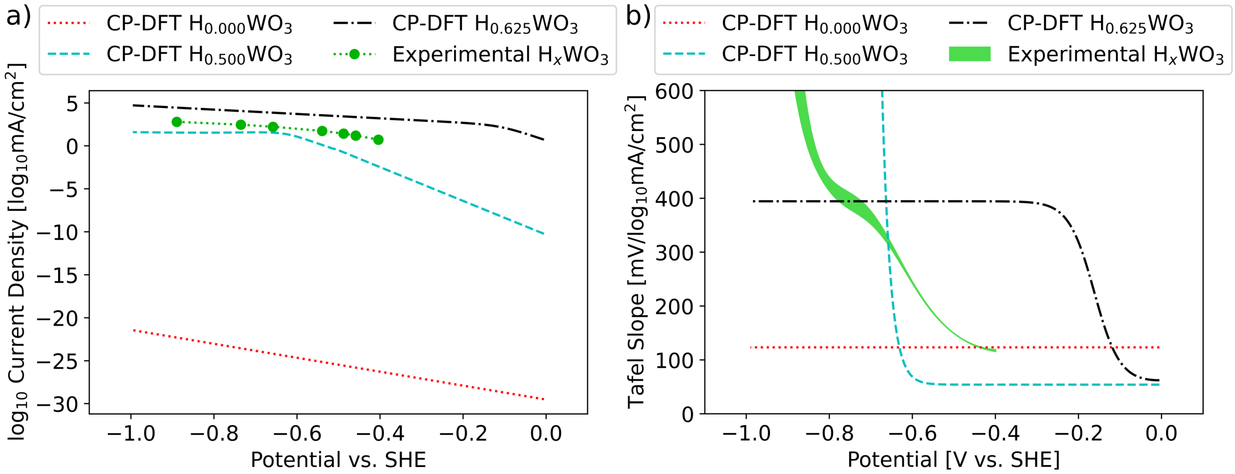

Figure 29: Comparison between microkinetic model rates and experimentally measured HER rates. a) Kinetic current densities as a function of potential, with the experimental data as points. The line connecting experimental data points are meant to guide the eye. Kinetic currents were extracted from total measured currents with the Koutecký-Levich equation. b) Tafel slopes computed from first-principles-based microkinetic rates and from the experimental data, with the green shaded area giving 99% confidence interval bounds for the experimental Tafel slope value.

near a value of 120 mV/decade, but it exhibits a strong potential dependence, increasing significantly at potentials negative of -0.5 V vs SHE. Note that we minimized the impact of transport limitations on the experimental current-potential measurements by using a rotating disk electrode with a rotation rate of 1600 rpm, and we further corrected for mass transfer limitations using the Koutecký-Levich equation as described in the experimental methods section[235]. We also accounted for uncompensated cell resistance, as detailed in the experimental methods section; thus we do not expect conductivity limitations. The steep Tafel slopes can therefore be interpreted as a manifestation of the small charge transfer coefficients shown in Figure 26, where applied potential has little effect on reducing activation barriers.

The large empirical Tafel slopes can also be rationalized from the microkinetic results. WO_3 shows a constant Tafel slope of ~ 123 mV/dec, suggesting consistent reaction dynamics across all applied potentials. On the other hand, $H_{0.500}WO_3$ and $H_{0.625}WO_3$ show increasing Tafel slopes as the applied potential becomes more negative, which generally agrees with the experimental result. The former starts at $\sim$ 65 mV/dec, and negative of -0.6 V vs. SHE the Tafel slope rapidly increases toward infinity. This is because the current density becomes independent of applied potential below -0.6 V vs. SHE, as apparent from Figure 29a. The barriers for both H adsorption and H_2-coupling become low enough at these potentials that the HER reaches a maximum rate that is no longer dictated by a potential-dependent activation energy, but instead by site density, surface coverage, and the magnitude of the Arrhenius prefactor. Nonetheless, the maximum rate predicted for $H_{0.500}WO_3$ is smaller than rates predicted for $H_{0.625}WO_3$ over the same range of overpotentials; this is because the $H^*/H_2{}^*$ equilibrium on $H_{0.500}WO_3$ favors H^*, as discussed above. $H_{0.625}WO_3$ also exhibits a large increase in Tafel slope beginning at more modest potentials near -0.15 V vs. SHE. This shift is due to the change in initial H adsorption from endergonic to exergonic. The H_2 formation barrier then limits HER turnover on the $H_{0.625}WO_3$ surface, leading to a large $\sim$ 400 mV/dec Tafel slope at potentials lower than ~ -0.3 V vs. SHE.

At large negative potentials the experimental Tafel slope steadily increases at a rate that is between those computed for $H_{0.500}WO_3$ and $H_{0.625}WO_3$. We observed two contributions to shifting Tafel slopes in the microkinetic data, with the presence of non-zero barriers causing large, finite Tafel slopes, and low barriers for all elementary steps causing potential-independent behavior. Notably, there is a slight shoulder corresponding to a Tafel slope of ∼ 400 mV/decade between −0.7 and −0.8 V vs. SHE that agrees quite well with the microkinetic result for $H_{0.625}WO_3$. However, at still larger overpotentials the Tafel slope increases toward infinity, suggesting barrierless reactivity. At large overpotentials this behavior can be expected for reduction reactions, since the barriers will become small enough to cause potential independence. We also cannot rule out transport limitations at the largest overpotentials we measured, as the Tafel slope would be expected approach infinity as the reaction rate approaches an external mass transfer limit. Nevertheless, the potential-dependent behavior of the experimental Tafel slopes are generally consistent with the microkinetic data such that the intercalated $H_{0.500}WO_3$ and $H_{0.625}WO_3$ bronzes are likely responsible for the HER.

4.4.5 Prevalence of Exposed Metal Sites in an Electrochemical Environment

Metal oxides are known to interact strongly with water, resulting in adsorbed hydroxyls, protons, and associated water molecules that can block surface active sites[248, 249]. Thus, despite the agreement between experimental and computational results, we remained concerned that the aqueous electrochemical environment could facilitate strong surface hydration and limit H adsorption at active W sites. Since metal site blocking via hydration would inhibit the HER mechanism we proposed in Figure 27, we further examined the free energies of water interacting with various surface sites. The results are shown in Figure 30, and the specific configurations in Figure 83 of Appendix C.

Examination of the relative free energies compiled in Figure 30 show that only intercalated H_xWO_3 exhibits accessible and exposed metal sites. The first step depicted in these reaction coordinate diagrams is the association of a tungsten-bound hydroxyl and a bridging oxygen-bound hydrogen to form an adsorbed water at the tungsten atom. This is followed by the desorption of the formed water molecule and exposure of the metal site. A final step involves population of the bare W site with an H atom, and the thermodynamics of this reaction are potential-dependent—thus, applied potential can drive the equilibrium toward

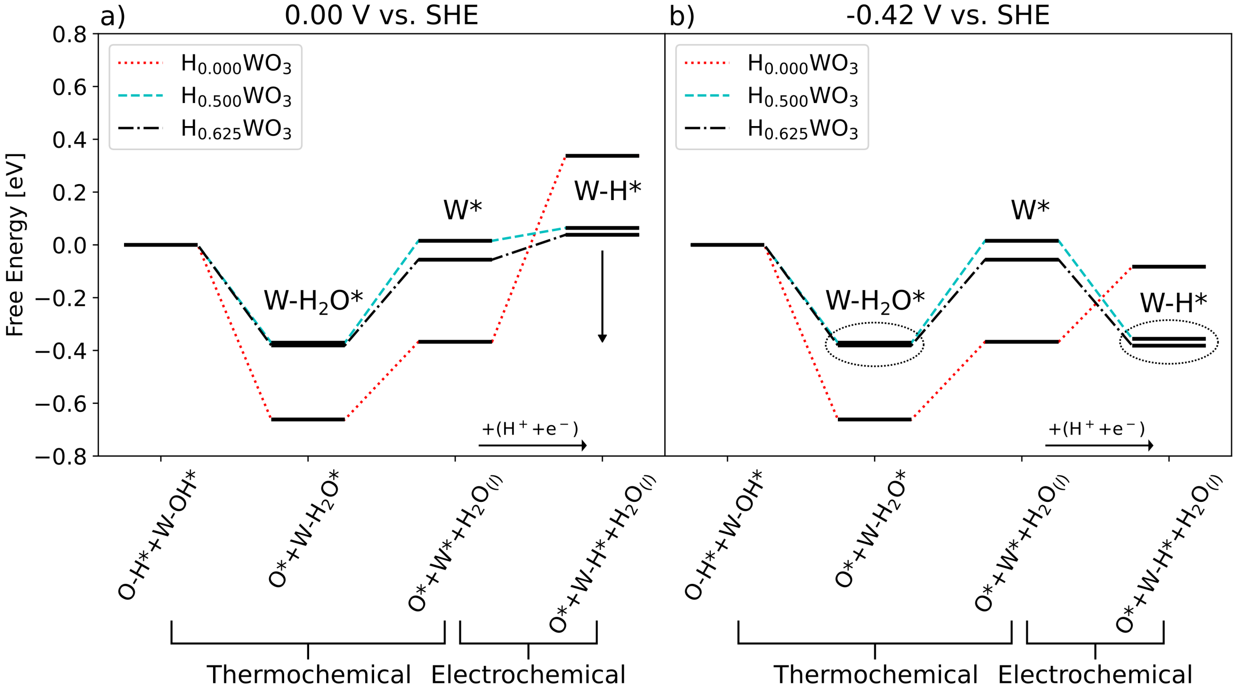

Figure 30: Reaction coordinate diagrams depicting dehydration of fully hydrated oxide surfaces, wherein each W atom is covered by a hydroxyl group and an adjacent bridge oxygen is protonated. a) The pathway at 0.00 V vs. SHE. b) The pathway at -0.42 V vs. SHE, which is near the experimental onset potential for the HER. Only the last step of the dehydration pathway is electrochemical, and therefore only the final configuration shifts in free energy between the two applied potentials. At the experimental HER onset potential, the relative energies of the water-blocked metal site and the adsorbed hydrogen states become equivalent, allowing the HER to proceed.

the dehydrated, H-adsorbed state. Comparing the second and fourth states shown in Figures 30a and 30b, H atoms at the exposed H_xWO_3 surface W sites are stabilized related to surface-bound water at potentials more negative than approximately -0.4 V vs. SHE. Hence, applying a sufficiently negative bias to the intercalated bronzes brings the hydrogen- and water-terminated W sites to similar relative free energies, allowing the electrochemical HER to compete with surface hydration. At potentials lower than -0.4 V vs. SHE—near the experimental onset potential for the HER—the W site will be preferentially populated with a hydrogen atom instead of a water molecule, allowing the HER to proceed unhindered by water molecules. Notably, this contrasts with non-intercalated WO_3, where water remains strongly bound to surface W atoms even at potentials far negative of the onset of H intercalation. This agrees well with our previous observation that the O sites are the ones that accomodate H binding on $H_{0.000}WO_3$ (Figure 24). Thus, it is plausible that bulk H intercalation proceeds primarily via H adsorbed to surface O atoms in WO_3, whereas the HER proceeds primarily at W sites on the intercalated compound. We reiterate, however, that it remains unlikely that WO_3 is an effective catalyst for the HER, as the rates we have calculated and shown for $H_{0.000}WO_3$ in Figure 29 are much too slow to explain the experimentally measured HER currents. Overall, the results shown in Figure 30 further support the conclusion that bulk hydrogen intercalation enhances HER catalysis by activating surface W atoms that would otherwise be blocked by water and unreactive toward protons in solution.

4.5 Conclusions

In summary, this work presented DFT calculations, microkinetic modeling, and experimental electrochemical measurements directed at understanding the HER on WO_3. The main finding of this work is that hydrogen intercalation changes the chemical identity of WO_3, leading to enhanced catalytic activity for the HER. Under reducing conditions, WO_3 is converted into H_xWO_3, which has a higher prevalence of active metal surface sites. These sites are virtually inaccessible on the initial WO_3 surface, and H_2 generation is only feasible on H_xWO_3. This is important to recognize, because many catalytic modeling and experimental studies do not consider the possibility of bulk changes, and therefore may not be addressing the true active catalyst.

More specifically, the increase in HER activity with H-insertion occurs because of modulations in the oxide electronic structure, whereby electronic conductivity is enhanced, surface metal sites become more acidic, oxygen sites become less basic, and W-H bonds are stabilized. We also found that the HER rate on H_xWO_3 is not accelerated efficiently with increased overpotential for any single H stoichiometry. Instead, applying an electrochemical bias mainly serves to set the bulk hydrogen stoichiometry of the oxide, thereby enabling access to surfaces that are much more intrinsically HER active. Furthermore, the charge transfer coefficients for each elementary step on H_xWO_3 correlate tightly with the fractional number of electrons transferred for the respective steps. This observation gives avenues for simplifying CP-DFT analyses, whereby electron transfer numbers can be used as proxies for charge transfer coefficients in kinetic models involving modest changes (up to a few hundreds of mV) in applied potential.

More broadly, our findings highlight an under-explored complexity of metal oxide catalysts, wherein their bulk redox reactivity is at least as important as their surface reactivity in the context of cathodic (reductive) electrocatalysis. These results underscore the importance of considering how reaction conditions impact bulk catalyst composition and the associated surface reactivity. Owing to the fact that many redox-active metal oxides insert protons under aqueous electrochemical conditions, it is highly likely that hydrogen intercalation plays a critical role in the electrocatalytic activity of metal oxides toward numerous reactions involving hydrogen intermediates. Accordingly, it is important consider the reducibility of a candidate metal oxide along with the relevant reaction conditions to determine whether bulk hydrogen intercalation will occur alongside to the reaction of interest. Our results also suggest that the insertion of sodium, potassium, or other cations could influence catalytic activity in a similar way to proton insertion, thereby offering a potential route to dynamically tune the catalytic activity of metal oxides. Even further, this phenomenon may not be restricted to the family of metal oxide bronzes, but could extend to any material which can accept a guest ion. Outside of electrochemical environments, the impact of hydrogen intercalation on catalysis may also be relevant in thermochemical reactions in which hydrogen spillover to oxide supports has been observed. In these situations, the associated changes in the electronic structure and surface chemistry of the oxide are not often interrogated in detail. Future materials screening efforts, kinetic analyses, and characterizations of metal oxides as catalysts and supports for, e.g., hydrogenation reactions would therefore benefit from careful consideration of their H insertion chemistry.

5.0 Activating Hydrogen Equivalents from Water and Delivering Them to Reactive Substrates

5.1 Context

Chapters 2, 3, and 4 explored the fundamental thermodynamics, transport phenomena, and kinetics of hydrogen transfers with metal oxides. Together, those efforts outline a foundational understanding of how metal oxides might be used to enable water as a source of reactive hydrogen. This Chapter leverages these earlier learnings to demonstrate oxide-mediated hydrogen transfer from water to a model organic oxidant. The reactor design and associated experiments discussed below were designed to test the hypothesis that a metal oxide bronze could intercalate hydrogen and deliver hydrogen to an appropriate hydrogen acceptor.

5.2 Introduction

In Chapter 1, a thermodynamic framework was presented that can be used to pair metal oxide hydrogen donors with candidate hydrogen acceptors. This framework required an understanding of the equilibrium reduction potentials for H transfer to both the oxide and the hydrogenation target. WO_3 is the most well understood hydrogen bronze in terms of H intercalation thermodynamics, and so we chose it as a model bronze to carry out all following experiments. [250, 51, 251, 252] Taking WO_3 as a model hydrogen bronze, we selected the hydrogenation of 2,2,6,6-tetramethyl-piperidin-1-yl-oxyl (TEMPO) to 1-hydroxy-2,2,6,6-tetramethyl-piperidine (TEMPO-H) as a model hydrogenation chemistry. TEMPO is a stable nitroxyl radical which readily engages in reversible H atom (or 1 H^+ / 1 e^-) transfer. This radical was selected as a model hydrogenation target for three reasons:

1. The TEMPO/TEMPO-H couple exhibits a standard reduction potential for 1 H^+ / 1 e^- transfer (>+0.5 V vs. SHE[253, 254]) that is sufficiently positive of $WO_3/H_{0.250}WO_3$

equilibrium (∼+0.2 V vs. SHE[51]).

2. The hydrogenation of TEMPO to TEMPO-H is accompanied by a stark disappearance of UV-Vis absorbance, providing a straightforward means of quantifying conversion.[255]
3. TEMPO/TEMPO-H PCET has been previously used to successfully study PCET to/from metal oxides.[24]

Chapter 1 also introduced two schemes for activating and delivering hydrogen from water to a reactive substrate. These were either spatially decoupled or temporally decoupled hydrogenations. Each of these processes relied on two different reactor architectures. Spatially decoupled hydrogenations have been demonstrated previously in both fundamental[256] and applied[257] settings. In terms of spatially decoupled reactor construction, H equivalents are required to move through the bulk of some solid phase active material. Chapter 3 made explicit measurements of the diffusion coefficient of hydrogen in WO_3, and it is prohibitively small (1.3 x 10 $^{-7}$ cm^{s}/s). Such a mass transfer limitation requires oxide membrane thicknesses on the order of ∼100 μm to allow for sufficiently rapid H transport from an electrolyzer chamber to a hydrogenation chamber; currently, our membrane fabrication techniques do not allow for such thin architectures. Acknowledging this limitation and previous demonstrations of spatially decoupled hydrogenations, we chose to focus on demonstrating H transfer from water to TEMPO in a temporally decoupled manner. These efforts therefore present two interesting advances: 1. the demonstration of a metal oxide bronze as a competent H mediator and 2. the implementation of temporally decoupled H transfer.

5.3 Materials & Methods

2,2,6,6-tetramethyl-piperidin-1-yl-oxyl (TEMPO, Sigma Aldrich, 214000) and 4-hydroxy-2,2,6,6-tetramethyl-piperidin-1-yl-oxyl (TEMPOL, Sigma Aldrich, 176141) were used as received. Aqueous solutions of the radicals were prepared by dissolving each in de-ionized (DI) water (Milli-Q).

All electrochemical experiments were conducted using a Gamry Reference 600 potentiostat. Constant potential measurements were performed in a reactor using a three electrode setup, with a Ag/AgCl reference (CH Instruments, CHI111), a RuO_2/Ti counter electrode, and a WO_3 composite working electrode. Open circuit potential measurements were completed with the same setup. The reference electrode was experimentally calibrated to the reversible hydrogen electrode scale using a separate three electrode setup. This setup consisted of the same reference electrode, a graphite rod counter electrode (Electron Microscopy Sciences, 0.25 in. diameter, Spectro-Grade), and a platinum disk working electrode (CH Instruments, CHI102) in a glass electrochemical cell. H_2 gas (Matheson, 99.999%) was bubbled through the cell until a stable potential was measured ($<$ 1 mV change for 1 minute).

The RuO_2/Ti electrode was prepared starting from a Ti foil (Alfa Aesar, 00971, 0.127 mm thickness). Ti was sanded and then washed with acetone, followed by ethanol, and finished with water. The cleaned foil was then dipped into a 0.1 M solution of $RuCl_3$ (Alfa Aesar, 11043) in de-ionized water (Milli-Q). This treated foil was then dried with a heat gun. After drying, the Ru-coated foil was calcined in a box furnace for 10 minutes at 450 °C. Once cooled, the calcined foil was again dipped into the 0.1 M $RuCl_3$ solution, dried, and calcined. A total of nine dip-dry-calcine cycles were completed. Finally, the electrode was annealed for 4 hours at 450 °C.

WO_3 composite electrodes were prepared from WO_3 inks. In a typical preparation, 1.275 g of WO_3 (Sigma Aldrich, 550086) was mixed with 0.225 g of polyvinylidene difluoride (PVDF, MTI, HSV900) and dispersed in 2 mL of 1-methyl-2-pyrrolidinone (NMP, Acros Organics, 390682500). This ink was then sonicated for 30 minutes. The WO_3/PVDF ink was then coated onto the microporous side of a Teflon-treated carbon gas diffusion electrode (Sigracet 22 BB, Fuel Cell Store) and dried under an infrared heat lamp. Total dry masses of deposited WO_3/PVDF were recorded by measuring the weight of the Sigracet before coating and the full composite after coating.

The reactor used for all experiments in this work is schematized in Figure 31 and visualized in 32. Endplates and the electrolyzer-side flowfield were cut from polyetherimide (PEI, Ultem, McMaster Carr, 3/8 in. thickness) sheets using a benchtop mill (Carbide 3D, Nomad 3). The graphite flowfield was cut from graphite (McMaster Carr, 1/4 in. thickness) sheet, also using the benchtop mill. The RuO_2/Ti dimensionally stable anode (DSA) and oxide membrane were made as described above. The accessible geometric surface areas of the DSA and WO_3/PVDF were 33 mm x 33 mm, as determined by a fluorosilicone gasket which was set between the composite electrode and the PEI flowfield. Electrical contact was made by inserting copper shim stock into the stack between the endplate/DSA and between the graphite flowfield/endplate. In this work, no material passed through the graphite flowfield—it is only used as an electrical contact to the oxide working electrode. Only the PEI flowfield (electrolyzer-side chamber) was used in these experiments. Figure 32 shows all fabricated components except for the DSA and the composite oxide electrode.

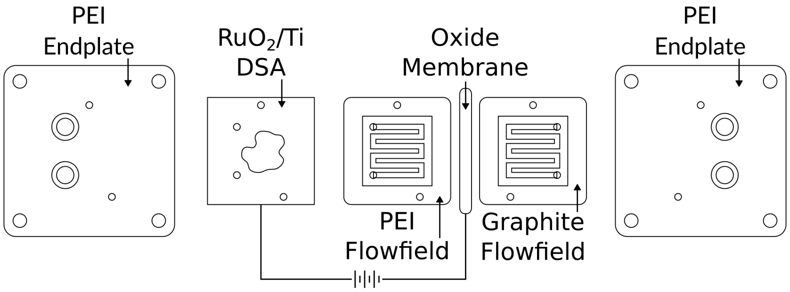

Figure 31: Schematic of thermoelectrochemical reactor. Endplates were constructed from polyetherimide. The electrochemical chamber flowfield was also made of polyetherimide. Electrodes were a dimensionally stable anode and a metal oxide/PVDF composite, both fabricated in-house. An optional graphite flowfield was included in the stack to allow for continuous, through-membrane hydrogenations. The current experiments only used the electrochemical side of the full reactor stack in a looping modality.

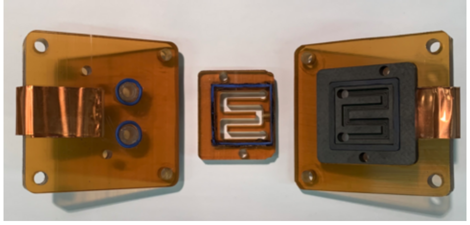

Figure 32: A photograph of the actual reactor which is schematized in Figure 31. Not shown are the dimensionally stable anode and the oxide/PVDF composite cathode.

UV-Vis measurements were made using an Agilent Cary 60 spectrophotometer equipped with a fiber optic coupler. Fiber optics were used to route the instrument optical path through a flow cell (Ocean Insights, FIA-USP-100, 100 μm pathlength). This flow cell has been previously used to track PCET reactions of quinones for applications in redox flor batteris.[258] As shown in Figure 33, this flow cell was connected to the outlet of the reactor.

Spectra were collected from 350 nm to 200 nm at scan speed of 300 nm/s. The particular timing intervals for scans varied for each experiment, and are noted below where appropriate. All reported spectra, represented here as $\tilde{A}_{solution}$, were referenced to de-ionized water.

$$\tilde{A}_{solution} = A_{solution} - A_{H2O} \tag{5.3.1}$$

Here, $\tilde{A}_{solution}$ is the normalized absorbance spectrum of a sample, $A_{solution}$ is the raw absorbance of a sample measured directly with the spectrophotometer, and A_{H2O} is the raw absorbance measured for a blank de-ionized water sample. Reference molar absorption coefficients, ϵ, for TEMPO and TEMPOL in de-ionized water and in 0.2 M sulfuric acid (Fisher, A300-212) were collected in a separate 1 mm pathlength quartz cell (BASi EF-1358) and are shown in Figure 34. The magnitude of the spectra in de-ionized water are consistent with values reported by NIST.[259] We note that the acid-containing solutions exhibit smaller absorption coefficients than the acid-free solutions. This is likely due to the conversion of the radicals to their oxoammonium analogs at low pH, which have characteristically lower absorptivities.[253] Effects of this conversion will be briefly discussed later in this work.

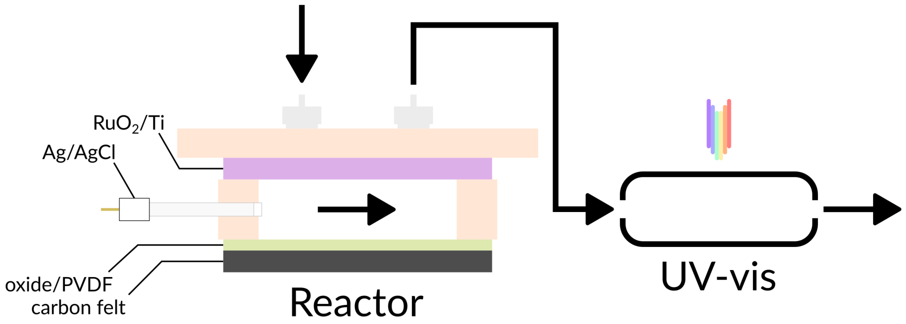

Figure 33: Depiction of single-pass hydrogenation experiments. The reactor was used in a three-electrode setup. Solution flowed first through the reactor, then through a UV-Vis cell for in-line concentration measurements. After exiting the flow cell, all effluent was sent to waste.

These coefficients were measured by recording individual absorbance spectra for series of 1, 2, 3, 4, and 5 mM solutions. Absorbances were converted to molar absorption coefficients using the Beer-Lambert Law.

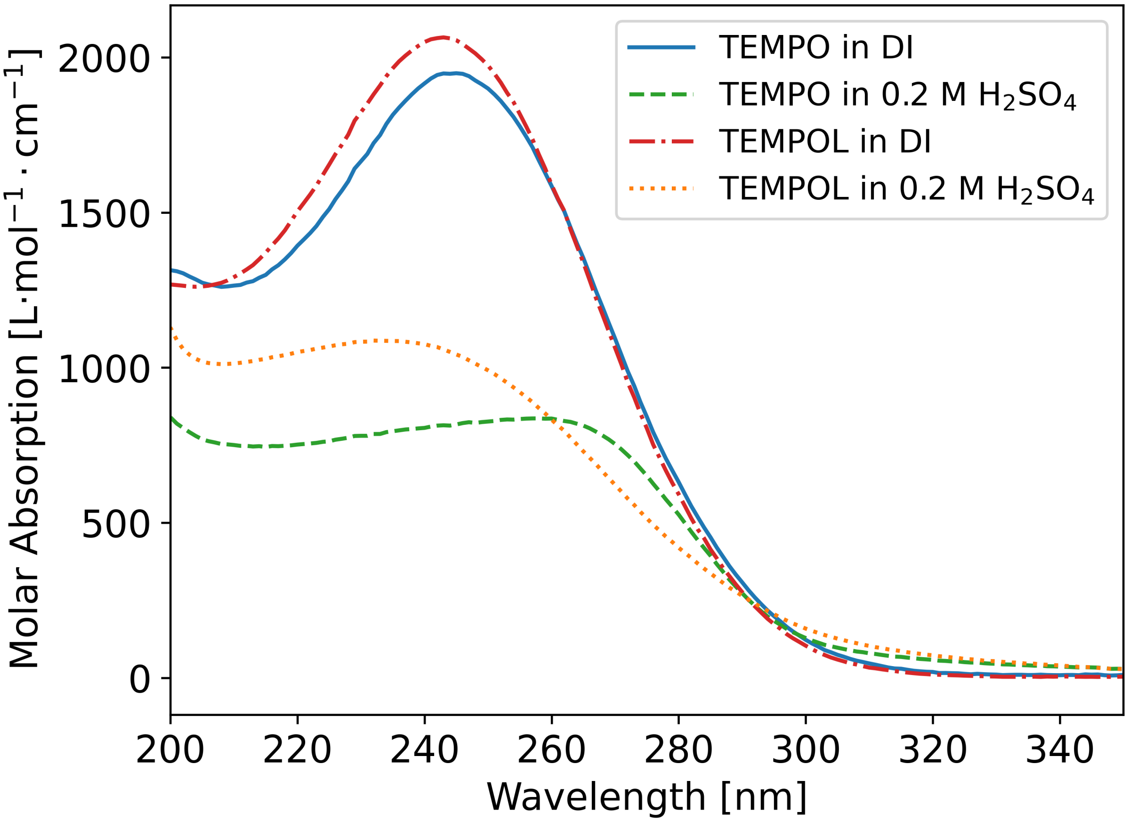

Figure 34: Reference molar absorption coefficients for TEMPO(L) in DI water and 0.2 M H_2SO_4

$$\tilde{A}_{solution} = \epsilon \cdot c \cdot l \tag{5.3.2}$$

In equation 5.3.2, $\tilde{A}_{solution}$ is the same normalized absorbance mentioned previously, ϵ is the molar absorption coefficient, c is the concentration of the substance of interest, and l is the pathlength of the cell. The ϵ values reported in Figure 34 are averaged across the five samples recorded at c = 1, 2, 3, 4, and 5 mM radical concentrations. These reference ϵ values were then used with Equation 5.3.2 to convert measured absorbance spectra to concentrations. Concentrations were determined by fitting ϵ values to absorbances using Equation 5.3.2 and non-linear least squares. The measured $\tilde{A}_{solution}$ values of a sample, reference ϵ values, and the pathlength were used as inputs. The concentration was the single free parameter in the fits.

The transfer of hydrogen from water to TEMPO via WO_3 can be summarized in three separate reactions:

1. Oxygen evolution reaction: $\frac{n}{2}H_2O \rightleftharpoons n(H^+{+}e^-) + \frac{n}{4}O_2$
2. Hydrogen intercalation: $n(H^+{+}e^-) + H_{x-n}WO_3 \rightleftharpoons H_xWO_3$
3. TEMPO hydrogenation: $H_xWO_3 + n\text{TEMPO} \rightleftharpoons H_{x-n}WO_3 + n\text{TEMPO-H}$

In these reactions, n is the number of H^+ and e^- pairs which are transferred. The first reaction is the oxygen evolution reaction, which in this case serves as the terminal source of hydrogen equivalents. It is an electrochemical half reaction and is shown in the direction of oxidation because it occurs at the RuO_2/Ti anode. The second reaction is electrochemical hydrogen intercalation into WO_3. It is also an electrochemical half reaction and is shown in the direction of reduction because it occurs at the WO_3/PVDF cathode. These first two reactions comprise the full electrochemical reaction which activates hydrogen equivalents from water:

$$\frac{n}{2}H_2O + H_{x-n}WO_3 \rightleftharpoons H_xWO_3 + \frac{n}{4}O_2 \tag{5.3.3}$$

We note that Equation 5.3.3 is written such that the stoichiometry reflects the reaction of a single H^+ and e^- pair. Although it is feasible to have $n = 1$ H^+ and e^- pairs, the oxygen evolution reaction always generates $n = 4$ protons and 1 dioxygen molecule. This ratio of protons to dioxygens is the reason for the $\frac{n}{4}$ stoichiometric coefficient on O_2.

Once H^+ and e^- pairs are intercalated into WO_3, it forms a hydrogen containing bronze which can donate hydrogen to TEMPO. This is the third reaction, which is non-electrochemical. Combining the full electrochemical intercalation with TEMPO hydrogenation (or combining all three reactions directly) yields the following net hydrogenation reaction:

$$\frac{n}{2}H_2O + n\text{TEMPO} \rightleftharpoons +n\text{TEMPO} - \text{H} + \frac{n}{4}O_2 \tag{5.3.4}$$

In this work, Equation 5.3.4 was achieved in two temporally decoupled reaction steps: 1. electrochemical charging (hydrogen intercalation into WO_3) and 2. reactive discharging (hydrogen de-intercalation from WO_3). First, the reactor shown in Figure 33 was operated in an electrochemical mode (step 1). A sufficiently negative constant potential was applied to the WO_3/PVDF working electrode such that the electrochemical intercalation shown in

Equation 5.3.3 was achieved. In all experiments, this electrochemical charging step was performed while flowing 0.2 M H_2SO_4 at 1.6 mL/min. The particular potentials used for charging depended on the desired final hydrogen:tungsten stoichiometry, and are shown later for each relevant experiment. Charging was performed until the measured current was less than 2 mA, at which point polarization was disengaged. De-ionized water was then run through the reactor at 2.6 mL/min for 3 minutes to clear any residual acid. The moles of injected H^+ and e^- pairs were calculated by assuming that every electron passed during charging was involved in the reduction of one proton. The total number electrons, Q, was determined by integrating the recorded current.

$$Q = \int_{t_0}^{t_{end}} i(t)\, dt \tag{5.3.5}$$

Here, t_0 is the start time of charging and t_{end} is the finishing time. i is the measured current trace in units of amps. This total charge was then converted to moles of electrons and protons through division by Faraday's constant.

$$N_H = \frac{Q}{F} \tag{5.3.6}$$

Here, N_H is the moles of H^+ and e^- pairs which are intercalated. The total deposited mass of WO_3 was recorded during coating, and the available moles of WO_3 for intercalation was computed as follows.

$$N_{WO3} = \frac{m_{WO3}}{MW_{WO3}} \cdot \frac{A_{active}}{A_{coated}} \tag{5.3.7}$$

Here, N_{WO3} is the number of moles of WO_3 accessible for intercalation, m_{WO3} is the total coated mass of WO_3, MW_{WO3} is the molecular weight of WO_3, A_{active} is the 33 mm x 33 mm gasket-defined electrode area, and A_{coated} is the total area that was coated with WO_3 ink.

The second reaction step was then conducted by flowing TEMPO (or TEMPOL) through the reactor at 2.6 mL/min (step 2). UV-Vis measurements were initiated at the same time TEMPO (or TEMPOL) flow began. In certain cases, open circuit potentials were also recorded through the course of the reactive discharge step.

TEMPO (or TEMPOL) concentrations were converted to by taking the difference in measured concentrations for a blank reactor run and a charged reactor run. In the blank reactor run, no charging step occurred, and the reactant was flowed through the reactor. Since there were H equivalents available for hydrogenation to occur, this experiment measured the breakthrough of TEMPO (or TEMPOL) through the reactor. By taking the difference between a charged reactor run and this blank run,

$$X = 100 * \frac{c_{blank} - c_{charged}}{c_{blank}} \tag{5.3.8}$$

Here, X is the total conversion in %, c_{blank} is the concentration trace measured in a blank run, and $c_{charged}$ is the concentration trace measured in a charged, live run. Since the net hydrogenation results in a decrease in TEMPO (or TEMPOL) concentration, c_{blank} should always be larger than $c_{charged}$.

5.4 Results & Discussion

Figure 35 shows our first results in performing net hydrogenations using water as a hydrogen source. In this experiment, the reactive discharge (step 2) was performed using 20 mM TEMPO in 0.2 M H_2SO_4. Spectra were collected every 30 seconds for a total of 30 minutes. Figure 35a visualizes data collected by the spectrophotometer (red solid lines) and the resulting Beer-Lambert fits (black dashed lines) for a run in which the WO_3/PVDF cathode was polarized at +0.5 V vs. RHE. This potential is situated positive of the first reduction potential for WO_3 ($\sim$+0.2 V vs. RHE[51]), and so no H insertion was expected. Indeed, essentially no current was passed and charging ended immediately. Notably, the raw absorbance spectra in Figure 35a exhibit periodic waves in intensity. This corresponds to the period of the peristaltic pump that was used to control flow through the reactor test stand. Utilizing fits across the full spectrum dampens the total effect of this noise on resulting concentration estimates. The lighter red lines correspond to early time data, and the darker ones are later time data. As can be seen, TEMPO concentration start near zero, but rapidly increase and approach a maximum. This is the breakthrough of the TEMPO through the reactor.

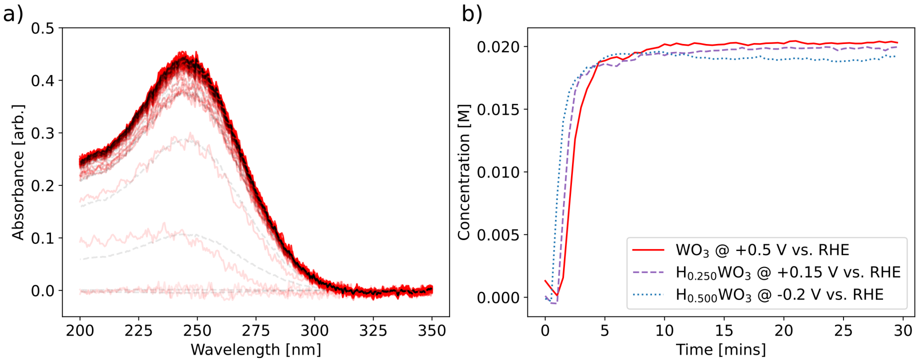

Figure 35: UV-Vis and concentration data measured for a typical single-pass hydrogenation. a) UV-Vis spectra (red lines) recorded every 30 seconds for 30 minutes of reaction time. Lighter lines are earlier in time, and darker lines are later in time. The black lines are Beer-Lambert fits using reference molar absorption coefficients shown in Figure 34. b) Concentration vs. time data extracted via Beer-Lambert fitting of the recorded spectra. Three traces are shown for three different levels of H insertion in H_xWO_3. Higher amounts of intercalated H give lower steady-state TEMPO concentrations.

Figure 35b then shows the resulting concentration traces which are extracted from the measured absorbance data. Beyond the +0.5 V vs. RHE data that was shown in Figure 35a, also shown are data for step 1 polarizations at +0.15 V vs. RHE and -0.2 V vs. RHE. These potentials are situated just negative of the equilibrium potentials for $WO_3/H_{0.250}WO_3$ and $H_{0.250}WO_3/H_{0.500}WO_3$, respectively. Thus, the expected stoichiometries for each case are $H_{0.250}WO_3$ and $H_{0.500}WO_3$. After approximately 2.5 minutes, concentrations of TEMPO begin to increase rapidly. This 2.5 minute delay corresponds to the total volume of the reactor and tubing ($\sim$ 7 mL) and the flow rate of the TEMPO in step 2 (2.6 mL/min). The +0.5 V vs. RHE sample reached a concentration of approximately 20 mM, which is the same as the solution fed into the reactor. As expected for this non-intercalated sample, no hydrogenation appeared to occur. However, the +0.15 and -0.2 V vs. RHE samples showed lower steady-state concentrations, indicating a small amount of TEMPO hydrogenation.

The breakthrough times of each trace also follow an interesting trend, where systems that were charged at more negative potentials seem to show faster breakthrough. This indicates either the TEMPO moves through the system faster when contacting a bronze instead of an oxide, or the bronze creates more TEMPO. Since there is no reactant which can allow for the former, there must be some an effect of the various charged interfaces on the boundary conditions of flow in the reactor channels. The current experiments are focused on steady-state and long-term behavior, and we leave the study of short-term reaction and flow dynamics for future work.

Figure 36 shows the same data presented by Figure 35 as total chemical conversions. The lines represent the average conversions measured across three unique replicates, with the shaded areas illustrating a 95% confidence interval. At short times, both the low- and high-hydrogen samples exhibit approximately 5% conversions of TEMPO. After 10 minutes, the $H_{0.250}WO_3$ sample lowers to essentially zero conversion The $H_{0.500}WO_3$ sample remains around 3–4% conversion for the remainder of the experiment, although these values are not significantly different from zero. Still, these small conversions hint at a successful hydrogenation of TEMPO, illustrating how WO_3 can electrochemically activate hydrogen from water and the ability of H_xWO_3 to donate hydrogen to an appropriate acceptor.

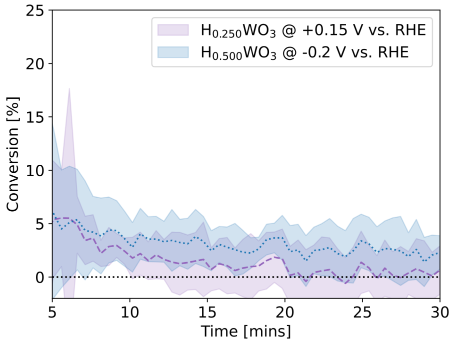

Figure 36: TEMPO conversion vs. time for two different H_xWO_3 stoichiometries in a single-pass hydrogenation. Lines show the average conversions over 3 unique samples, and shaded areas give 95% confidence intervals.

These small single-pass conversions suggested that a modified experimental procedure was needed to show substantial TEMPO hydrogenation. In this direction, we modified the configuration of the reactor during reactive discharge (step 2) as shown in Figure 37. Instead of flowing TEMPO through the reactor and UV-Vis cell one single time, we routed the outlet of the flow cell to the inlet of the reactor. The same TEMPO aliquot could then recirculate indefinitely through the reactor until all hydrogen was pulled out of the

WO_3 and all TEMPO was converted to TEMPO-H. During these recirculation experiments, the charging cycle (step 1) remained unchanged. Upon initiating TEMPO flow and UV-vis recording in step 2, reactor effluent was sent to waste for 3 minutes (i.e. run in single-pass mode). At 3 minutes, which was slightly longer than the breakthrough time, the reactor effluent was recirculated for the remainder of the experiment. Spectra were recorded every 5 minutes for 12 hours in the recirculation experiments. A total of 15 mL of TEMPO solution was retained in the system. Results of these modified experiments are shown in Figure 38.

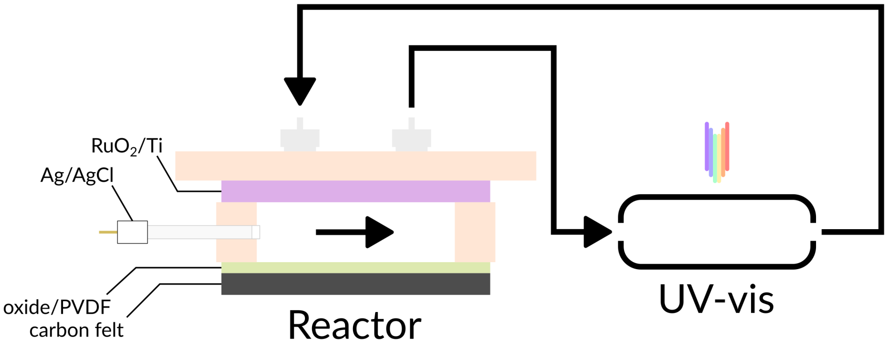

Figure 37: Setup for multi-pass, recirculating hydrogenations. The only change from single-pass experiments is the re-routing of flow cell effluent from waste to the reactor inlet.

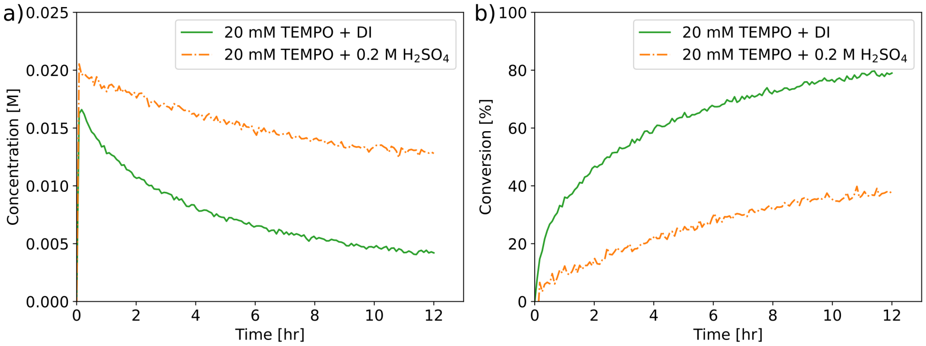

Figure 38: Results for multi-pass hydrogenations. a) Concentration vs. time data for 20 mM TEMPO solutions in DI (green) or 0.2 M H_2SO_4 (orange). b) Conversion vs. time data for 20 mM TEMPO solutions in DI (green) or 0.2 M H_2SO_4 (orange).

The recirculating hydrogenations were performed for both 20 mM TEMPO in DI and 20 mM TEMPO in 0.2 M H_2SO_4. Concentration traces for each case are shown in Figure 38a. Charging for each case was performed at -0.2 V vs. RHE, consistent with the formation of $H_{0.500}WO_3$. Both samples started near 20 mM concentration, but then dropped significantly after multiple passes through the charged reactor. After 12 hours, the DI sample concentration dropped to about 4 mM, while the acid sample reached around 13 mM. The corresponding conversion are shown in Figure 38b, where the DI sample reached a total conversion near 80% and the acid sample achieved just over 30%. These measurements confirmed that WO_3 can mediate the transfer of hydrogen from water to TEMPO.

As further qualitative evidence of successful TEMPO hydrogenation, Figure 39 shows images of the oxide cathode and TEMPO solutions through the course of the different net hydrogenation steps. Figure 39a is an image of a typical WO_3/PVDF cathode on carbon felt. Figure 39b is the same electrode after a charging step at -0.2 V vs. RHE. The intense blue coloration is indicative of hydrogen insertion.[250, 260, 261] Figure 39c then shows the electrode after a partial reactive discharge. There was a clear reversal of color back to the original green, suggesting hydrogen was removed from the oxide upon exposure to TEMPO. Figure 39d shows a vial of 20 mM TEMPO in 0.2 M H_2SO_4 with its characteristic yellow hue. Figure 39e is the same sample after contacting the electrode shown in Figure 39b and is markedly less yellow and more clear. This is consistent with the addition of hydrogen to TEMPO and the formation of TEMPO-H. These qualitative observations and the quantitative conversion data presented above provide strong evidence for the successful hydrogenation of TEMPO.

We were also able to infer changes in the composition of the H_xWO_3 by combining the coulometry data collected during charging and the TEMPO concentration data collected during reactive discharge. The starting composition of the oxides charged to at -0.2 V vs. RHE were almost exactly $H_{0.5}WO_3$. Assuming that the hydrogenation of one mole of TEMPO required one mole of hydrogen atom equivalents, then the TEMPO conversions could be converted to changes in H_xWO_3 stoichiometries using Equation 5.4.1.

$$x(t) = x(t=0) \cdot (1 - \frac{X(t)}{100}) \tag{5.4.1}$$

In Equation 5.4.1, x is the molar ratio of hydrogen to tungsten in the oxide and X is the total conversion of TEMPO at a given point in time.

Applying Equation 5.4.1 to the conversion data shown in Figure 38b gives Figure 40a. As expected, the DI sample that showed higher TEMPO conversions also showed a larger

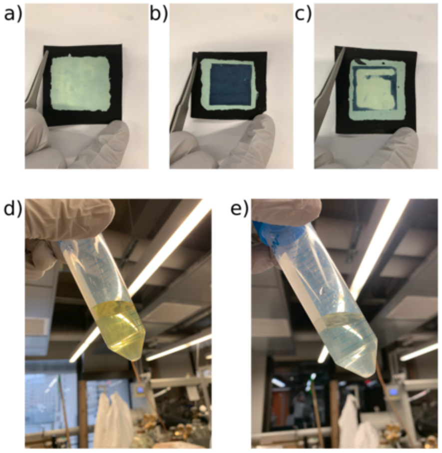

Figure 39: Qualitative observations supporting TEMPO hydrogenation. a) WO_3/PVDF cathode before intercalation, showing a green oxide. b) WO_3/PVDF cathode after charging. The blue coloration indicated H insertion into WO_3. c) WO_3/PVDF cathode after partial reactive discharge. There is a clear return to green, indicating removal of H. d) 20 mM TEMPO in 0.2 M H_2SO_4 before exposure to charged H_xWO_3 showing characteristic yellow color. e) 20 mM TEMPO in 0.2 M H_2SO_4 after exposure to charged H_xWO_3 illustrating disappearance of characteristic yellow color.

reduction in intercalated hydrogen when compared to the acid sample. Specifically, the 20 mM TEMPO solution in DI water reduced the hydrogen:tungsten ratio to slightly above 0.1. Interestingly, this value was consistent with the amount of stranded hydrogen in H_xWO_3 electrodes which were electrochemically de-intercalated using cyclic voltammmetry.[51] Conversely, the 20 mM TEMPO + 0.2 M H_2SO_4 solution reduced the hydrogen content of the oxide to a ratio of about 0.3.

Figure 40b then shows the open circuit potential recorded through the course of reactive discharge with the 20 mM TEMPO sample in DI water. Three different traces are shown. The solid line is the data vs. Ag/AgCl, the dashed line is shifted vs. RHE assuming a solution pH of 4, and the dotted line is shown vs. RHE assuming a pH of 7. Since the TEMPO was in DI water and it could have been mixed with residual acid from the charging step, solution pH was not clearly defined. Measuring with pH paper did not give conclusive pH values. However, applying the Nernst equation to the compositions reported in Figure 40a allowed us to compute apparent equilibrium potentials based on oxide stoichiometries and known standard reduction potentials for the $WO_3/H_{0.250}WO_3$ and $H_{0.250}WO_3/H_{0.500}WO_3$ couples.

$$E = E^o - \frac{RT}{nF} \cdot ln\frac{R}{O} \tag{5.4.2}$$

Here, E is the expected reduction potential, E^o is the standard reduction potential, R is the universal gas constant, T is temperature, n is the number of electrons transferred (i.e. 1), F is Faraday's constant, R is the concentration of reduced species, and O is the concentration of oxidized species. E^o values were assigned as $+0.20\pm0.02$ and $+0.10\pm0.02$ V vs. RHE for $WO_3/H_{0.250}WO_3$ and $H_{0.250}WO_3/H_{0.500}WO_3$, respectively. The resulting E values are shown as the shaded areas in Figure 40b, with the upper and lower limits showing a range of ±0.02 V on the assigned standard reduction potentials. The areas trend in the same increasing direction as the experiment proceeds, and also agree most closely with the pH = 4 data. A pH of 4 could arise from dissolved CO_2 and the formation of carbonic acid in the samples, which is feasible. These open circuit measurements further support the conclusion that TEMPO reactively discharged hydrogen from WO_3.

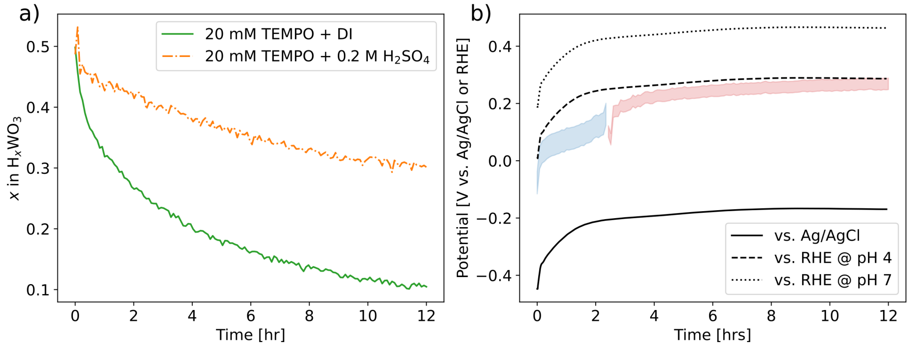

Figure 40: Oxide composition and open circuit potential comparisons. a) Composition of the H_xWO_3 cathode assuming 1 H^+ / 1 e^- hydrogenations of TEMPO. These compositions are calculated from the TEMPO conversions reported in Figure 38b. b) Measured vs. calculated open circuit potentials. The lines are measured, and the shaded areas are calculated allowing for an error of ±0.02 V on the standard reduction potential for H insertion.

In a final effort to validate the net hydrogenations investigated above, we performed a recirculated hydrogenation with excess reactant. The purpose of this experiment was to fully remove all hydrogen from the H_xWO_3. Since TEMPO is difficult to dissolve in water at high concentrations, we instead used a highly water soluble derivative known as TEMPOL. The additional hydroxyl group is not expected to significantly alter the PCET characteristics of the TEMPO radical.[253] In this experiment, we performed the same charging as previous experiments at -0.2 V vs. RHE. During reactive discharge, we fed 50 mM TEMPOL in DI and recirculated a volume of 15 mL. This corresponds to a total of 750 mmmol of TEMPOL. By contrast, only ∼367 mmol of H equivalents were intercalated during charging. The maximum possible conversion of TEMPOL was therefore 49%.

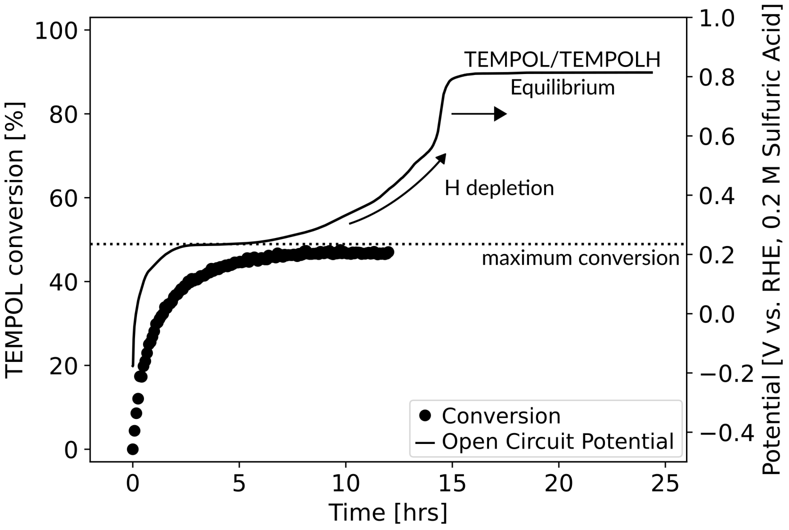

Figure 41: Complete reactive discharge of a tungsten oxide hydrogen bronze. Total conversion of TEMPOL as it was exposed to a pre-charged WO_3/PVDF electrode is shown on the left y-axis. The measured open circuit potential of the WO_3/PVDF electrode is shown on the right y-axis. 15 mL of 50 mM TEMPOL (750 mmol) was circulated through the reactor for 24 hours. The WO_3 was pre-charged at -0.2 V vs. RHE, which inserted ∼367 mmol of H atom equivalents. The TEMPOL was dehydrogenated the WO_3 through the course of the experiment, depleting essentially all H from the oxide. Once all H was removed, the open circuit potential pinned to a potential of +0.814 V vs. RHE, corresponding to the TEMPOL/TEMPOL-H equilibrium potential.

The results of a reactive discharge using excess TEMPOL is shown in Figure 41. Both the conversion data (circles, left y-axis) and open circuit potential data (line, right y-axis) are shown. At first, both the conversion and open circuit potential rapidly increased. After about 1 hour, the potential pinned to approximately +0.22 V vs. RHE and remained there until about 7 hours. At 7 hours, the potential began to climb again, and the conversion plateaued at a final value of about 46%. This conversion is slightly below the maximum possible value of 49%. As the final H units were depleted from the WO_3, the increase in open circuit potential accelerated. This corresponds to oxide being enriched in the oxidized form of the $WO_3/H_{0.250}WO_3$ couple, which is non-intercalated WO_3. Once all the hydrogen was removed, a new chemical equilibrium was established and the open circuit potential pinned at +0.814 V vs. RHE. At this point, about half of the TEMPOL was converted to TEMPOL-H. The solution was therefore near a 50:50 concentration ratio of TEMPOL/TEMPOL-H. The standard reduction potential of TEMPO in acid has been reported to be in the range of +0.5 to +1.0 V vs. RHE, which is consistent with the value of +0.814 V vs. RHE measured here. Accordingly, we assign this equilibrium to the TEMPOL/TEMPOL-H couple. It is important to note that, this only became a measurable redox couple once the WO_3 was completely depleted of hydrogen. Visual inspection of the cathode after the complete reactive discharge showed that it was essentially identical to the image shown in Figure 39a, confirming near complete depletion of H from the electrode.

Although there is strong quantitative and qualitative evidence for the successful hydrogenation of TEMPO (or TEMPOL), further work is needed to complete this study. Most notable is the fact that we have not observed aerobic reoxidation of the hydroxylamines to their nitroxyl radical form. This might be expected to occur spontaneously owing to the positions of the TEMPO/TEMPO-H and O_2/H_2O redox couples ($\sim$+0.8 V vs. RHE and +1.23 V vs. RHE, respectively), however, studies have shown that un-catalyzed aerobic oxidation of TEMPO-H is slow.[262] Still, to confirm the successful hydrogenation of TEMPO to TEMPO-H, further characterization (e.g. NMR) is required. Further work could also be focused on reactor optimization to facilitate higher single-pass conversions and faster reactive discharges. Specifically, the oxide surface area to reactant volume ratio should be minimized to ensure all material moving through the reactor can “see” the active H donor and react accordingly.

5.5 Conclusions

These experiments outline a preliminary investigation into temporally decoupled hydrogenations. The two principal reaction steps, hydrogen intercalation and reactive discharge, constituted electrochemical and thermochemical processes, respectively. A full hydrogenation scheme was realized through the design and construction of a specialized reactor, which operated flexibly between electrochemical and thermochemical modes. WO_3 was selected as a H mediator and TEMPO or TEMPOL were used as H acceptors. These materials successfully demonstrated the transfer of H from water to WO_3, and then the reactive discharge of the H. UV-Vis spectroscopy was used to evaluate nitroxyl radical conversions and consistently showed non-zero conversion in long-term recycle hydrogenations. Open circuit potentials computed using the Nernst equation and apparent oxide bronze compositions agreed well with measured open circuit potentials during the reactive discharge phase. It is still uncertain as to whether TEMPO-H or TEMPOL-H is formed as a stable product, and further characterization is necessary. Nonetheless, these experiments provide promising evidence for WO_3, and more generally the family of metal oxide hydrogen bronzes, as solid-state H mediators.

6.0 Conclusions and Future Directions

This dissertation describes a body of work which has been completed over the last few years in the Mpourmpakis and McKone labs at the University of Pittsburgh. The overarching vision of this research—using water as a hydrogen source for general chemical conversions—is summarized in Figure 42. Overall, this work advanced our fundamental understanding of the thermodynamics, transport phenomena, and kinetics governing the interaction of protons and electrons with metal oxides. It then leveraged these fundamentals to demonstrate metal oxide-mediated hydrogen transfer using water as a hydrogen source. These results motivate the further engineering, design, application of metal oxide-based hydrogenation reactors. Although the research herein provided many findings and built a strong foundational understanding of mediated hydrogenations, there are several exciting open questions and avenues of research which should be pursued.

One direction of research can investigate the thermodynamic framework for mediated hydrogenations presented in Chapter 1. Central to this framework is the idea of coupling two redox half reactions to achieve a net hydrogen transfer. Although this dissertation explored one oxide-mediated hydrogenation (WO_3 + TEMPO), further examples of this chemistry need to be tested. Specifically, future work should test the hypothesis that the oxide bronze needs to be more reducing than the target hydrogen acceptor. This can be achieved in two ways: 1. test numerous oxides of different intercalation potentials against a model H acceptor, or 2. test numerous hydrogen acceptors of different reduction potentials against a model oxide. In this approach, one could develop important insights into reaction dynamics as a function of the driving force for H transfer (the differences in reduction potentials of oxides and H acceptors). One particularly interesting experiment would be the pairing of TiO_2 and WO_3 with anthraquinone-1,5-disulfonic acid (AQDS). The reduction potential of AQDS is slightly negative of the H insertion potential for WO_3, but is positive of the H insertion potential for TiO_2. If the thermodynamic hypothesis is valid, then only H_xTiO_2 should be able to donate hydrogen to AQDS.

Other extensions of this research could pursue further development of the geometric

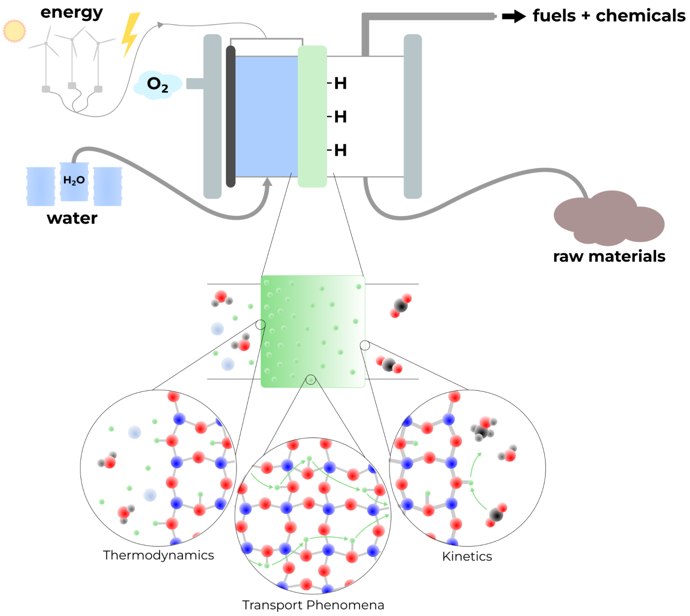

Figure 42: Visual summary of the research performed in this dissertation, including fundamental studies of H insertion in metal oxides and their use as H mediators for general hydrogenations.

descriptors described in Chapter 2. Currently, no atomic identities or chemical information is directly included in the geometric descriptors. Systems of identical structure, but different chemical ordering, would therefore not be distinguished by those descriptors. A needed development is the inclusion of atom identities in the description of structure. In this way, the connectivities of Chapter 2 could be made more flexible and possibly more useful in the screening of materials beyond the specific application of determining hydrogen intercalation potentials for metal oxides.

Chapter 3 established a protocol for quantifying H transport in WO_3. One of the main limitations of this material is its slow bulk H diffusion rates. It would therefore be valuable to identify trends among other metal oxides, and possibly other material classes, between material properties and H diffusion coefficients. Doing so would help to develop quantitative structure-property relationships that could be used to intentionally design fast H transporters, enabling spatially decoupled hydrogenations. This is the focus of ongoing work in the McKone lab.

One of the most unique outcomes of Chapter 4 was the observation that hydrogen intercalation causes WO_3 to become a significantly more active catalyst for the hydrogen evolution reaction than the non-intercalated oxide. Recalling that the optical measurements of Chapter 3 showed that H intercalation can occur either electrochemically or thermochemically, we can formulate an exciting implication for a huge class of catalysts. In particular, catalysts for (de)hydrogenations that rely on reducible metal oxides as supports for active metals might be incredibly misunderstood. With the presence of hydrogen in a reaction environment, reducible metal oxide supports could feasibly form their analogous hydrogen bronze phases. Applying the learnings of Chapter 4, this H intercalation could confer catalytic activity to these oxide supports. It could be fruitful to re-examine the *operando* composition of reducible oxide-supported catalysts under reactions conditions to see if the support might be playing a significant role in catalytic turnover. This would be equally applicable to electrochemical and thermochemical reactions.

The culmination of the fundamental work performed in Chapters 2, 3, and 4 was the demonstration of WO_3-mediated H transfer from water to TEMPO. Unfortunately, this process was extremely slow and took many hours to proceed at a noticeable rate. Taking inspiration from prior work on hydrogen reverse spillover, one potentially valuable experiment would be the inclusion of a co-catalyst on the active WO_3 phase. Instead of relying on the H in H_xWO_3 to delivered directly from the oxide surface, use of a promiscuous H mediator, such as Pt, could greatly accelerate the hydrogenation of TEMPO. Such a route might also make other, more difficult, reactions more accessible, such as the hydrogenation of CO_2 to value added products.

In closing, there are many exciting routes to pursue following this work. My hope is that this dissertation provides a sturdy foundation for the continued exploration of metal oxides as hydrogen mediators, with the express goal of enabling sustainable chemical conversions.

Appendix A Supporting Information for Chapter 2

A.1 Tungsten Trioxide Lattice Parameters

Table 4 compares the experimental and DFT relaxed lattice parameters for monoclinic WO_3. Experimental values were taken from reference [88].

Table 4: Comparison of experimental and DFT relaxed bulk WO_3 lattice parameters.

Parameter	Experimental	DFT
a	7.301 Å	7.453 Å
b	7.539 Å	7.650 Å
c	7.690 Å	7.933 Å
β	90.892°	90.233°

A.2 Performance Comparison for Different Tungsten Trioxide Morphologies

All experiments reported in the main text were performed on nanoparticulate WO_3 produced via ion exchange. This material was selected for its ease of synthesis and its amenability to electrochemical analysis. As a comparison, we also prepared dense films of WO_3 by thermally oxidizing sheets of tungsten metal. Briefly, W metal sheets (MTI Corporation MF-W200L) were cut to size and placed in a box furnace for 1 hr at 500 °C under ambient air.

For this comparison, cyclic voltammetry was performed in a different setup than described in the main text. Since the dense film material was cut from a tungsten foil, this sample could not be supported on a glassy carbon electrode. It was instead tested as a self-supported working electrode using a custom acrylic sandwich-type cell. The working area of this cell setup was 0.495 cm^2. Counter and reference electrodes were as described in the main text, as was the potentiostat.

To maintain a good comparison, the nanoparticle material was also tested in this setup. Instead of a glassy carbon substrate, the nanoparticulate WO_3 was supported on thin film of Au that was deposited onto standard microscope glass slide using a Plassys MEB550S E-Beam Evaporator. The Au layer was 100 nm in thickness and adhered to the microscope glass using a 5 nm Ti film. Nanoparticulate WO_3 was doctor-bladed onto this substrate and the full working electrode (microscope glass, Ti, Au, WO_3) was calcined for 1 hr at 500 °C. Figure 43 shows the results of cyclic voltammetry experiments run at 100 mV/s in 0.5 M H_2SO_4. As can be seen, the WO_3 nanoparticles show generally larger current densities along with multiple distinguishable reduction events. The Au background signal is shown to illustrate that the cathodic currents are due to the nanoparticle WO_3 and that there is minimal contribution from the Au support. Based on these results, we chose to focus on the nanoparticulate material.

A.3 Bulk Oxide Stability and Electronic Structure Heterogeneity

The heterogeneity of the electronic properties of intercalated oxides can be characterized via the standard deviation, σ, of a property across the entire unit cell. In the main text, we considered the σ of Bader charges on O and W atoms as well as O p-band and W d-band centers as potential descriptors for the binding energy model. While these standard deviations were not used in the final model, they are useful quantities that may relate to the stability of the bronzes formed by hydrogen intercalation. Figure 44 shows the relationship between DFT calculated H binding energy and the standard deviation of W d-band centers.

The data are partitioned according to composition, as was done for each binding energy model constructed in the main text. Within a constant value of composition (constant color), the oxides with lower values of $\sigma\ \epsilon_{d,after}$ generally show more exothermic binding energies. There is a positive linear correlation between the $\sigma\ \epsilon_{d,after}$ and binding energy, as revealed in the Pearson correlation matrix in Figure 7. The standard deviations of charges and band centers were not used in any binding energy model because they are only available after a DFT calculation has already been completed.

A.4 Decomposition of Low-Lying Unoccupied Electronic States

The total and decomposed electronic densities of states for a W atom in the WO_3 lattice are shown in Figure 45. The W *d*-bands dominate the low-lying unoccupied states, consistent with the common description of wide-bandgap transition metal oxides as having metal-centered conduction band edges. As a result, we consider the unoccupied W *d*-bands as descriptive of acid character.

A.5 Effect of Intercalation on DOS and Validation of PBE-D3 Electronic Structures

As hydrogen (proton and electron pair) is inserted into the tungsten trioxide lattice, we observe an immediate loss of semiconducting character and a downward shift of the unoccupied *d*-states. Figure 46 shows this for a representative W atom (one of the coordinating first neighbors to the O that receives H with intercalation) in the WO_3 and $H_{0.125}WO_3$ lattices. Initially, the WO_3 in Figure 46a appears to have a band gap, with the unoccupied *d*-band situated well above the Fermi level. Insertion of the first H unit drops these unoccupied states down in energy and causes the band to intersect with the Fermi level, suggesting $H_{0.125}WO_3$ is either a degenerate semiconductor or metallic. This is indicative of the low-lying unoccupied *d*-states in WO_3 being filled by the electron introduced via intercalation to $H_{0.125}WO_3$.

Furthermore, it is well known that PBE (and more generally, the GGA class of functionals) severely underestimates electronic bandgaps.[263] As an alternative, hybrid functionals, such as HSE06, are much better at band gap identifications, with an associated increase in cost. Therefore, to assess whether our approach using PBE-D3 was acceptable, we performed HSE06 calculations on the PBE-D3 optimized geometries to confirm the general trends in expected electronic structures. Our calculations show the WO_3 band gap is 1.39 eV by PBE-D3 and 2.49 eV by HSE06. UV-vis measurements shown below indicate an optical gap of ∼2.69 eV, which agrees better with the HSE06 result than the PBE-D3 one. However, as can be seen in Figure 46, the differences between PBE-D3 and HSE06 DOS only manifest in a constant offset in energies; the overall shape and character of the bands is similar. Therefore, using either of these two functionals would be expected to give similar accuracy in the predicted energetics for H-uptake because the regression models in this work employ free intercepts. This is significant because it is only the slope of the relationships between the descriptors (band centers) and targets (binding energies) that are mathematically important, not necessarily the absolute value of the descriptors themselves. The unoccupied band centers in the intercalated bronze (Figure 46b) are also in near exact agreement between PBE-D3 and HSE06. Although the difference in WO_3 unoccupied d-band centers is not negligible, the regression models would effectively erase this offset via the intercept. Thus, we conclude that PBE-D3 offers an excellent compromise between accuracy and cost.

A.6 Local vs. Global Screening Model Construction

The initial stage of the computational methodology proposed in the main text comprises a series of local (i.e., binned by hydrogen stoichiometry) linear models. Logistically, these are more useful than one large global model because they enable a step-wise identification of exothermic sites. A global model would require a recursive approach, whereas the step-wise local models efficiently locate hydrogen binding sites, allowing for efficient identification of low-energy bronze configurations.

Figure 47 further motivates the construction of local linear regression models rather than a global one. A clear reversal paradox is observed for the relationship between hydrogen BE and absolute energy. These quantities have a known mathematical relationship (Eq. 1 in the main text). This is represented by the colored lines drawn through each stoichiometry in Figure 47. The black dotted line shows the best fit to the global dataset: the slope of the relationship is inverted and the accuracy is well below that of the local models, demonstrating the utility of considering local linear screening relationships.

A.7 Hyperparameter Optimization for Acid-Base Kernel Ridge Regression

The kernel ridge regression model implemented in the `scikit-learn` package can be controlled using two hyperparameters. The first is regularization strength, which affects the degree of L_2 regularization, and the second is the width of the kernel. A Laplacian kernel was selected because it gave the lowest MAE values out of the kernels that were tested. Figure 48 illustrates the average model MAE for training and validation sets of data as functions of the hyperparameters. The combination of parameters that gave the lowest average MAE from cross-validation runs was a regularization strength of 0.03 and a kernel width of 2. The descriptors were not standardized or normalized because they were all within the same scale.

A.8 UV-vis Measurements as a Function of Bronze Composition

Intercalation of tungsten trioxide is known to induce electrochromism, characterized by a shift from bright yellow-green to dark blue-indigo.[48] We performed UV-vis measurements in reflectance mode to investigate the relationship between polarization, optical response, and semiconducting character of the intercalated bronzes. The samples were polarized for 5 minutes at potentials of +0.45, +0.15, and 0.00 V vs. RHE, corresponding to voltammogram features that we have assigned to the parent oxide, formation of $H_{0.250}WO_3$, and formation of $H_{0.500}WO_3$, respectively. The cell setup for pretreatment was identical to the CV and EIS setups. Immediately after pretreatment was finished, the films were lifted from the glassy carbon electrode using adhesive tape (Scotch magic tape) and then pressed onto a glass microscope slide. This was done to minimize contact with air, which re-oxidizes the bronze to WO_3. Tests showed that samples collected and preserved in this manner retained their coloration for several days after preparation.

A Craic QDI 2010 UV-vis/NIR microspectrophotomer in reflectance mode was used to collect the spectra shown in Figure 49. KCl was used as a 100 % reflectance reference, and spectra were collected in the 300-800 nm range. Reflectance data were transformed to the corresponding Kubelka-Munk function, $F(R) = (1 - R)^2/(2R)$, where $R =$ the percent reflectance. Tauc plots were then constructed considering WO_3 as an indirect semiconductor. Figure 49a illustrates $F(R)$ versus wavelength for three levels of intercalation. $H_{0.250}WO_3$ shows an marked increase in absorption across the visible spectrum relative to WO_3. Intercalation to $H_{0.500}WO_3$ shows an even larger absorbance across the visible wavelengths, illustrating composition-dependent coloration as expected for an electrochromic oxide.

The Tauc interpretation of the reflectance data for WO_3, as seen in Figure 49b, shows clear semiconducting character, with a linear region fit returning an indirect band gap of 2.69 eV. The hydrogen bronzes, by contrast, show no evidence for a bandgap. This is consistent with the impedance data in the following section, where intercalation brings about a drastic reduction in charge transfer resistance. Altogether, this suggests a transition from semiconducting to metallic behavior that occurs with intercalation, as expected from prior work on H_xWO_3 and the DOS data shown above.[116, 264] Furthermore, the semiconducting profile of the Tauc plot and the yellow-green coloration of WO_3 suggest that the starting material is not significantly substoichiometric. WO_{3-x} is known to have increased absorption across visible wavelengths and appears dark blue even at very small values of x.[265]

A.9 Structural Evolution with Bronze Composition and the Validity of a Fixed-Volume Calculation Approach

Prior work has shown that H-intercalation in the H_xWO_3 bronze system coincides with an increase in crystal symmetry.[252] Initially, the low symmetry monoclinic material shows three lattice parameters that are distinct. From $H_{0.150}WO_3$ to $H_{0.500}WO_3$ there is an expected transition through two tetragonal crystal structures. Accordingly, we performed x-ray diffraction (XRD) measurements to track this structural change in our material and provide further evidence of hydrogen intercalation. Measurements were taken with a Bruker D8 Discover instrument equipped with a LynxEye detector using Cu K-α radiation and step increments of 0.01° at 1.5 secs / step. Figure 50 shows the results of these measurements on samples prepared identically to those described above for UV-vis experiments.

The XRD pattern for the initial material is consistent with monolinic WO_3 exhibiting a high degree of crystallographic orientation (texturing), where increased intensity in the (002) feature occurs due to the disk-like shape of the nanoparticles. After H-intercalation at +0.15 V vs. RHE, which we expect to coincide with the formation of $H_{0.250}WO_3$, we observe a slight expansion in d-spacing (decrease in 2θ) for the (002) reflection along with the disappearance of the shoulder associated with the (020) crystal direction. This suggests the (002) and (020) directions adopt similar d-spacings, reflecting an increase in symmetry. By contrast, further polarization to 0.00 V vs. RHE shows a decrease in d-spacing for the main feature and a coalescence of the diffraction features, implying a further increase in crystal symmetry.

The computational framework proposed by this work was accelerated by restricting the DFT calculations to fixed volume and constant cell parameters for each intercalation. This was done to reduce the computational cost of geometric optimizations, where volume and cell parameter relaxations introduce more degrees of freedom into the overall structure search. It is possible, however, that this simplification introduced errors by ignoring the energy change associated with changes in the cell shape induced by intercalation. Furthermore, the fixed volume approach restricts the structure to a single system (monoclinic, in this case). To assess the accuracy of the energies obtained by fixed volume approach, we performed full volume and cell parameter relaxations of the most exothermic configurations for each investigated bronze stoichiometry. The results are listed in Table 5. Volume relaxation energies were calculated as the ground-state energy of the shape- and volume-relaxed structure minus the fixed volume structure energy (those reported as the convex hull in the main text). Intercalation potential corrections follow the calculation in the main text, where we calculated the slope of the convex hull between the stoichiometries of interest. The potential corrections due to volume relaxation resulted in a systematic positive shift in the predicted intercalation potentials, but the differences were similar in magnitude to the 95% confidence intervals given by our Boltzmann weighting procedure. The exception is $H_{0.125}WO_3$, which shifted positive by > 0.1 V. While this does not change the main conclusions from the fixed-volume calculations, it adds further evidence that either $H_{0.125}O_3$ does not form or the DFT-predicted equilibrium potential for this intercalation event is less accurate than for higher H-stoichiometries.

With the volume and cell shape changes in hand, we can also obtain information about the changing crystal structure with intercalation. Using the powder diffraction pattern module included in VESTA, we identified the (002), (020), and (200) d-spacings that are calculated from the volume relaxed structures. These are listed in Table 6. We observe three distinct spacings for the initial material, followed by an expansion of the (002) spacing in $H_{0.250}WO_3$ as was observed via XRD. Interestingly, the (200) and (020) spacings were found to be almost the same, rather than the (002) and (020) combination that is expected upon inspection of the XRD data. Despite this disagreement, the grouping of the (200) and (020) spacings determined by DFT highlights the expected increase in symmetry, as well as the slight expansion of the lattice. The $H_{0.500}WO_3$ spacings follow this trend as well, and show the (200) and (020) spacings are similar, with (002) distinct. This finding is in line with the XRD pattern for $H_{0.500}WO_3$, showing that the general trend in increased symmetry with hydrogen intercalation is captured by the volume-relaxed DFT calculations. In summary, the fixed volume approach seems appropriate for energetic predictions, and additional volume relaxations can be performed for the most exothermic configurations to elucidate additional structural information.

A.10 Control Experiments for Window-Opening Voltammetry

To rule out the effect of contaminants or exogenous components of the electrochemical cell on the observed oxidation feature at ∼1.5 V vs. RHE, we performed the control experiment shown in Figure 51. The red curve represents the initial, positive-going sweep; this is also indicated by the red arrow. Non-intercalated bronze was polarized until the onset of oxygen evolution, where there was no observation of any anodic current in the strongly oxidizing region. However, cycling to these positive potentials after a negative-going sweep that formed H_xWO_3 resulted in the emergence of peak III alongside a broad anodic current across the positive-going sweep. This is consistent with kinetic or transport-limited oxidation, as discussed in the main text.

A.11 EIS data fits

The raw electrochemical impedance spectroscopy (EIS) data and equivalent circuit fits are shown in Figure 52. Raw data are shown as circles, where the calculated fits are shown as solid lines. Fit parameters are shown in the main text in Figure 10.

A.12 Scan Rate Effect on Intercalation and De-Intercalation

To use the voltammetry data in Figures 8 and 9 of the main text as indicators of equilibrium potentials, the scan rate must be slow enough to approximate equilibrium and not introduce significant peak shifts associated with kinetic or transport limitations. Figure 53 compares the 1 mV/s voltammogram shown in Figure 8 of the main text against a slower 0.3 mV/s scan rate in an identical cell setup. As can be seen, there is a slight positive shift in the first two reduction features, and a very small negative shift in the corresponding oxidation features. These differences do not significantly influence the identification of equilibrium potentials made using the 1 mV/s scan rate data.

Interestingly, the third reduction feature associated with the $H_{0.500}WO_3/H_{0.625}WO_3$ redox couple is shifted slightly more negative in the slower scan rate data. It is likely that this feature is broad and overlaps with the large shoulder of the second reduction feature. This is motivated by the magnitudes of the charges shown in Figure S11. The total charge associated with reductions are slightly larger than that for oxidation, which is broadly consistent with background hydrogen evolution. It is noteworthy, however, that peak III disappeared with the slower sweep. This is again consistent with the notion of “stranded hydrogen,” where the slow scan rate allows the diffusion of bulk hydrogen equivalents to keep up with the changing electrode potential.

A.13 Anion Effects on Hydrogen Intercalation

We also tested the effect of a different supporting electrolyte on the cyclic voltammograms, to determine whether equilibrium potentials were signifcantly influenced by anion effects. Figure 54 shows the intercalation and oxidation of H_xWO_3 in sulfuric and perchloric acids. The use of perchloric acid results in a slight negative shift in the reductive peaks by up to ∼60 mV. There is no concurrent shift in the oxidative peaks. This difference may be indicative of influence by anion adsorption (e.g., displacement of bisulfate concurrent with H-intercalation), but it again has no significant impact on the assignment of redox features with H-stoichiometries and again remains within the error of the computational predictions (which did not consider anionic adsorbates).

A.14 Disk-like Morphology of Synthesized Nanoparticles

We previously reported the synthesis procedure for the nanoparticulate WO_3 used here, along with extensive materials characterization.[261] To confirm that the specific samples used for this study were comparable to that in our prior report, Figure 55 depicts a representative SEM image. A Zeiss Sigma 500VP field emission scanning electron microscope was used to collect the image using an accelerating voltage of 10 keV and a backscatter detector. The nanoparticles clearly exhibit a disk shape with diameters of a few hundred nanometers, consistent with our prior report. XRD measurements of the WO_3 are also consistent with previous measurements.

A.15 Details on Atomic Graph Definitions Used in this Work

Graph representations of atoms and bonds can hold node-level and edge-level information. In this work, each atom center corresponds to a node and each pairwise interaction between atoms corresponds to an edge. Unless otherwise noted, all graph representations of metal oxides are node-level matrices—they do not contain edge-level information. Only the distance Laplacians of Section S8 and Figure S6d are edge-level graph representations. All other Laplacians follow the definition given by Equation 1 in the main text, with each entry in the matrix depending on the degree of each atom. The atoms included in the matrix are all those present in the system. We considered the degree of each atom as the atom's local coordination number (LCN). Practically, these were determined by considering pairs of atoms as neighbors if their atomic radii overlapped. In this work, we fine-tuned the apparent atomic radii of the metal atoms, oxygens, and hydrogens to reproduce typical LCNs observed for metal oxides (e.g. 6 for most metal atoms and 5 for some under-coordinated cases, 2 or 3 for oxygens, and 1 for hydrogens). Entries marked with a * in Table 7 are the ones which were slightly adjusted from tabulated covalent atomic radii to achieve the expected LCNs [266]. The specific radii used were as follows:

Laplacians were constructed from DFT-optimized structure files using Python code leveraging the `Atomic Simulation Environment` [223]. Graph Laplacians of Atoms and Bonds (`gloab`) is a publicly available repository on the Mpourmpakis group Github which contains the code used to convert the structure files to connectivity values. In this repository we include all structure files used in this work and some example scripts.

A.16 Density Functional Theory Calculations

Calculations were performed using the VASP [267] software package, with wavefunctions approximated by PAW pseudopotentials and exchange-correlation modeled using the Perdew-Burke-Ernzerhof functional [268]. Dispersion corrections were included using Grimme's D3 correction [269] with Becke-Johnson damping [270]. The PBE-D3 level of theory has been shown to satisfactorily describe the formation energies and geometries of metal oxides [86]. A kinetic energy cutoff of 520 eV was used in conjunction with a 0.3 Å^{-1} k-point sampling density. Integration of k-space was performed using the tetrahedron method including Blöchl corrections [271]. Electronic SCF loops were terminated once energy differences were smaller than $1\text{x}10^{-6}$ eV. Geometries were optimized until all forces were smaller than at least 0.05

eV/Å. Oxide unit cells were tessellated as necessary to achieve a total of 8 metal atoms in the base simulation cell, to allow for a consistent comparison of hydrogen stoichiometries. Initial geometries were first allowed to relax with respect to cell shape and size according to the above criteria. Subsequent calculations regarding the insertion of hydrogen into the respective lattices were held at fixed volume, allowing only atom positions to change.

Hydrogen atoms were placed into each cell in increments of one atom. Starting from the empty oxides, a calculation was performed for each lattice oxygen bonding to the guest H atom. The lowest energy configuration was selected to probe the next binding site, and again every possible subsequent location was tested. For example, in WO_3 there are 24 oxygens. Intercalation to $H_{0.125}WO_3$ therefore considered 24 different configurations. Intercalation to $H_{0.250}WO_3$ considered 23, and so on. All tested configurations were used to train the KRR and CNN models discussed in this work.

Hydrogen intercalation potentials were determined from hydrogen binding energies and convex energy hulls according to Equation A.16.1:

$$U_H = \frac{\Delta E_{H_{x+\Delta x}M_yO_z} - \Delta E_{H_xM_yO_z}}{N_M \Delta x e} \tag{A.16.1}$$

In Equation A.16.1, U_H is the equilibrium potential for the hydrogen intercalation reaction corresponding to the conversion of $H_xM_yO_z$ into $H_{x+\Delta x}M_yO_z$. $\Delta E_{H_{x+\Delta x}M_yO_z}$ is the hydrogen binding energy of the next incremental H unit, $\Delta E_{H_xM_yO_z}$ is the hydrogen binding energy at a state prior to the intercalation of the next H unit, N_M is the number of metal atoms contained in the unit cell, Δx is the change in hydrogen-to-metal stoichiometry induced by the addition of an incremental H unit, and e is the elementary charge of an electron (-1). The quantity $N_M\Delta x$ is the change in number of H atoms per unit cell required for the conversion of $H_xM_yO_z$ into $H_{x+\Delta x}M_yO_z$.

A.17 Oxides Considered in this Work

Orthorhombic V_2O_5, orthorhombic MoO_3, monoclinic WO_3, monoclinic VO_2, and anatase TiO_2 were considered as hydrogen intercalation candidates in this work. Starting structures were taken from the Materials Project database [78]. Table 8 contains the total number of metal and oxygen atoms in the non-intercalated starting structures. As mentioned in the previous section, primitive unit cells were tessellated such that each oxide cell contained 8 total metal atoms. Incremental hydrogen additions increase the total number of atoms, N, in a given system by 1. For example, $H_{0.125}WO_3$ contains $N = 33$ atoms: 8 tungsten, 24 oxygen, and 1 hydrogen. Then, $H_{0.250}WO_3$ contains $N = 34$ atoms: 8 tungsten, 24 oxygen, and 2 hydrogens. In Figure 56, each oxide is shown containing intercalated hydrogen atoms to illustrate how hydrogen prefers to bond in the oxide lattices. The lowest energy configurations are shown for each system at an example hydrogen:metal stoichiometry of 1:2. However, we note that many unique configurations exist (i.e. hydrogen atoms can bond to lattice oxygens in various combinations). These alternative configurations were considered as discussed above in Section S2.

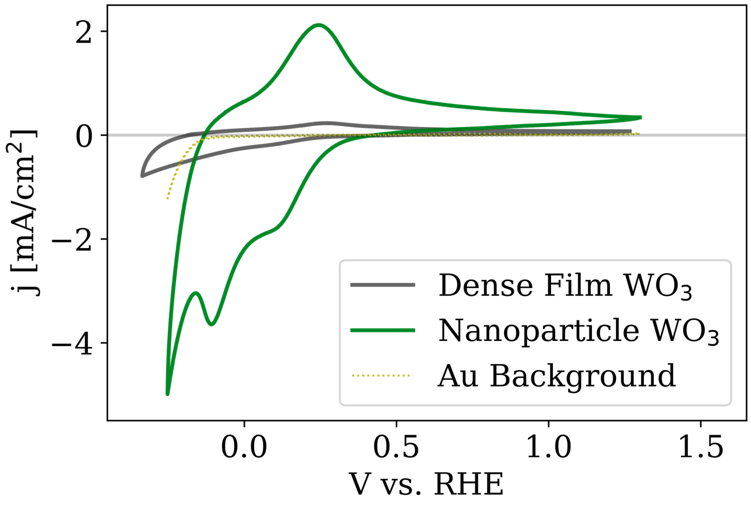

Figure 43: Comparison of 100 mV/s cyclic voltammetry data on WO_3 synthesized via two methods. Nanoparticulate WO_3 produced via ion-exchange shows significantly clearer and more reversible redox reactivity than WO_3 prepared via thermal oxidation of W metal.

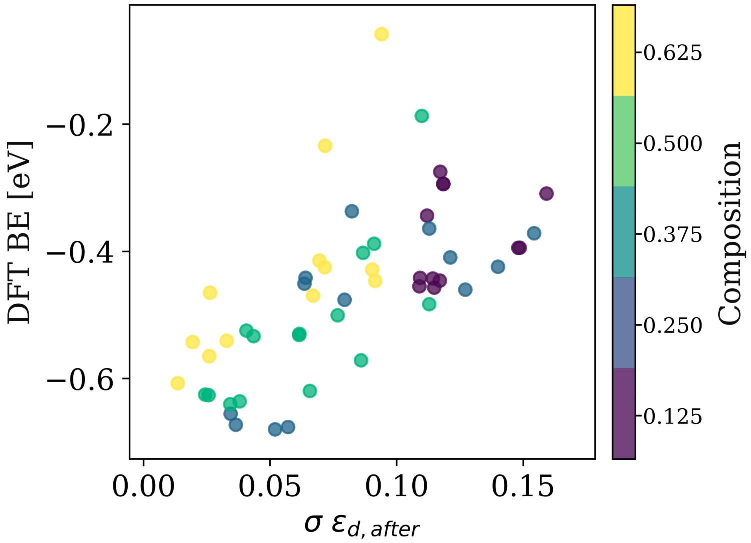

Figure 44: Relationship between DFT calculated binding energy and standard deviation of $\epsilon_{d,after}$. The coloration follows the composition of the bronze.

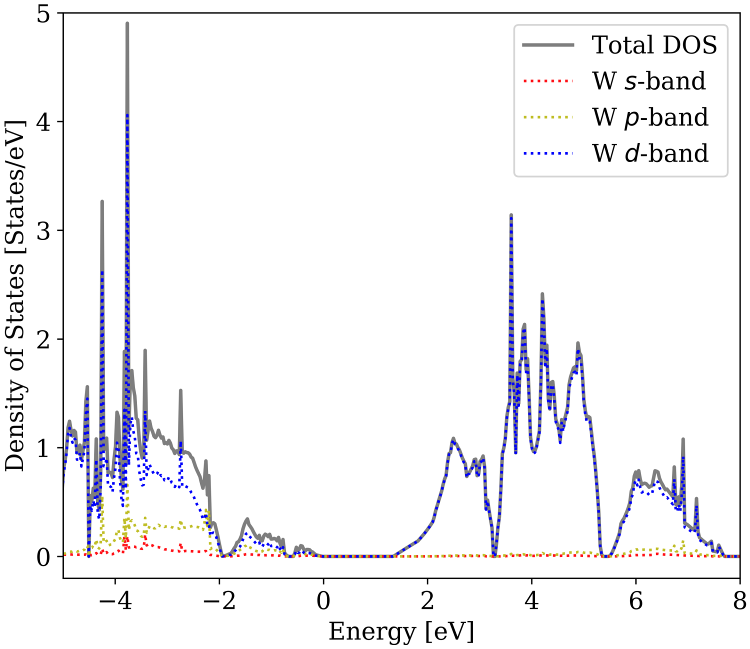

Figure 45: Total and projected electronic density of states on a representative W atom in a WO_3 lattice.

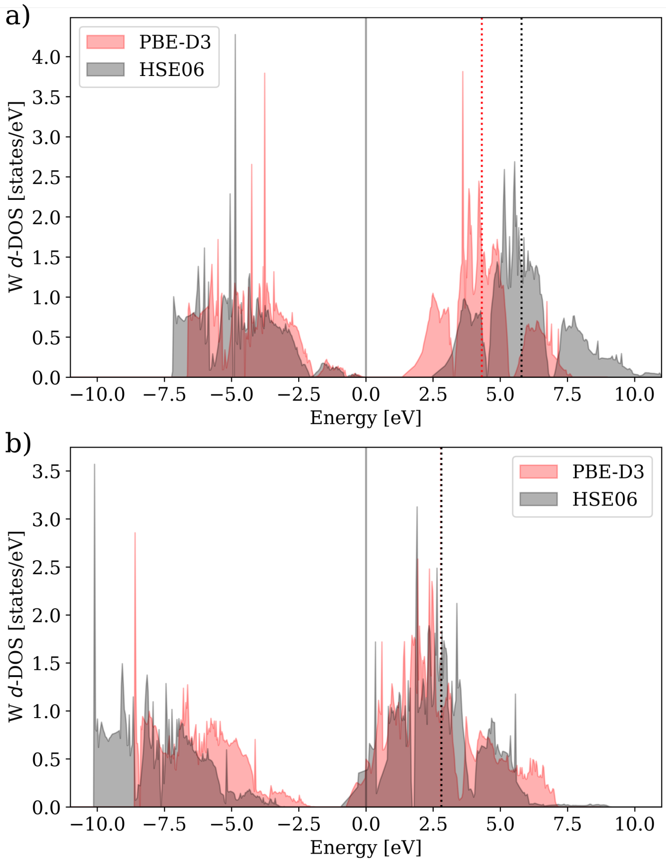

Figure 46: W *d*-projected DOS for a) WO_3 and b) $H_{0.125}WO_3$ at PBE-D3 and HSE06 levels of theory.

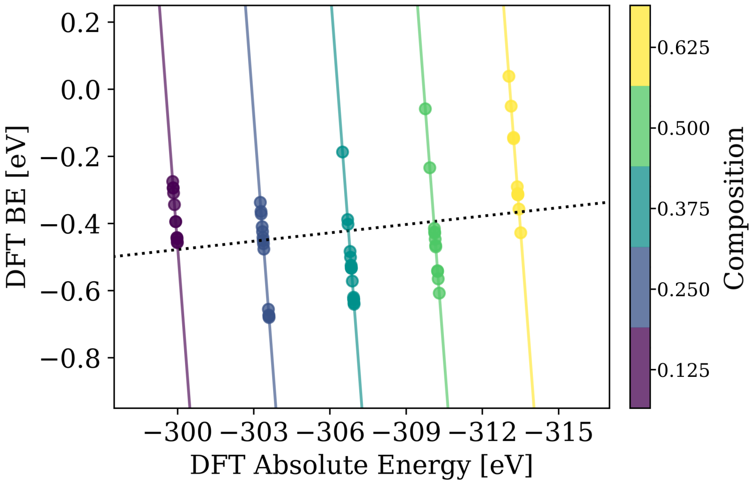

Figure 47: Comparison of absolute DFT energy to hydrogen binding energy, split by composition.

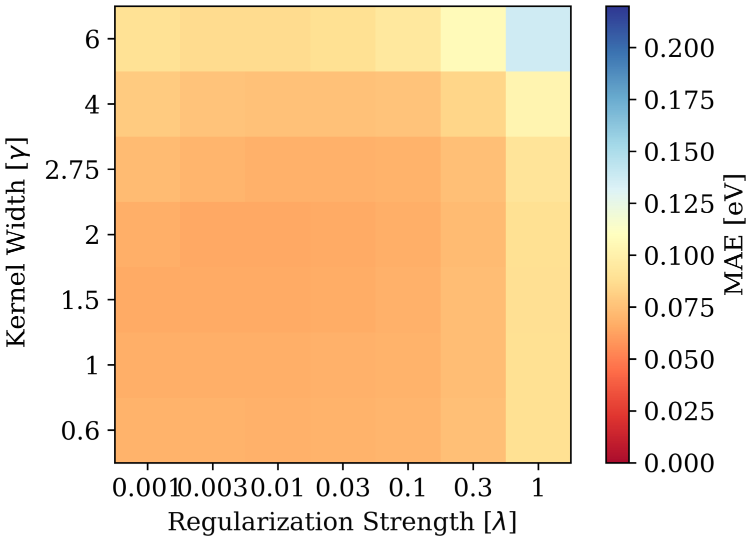

Figure 48: Average MAE of acid-base models generated by 10-fold cross-validation repeated 200 times, shown as a function of regularization strength and kernel smearing width.

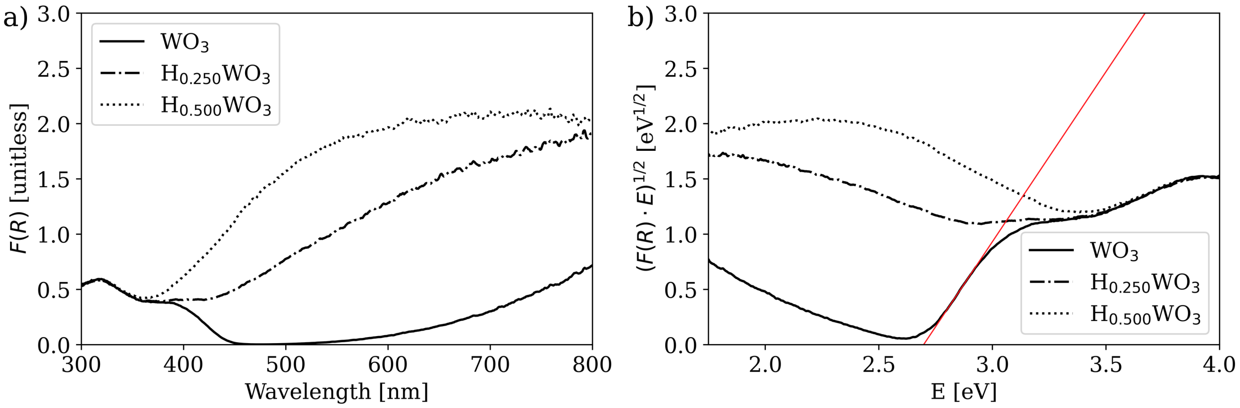

Figure 49: a) Kubelka-Munk function, $F(R)$, and b) Tauc plots for three levels of hydrogen intercalation in WO_3. The stiochimetries are labeled according to the assignments from modeling and voltammetric features in the main text. The red line in b) corresponds to the fit of the linear Tauc region, which returns an indirect band gap of 2.69 eV.

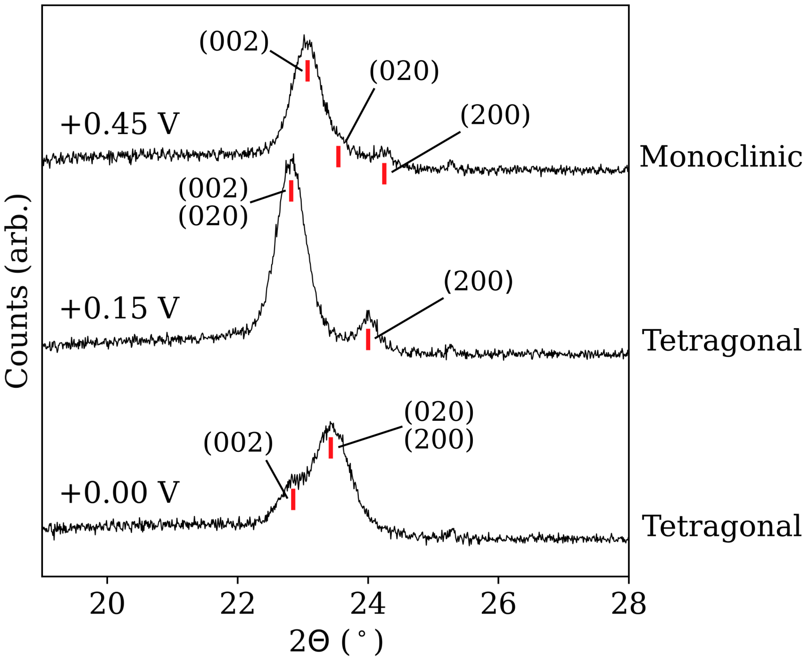

Figure 50: X-ray diffractograms for various levels of hydrogen intercalation, shown as polarization vs. RHE, illustrating a clear increase in crystal symmetry.

Table 5: Volume relaxation energy corrections and the resulting change in predicted intercalation potentials for each stoichiometry, compared to the 95% confidence intervals calculated from the fixed volume configuration ensembles.

Stoichiometry	Volume Relaxation Energy [eV]	Change in Potential [eV]	95% Confidence Interval [eV]
WO_3	—	—	—
$H_{0.125}WO_3$	-0.1138	+0.1138	0.0350
$H_{0.250}WO_3$	-0.1409	+0.0271	0.0205
$H_{0.375}WO_3$	-0.1639	+0.0230	0.0435
$H_{0.500}WO_3$	-0.2095	+0.0456	0.0526

Table 6: Calculated d-spacings in nm for volume-relaxed cells corresponding to stoichiometries investigated via XRD.

Stoichiometry	(002)	(020)	(200)
WO_3	3.966	3.825	3.727
$H_{0.250}WO_3$	4.036	3.771	3.706
$H_{0.500}WO_3$	4.033	3.739	3.765

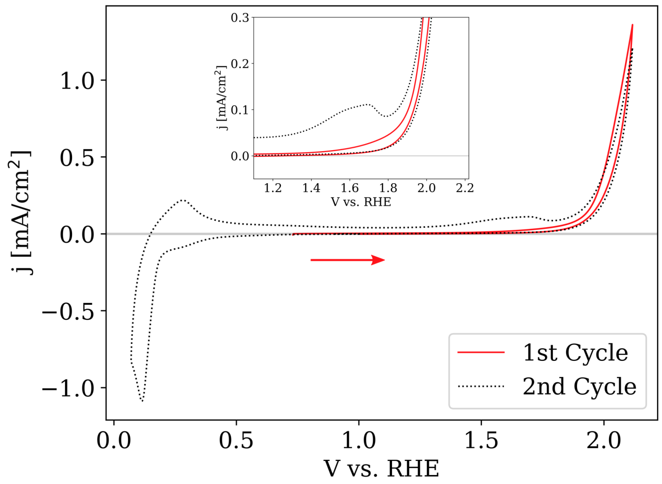

Figure 51: Comparison of two positive-going sweeps at 1 mV/s. The solid red curve shows oxidation of the non-intercalated metal oxide, and the dotted black curve shows oxidation of an intercalated oxide. Inset is an up-close look at the anodic feature at ~1.5 V vs. RHE.

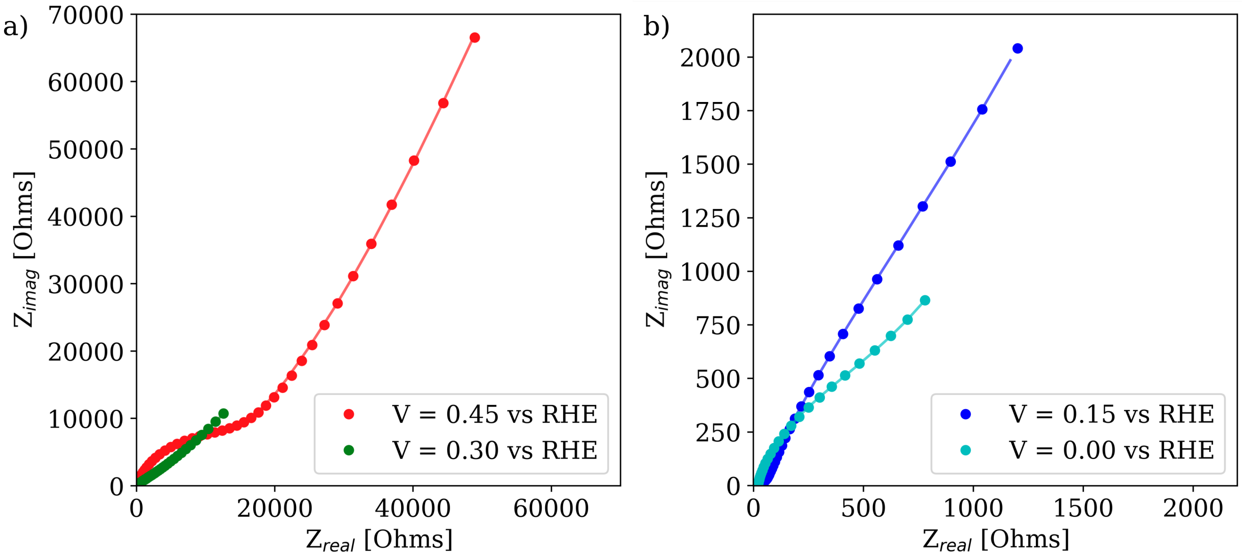

Figure 52: Nyquist plots of the complex plane impedance data for the H_xWO_3 system at varying DC potentials: a) +0.45 and +0.30 V vs. RHE; b) +0.15 and 0.00 V vs. RHE. Note the difference in magnitudes for the axes in a) and b).

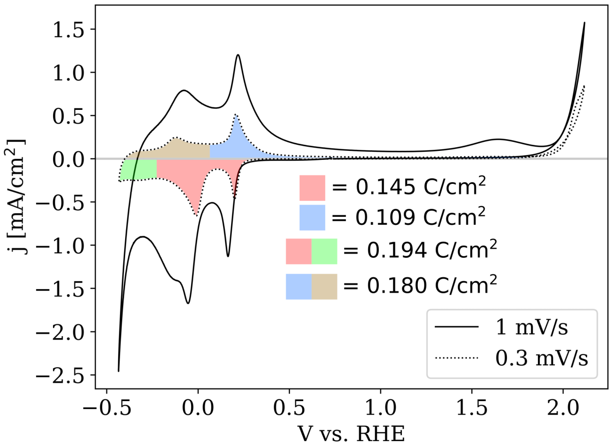

Figure 53: Comparison of 1 mV/s and 0.3 mV/s scan rates and the resulting shifts in voltammograms.

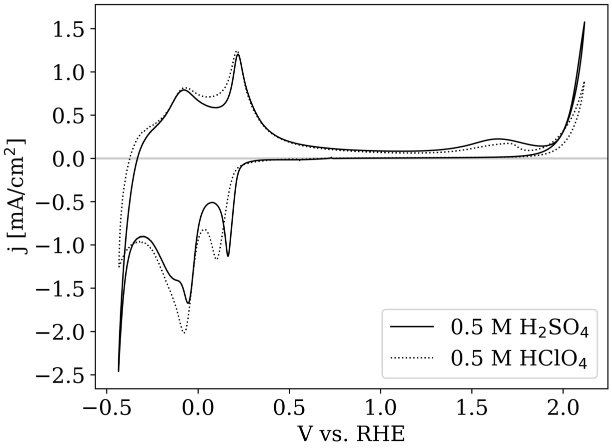

Figure 54: Comparison of voltammograms in 0.5 M H_2SO_4 and 0.5 M $HClO_4$.

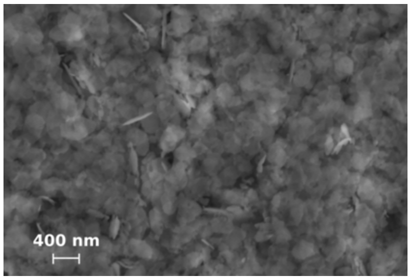

Figure 55: Scanning electron micrograph of a representative sample of as-synthesized nanoparticle WO_3.

Table 7: Atomic radii considered for neighbor assignments.

Element	Radius
V*	1.44 Å
Mo*	1.70 Å
W	1.62 Å
Ti*	1.38 Å
O*	0.89 Å
H	0.31 Å

Table 8: Metal and oxygen content of each oxide evaluated in this work.

Oxide	# Metals	# Oxygens
V_2O_5	8	20
MoO_3	8	24
WO_3	8	24
VO_2	8	16
TiO_2	8	16

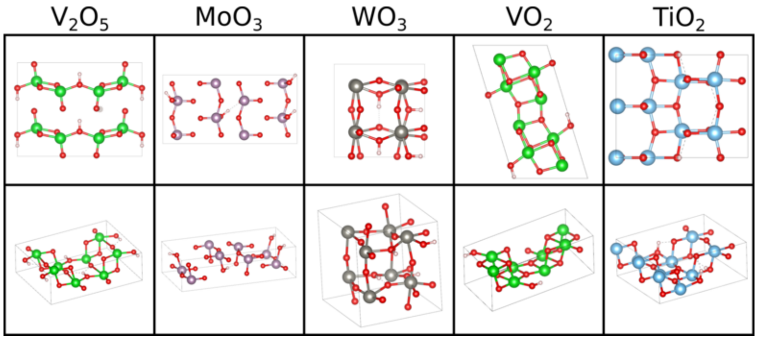

Figure 56: The five different metal oxides considered in this work.

A.18 Illustrating Scaled Coordination, CN$_s$

Figure 57 shows how CN$_s$ values were calculated using the same connected and layered oxides as in Figure 1 of the main text. The colored oxygen with an 'X' is the nominal binding site for hydrogen and the atom for which CN$_s$ is calculated. The neighboring metals are the first neighbors, and the next nearest oxygens are the second neighbors. All colored atoms make up the local environment of the binding site. Each bond that exists among these specific atoms is considered to be in the neighborhood of the binding site. The sum of these bonds divided by the total number of bonds present in the unit cell then gives CN$_s$.

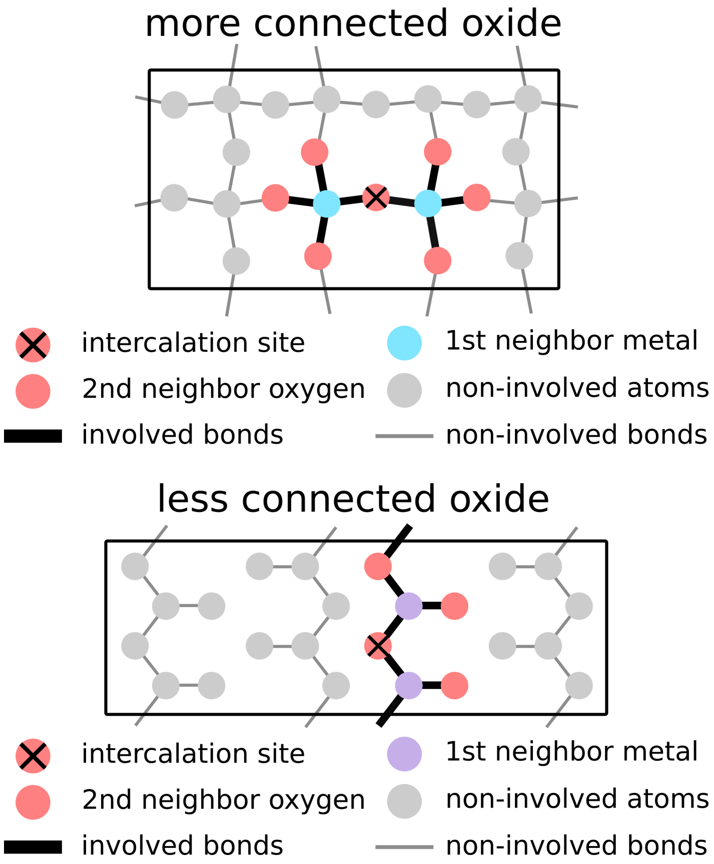

Figure 57: Illustrating the close neighborhood of a binding site used to define the scaled coordination, CN$_s$.

In addition to the bond-centric interpretation of CN$_s$ that is illustrated by Figure 57 and shown in Equation 5 of the main text, it can also be understood as a function of the nearest neighbor coordination numbers. Since the binding sites for H atoms are always oxygen centers in the oxide lattices, the first nearest neighbors will be metal atoms. CN$_s$

can therefore also be written as:

$$CN_s = \frac{\sum_p CN_{metal,p}}{E} \tag{A.18.1}$$

In Equation A.18.1, CN_{metal} is the local coordination number of a metal atom neighboring the oxygen site of interest and the summation considers all p metal atoms neighboring said oxygen. E is then the total number of bonds in the unit cell under consideration. In Figure 57, the more connected oxide has neighboring metal atoms with individual coordination numbers of 4, while in the less connected oxide the metal coordination numbers are 3. Equation A.18.1 can be used interchangeably with the main text definition when determining CN$_s$.

A.19 Details on Kernel Ridge Regression

All regression and data manipulation was performed using Python with the `scikit-learn` [272] and `pandas` [273] software packages. The kernel ridge regression model considered the global connectivity, Ω, and scaled coordination, CN_s, as features. These features were scaled and normalized using the Yeo-Johnson power transform [274]. Data normalization was performed using the training data only to prevent data leakage. Model hyperparameters were set to a kernel width of 2 and a regularization strength of 0.02. Training was performed on a randomly selected 70% portion of the full dataset and tested against the remaining 30%. The target outcome variable was selected as the hydrogen binding energy in each metal oxide candidate. These energies were calculated using DFT, as detailed in Section S2.

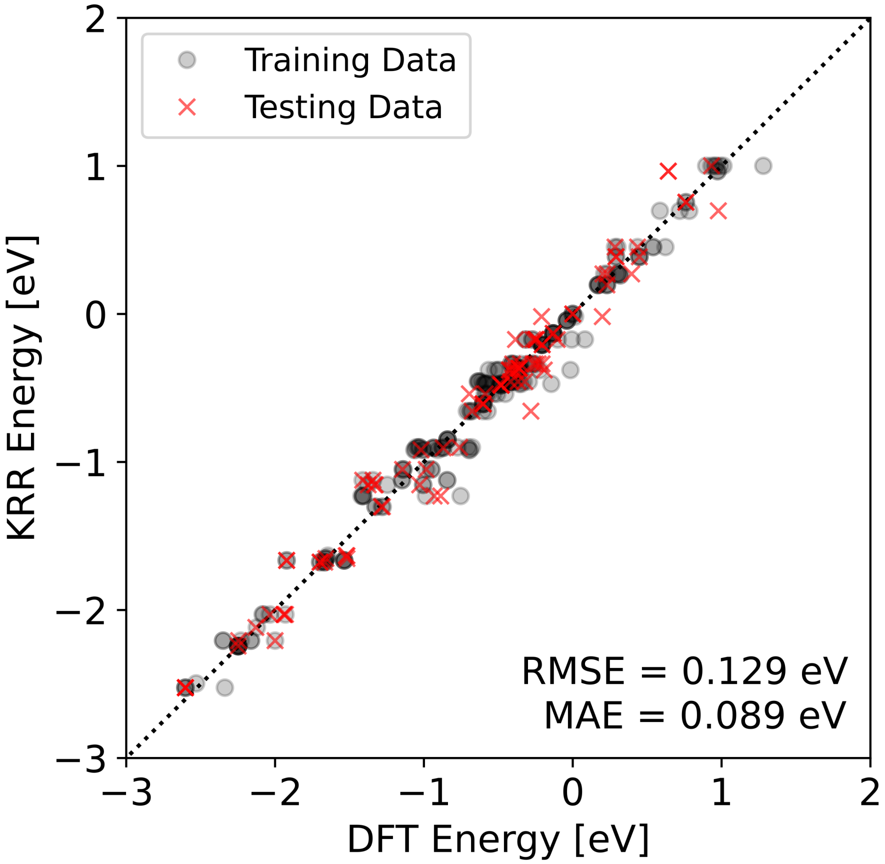

Figure 58: Parity plot illustrating performance of the KRR intercalation model versus the DFT benchmark data. Black circles indicate training data and red exes are testing data. The dotted diagonal line indicates 1:1 parity between the two datasets.

A.20 Estimation of Experimental Equilibrium Intercalation Potentials

Table 9 summarizes the intercalation equilibria and potentials gathered from literature and our own experiments. Each entry includes an explanation of which dataset was used from each paper and our method for extracting a particular potential. Our search was intended to capture experimental reports with the following characteristics:

1. investigated the same oxide crystal structures as those examined in our calculations,
2. specifically implicated proton intercalation as the operative redox phenomenon, and
3. described methods and data analysis in a way that facilitated translation to the RHE potential scale.

Table 9: Each row represents an individual data point plotted in Figure 3b of the main text. The "Couple" column refers to the redox couple. The "Ref." column is the literature reference. The "Origin" and "Method" columns are the location in the reference and the method by which the data were recorded and interpreted, respectively. "Lit. Potential" is the corresponding intercalation potential, and the "KRR Potential" is the model-predicted potential generated in this work. †Converted from Ag/AgCl to SHE considering 3.0 M KCl filling solution, and from SHE to RHE assuming pH 0 electrolyte.

Couple	Ref.	Origin	Method	KRR Potential [V vs. RHE]	Lit. Potential [V vs. RHE]
$V_2O_5/H_{0.125}V_2O_5$	[33]	Figure 2	CV, halfway between redox peaks	+0.78	+0.74†
$V_2O_5/H_{0.125}V_2O_5$	this work	this work	CV, halfway between redox peaks	+0.78	+0.83
$MoO_3/H_{0.250}MoO_3$	[34]	Figure 2a	CV, halfway between redox peaks	+0.42	+0.26
$MoO_3/H_{0.250}MoO_3$	[35]	Figure 1a	CV, halfway between redox peaks	+0.42	+0.31
$MoO_3/H_{0.250}MoO_3$	[36]	Figure 1	CA, plateau	+0.42	+0.40
$MoO_3/H_{0.250}MoO_3$	[37]	Figure 5	CA, plateau	+0.42	+0.40
$H_{0.250}MoO_3/H_{0.500}MoO_3$	[34]	Figure 2a	CV, halfway between redox peaks	+0.35	+0.23
$H_{0.250}MoO_3/H_{0.500}MoO_3$	[35]	Figure 1a	CV, halfway between redox peaks	+0.35	+0.27
$H_{0.250}MoO_3/H_{0.500}MoO_3$	[36]	Figure 1	CA, plateau	+0.35	+0.18
$H_{0.250}MoO_3/H_{0.500}MoO_3$	[37]	Figure 5	CA, plateau	+0.35	+0.20
$WoO_3/H_{0.250}WO_3$	[38]	Figure 4b	CV, halfway between redox peaks	+0.34	+0.29
$WoO_3/H_{0.250}WO_3$	[39]	Figure 8	CV, halfway between redox peaks	+0.34	+0.24
$H_{0.250}WoO_3/H_{0.500}WO_3$	[38]	Figure 4b	CV, halfway between redox peaks	+0.02	+0.11
$H_{0.250}WoO_3/H_{0.500}WO_3$	[39]	Figure 8	CV, halfway between redox peaks	+0.02	+0.08
$VO_2/H_{0.125}VO_2$	[40]	Figure 5b	CA, plateau	+0.04	+0.14
$TiO_2/H_{0.125}TiO_2$	[41]	Figure 2 (left)	CV, halfway between redox peaks	-0.39	-0.35
$TiO_2/H_{0.125}TiO_2$	[42]	Figure 2a	CV, halfway between redox peaks	-0.39	-0.64
$TiO_2/H_{0.125}TiO_2$	this work	this work	CV, halfway between redox peaks	-0.39	-0.56

A.21 Electrochemical Hydrogen Intercalation Measurements

We performed experiments on anatase TiO_2 (Sigma Aldrich 637254) and orthorhombic V_2O_5 (Sigma Aldrich 221899) to supplement the published data compiled in Section S6. The materials were used as received without further modification. Each were dispersed into inks and then drop-casted onto glassy carbon (GC) working electrodes (CH Instruments CHI104). For TiO_2, 0.05 g of the oxide was mixed with 0.02 g of PVDF (MTI HSV900) and 500 μL of *N*-methyl-2-pyrrolidone (Thermo Scientific 390682500). For V_2O_5, 0.0425 g of the oxide was mixed with 0.0075 g of PVDF and 500 μL of *N*-methyl-2-pyrrolidone. Each ink was sonicated for 30 minutes upon mixing, and then re-sonicated for at least 5 minutes prior to any subsequent depositions. 1 μL of ink was dropped onto the GC electrode and allowed to dry in ambient air under an IR heat lamp. The films were usually fully dried within approximately 1 hr. A Gamry Reference 600 potentiostat was used for all electrochemical measurements, with a graphite rod (Electron Microscopy Sciences 0.25 in. diameter, Spectro-Grade) counter electrode and a Ag/AgCl (CH Instruments CHI111) reference electrode. All recorded potentials were converted to the RHE scale by measuring the open circuit potential of a platinum electrode (0.5 mm Pt wire, 99.997% metals basis, Alfa Aesar) submerged in H_2 (99.999%, Matheson) saturated electrolyte. The electrolytes used for voltammetry were different for each oxide and are further detailed below.

Figure S4 summarizes the experiments we conducted to determine the equilibrium hydrogen intercalation potential in TiO_2. The TiO_2 films were submerged in 0.5 M H_2SO_4 (Fisher A300-212, >18.2 MΩ·cm water) and cycled at scan rates ranging from 10 mV/s to 1000 mV/s. A subset of the data spanning this range of scan rates is shown in Figure S4a. As it can be seen, the peak magnitudes and their separation generally increase with larger scan rates, as expected. However, in some cases peak positions and magnitudes did not vary in the expected fashion with scan rate, as exemplified by the reduction peak in the 10 mV/s scan and the oxidation peak in the 100 mV/s scan. This variation occurred across the various films we tested, and so we recorded at least 3 replicates per scan rate to develop a clearer estimate of peak potentials and the resulting half-wave potentials, $E_{1/2}$. These data are summarized in Figure S4b. The vertical error bars show the 95% confidence interval for a each peak position at a given scan rate. Consistent with Figure S4a, the separation between peaks along the voltage axes increases as scan rates increase. However, the $E_{1/2}$ values for each scan rate (black x's) do not significantly deviate across the scan rates investigated here. The average $E_{1/2}$ is -0.56 V vs. RHE, which we have taken as an estimate of the standard reduction potential for hydrogen intercalation in anatase TiO_2.

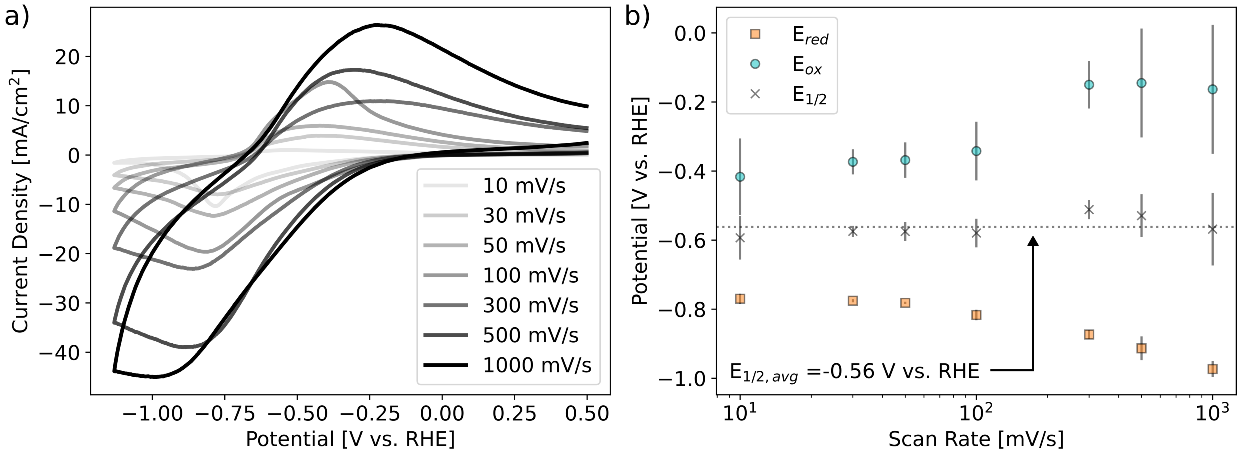

Figure 59: Experimental determination of hydrogen intercalation potentials in TiO_2. a) Representative voltammograms showing scan rate dependence of TiO_2/PVDF composite films on GC electrodes in 0.5 M H_2SO_4. b) Variation of peak potentials and half-wave potential across scan rates from 10 to 1000 mV/s. Vertical error bars show 95% confidence intervals from at least three individual samples.

Although the TiO_2 films were stable, we were not able to perform scan rate-dependence measurements on films of V_2O_5 owing to their dissolution. We attempted voltammetry measurements in a variety of electrolytes, including multiple concentrations of unbuffered sulfuric acid and citrate buffers of varying pH and total ionic strength. We found the V_2O_5 films were most stable in a 0.1 M citrate buffer (CB) adjusted to pH 3. This buffer was prepared by adding citric acid (Thermo Scientific J13729.A1) to >18.2 MΩ·cm water to achieve a citrate concentration of 0.1 M. The pH was adjusted to via the addition of 2 M NaOH (Alfa Aesar A16037, >18.2 MΩ·cm water). Use of the pH 3 CB allowed us to observe intercalation redox chemistry on a timescale that was shorter than film dissolution. Although the V_2O_5 still dissolved after extended cycling under these conditions, we were able to record voltammograms that indicated proton intercalation into V_2O_5.

Representative voltammetric measurements on V_2O_5 are shown in Figure S5a. The 1st and 50th cycles are shown for a V_2O_5 film on GC scanned at 25 mV/s in pH 3 CB. The 1st cycle exhibited a redox couple centered around a $E_{1/2}$ of +0.825 V vs. RHE. After 50 cycles, this feature completely disappeared and only a small capacitive background current remained, consistent with dissolution of the oxide layer. Since there were no remaining redox features in the 50th cycle, we tentatively concluded that any dissolved vanadium ions could not be responsible for the redox peaks observed in the 1st cycle.

To further address the possibility that the observed redox features for V_2O_5 were from dissolved species, we ran additional voltammograms on a bare GC electrode in pH 3 CB electrolytes containing a 10 mM concentration of pre-dissolved V_2O_5. This concentration is 1000-fold larger than would result from complete dissolution of V_2O_5 films from the experiments conducted in Figure S5a. Figure S5b shows voltammograms of V_2O_5 pre-dissolved in pH 3 CB at three different timescales overlaid with the V_2O_5 films measured in pH 3 CB. Figure S5c demonstrates the significant color changes in the V_2O_5-treated CB that we observed during storage. We included voltammograms at each of the noted time points to be sure that the changes in coloration—which suggest changes in average oxidation state of the V in the dissolved complex—did not significantly influence voltammetric behavior. As can be seen for all time points, dissolved vanadium does not replicate the redox features seen for the solid-state V_2O_5 films measured in pure pH 3 CB. Most notably, the reduction feature with an onset potential around +0.9 V vs RHE in the V_2O_5 film sample is absent from the measurements made on pre-dissolved V_2O_5. Furthermore, the oxidation peak positions are positively shifted for all three measurements of the pre-dissolved V_2O_5 electrolytes, including the case after 2 hours of dissolution in which the magnitude of the oxidation feature is similar (implying the electrode had access to a similar overall quantity of vanadium during the timescale of the measurement). To summarize, the V_2O_5 films showed a reversible redox wave with a $E_{1/2}$ of +0.825 V vs. RHE, which we have taken as an estimation of the standard reduction potential for hydrogen intercalation in orthorhombic V_2O_5.

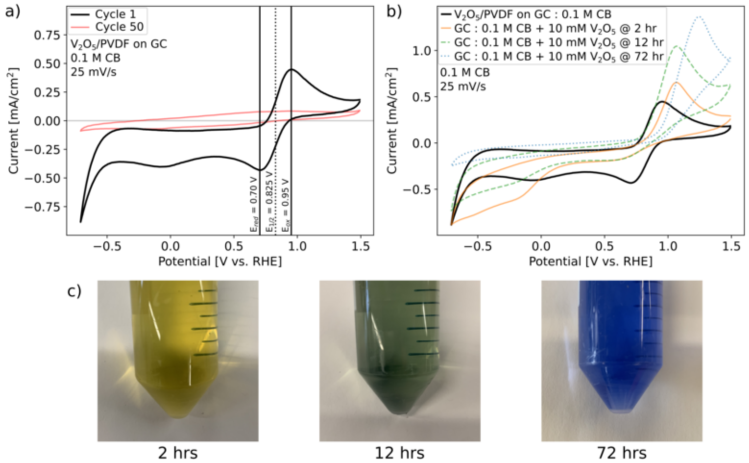

Figure 60: Experimental determination of hydrogen intercalation potentials in V_2O_5. a) Cyclic voltammograms of V_2O_5/PVDF composite on GC electrode in 0.1 M citrate buffer at a scan rate of 25 mV/s. The 1st and 50th cycles are shown to illustrate disappearance of the redox feature centered on +0.825 V vs. RHE. b) Cyclic voltammograms of V_2O_5/PVDF composite on GC electrode in 0.1 M citrate buffer overlaid with voltammograms of bare GC electrodes in 0.1 M citrate buffer pre-spiked with high background concentrations of V_2O_5. The bare GC cycles are shown for V_2O_5-containing electrolytes at three different ages. No dissolved V_2O_5 can replicate the behavior of the V_2O_5/PVDF composite on GC electrode. c) Images of the V_2O_5-spiked electrolytes at 2, 12, and 72 hrs.

A.22 Comparing Different Interpretations of Structure

The relative importance of Ω vs. CN_s can be interpreted from regressions trained using only one of each descriptor. KRR models trained on only Ω values, and only CN_s values, are shown in Figures 61a and 61b, respectively. As can be seen, the model trained only on Ω performs better than the one trained on CN_s, achieving a RMSE of 0.217 eV vs. 0.335 eV. However, it is notable that these models on their own are not sufficiently accurate, motivating the combination of the global and local geometry descriptors in the model used in this work (Figure S3). Together, Ω and CN_s capture orthogonal information to accurately describe hydrogen intercalation in the tested metal oxides.

In order to demonstrate the utility of CN_s as a quantitative descriptor of local site geometries, we compared its performance to the generalized coordination number, $\overline{\mathrm{CN}}$ [130]. $\overline{\mathrm{CN}}$ was originally defined for use with metal nanoparticles, and the normalization was based on metal packing. We computed $\overline{\mathrm{CN}}$ according to reference [130] and set the maximum coordination to 6, which is the highest observed coordination for metal atoms in the bulk oxides investigated here. The performance of a KRR model trained only on $\overline{\mathrm{CN}}$ is shown in Figure 61c. This $\overline{\mathrm{CN}}$ model achieves an error of 0.558 eV and shows strong horizontal streaking, indicating that CN_s could be a more flexible descriptor of local site geometries.

The definition of Ω presented in the main text is based on atomic neighbor information (accounting for which atoms are bonded to one another in an arbitrary structure of interest). An alternative definition of the symmetric normalized Laplacian matrices can be made by instead basing the entries of the matrix as the atom-to-atom distances, rather than basing them on local coordination numbers (atom degrees). In this manner, the resulting matrices would contain information about the atomic graph edges (e.g. the distances). This alternative definition begins from the construction of an adjacency matrix with each entry corresponding to the distances between atoms.

$$A_{dist}(u,v) = \begin{cases} 0, & \text{if } u = v \\ D_{uv}, & \text{if } u \neq v \end{cases} \tag{A.22.1}$$

In Equation A.22.1, A_{dist} is the unnormalized edge adjacency matrix. Atom indices are given by u and v, and D_{uv} is the distance between atom u and atom v. The corresponding unnormalized distance degree matrix can be determined from A_{dist} by assigning to the diagonal the sum of either the rows or columns of A_{dist}.

$$D_{dist}(u,v) = \begin{cases} \sum_{v=0}^{v=N} A_{dist}(u,v), & \text{if } u = v \\ 0, & \text{if } u \neq v \end{cases} \tag{A.22.2}$$

In Equation A.22.2, D_{dist} is the unnormalized distance degree matrix. The summation runs across one atom index and through all atoms (e.g. sums a full column or full row of A_{dist}). The unnormalized distance Laplacian, $L_{dist}(u,v)$, is then computed as:

$$L_{dist}(u,v) = D_{dist}(u,v) - A_{dist}(u,v) \tag{A.22.3}$$

Since all of these matrices are by definition symmetric and real in the current use case, $L_{dist}(u,v)$ can be normalized using [136]:

$$\mathcal{L}_{dist}(u,v) = D_{dist}(u,v)^{1/2} L_{dist}(u,v) D_{dist}(u,v)^{1/2} \tag{A.22.4}$$

Equations 2, 3, and 4 from the main text can then be applied to generate Ω_{dist} values based on distance Laplacians. Using these Ω_{dist} values alongside the same CN$_s$ values discussed in the main text results in model performance shown in Figure 61d. The distance-based model gives errors that are slightly higher than that achieved by the KRR model built on the neighbor-based Ω defined by Equation 1 of the main text and CN$_s$ (Figure 58). Although there is no major improvement by including distance information, there is also no significant detriment to model performance. Distance-based Laplacians could therefore be alternative tools for exploring future applications of global connectivity.

All of the models described in this section were held at constant hyperparameter values (kernel width of 2 and regularization strength of 0.02) in order to make fair comparisons strictly on the basis of the selected features. The same training and testing data sets were also used between the different models, again to ensure resulting performance metrics were differentiated solely by structural descriptors.

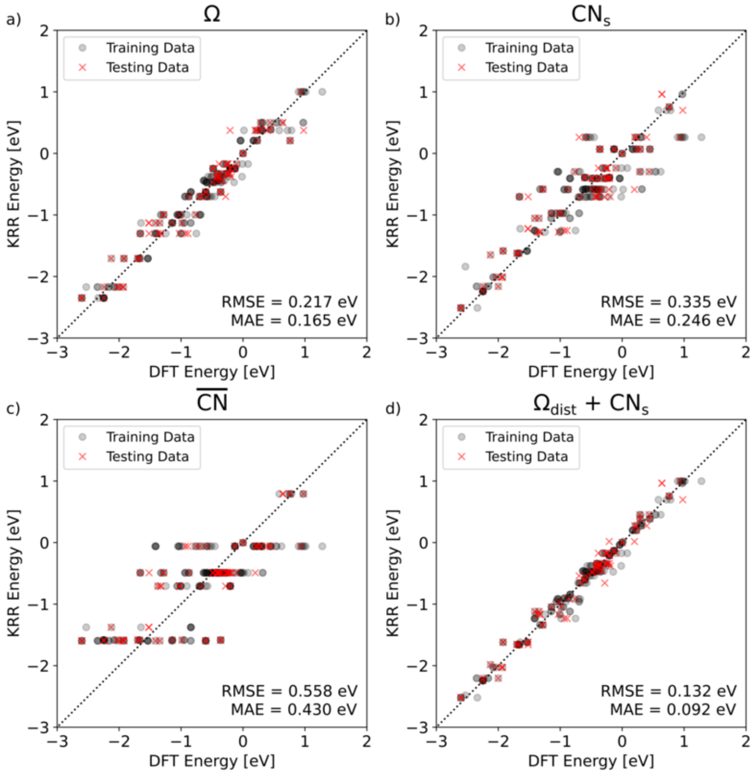

Figure 61: Comparing KRR models constructed from different geometry descriptors. a) Model trained only on Ω values computed using equations 1–4 in the main text. b) Model considering only CN$_s$. c) Model incorporating solely the generalized coordination number. d) Model relying on distance Laplacian and CN$_s$.

A.23 Details on Convolutional Neural Network

The CNN employed in this work is shown in Figure 62. The symmetric normalized Laplacian matrices $\mathcal{L}$ [136] for each intercalated oxide were used as inputs. Matrices were first run through two 2D convolutional layers. The first consisted of 64 filters with 3x3 kernels. The second was a set of 8 filters, each with 9x9 kernels. Both convolutional layers used rectified linear unit activation functions. After the two convolutional layers, data was regularized with a dropout layer that removed information at a rate of 10%. The data then was run through a 2D average pooling layer that used a 3x3 window. This information was then flattened and fed into three sequential feed forward layers that contained 16 nodes each. Another 10% dropout pass was included after the first of the dense layers for further regularization. Each of the nodes in the dense layers used linear activation functions. The final output node also used a linear activation function. The final hidden layer—highlighted in green—was decomposed using principal component analysis (PCA) to generate Figure 4 of the main text.

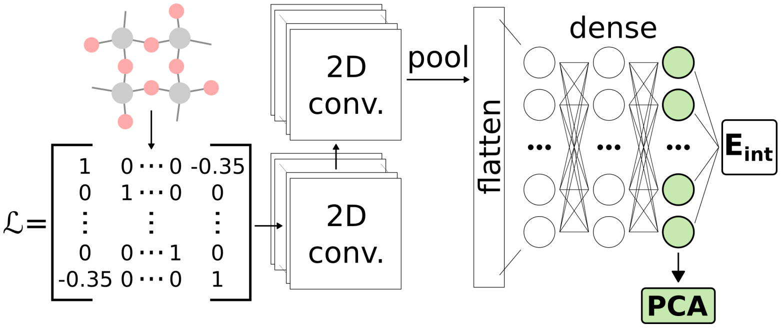

Figure 62: Visualization of the CNN architecture used in this work. Principal component analysis was performed on the last hidden layer of the network, highlighted in green.

Network construction and training was performed using `Tensorflow` [275] with the `Keras` [276] API. Network training was performed on 70% of the total data, with the remaining used as validation/testing data. Optimization of network parameters was conducted over 100 epochs using the Adam optimizer [277]. Figure 63a shows the evolution of training and testing data RMSE's over the course of the 100 epochs. The validation error did not greatly exceed training error, suggesting minimal overfitting. Figure 63b compares H-binding energies calculated by the CNN to the benchmark DFT data. The RMSE and MAE approach the error of the KRR model discussed in the main text and in Section S5.

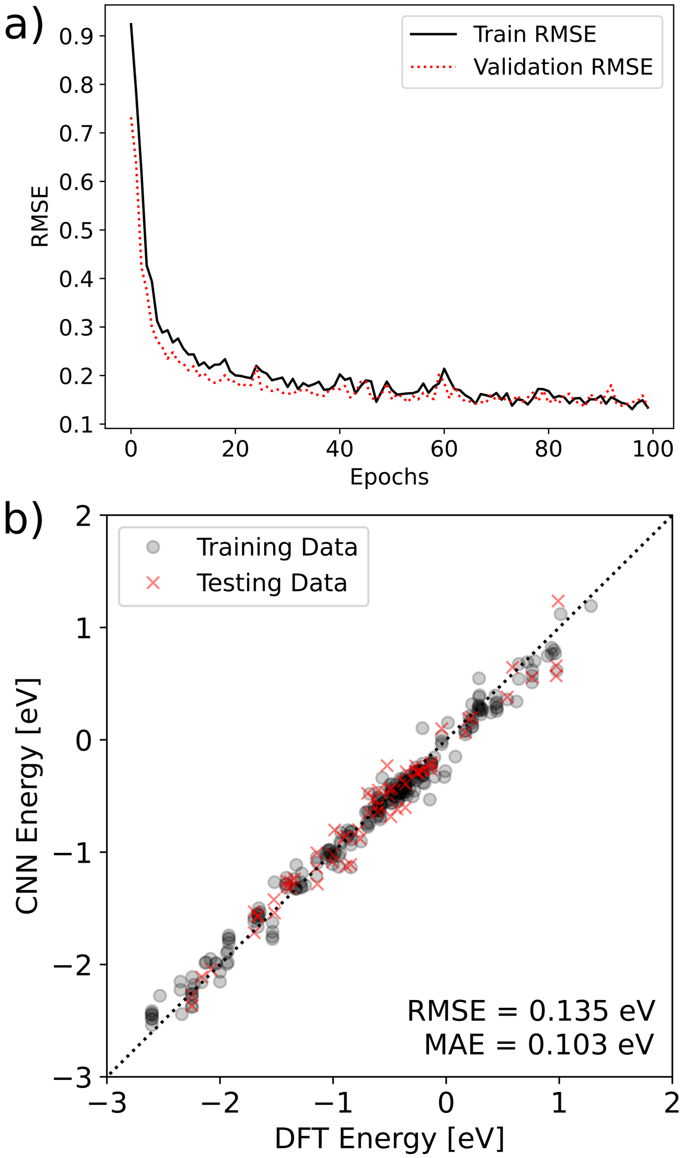

Figure 63: Training and performance of the CNN. a) Per epoch evolution of training and validation set RMSEs. Validation error did not greatly exceed training error at any point, indicating limited overfitting. b) Comparison of CNN binding energies to DFT binding energies. Model errors approached those of the KRR model shown in Figure S3.

In addition to the final hidden layer PCA shown for Ω in the main text, Figure 64 shows a comparison between the CNN embeddings and CN_s. As can be seen, there is noticeably less correlation (i.e. there is less of a clear gradient and relatively more randomness in color) between the embeddings and CN_s than is observed for the embeddings and Ω in Figure 4 of the main text. This suggests that Ω is more similar to the CNN embeddings than CN_s, providing further evidence for its importance as a structural descriptor when evaluating hydrogen intercalation in metal oxides.

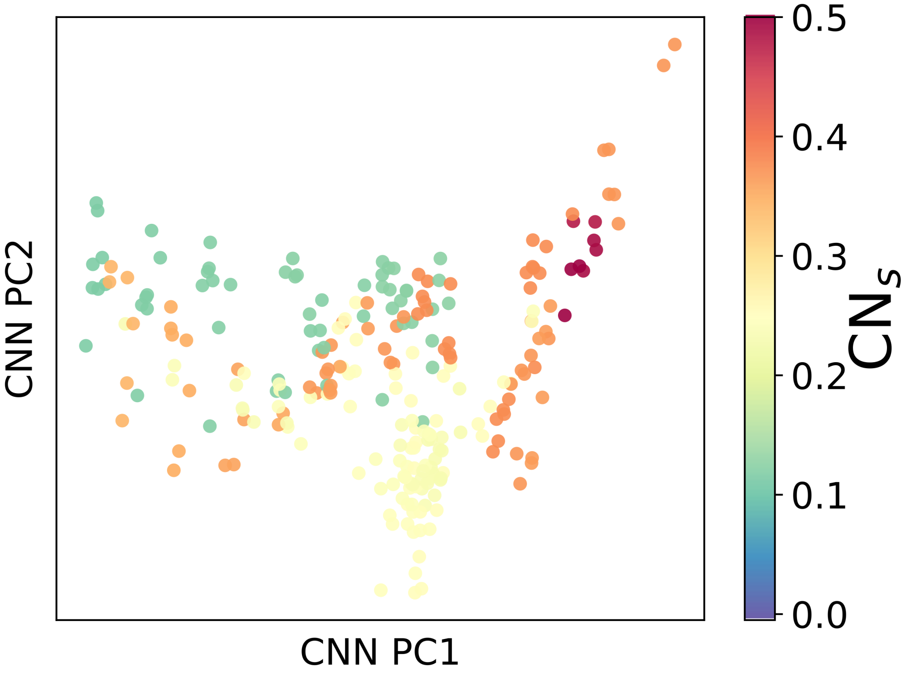

Figure 64: 2D heat map demonstrating how CN_s weakly correlates with the final hidden layer embeddings of the trained CNN. Comparing with Figure 4 of the main text provides evidence for Ω as a more significant descriptor of structure than CN_s in the context of hydrogen intercalation in metal oxides.

Appendix B Supporting Information for Chapter 3

B.1 Detailed Experimental Methods

The WO_3 nanodisks used in this study were prepared using a method adapted from Wolcott et al.[182] In a representative synthesis, 0.8225 grams of Na_2WO_4 hydrate (Sigma Aldrich, $\geq$ 99%) was dissolved in 10 mL of deionized water (>18 MΩ, Millipore Advantage A-10) to form a 0.25 M solution. A liquid chromatography column wth a 1.5 cm ID was packed with 5 cm of hydrogen-form Dowex 50WX8 ion exchange resin (200–400 mesh, Sigma Aldrich) and washed with water to remove any remaining free acid. A 1 cm layer of sand was packed on top of the resin to ensure even propagation of solution through the column. The 10 mL of Na_2WO_4 solution was then passed through the column in three approximately equal aliquots and collected. The first aliquot was discarded and only the second and third were used in experiments. The exchanged material (nominally 0.25 M tungstic acid) was allowed to rest on the benchtop at room temperature (~21° C) for at least 3 days, whereupon the material geometry was found to converge to a nanodisk morphology. Nanodisk formation was further investigated via SEM, XRD, and TEM, as shown in the main text and Section B.2 below.

The aged WO_3 was deposited without any further processing via a doctor-blade method onto glass substrates that had been pre-coated with either FTO, metal thin films, or Pt/WO_3 films. FTO glass was purchased from MTI Corp., where metal thin films and Pt/WO_3 films were applied in-house (see below). The deposition areas were outlined with a single layer of 3M brand Scotch tape and 50 μL of tungstic acid were placed in the center of the boundary. A flint glass tube was used to form an even coat and remove excess material, after which a Steinel HL 1610 S heat gun on the low setting was used to dry the wet films. After drying, the tape was removed and the samples were calcined at 500 °C for one hour in air. Pure WO_3 nanodisk films were allowed to overlap with the pre-deposited metal or Pt/WO_3 films. This overlap region allowed for electrical and chemical interaction between the different materials.

Pt- and Au-coated substrates were prepared using a Plassys MEB550S Electron Beam

Evaporator. All depositions were performed at pressures lower than 1E-6 mbar. Corning 75 x 25 mm glass microscope slides were masked using single-sided Kapton tape and initially coated with a 5 nm titanium adhesion layer at a rate of 0.02 nm/sec. A 100 nm layer of either Pt or Au was then deposited onto the Ti-coated glass at respective rates of 0.1 nm/sec and 0.05 nm/sec.

Powder X-ray diffraction (XRD) measurements were performed on a Bruker D-8 instrument equipped with a LynxEye detector and using Cu K-α radiation with a wavelength of 0.15406 Å. Measurements were made with a step size of 0.02° at 1.25 s/step. Scanning electron microscope (SEM) images were taken using a Zeiss Sigma 500VP field emission instrument. Samples were prepared on FTO glass and images were captured using accelerating voltages of 10 keV using a backscatter (SE2) detector. Transmission electron microscopy (TEM) was performed using a Hitachi 9500 ETEM at an accelerating voltage of 300 keV. Samples were dispersed onto dual-sided copper-carbon TEM grids from Ted Pella, Inc. using a 4:1 mixture of IPA:water.

Electrochemical measurements were carried out using a Gamry Interface 1000 potentiostat in a 3-electrode configuration with graphite rod counter and 1 M KCl Ag/AgCl reference electrodes. Samples were tested an acrylic cell that was fabricated in-house, with a 0.495 cm^2 working area. The RHE potential was explicitly calibrated for the 1 M KCl Ag/AgCl reference electrode via open circuit potential (OCP) measurements in a cell consisting of a Pt working electrode, a graphite counter electrode, and 0.5 M sulfuric acid electrolyte.

Time-resolved optical microscopy measurements were carried out on a Pace Technologies IM-5000 Inverted Microscope mounted with a Sony a6300 digital camera. Figure 65 shows the electrochemical configuration of the experimental setup employed for these measurements. The same acrylic cell was used for H-spillover measurements. The sampling area of a given video recording was a 3 mm diameter circle, which limited the measurable coloration distance. Both ambient light and a Thorlabs M625L3 625 nm red LED were used as light sources, which gave comparable results. Electrochemical intercalation or thermochemical spillover was instigated at one end of a film, respectively by chronoamperometry or by exposure to hydrogen gas-saturated 0.5 M sulfuric acid. As the respective reductions were induced, WO_3 was progressively converted to its bronze. The conversion from oxide to bronze progressed

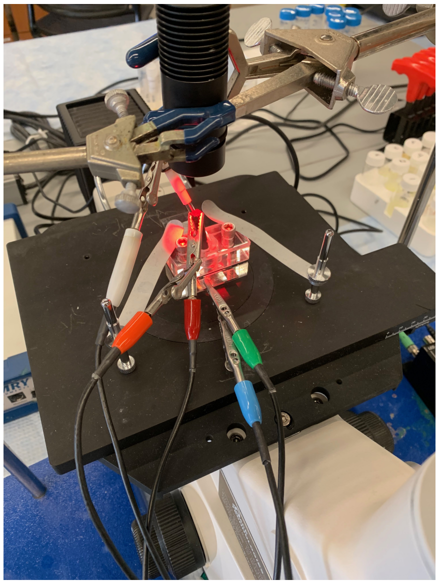

Figure 65: Experimental setup for optical microscopy, shown in the configuration for electrochemical hydrogen insertion with red LED illumination. Camera mounted to microscope not shown.

parallel to the film, evidenced by a coloration front originating at the bias location and extending outwards.

Front progression was explicitly measured only in areas of pure WO_3/H_xWO_3 directly on glass. Videos were recorded at a resolution of 1920 x 1080 and a framerate of 60 fps while either electrochemical (chronoamperometric) or thermochemical (H_2-saturated water) experiments were carried out. A Python script using the `ffmpeg` and `scikit-image` packages was used to convert the raw video file into a series of images with timestamps. Raw pixel-by-pixel intensity data were then collected from each image and converted from RGB color channels to a single gray color channel using the `scikit-image` package's `rgb2gray` function. This converted the multi-channel information to a single-valued pixel intensity. These intensity data were then interpreted as relative transmittance values under the assumption that pixel intensities were linearly proportional to the number of transmitted photons. The resulting data were then converted to relative absorbances by referencing the transmittance at each timepoint to the initial transmittance and assuming that the quantity of scattered light remained constant for all concentrations of H in WO_3:

$$\alpha(x,y,t) = T(x,y,t=0) - T(x,y,t) \tag{B.1.1}$$

In Equation B.1.1, T is the measured transmittance and α is the corresponding absorbance at pixel position (x, y) and time t. As the oxide films are reduced to bronzes, they shift to deep blue and absorb more of the incident light, where the first image of each experiment is of pure WO_3 and transmits the most light. In the formalism of Equation B.1.1, $T(x, y, t = 0)$ will always be larger than $T(x, y, t)$ and will result in positive values of $\alpha(x, y, t)$. Extinction coefficients for various wavelengths of light interacting with H_xWO_3 have been determined for a range of hydrogen stoichiometries, x, for values ¡ 0.4.[278] There is a monotonic increase in extinction coefficient with hydrogen content, which leads to a similar monotonic relationship between hydrogen content and absorbance. Therefore, although $\alpha(x, y, t)$ is not a rigorous measurement of absorbance, it is suitable for estimating relative hydrogen concentrations. We defined the edge of the moving front as the position of the leading edge of the absorbance profile at approximately half of the maximum observed value, which should correspond to a constant value of x in H_xWO_3.

B.2 Additional Materials Characterization

Samples were allowed to incubate at room temperature for at least three days after ion exchange, which allowed for full formation of the crystalline nanodisk morphology without the use of structure-directing agents. The tungstic acid solutions changed from clear yellow to opaque yellow in appearance over that timespan. Figure 66 shows SEM images the daily progression of product morphology. Each sample was prepared from the same batch of material and was calcined at 500 °C for one hour prior to imaging.

X-Ray diffraction was performed alongside SEM to investigate any shifts in crystal structure that accompanied the development of the nanodisks. The results are shown in Figure 67. These data show clear increases in crystallinity and texture through the three days of incubation. As discussed in the main text, TEM imaging showed the zone-axis and crystal facets exposed on the plane-edge of the nanodisks to be in the (100)-family. XRD con-

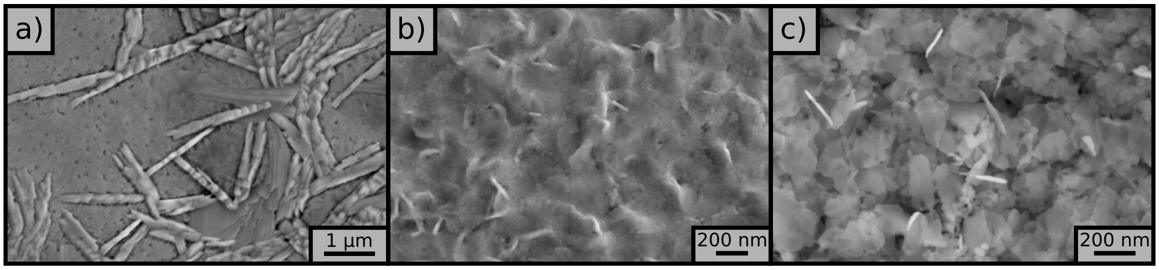

Figure 66: SEM images of tungsten trioxide thin films as a function of incubation time. Panel (a) shows the film morphology on the first day after ion exchange, which exhibits a distinct columnar structure interpenetrating a featureless background material. The Day 2 material in (b) shows the first indication of disk-like structure, with no remaining columnar shapes visible. Panel (c) confirms that on Day 3 the thin films achieve a consistent nanodisk morphology. There was no observed change in morphology after the third day of incubation.

firms a development of increased crystalline fraction in the (002) and (020) alongside the development of the disk shape.

Although the disks were uniform at the micro-scale, we observed a considerable density of crystalline imperfection at the nano-scale. Figure 68 shows additional TEM images confirming observations made in SEM and illustrating these defects.

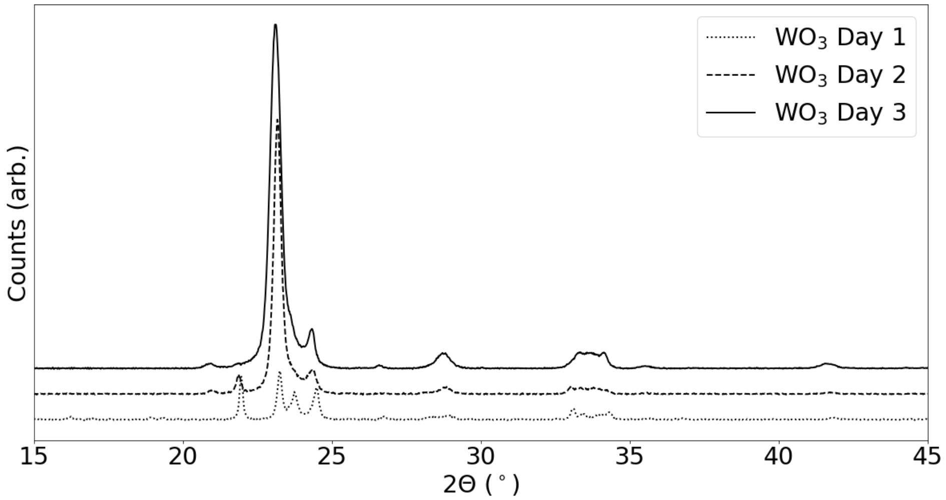

Figure 67: X-Ray spectra following the same temporal pattern as those shown above for SEM. A clear increase in diffraction intensity occurs alongside preferential texturing of the material in the (002) and (020) directions, consistent with the formation of nanodisks with predominantly (100)-family facets exposed on the plane face.

B.3 Effect of Restricting Proton Access

As noted in the main text, the observed migration rates of the coloration fronts were too fast to be attributed to proton diffusion in bulk tungsten trioxide when the WO_3 films were wetted with H_2SO_4 electrolyte. Hence, we argued that the electrolyte acts as proton source for bronze formation independent of the source of reducing equivalents. To further test this hypothesis, an electrochemical measurement was made on a sample identical to that in normal chronoamperometric experiments with the addition of a silicone layer on top of the pure WO_3. This was done to "shut-off" the electrolyte as a proton source, as illustrated in Figure 69.

Dow Sylgard 184 polydimethylsiloxane was employed as the silicone encapsulant, cured at 100 °C for 35 minutes at a ratio of 10:1 elastomer base to curing agent. A small gap was retained between the edge of the electrode and the beginning of the silicone layer. This allowed for direct comparison of electrolyte-exposed and electrolyte-isolated coloration fronts. The initial migration of protons occured rapidly, traversing the pure WO_3 area in seconds. Upon reaching the silicone covered WO_3, front progression was significantly slowed. Figure 70 shows a representative position vs. time curve collected for a silicone-covered region of a WO_3 film. The position of the silicone layer edge is taken as the zero position, and the time at which the front reached this edge (i.e. the time at which the front completely traversed the exposed WO_3 film) is taken as zero time. As can be seen, the front was found to move only ~150 microns from the leading edge of the isolated film after 500 seconds. Furthermore, the shape of the position vs. time data are very well described by an equation of the form $x = At^{0.5}$, which suggests purely diffusional behavior. We further estimated a diffusion coefficient using $\delta = \sqrt{4Dt}$, resulting in an apparent diffusion coefficient of 1.30 x 10^{-7} cm^2/s.

The value above roughly agrees with the upper bound of diffusion coefficients that have been previously reported for proton diffusion in H_xWO_3.[169, 192, 193] However, it is considerably greater than that reported by Bohnke and Vuillemin for proton diffusion through dense WO_3 films also via optical measurements.[191, 279] One major difference between these measurements is the sample geometry. In Bohnke and Vuillemin's case, diffusion rates were extracted from optical spectroscopy conducted normal to the direction of diffusion, which requires sampling the entire gradient of compositions (value of x in H_xWO_3). By contrast, our lateral measurements treat the H_xWO_3 propagation front at a single absorbance value corresponding to an intermediate state of hydrogenation. Hence, it is possible that the average rate of diffusion is in fact constrained by relatively slow transport at one particular composition (e.g., high or low H concentration). Another difference is that Bohnke and Vuillemin's experiments were carried out on dense WOx films, while ours were on porous films of WO3 nanocrystals. In our case, it would be reasonable to conjecture that proton transport is predominantly occurring along WO_3 nanodisk surfaces, in which case it could be substantially enhanced by a hydrogen-bond network at the oxide/electrolyte interface.

B.4 Mechanistic Formulation

The results of this study indicate that in the presence of a proton-conducting medium, H-intercalation and H-spillover in WO_3 proceed by the same mechanism involving proton and electron transfer, wherein the proton and electron need not originate from the same source. However, it remains unclear whether the temporal course of the reaction involves sequential or concurrent proton and electron transfer steps. Figure 71 compiles a family of candidate reaction mechanisms comprising a series of electron tranfer (ET), proton transfer, (PT) or proton-coupled electron transfer (PCET) steps first to a surface WO_3 site and then into the bulk of the WO_3 crystal.[280] We speculate that the predominant mechanism in this system involves two concurrent PCET steps—corresponding to the diagonal path through this diagram—due to the delocalization of electrons in the WO_3 conduction band, which could facilitate rapid charge compensation of protons as they adsorb and intercalate. Additional experiments (e.g., pH dependence, kinetic isotope effect, etc.) would be warranted to further distinguish between these mechanisms.

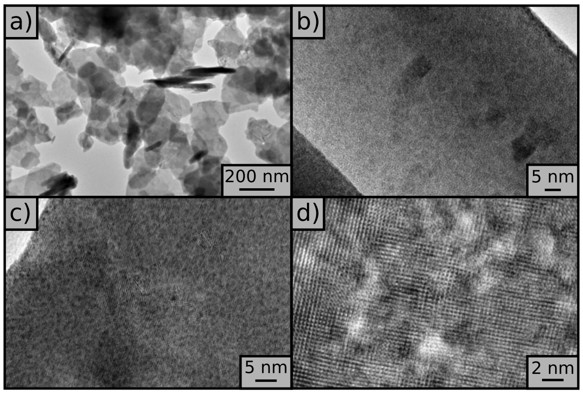

Figure 68: TEM micrographs showing key characteristics of the as-synthesized material at several length scales. Panel (a) shows a grouping of disks, confirming the micro-scale structure and the dimensions observed in SEM. Panels (b) and (c) show regions of the plane face of the nanodisks where various grain sizes and multiple defects are evident. Panel (d) shows lattice fringes indicative of numerous stacking faults and other crystallographic irregularities.

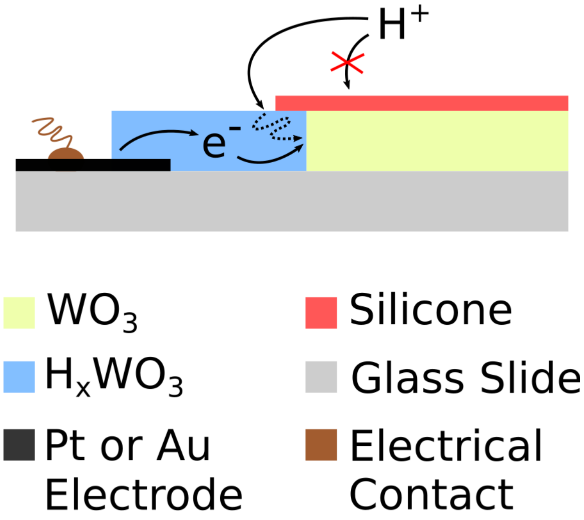

Figure 69: Schematic describing the function of the additional silicone elastomer film to eliminate direct proton transfer to the WO_3 film. Restricting access to the electrolyte-sourced protons would require bronze formation to occur by sourcing protons from through the already reduced bronze; in other words, the system would be dependent on proton and electron diffusion through the H_xWO_3 film. This process is represented by the dotted arrow and is expected to be slower than the incorporation of protons from the local electrolyte.

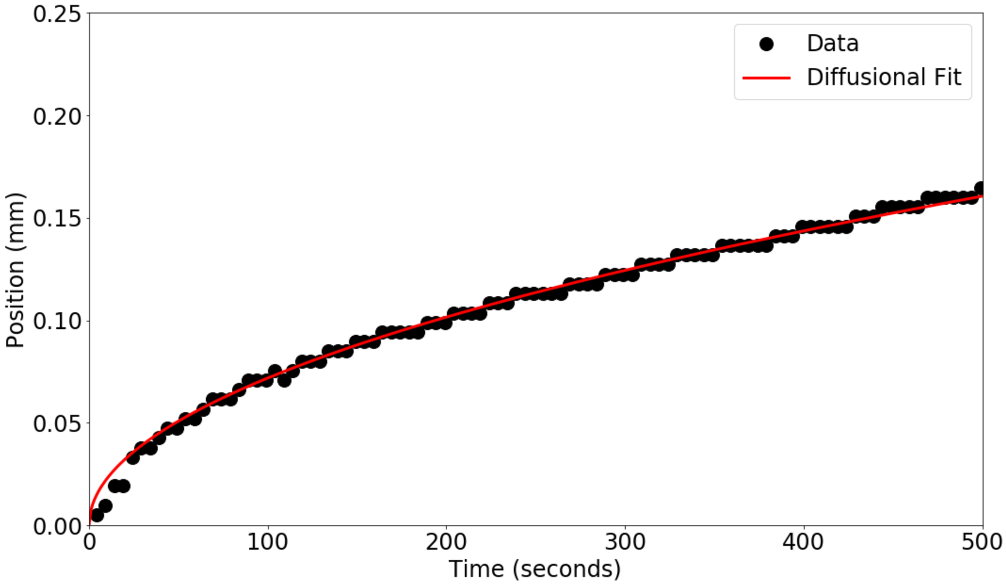

Figure 70: Position vs. time data for lateral propagation of a H_xWO_3 diffusion front using the experimental configuration in Figure 69. The linear fit corresponds to the predicted position vs. time data for a diffusion coefficient of 1.3x10^{-7} cm^2/s

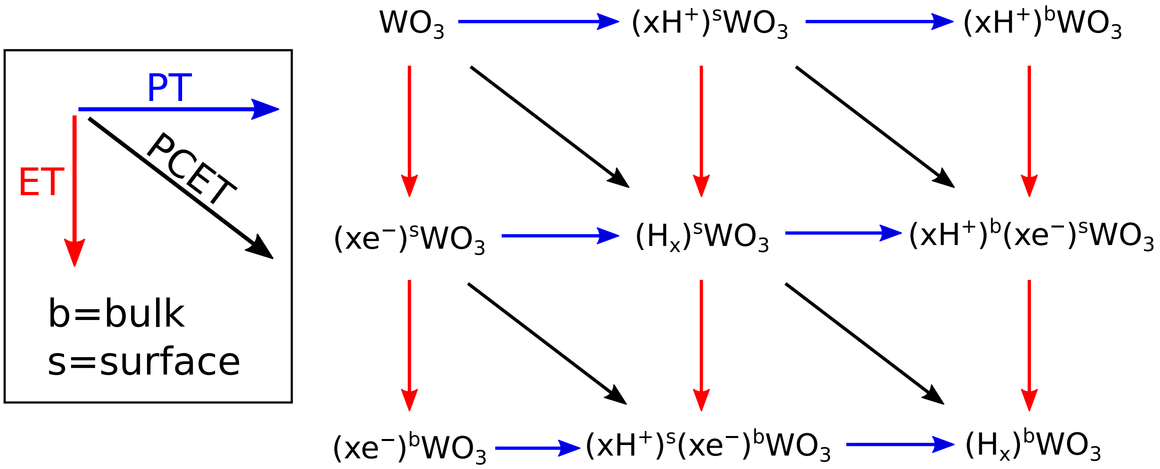

Figure 71: Compiled mechanistic pathways for H uptake in WO_3 according to a series of square schemes involving either sequential electron and proton transfers or concerted proton-coupled electron transfers first to the surface of a WO_3 crystallite and then into the bulk crystal lattice.

Appendix C Supporting Information for Chapter 4

C.1 Effect of Bulk H Intercalation on Surface Oxygen Basicity

Figure 72 shows that terminal oxygen site basicities decrease as bulk hydrogen content in H_xWO_3 increases. This is apparent from the stabilization of the O p band electrons, which move away from the Fermi level and therefore become weaker electron donors. The consequence of this change in chemical promiscuity is a deactivation of the terminal oxygen sites as candidate locations for H adsorption. Coupled with the fact that W sites are made more acidic (Figure 2c of the main text), along with the observation of metal site activation for H adsorption, the acid-base character of H_xWO_3 can be considered as the driving factor for interaction with amphoteric H equivalents.

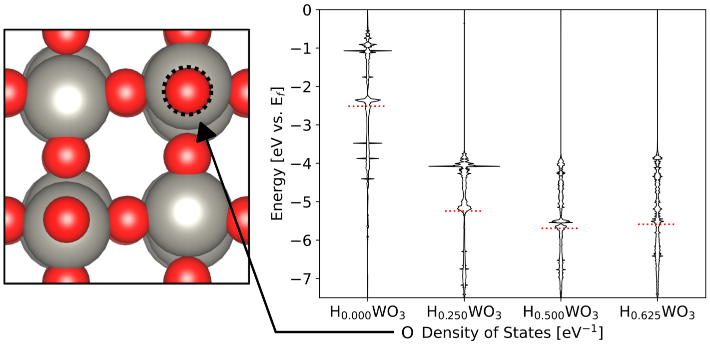

Figure 72: Modulations in occupied O p density of states for the under-coordinated terminal surface oxygen atom as a function of bulk H content. Red dotted horizontal lines indicate the position of the O p band center.

C.2 Active Surface Facets of H_xWO_3

Although the most thermodynamically stable surface of WO_3 is the (001) face, we also investigated the (100) face. Figure 73 summarizes this analysis. In this screening of adsorption sites, we examined every possible one- and two-fold combination of adsorption configurations on (001) and (100). To facilitate this, we removed explicit waters from the calculations and modeled the solvent only using the GLSSA-13 implicit approach. This was done to make the calculations more tractable, since there were a large number that needed to be completed. The energies in Figure 73 are the canonical free energies of adsorption, determined through the constant-charge DFT approach. The black data points and lines in the (100) panel correspond to those shows in Figure 2a of the main text. Overall, binding to the (100) surface is more feasible than to the (001) surface. For every investigated configuration, binding to the (100) surface is preferred. Although the (100) surface configuration is expected to be less frequently observed on a particle of WO_3 than the (001) surface, the fact that it can more easily interact with H warrants its investigation as the crystal facet responsible for catalysis of the HER.

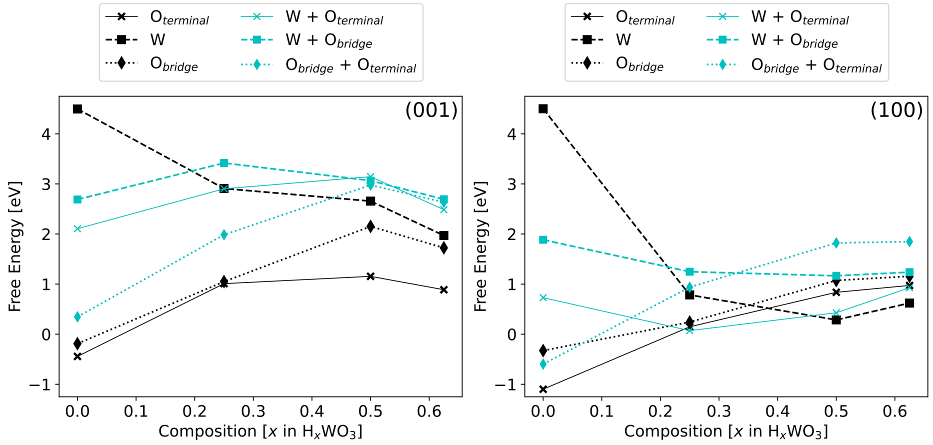

Figure 73: H adsorption energies for 1st and 2nd site adsorptions on the (001) and (100) surfaces of H_xWO_3. Black lines are for 1st site adsorption and cyan lines for 2nd site.

C.3 Equilibrium Potentials as Determined via CHE and CP-DFT

The computational hydrogen electrode approach for H adsorption on H_xWO_3 can be summarized in Equation C.3.1:

$$\Delta F_{ads} = F_{H-surface} - F_{surface} - \frac{n}{2} \cdot F_{H_2} - n \cdot eU \tag{C.3.1}$$

Here, ΔF_{ads} is the free energy of adsorption, $F_{H-surface}$ is the free energy of the adsorbed state, $F_{surface}$ is the free energy of the bare surface, F_{H_2} is the free energy of a hydrogen molecule, n is the number of H atom equivalents that are included in the adsorption reaction, and e is the charge of an electron. U is then the *a posteriori* applied potential which approximates the electrochemical biasing of the surface. The equilibrium potential, U_{eq}, of a given adsorption event is given by the value of U which drives ΔF_{ads} to zero. These U_{eq}'s are then the ones that are shown for the CHE method in Figure 3a of the main text.

In the CP-DFT approach, the effect of applied potential is included within a DFT calculation and therefore no correction to the energy is made:

$$\Delta\Omega_{ads} = \Omega_{H-surface} - \Omega_{surface} - \frac{m}{2} \cdot \Omega_{H_2} \tag{C.3.2}$$

In Equation C.3.2, $\Delta\Omega_{ads}$ is the grand canonical free energy of H adsorption, with $\Omega_{H-surface}$ of the adsorbed state, $\Omega_{H-surface}$ of the surface, and Ω_{H_2} of molecular H_2. The number of adsorbed H equivalents is given by m. For a general absolute grand canonical free energy, Ω_i, there is a related electrochemical potential that is defined by the difference between the Fermi level and the deep solvent electrostatic potential. Each energy can be considered in the following manner:

$$\Omega_i = f(U, N_e, ...) \tag{C.3.3}$$

$$U = f(N_e) \tag{C.3.4}$$

The grand canonical free energy, Ω, is a function of the applied potential, U, and the number of excess electrons, N_e. It is important to note that U is itself also a function of the N_e. Therefore, the identification of a U_{eq} value in the CP-DFT framework is an iterative procedure. The excess number of electrons, and thus the applied potential, is changed until a $\Delta\Omega_{ads}$ value of zero is achieved. The potential which dictates $\Delta\Omega_{ads} = 0$ is thus the equilibrium potential in the CP-DFT framework.

As was detailed in reference [232], the CHE model and the grand canonical approach to energies are equivalent, with the marked difference of relaxing the requirement of integer electron transfer. This is apparent when reconsidering Equation 6 of the main text, which is reprinted here for reference.

$$\Omega = F - N_e \cdot \epsilon_{fermi}$$

Grand canonical energy differences are then:

$$\Delta\Omega = F_{final} - N_{e,final} \cdot \epsilon_{fermi,final} - F_{initial} + N_{e,initial} \cdot \epsilon_{fermi,initial} \quad \text{(C.3.5)}$$

Given that initial and final states are evaluated at the same electrochemical potential, Equation C.3.5 simplifies to:

$$\Delta\Omega = \Delta F + \lambda_n \cdot \epsilon_{fermi} \quad \text{(C.3.6)}$$

In Equation C.3.6, $\lambda_n = N_{e,final} - N_{e,initial}$, which is the number of electrons (fractional or integer) exchanged between the final and initial states. The grand canonical energy difference is thus the canonical free energy difference plus a contribution from the number of electrons transferred for an elementary step. These definitions also apply to the initial-transition state pair and reverse reaction directions.

Reinterrogation of Equation 2 in conjunction with Equation C.3.6 of the main text reveals the requirement that ϕ_{SHE} (experimental SHE potential) and $\phi_{solvent}$ (vacuum electrostatic potential) must remain constant between the states of interest in order for Equation C.3.6 to be valid. Considering the experimental SHE potential is a fixed value, it can be assumed to remain constant between any compared states. The vacuum (deep implicit solvent) electrostatic potential can also be assumed to remain constant. This is in accordance with our observations of variations <1% in the deep solvent electrostatic potential for states compared at the same electrochemical potential. Therefore, $\epsilon_{fermi,initial} = \epsilon_{fermi,final}$ and the Fermi energy is the same between two states at a given constant electrochemical potential. This can be confirmed upon examination of the Fermi energies returned from the constant potential calculations, which themselves vary <1% between states evaluated at the same electrochemical condition.

C.4 Determining α, β and λ_n

As discussed in the main text, the charge transfer coefficients (α and β) are calculated as the slope of the $\Delta\Omega$ vs. U relationship. In practice, these are determined by fitting a line on CP-DFT data points, as shown in Figure 74. Over the potential ranges examined in this work, the Butler-Volmer approximation is expected to hold and reaction energies are virtually linear functions of applied potential. Figure 74 gives the $\Delta\Omega$ vs. U data for the H adsorption step on multiple compositions on WO_3. The exact steps are the initial adsorption steps in the full catalytic cycles, as detailed in the main text.

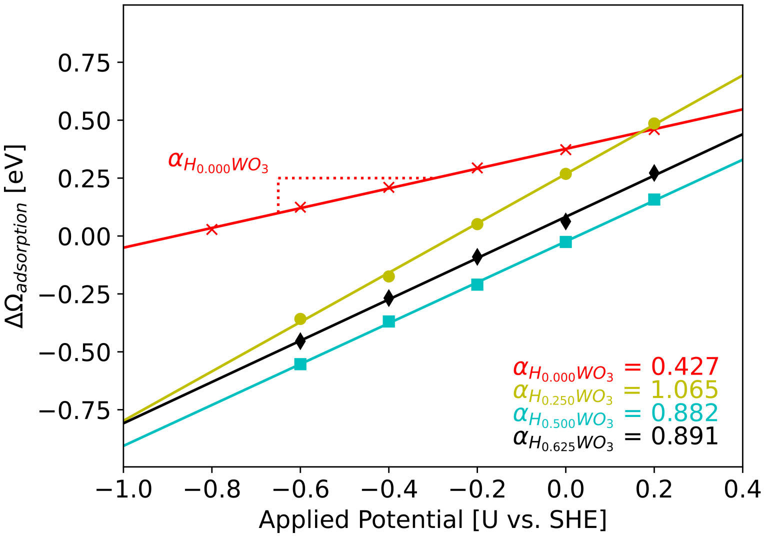

Figure 74: Data and fits for the functional relationship between applied potential and the grand canonical free energies of adsorption on various H_xWO_3 surfaces.

The unrestricted (i.e., allowed to take on non-integer values) charge transfer, λ_n, is a fundamental quantity in describing reaction energetics and kinetics. In CP-DFT, this charge transfer is determined through a comparison of excess electrons on the starting and ending states. As detailed in Section S3 and in the main text, N_e is a variational quantity that needs to be changed to achieve a desired electrochemical potential. Therefore, it is taken as an optimized input to any CP-DFT calculation. Figure 75 illustrates the variation in excess electrons with applied potential for H-adsorption on the $H_{0.625}WO_3$ surface.

In Figure 75, a negative quantity of excess e^- corresponds to electrons removed from the system, and a positive quantity indicated electrons have been added. Considering H

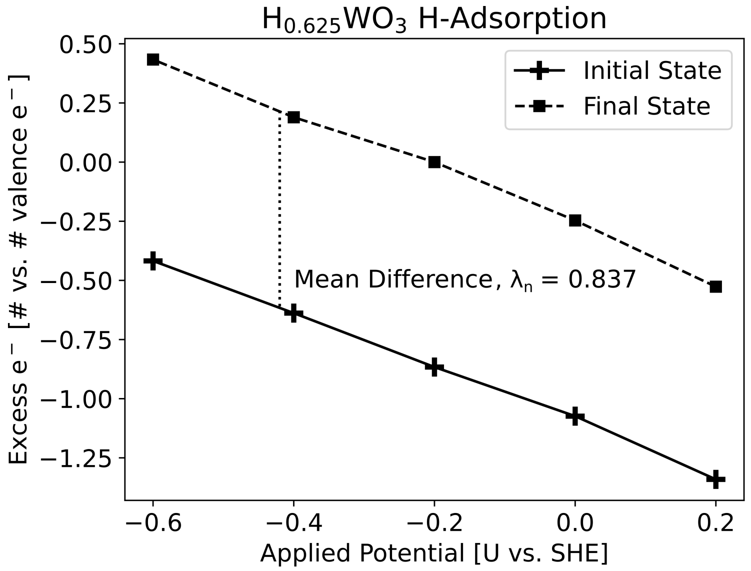

Figure 75: Change in excess electrons as a function of applied potential for initial and final states of H adsorption on $H_{0.625}WO_3$.

adsorption is a reduction reaction, the final state should have more excess electrons than the initial state; this is clearly seen in Figure 75. Furthermore, the difference in excess electrons at each potential defines λ_n. In this work, λ_n for a given elementary reaction was taken as the average difference in excess electrons across all investigated potentials. This was done because we observed essentially no change in the difference of excess electrons in the small potential ranges we considered. The lines in Figure 75 are included to guide the eye and are not linear regressions.

C.5 Energetics of Surface-Mediated H_2-coupling

There are two possible mechanisms that facilitate the formation of H_2 at a catalyst surface. The water-mediated route described in the main text is the most feasible pathway to H_2 on H_xWO_3, as evidenced by lower reaction barriers than for the surface-mediated case.

For comparison, the relevant energies and barriers for coupling two H atoms on the catalyst surface are shown in Figure 76.

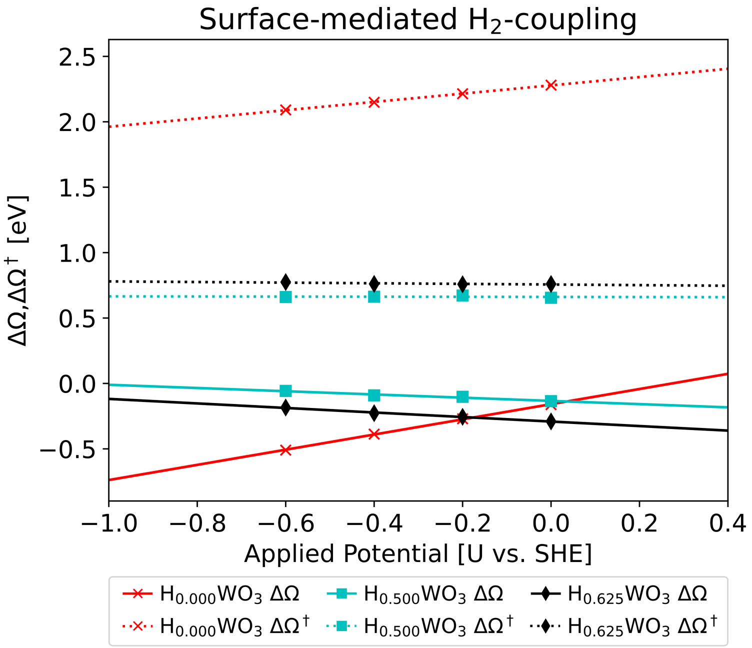

Figure 76: Reaction energies and barriers for surface-mediated H_2-coupling.

C.6 Microkinetic Model Construction and Execution

Microkinetic modeling was performed using the `fp_echem` package. This package was developed in Python and incorporates electrochemical effects on elementary step reaction energies, barriers, and rate constants. In the absence of a varying potential, the resulting microkinetic model is identical to thermocatalytic case. All elementary steps are modeled using transition state theory, with rate constants calculated as:

$$k = \frac{k_b T}{h} exp(\frac{-\Delta\Omega^*}{k_b T}) \tag{C.6.1}$$

The grand canonical free energy barriers, $\Delta\Omega^*$, are required for each elementary step if electrochemical modeling is desired. For thermocatalytic analyses these may be replaced with the canonical free energies. In the electrocatalytic case and in this work, the grand canonical barriers are assessed in the Butler-Volmer approximation, which assumes the energies vary linearly with applied potential:

$$\Delta\Omega^* = max \begin{cases} \Delta\Omega^o + \alpha \cdot U \\ \Delta\Omega^{\dagger,o} + \beta \cdot U \end{cases} \tag{C.6.2}$$

Both the reaction energies, $\Delta\Omega^o$, and the barriers, $\Delta\Omega^{\dagger,o}$, are considered at 0 V vs. SHE. Potential dependence is respectively captured by the charge transfer coefficients α and β. Both forward and reverse rates are determined using Equations C.6.1 and C.6.2, with the reverse barriers and energies determined from the reaction coordinate diagrams. This approach is mathematically equivalent to using an equilibrium constant to describe each forward and reverse elementary step. Energies and transfer coefficients are all calculated with CP-DFT, as detailed in the main text and sections S3 - S5. Both the barriers and reaction energies are considered at each applied potential, since the varying potential dependence can cause elementary steps to transition from activated to non-activated and vice versa. Variations in applied potential are evaluated as an additional differential equation in the solution of the microkinetic model governing equations.

For the construction of microkinetic model, we needed to make a few assumptions. First, we consider the desorption step to occur simultaneously with the formation of H_2. Since the desorbed surface is considered as the starting configuration in each reaction pathway, the influence of "spectator" H atoms bound to adjacent sites is retained. Second, we model the initial adsorption step as an unactivated process. This is because we observe spontaneous, barrierless transfer of H units from the water layer to the surface during ground state geometry optimizations. H transfer in this case occurs via the hydrogen bonding network with under-coordinated oxygen atoms. Further, the surface diffusion of H on a WO_3 surface occurs quickly in the presence of water, allowing non-rate-determining transfer to active sites.[76]

For the pathway on $H_{0.000}WO_3$, we do not explicitly consider the energetics of O-2H* to O-H_2* conversion. We were unable to locate a reasonable transition state for the conversion of two individually bound H atoms on a bridge oxygen (O-2H*) to molecular H_2 on a bridge oxygen (O-H_2*). This is somewhat expected, as the O-2H* species resembles a stable water molecule located at the bridge site and would not rearrange to form a bound molecule of H_2.

Thus, we omit the O-2H* to O-H$_2$* step and consider only H adsorption and the formation of the O-2H* intermediate in the mechanism on $H_{0.000}WO_3$. This is acceptable for two reasons:

1. if the H_2-coupling barrier were lower than the O-2H* formation barrier, then surface-mediated H_2-coupling would have minimal contribution to overall turnover
2. if the H_2-coupling barrier were higher than the O-2H* formation barrier, then the approximate rate would be an overestimate of catalytic activity

In the first case, the use of the O-2H* formation barrier would result in a rate that is similar to the one that would be computed if using the full pathway. In the second case, inserting the H_2-coupling step in the reaction mechanism would result in a slower calculated reaction rate. The calculated HER activity of WO_3 is many orders of magnitude lower than H_xWO_3, and so the inclusion of a H_2-coupling energy is not likely to influence the overall results.

The hydrogen evolution mechanism was modeled as a two step process, with H adsorption preceding H_2-coupling. Coupling was considered through the water-mediated pathway, as this gave the lowest barriers for all intercalated surfaces. Surface-mediated H_2-coupling was required for the $H_{0.000}WO_3$ surface; however, as detailed above, water-mediated coupling was taken as a proxy for activity of $H_{0.000}WO_3$. A single site approach was applied, with adsorption and coupling occurring at the same location. The relevant reactions are therefore:

$$1.\quad [*] + [H^+] + e^- \leftrightarrow [H^*] : r_1$$
$$2.\quad [H*] + [H^+] + e^- \leftrightarrow [H_2] + [*] : r_2$$

Mass balances for each reactant are constructed continuously in `fp_echem`, and for this particular reaction network they can be summarized as follows:

$$\frac{d\theta_*}{dt} = -r_{1,f} + r_{1,r} + r_{2,f} - r_{2,r}$$
$$\frac{d\theta_{H*}}{dt} = +r_{1,f} - r_{1,r} - r_{2,f} + r_{2,r}$$
$$\frac{da_{H_2}}{dt} = +r_{2,f} - r_{2,r}$$

Dimensionless surface coverages, θ, and activities, a, are used so that rate constants can be defined with units of 1/s regardless of the stoichiometries of elementary reaction steps. Proton activity, a_{H^+}, in solution is assumed to be constant. Each of the balances are solved simultaneously with the extra consideration of a linearly varying applied potential. This is defined as:

$$\frac{dU}{dt} = \nu \tag{C.6.3}$$

In Equation C.6.3, ν is the change in applied potential in units of V/s. This is essentially a scan rate that might be used in experimental linear sweep or cyclic voltammetry. By incorporating the applied potential as part of the solution to the set of differential equations, the rate constants can be directly tuned to the instantaneous applied potential while solving the full microkinetic model. This captures the electrochemical effects on the reaction energies and barriers, as derived from CP-DFT.

Current densities are calculated from the chemical rates using Equation C.6.4:

$$j_{mk} = n \cdot F \cdot \Gamma_{mk} \cdot \sigma \cdot A_{norm} \tag{C.6.4}$$

In Equation C.6.4, j_{mk} is the current density, n is the number of electrons transferred in the full reaction, F is Faraday's constant, Γ_{mk} is the rate extracted from microkinetics in units of 1/s, and σ is the surface site density in units of moles/cm^2. σ is calculated based on the number of sites per unit cell surface area (as the super cell used in DFT calculations). A_{norm} is then a normalization constant that is needed to translate between the fictitious pure (100) surface and the nanoparticle film electrode. Depending on particle morphology and film thickness, the ratio of (100) to geometric electrode area will change. This needs to be considered in order to compare first-principles-based microkinetic and experimental current densities. Calculation of A_{norm} is detailed in the next section.

Further details about the technical implementation and operation of the `fp_echem` code are included on Github.

C.7 Gaussian Process Regression for Calculation of Tafel Slopes

Gaussian process regression (GPR) was performed to more accurately assess the curvature of the current density vs. potential relationship obtained from chronopotentiometry experiments. Accurate curvatures are essential for providing reasonable estimates of Tafel slopes, especially when assessing the potential-dependence of the slopes. We demonstrate this first in Figure 77, which illustrates Tafel slope calculations using finite differences with hypothetical data.

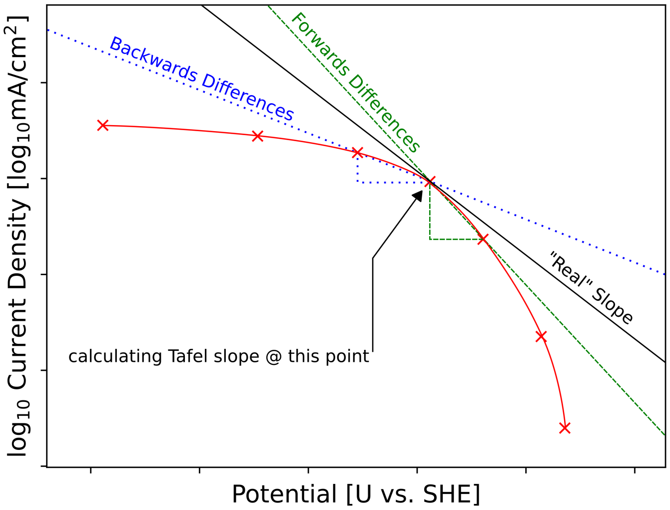

Figure 77: Tafel slope inaccuracies as a result of backward and forward difference methodologies typically used when analyzing experimental data. In this example case, backward differences overestimate and forward differences underestimate the 'true' Tafel slope (considering units of mv/dec).

Since experimental chronopotentiometry / chronoamperometry data are always discrete in potential vs. current space, finite difference approaches to calculating a Tafel slope can give errors with respect to the “true” slope. The magnitude of these errors is dependent on the degree of curvature, the sparsity of the data, and other factors. For concave down current vs. potential data, backwards differences will overestimate and forward differences will underestimate the Tafel slope at a given potential. This is the case shown in Figure 77. For concave up cases, the opposite trends will occur. The closer the data are to being perfectly linear, the smaller the error. However, interpolating between data points using a regression method helps to minimize error (and accurately express uncertainty) regardless of the degree of curvature. Depending on the method selected, confidence values can be assigned to the regions between experimental data points, giving ranges of expected Tafel slope values instead of singular predictions. A further benefit is the removal of bias from the

Tafel slope calculation.[247] It is common practice in experimental electrochemistry to fit a straight line through collected data points. This presents two problems:

1. the data might not be truly linear
2. the apparent Tafel slope can be a strong function of the selected data points

A non-parametric regression approach, such as GPR, helps alleviate these problems by not forcing a specific model type on the data.

The full regression approach was applied using the `GaussianProcessRegressor` implementation in `scikit-learn`. A prior distribution needs to be constructed in order to apply GPR. The mean of the Gaussian process was assumed to be constant and zero, and the covariance was modeled using a radial basis function (RBF) kernel. Hyperparameters for the RBF kernel and the regularization factor were chosen such that they maximized the log-marginal-likelihood of the model. The likelihood was maximized for an RBF length scale of 0.261. The regularization optimization is shown in Figure 78, which resulted in $\alpha = 0.345$.

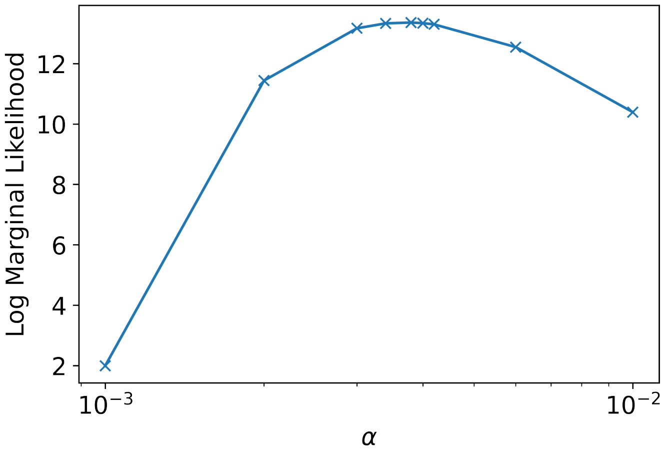

Figure 78: Variation of log-marginal-likelihood with the magnitude of the regularization parameter, α.

The GPR was optimized and trained on a dataset that mapped applied potential to the base-10 logarithm of current density. Semilog-space was chosen because Tafel slopes are the derivative of the semilog-space data and not the linear data (i.e. Tafel slope $= \frac{d\eta}{dlog_{10}j}$). The trained model and experimental data are shown in Figure 79. The model is shown as the red shaded area, which gives the 99% confidence interval for the current density at a given applied potential. Five representative samples from the Gaussian process posterior are shown as black lines. The learned model is arbitrarily differentiable, such that we can interpolate between the experimental data points. Confidence intervals shown in Figure 79 can be carried through to the resulting derivatives (Tafel slopes in mV/decade).

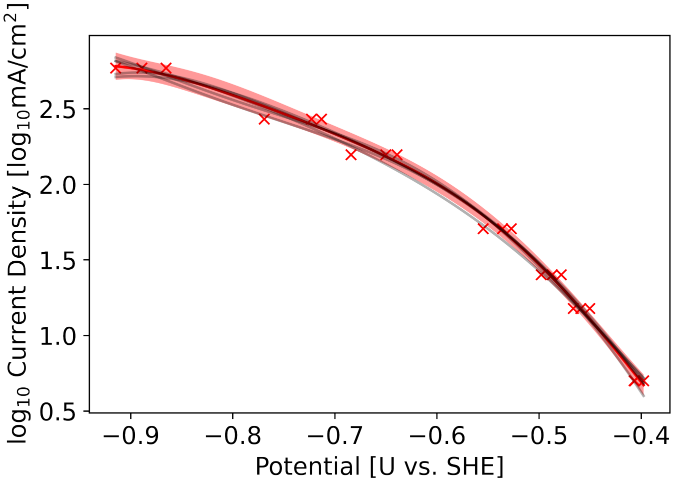

Figure 79: Chronopotentiometry data and GPR fits. The red shaded area shows the 99% confidence interval for the mean of the data, and the black lines represent five samples from the Gaussian process posterior.

The Tafel slopes computed directly from the experimental data using finite differences and from the GPR model results in Figure 79 are shown in Figure 80. Backward differences are used here to determine the slopes without GPR. They are also used to calculated the GPR differences, however, the model data are interpolated and determined across much finer potential steps. Although the general trend toward very high Tafel slopes with increased HER overpotential are evident from both approaches, the backwards differences approach overestimates the Tafel slopes given by GPR, in some cases by more than 100 mV/dec. The shaded area representing the GPR differences is showing the 99% confidence interval for the value of the Tafel slope.

C.8 Nanoparticle Characterization

Tungsten trioxide nanoparticles were confirmed to be similar to those used in prior reports ([234, 261]) through SEM and XRD measurements, shown in Figures 81 and 82. SEM images

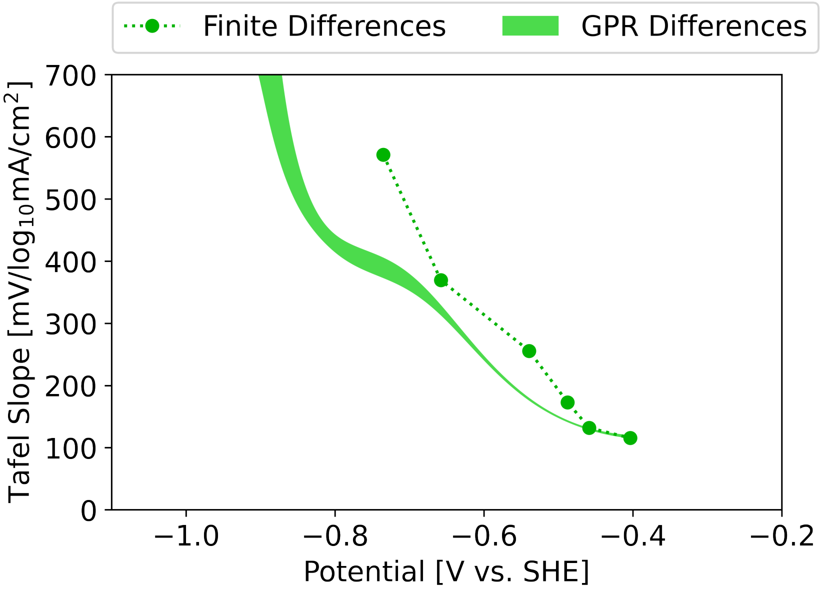

Figure 80: Apparent Tafel slopes from finite differences and GPR.

were recorded using a Zeiss Sigma 500VP field emission scanning electron microscope with10 keV accelerating voltage and a backscatter detector. XRD measurements were collected with a Bruker D8 Discover instrument using a LynxEye detector under Cu K-α radiation and with step increments of 0.01° at 1.5 secs / step. SEM images show a clear disk-like morphology, with nanoparticle dimensions on the order of 15 nm thick x 275 nm in diameter. Considering the XRD shows highly textured monoclinic WO_3 with a prevalence of (001) sites, the faces of the disks are assigned to be primarily (001). This work considered (100) surfaces as catalytically competent, and the total active surface area is calculated as:

$$A_{active} = \pi \cdot r_{disk} \cdot h_{disk} \tag{C.8.1}$$

This is done because the sides of the disks contain the majority of (100) surface sites. The full surface of the disk sides was assumed to contain a 50:50 mixture of (100) and (010) sites, therefore only half of the side surface area is taken into account. Equation C.8.1 gives the part of the factor used for geometric normalization of the current densities extracted from the microkinetic models. The models return current densities in units of mA per surface area of a purely (100) surface. In order to adjust to experimentally relevant areas, the model current densities need to be adjusted by an area factor that considers the area of (100) sites per area of electrode, which we call A_{norm}.

$$A_{norm} = \frac{A_{active}}{A_{electrode}} \tag{C.8.2}$$

$A_{electrode}$ is the geometric area of the supporting electrode on which the catalyst film was deposited. Electrode-scale and experimentally-relevant current densities are produced by considering A_{norm}. Considering nanoparticles that are 275 nm in diameter and 15 nm in height, with a typical deposition of ~ 0.2 mg of nanoparticles per experiment, we find A_{norm} to be 1.069.

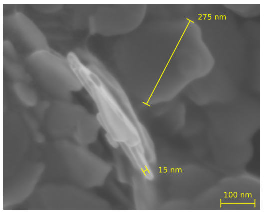

Figure 81: SEM images showing morphology and size of WO_3 nanoparticles.

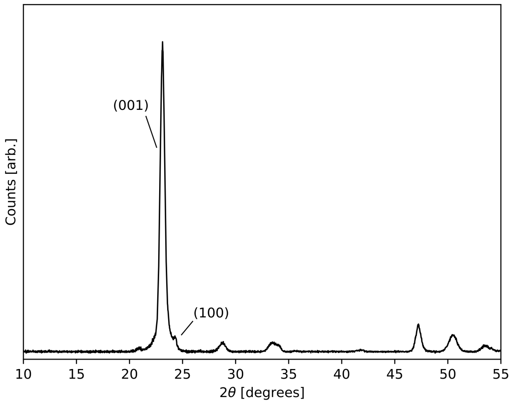

Figure 82: Representative XRD of WO_3 nanoparticles.

C.9 Hydrated and Dehydrated Surface Configurations

Figure 83 illustrates varying degrees of hydration of the $H_{0.000}WO_3$ surface. The intercalated bronzes were investigated using the same configurations, and only $H_{0.000}WO_3$ is shown for simplicity. Moving left to right, the panels show the dissociatively hydrated surface, the associatively hydrated surface, the dehydrated surface, and the hydrogen covered surface. The first two steps are thermochemical, proceeding respectively through surface combination and molecular desorption. The final step is electrochemical, and the associated potential-dependent reaction energies are modeled using the CHE framework. These surface calculations do not include explicit solvent waters, as the thermodynamics are expected to be well-captured by the CHE with implicit solvation (see main text).

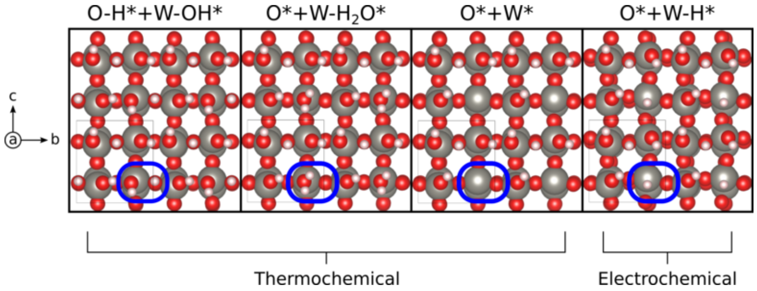

Figure 83: (100) surface corresponding to the states shown in main text Figure 8. Thin black lines show the unit cell, and thick blue lines highlight the W-O site pair where dehydration was investigated.

Bibliography

[1] Mitigation of climate change. Technical report, Working Group III, AR6, International Panel on Climate Change, April 2022.

[2] Corinne Le Quéré, Robert B Jackson, Matthew W Jones, Adam JP Smith, Sam Abernethy, Robbie M Andrew, Anthony J De-Gol, David R Willis, Yuli Shan, Josep G Canadell, et al. Temporary reduction in daily global CO_2 emissions during the covid-19 forced confinement. *Nature climate change*, 10(7):647–653, 2020.

[3] Jeff Tollefson. Covid curbed carbon emissions in 2020–but not by much, Jan 2021.

[4] Sonja van Renssen. The hydrogen solution? *Nature Climate Change*, 10(9):799–801, 2020.

[5] Hydrogen. Technical report, International Energy Administration, 2021.

[6] Hydrogen strategy, enabling a low-carbon economy. Technical report, Office of Fossil Energy, United States Department of Energy, Washington, DC 20585, July 2020.

[7] The future of hydrogen – analysis. Technical report, International Energy Administration, 2019.

[8] Robert W Howarth and Mark Z Jacobson. How green is blue hydrogen? *Energy Science & Engineering*, 9(10):1676–1687, 2021.

[9] Jose M Bermudez, Stavroula Evangelopoulou, and Francesco Pavan. Hydrogen supply – analysis.

[10] Mai Bui, Claire S Adjiman, André Bardow, Edward J Anthony, Andy Boston, Solomon Brown, Paul S Fennell, Sabine Fuss, Amparo Galindo, Leigh A Hackett, et al. Carbon capture and storage (ccs): the way forward. *Energy & Environmental Science*, 11(5):1062–1176, 2018.

[11] Ahmed Abdulla, Ryan Hanna, Kristen R Schell, Oytun Babacan, and David G Victor. Explaining successful and failed investments in us carbon capture and storage using empirical and expert assessments. *Environmental Research Letters*, 16(1):014036, 2020.

[12] Fiona Walman and Mo Chatterji. Why hydrogen will remain a carbon-intensive solution until we can produce it cleanly, Aug 2021.

[13] Energy technology perspectives. Technical report, International Energy Administration, 2017.

[14] IEA and Paris, 2021.

[15] Julia W Darcy, Brian Koronkiewicz, Giovanny A Parada, and James M Mayer. A continuum of proton-coupled electron transfer reactivity. *Accounts of chemical research*, 51(10):2391–2399, 2018.

[16] Jens Kehlet Nørskov, Jan Rossmeisl, Ashildur Logadottir, LRKJ Lindqvist, John R Kitchin, Thomas Bligaard, and Hannes Jonsson. Origin of the overpotential for oxygen reduction at a fuel-cell cathode. *The Journal of Physical Chemistry B*, 108(46):17886–17892, 2004.

[17] Jason S Adams, Matthew L Kromer, Joaquín Rodríguez-López, and David W Flaherty. Unifying concepts in electro-and thermocatalysis toward hydrogen peroxide production. *Journal of the American Chemical Society*, 143(21):7940–7957, 2021.

[18] Yuanya Zhao, Jason S Adams, Aravind Baby, Matthew L Kromer, David W Flaherty, and Joaquín Rodríguez-López. Electrochemical screening of au/pt catalysts for the thermocatalytic synthesis of hydrogen peroxide based on their oxygen reduction and hydrogen oxidation activities probed via voltammetric scanning electrochemical microscopy. *ACS Sustainable Chemistry & Engineering*, 2022.

[19] Kunal Lodaya, Bryan Yuk-Wah Tang, Ryan Bisbey, Sophia Weng, Karl Westendorff, Wei Lun Toh, Jaeyune Ryu, Yuriy Román-Leshkov, and Yogesh Surendranath. An electrochemical approach for designing thermochemical bimetallic nitrate hydrogenation catalysts. 2023.

[20] Takafumi Sato, Ayaka Takada, and Naotsugu Itoh. Low-temperature Hydrogenation of Toluene by Electrolysis of Water with Hydrogen Permeable Palladium Membrane Electrode. *Chemistry Letters*, 46(4):477–480, April 2017. Publisher: The Chemical Society of Japan.

[21] Takafumi Sato, Shuhei Sato, and Naotsugu Itoh. Using a hydrogen-permeable palladium membrane electrode to produce hydrogen from water and hydrogenate toluene. *International Journal of Hydrogen Energy*, 41(12):5419–5427, April 2016.

[22] Rebecca S. Sherbo, Roxanna S. Delima, Valerie A. Chiykowski, Benjamin P. MacLeod, and Curtis P. Berlinguette. Complete electron economy by pairing electrolysis with hydrogenation. *Nature Catalysis*, 1(7):501–507, July 2018. Number: 7 Publisher: Nature Publishing Group.

[23] Rebecca S. Sherbo, Aiko Kurimoto, Christopher M. Brown, and Curtis P. Berlinguette. Efficient Electrocatalytic Hydrogenation with a Palladium Membrane Reactor. *Journal of the American Chemical Society*, 141(19):7815–7821, May 2019. Publisher: American Chemical Society.

[24] Joel N Schrauben, Rebecca Hayoun, Carolyn N Valdez, Miles Braten, Lila Fridley, and James M Mayer. Titanium and zinc oxide nanoparticles are proton-coupled electron transfer agents. *Science*, 336(6086):1298–1301, 2012.

[25] Alicia W Cohn, Nils Janssen, James M Mayer, and Daniel R Gamelin. Photocharging zno nanocrystals: picosecond hole capture, electron accumulation, and auger recombination. *The Journal of Physical Chemistry C*, 116(38):20633–20642, 2012.

[26] Janelle Castillo-Lora, Murielle F. Delley, Stephanie M. Laga, and James M. Mayer. Two-Electron–Two-Proton Transfer from Colloidal ZnO and TiO2 Nanoparticles to Molecular Substrates. *The Journal of Physical Chemistry Letters*, 11(18):7687–7691, September 2020. Publisher: American Chemical Society.

[27] Amelia G Reid and Charles W Machan. Redox mediators in homogeneous co-electrocatalysis. *Journal of the American Chemical Society*, 2023.

[28] Rebecca S Sherbo, Aiko Kurimoto, Christopher M Brown, and Curtis P Berlinguette. Efficient electrocatalytic hydrogenation with a palladium membrane reactor. *Journal of the American Chemical Society*, 141(19):7815–7821, 2019.

[29] Ryan P Jansonius, Aiko Kurimoto, Antonio M Marelli, Aoxue Huang, Rebecca S Sherbo, and Curtis P Berlinguette. Hydrogenation without h2 using a palladium membrane flow cell. *Cell Reports Physical Science*, 1(7):100105, 2020.

[30] Aoxue Huang, Yang Cao, Roxanna S Delima, Tengxiao Ji, Ryan P Jansonius, Noah JJ Johnson, Camden Hunt, Jingfu He, Aiko Kurimoto, Zishuai Zhang, et al. Electrolysis can be used to resolve hydrogenation pathways at palladium surfaces in a membrane reactor. *JACS Au*, 1(3):336–343, 2021.

[31] Sri Krishna Murthy Padavala and Kelsey A. Stoerzinger. Role of Hydride Formation in Electrocatalysis for Sustainable Chemical Transformations. *ACS Catalysis*, pages 4544–4551, March 2023. Publisher: American Chemical Society.

[32] Matthew J Liu, Jinyu Guo, Adam S Hoffman, Joakim Halldin Stenlid, Michael T Tang, Elizabeth R Corson, Kevin H Stone, Frank Abild-Pedersen, Simon R Bare, and William A Tarpeh. Catalytic performance and near-surface x-ray characterization of titanium hydride electrodes for the electrochemical nitrate reduction reaction. *Journal of the American Chemical Society*, 144(13):5739–5744, 2022.

[33] Annika Buchheit, Britta Teßmer, Marina Muñoz-Castro, Hartmut Bracht, and Hans-Dieter Wiemhöfer. Electrochemical proton intercalation in vanadium pentoxide thin films and its electrochromic behavior in the near-ir region. *ChemistryOpen*, 10(3):340–346, 2021.

[34] Xianfu Wang, Yiming Xie, Kai Tang, Chao Wang, and Chenglin Yan. Redox chemistry of molybdenum trioxide for ultrafast hydrogen-ion storage. *Angewandte Chemie International Edition*, 57(36):11569–11573, 2018.

[35] Haocheng Guo, Damian Goonetilleke, Neeraj Sharma, Wenhao Ren, Zhen Su, Aditya Rawal, and Chuan Zhao. Two-phase electrochemical proton transport and storage in α-MoO_3 for proton batteries. *Cell Reports Physical Science*, 1(10):100225, 2020.

[36] F Endres and G Schwitzgebel. Cyclic voltammetry of polyethylene stabilized hydrogen molybdenum bronzes. *Journal of Electroanalytical Chemistry*, 415(1-2):23–26, 1996.

[37] G Schwitzgebel and St Adams. Electrochemical determination of the small hydrogen decomposition pressures in H_xMoO_3. *Berichte der Bunsengesellschaft für physikalische Chemie*, 92(11):1426–1430, 1988.

[38] James B Mitchell, Natalie R Geise, Alisa R Paterson, Naresh C Osti, Yangyunli Sun, Simon Fleischmann, Rui Zhang, Louis A Madsen, Michael F Toney, D Jiang, et al. Confined interlayer water promotes structural stability for high-rate electrochemical proton intercalation in tungsten oxide hydrates. *ACS Energy Letters*, 4(12):2805–2812, 2019.

[39] Evan V Miu, Giannis Mpourmpakis, and James R McKone. Predicting the energetics of hydrogen intercalation in metal oxides using acid–base properties. *ACS Applied Materials & Interfaces*, 12(40):44658–44670, 2020.

[40] Zhaolong Li, Swapna Ganapathy, Yaolin Xu, Zhou Zhou, Mehmet Sarilar, and Marnix Wagemaker. Mechanistic insight into the electrochemical performance of Zn/VO_2 batteries with an aqueous $ZnSO_4$ electrolyte. *Advanced Energy Materials*, 9(22):1900237, 2019.

[41] Yee-Seul Kim, Sébastien Kriegel, Kenneth D Harris, Cyrille Costentin, Benoît Limoges, and Véronique Balland. Evidencing fast, massive, and reversible H^+ insertion in nanostructured TiO_2 electrodes at neutral ph. where do protons come from? *The Journal of Physical Chemistry C*, 121(19):10325–10335, 2017.

[42] Chao Geng, Tulai Sun, Zhencui Wang, Jin-Ming Wu, Yi-Jie Gu, Hisayoshi Kobayashi, Peng Yang, Jianhang Hai, and Wei Wen. Surface-induced desolvation of hydronium ion enables anatase TiO_2 as an efficient anode for proton batteries. *Nano Letters*, 21(16):7021–7029, 2021.

[43] PG Dickens, JH Moore, and DJ Neild. Thermochemistry of hydrogen tungsten bronze phases hxwo3. *Journal of Solid State Chemistry*, 7(2):241–244, 1973.

[44] Paul A Sermon and Geoffrey C Bond. Studies of hydrogen spillover. part 4.—factors affecting hydrogen spillover and its reversal. *Journal of the Chemical Society, Faraday Transactions 1: Physical Chemistry in Condensed Phases*, 76:889–900, 1980.

[45] Xianfu Wang, Yiming Xie, Kai Tang, Chao Wang, and Chenglin Yan. Redox chemistry of molybdenum trioxide for ultrafast hydrogen-ion storage. *Angewandte Chemie International Edition*, 57(36):11569–11573, 2018.

[46] Annika Buchheit, Britta Teßmer, Marina Muñoz-Castro, Hartmut Bracht, and Hans-Dieter Wiemhöfer. Electrochemical proton intercalation in vanadium pentoxide thin films and its electrochromic behavior in the near-ir region. *ChemistryOpen*, 10(3):340–346, 2021.

[47] Yee-Seul Kim, Sébastien Kriegel, Kenneth D Harris, Cyrille Costentin, Benoît Limoges, and Véronique Balland. Evidencing fast, massive, and reversible h^+ insertion in nanostructured TiO_2 electrodes at neutral ph. where do protons come from? *The Journal of Physical Chemistry C*, 121(19):10325–10335, 2017.

[48] Oskar Glemser and Hubert Sauer. Die zusammensetzung von wolframblau. *Zeitschrift für Anorganische Chemie*, 252(3-4):160–163, 1943.

[49] Paul A Sermon and Geoffrey C Bond. Studies of hydrogen spillover. part 1.—study of the rate, extent and products of hydrogen spillover from platinum to the trioxides of tungsten and molybdenum. *Journal of the Chemical Society, Faraday Transactions 1: Physical Chemistry in Condensed Phases*, 72:730–744, 1976.

[50] K Bange. Colouration of tungsten oxide films: a model for optically active coatings. *Solar energy materials and solar cells*, 58(1):1, 1999.

[51] Evan V Miu, Giannis Mpourmpakis, and James R McKone. Predicting the energetics of hydrogen intercalation in metal oxides using acid–base properties. *ACS Applied Materials & Interfaces*, 12(40):44658–44670, 2020.

[52] HN Hersh, WE Kramer, and JH McGee. Mechanism of electrochromism in wo3. *Applied Physics Letters*, 27(12):646–648, 1975.

[53] Zhihui Jiao, Jinmin Wang, Lin Ke, Xuewei Liu, Hilmi Volkan Demir, Ming Fei Yang, and Xiao Wei Sun. Electrochromic properties of nanostructured tungsten trioxide (hydrate) films and their applications in a complementary electrochromic device. *Electrochimica Acta*, 63:153–160, 2012.

[54] M Penza, MA Tagliente, L Mirenghi, C Gerardi, C Martucci, and G Cassano. Tungsten trioxide (wo3) sputtered thin films for a nox gas sensor. *Sensors and Actuators B: Chemical*, 50(1):9–18, 1998.

[55] Hong-Ming Lin, Chi-Ming Hsu, Huey-Yih Yang, Pee-Yew Lee, and Chao-Cheng Yang. Nanocrystalline wo3-based h2s sensors. *Sensors and Actuators B: Chemical*, 22(1):63–68, 1994.

[56] Wen-Jing Li and Zheng-Wen Fu. Nanostructured wo3 thin film as a new anode material for lithium-ion batteries. *Applied Surface Science*, 256(8):2447–2452, 2010.

[57] Kai Huang, Qingtao Pan, Feng Yang, Shibing Ni, Xiucheng Wei, and Deyan He. Controllable synthesis of hexagonal wo3 nanostructures and their application in lithium batteries. *Journal of Physics D: Applied Physics*, 41(15):155417–155422, 2008.

[58] Shrisudersan Jayaraman, Thomas F Jaramillo, Sung-Hyeon Baeck, and Eric W McFarland. Synthesis and characterization of pt-wo3 as methanol oxidation catalysts for fuel cells. *The Journal of Physical Chemistry B*, 109(48):22958–22966, 2005.

[59] PK Shen and ACC Tseung. Anodic oxidation of methanol on pt/wo3 in acidic media. *Journal of the Electrochemical Society*, 141(11):3082–3090, 1994.

[60] ACC Tseung, PK Shen, and KY Chen. Precious metal/hydrogen bronze anode catalysts for the oxidation of small organic molecules and impure hydrogen. *Journal of power sources*, 61(1-2):223–225, 1996.

[61] Jin Hyun Kim, Ganesan Magesh, Hyun Joon Kang, Marimuthu Banu, Ju Hun Kim, Jinwoo Lee, and Jae Sung Lee. Carbonate-coordinated cobalt co-catalyzed bivo4/wo3 composite photoanode tailored for co2 reduction to fuels. *Nano Energy*, 15:153–163, 2015.

[62] Jian Jin, Jiaguo Yu, Daipeng Guo, Can Cui, and Wingkei Ho. A hierarchical z-scheme cds–wo3 photocatalyst with enhanced co2 reduction activity. *Small*, 11(39):5262–5271, 2015.

[63] Ken-ichi Machida and Michio Enyo. Structural and electrochromic properties of tungsten and molybdenum trioxide electrodes in acidic media. *Journal of the Electrochemical Society*, 137(4):1169–1175, 1990.

[64] Arne Magnéli and Birgitta Blomberg. Contribution to the knowledge of the alkali tungsten bronzes. *Acta chem. scand*, 5:372–378, 1951.

[65] O Bohnke and G Robert. Electrochemical lithium incorporation into wo3 and moo3 thin films. *Solid State Ionics*, 6(2):115–120, 1982.

[66] Yang He, Meng Gu, Haiyan Xiao, Langli Luo, Yuyan Shao, Fei Gao, Yingge Du, Scott X Mao, and Chongmin Wang. Atomistic conversion reaction mechanism of wo3 in secondary ion batteries of li, na, and ca. *Angewandte Chemie International Edition*, 55(21):6244–6247, 2016.

[67] James B Mitchell, William C Lo, Arda Genc, James LeBeau, and Veronica Augustyn. Transition from battery to pseudocapacitor behavior via structural water in tungsten oxide. *Chemistry of Materials*, 29(9):3928–3937, 2017.

[68] James B Mitchell, Natalie R Geise, Alisa R Paterson, Naresh C Osti, Yangyunli Sun, Simon Fleischmann, Rui Zhang, Louis A Madsen, Michael F Toney, De-en Jiang, Alexander I Kolesnikov, Eugene Mamontov, and Veronica Augustyn. Confined interlayer water promotes structural stability for high-rate electrochemical proton intercalation in tungsten oxide hydrates. *ACS Energy Letters*, 4(12):2805–2812, 2019.

[69] Evan V Miu and James R McKone. Comparisons of wo3 reduction to hxwo3 under thermochemical and electrochemical control. *Journal of Materials Chemistry A*, 7(41):23756–23761, 2019.

[70] B Yan, RP Bisbey, A Alabugin, and Y Surendranath. Mixed electron–proton conductors enable spatial separation of bond activation and charge transfer in electrocatalysis. *Journal of the American Chemical Society*, 141(28):11115–11122, 2019.

[71] Jennifer L Peper and James M Mayer. Manifesto on the thermochemistry of nanoscale redox reactions for energy conversion. *ACS Energy Letters*, 4(4):866–872, 2019.

[72] B Ingham, SC Hendy, SV Chong, and JL Tallon. Density-functional studies of tungsten trioxide, tungsten bronzes, and related systems. *Physical Review B*, 72(7):075109–1–075109–9, 2005.

[73] Cristiana Di Valentin, Fenggong Wang, and Gianfranco Pacchioni. Tungsten oxide in catalysis and photocatalysis: Hints from dft. *Topics in Catalysis*, 56(15-17):1404–1419, 2013.

[74] Fenggong Wang, Cristiana Di Valentin, and Gianfranco Pacchioni. Dft study of hydrogen adsorption on the monoclinic wo3 (001) surface. *The Journal of Physical Chemistry C*, 116(19):10672–10679, 2012.

[75] Hao Lin, Fei Zhou, Chi-Ping Liu, and Vidvuds Ozoliņš. Non-grotthuss proton diffusion mechanism in tungsten oxide dihydrate from first-principles calculations. *Journal of Materials Chemistry A*, 2(31):12280–12288, 2014.

[76] Yongjie Xi, Qingfan Zhang, and Hansong Cheng. Mechanism of hydrogen spillover on wo3 (001) and formation of h x wo3 (x= 0.125, 0.25, 0.375, and 0.5). *The Journal of Physical Chemistry C*, 118(1):494–501, 2014.

[77] A Urban, DH Seo, and G Ceder. Computational understanding of li-ion batteries. *npj Computational Materials*, 2(1):1–13, 2016.

[78] A Jain, G Hautier, C Moore, B Kang, J Lee, H Chen, N Twu, and G Ceder. A computational investigation of li9m3 (p2o7) 3 (po4) 2 (m= v, mo) as cathodes for li ion batteries. *Journal of the Electrochemical Society*, 159(5):A622–A633, 2012.

[79] G Hautier, A Jain, H Chen, C Moore, SP Ong, and G Ceder. Novel mixed polyanions lithium-ion battery cathode materials predicted by high-throughput ab initio computations. *Journal of Materials Chemistry*, 21(43):17147–17153, 2011.

[80] Georg Kresse and Jürgen Furthmüller. Efficient iterative schemes for ab initio total-energy calculations using a plane-wave basis set. *Physical review B*, 54(16):11169–11186, 1996.

[81] Koichi Momma and Fujio Izumi. Vesta 3 for three-dimensional visualization of crystal, volumetric and morphology data. *Journal of applied crystallography*, 44(6):1272–1276, 2011.

[82] John P Perdew, Kieron Burke, and Matthias Ernzerhof. Generalized gradient approximation made simple. *Physical review letters*, 77(18):3865–3868, 1996.

[83] Stefan Grimme, Jens Antony, Stephan Ehrlich, and Helge Krieg. A consistent and accurate ab initio parametrization of density functional dispersion correction (dft-d) for the 94 elements h-pu. *The Journal of chemical physics*, 132(15):154104–154122, 2010.

[84] Stefan Grimme, Stephan Ehrlich, and Lars Goerigk. Effect of the damping function in dispersion corrected density functional theory. *Journal of computational chemistry*, 32(7):1456–1465, 2011.

[85] Yonghyuk Lee, Taehun Lee, Woosun Jang, and Aloysius Soon. Unraveling the intercalation chemistry of hexagonal tungsten bronze and its optical responses. *Chemistry of Materials*, 28(13):4528–4535, 2016.

[86] Yoyo Hinuma, Hiroyuki Hayashi, Yu Kumagai, Isao Tanaka, and Fumiyasu Oba. Comparison of approximations in density functional theory calculations: Energetics and structure of binary oxides. *Physical Review B*, 96(9):094102–094123, 2017.

[87] Peter E Blöchl, Ove Jepsen, and Ole Krogh Andersen. Improved tetrahedron method for brillouin-zone integrations. *Physical Review B*, 49(23):16223–16234, 1994.

[88] PM Woodward, AW Sleight, and T Vogt. Structure refinement of triclinic tungsten trioxide. *Journal of Physics and Chemistry of Solids*, 56(10):1305–1315, 1995.

[89] Edward Sanville, Steven D Kenny, Roger Smith, and Graeme Henkelman. Improved grid-based algorithm for bader charge allocation. *Journal of computational chemistry*, 28(5):899–908, 2007.

[90] Mitchell C Cholewinski, Mudit Dixit, and Giannis Mpourmpakis. Computational study of methane activation on γ-al2o3. *ACS omega*, 3(12):18242–18250, 2018.

[91] F. Pedregosa, G. Varoquaux, A. Gramfort, V. Michel, B. Thirion, O. Grisel, M. Blondel, P. Prettenhofer, R. Weiss, V. Dubourg, J. Vanderplas, A. Passos, D. Cournapeau, M. Brucher, M. Perrot, and E. Duchesnay. Scikit-learn: Machine learning in Python. *Journal of Machine Learning Research*, 12:2825–2830, 2011.

[92] Jens Kehlet Nørskov, Jan Rossmeisl, Ashildur Logadottir, LRKJ Lindqvist, John R Kitchin, Thomas Bligaard, and Hannes Jonsson. Origin of the overpotential for oxygen reduction at a fuel-cell cathode. *The Journal of Physical Chemistry B*, 108(46):17886–17892, 2004.

[93] Simon Burkhardt, Matthias T Elm, Bernhard Lani-Wayda, and Peter J Klar. In situ monitoring of lateral hydrogen diffusion in amorphous and polycrystalline wo3 thin films. *Advanced Materials Interfaces*, 5(6):1701587–170195, 2018.

[94] A Di Paola, F Di Quarto, and C Sunseri. Electrochromism in anodically formed tungsten oxide films. *Journal of the Electrochemical Society*, 125(8):1344–1347, 1978.

[95] M Regragui, M Addou, A Outzourhit, JC Bernede, Elb El Idrissi, E Benseddik, and A Kachouane. Preparation and characterization of pyrolytic spray deposited electrochromic tungsten trioxide films. *Thin solid films*, 358(1-2):40–45, 2000.

[96] PK Shen, HT Huang, and ACC Tseung. A study of tungsten trioxide and polyaniline composite films i. electrochemical and electrochromic behavior. *Journal of the Electrochemical Society*, 139(7):1840–1845, 1992.

[97] Sergio Tosoni, Cristiana Di Valentin, and Gianfranco Pacchioni. Effect of alkali metals interstitial doping on structural and electronic properties of wo3. *The Journal of Physical Chemistry C*, 118(6):3000–3006, 2014.

[98] Anton Van der Ven, MK Aydinol, G Ceder, G Kresse, and J Hafner. First-principles investigation of phase stability in li x coo 2. *Physical Review B*, 58(6):2975–2987, 1998.

[99] C Wolverton and Alex Zunger. First-principles prediction of vacancy order-disorder and intercalation battery voltages in li x coo 2. *Physical review letters*, 81(3):606–609, 1998.

[100] Kevin P Murphy. *Machine Learning: a Probabilistic Perspective.* MIT press, 2012.

[101] EW McFarland and H Metiu. Catalysis by doped oxides. *Chemical Reviews*, 113(6):4391–4427, 2013.

[102] H Metiu, S Chretien, Z Hu, B Li, and X Sun. Chemistry of lewis acid–base pairs on oxide surfaces. *The Journal of Physical Chemistry C*, 116(19):10439–10450, 2012.

[103] S Chretien and H Metiu. Acid–base interaction and its role in alkane dissociative chemisorption on oxide surfaces. *The Journal of Physical Chemistry C*, 118(47):27336–27342, 2014.

[104] P Kostetskyy, J Yu, RJ Gorte, and G Mpourmpakis. Structure–activity relationships on metal-oxides: Alcohol dehydration. *Catalysis Science & Technology*, 4(1):3861–3869, 2014.

[105] Mudit Dixit, Pavlo Kostetskyy, and Giannis Mpourmpakis. Structure-activity relationships in alkane dehydrogenation on γ-al2o3: Site-dependent reactions. *ACS Catalysis*, 8(12):11570–11578, 2018.

[106] MA Christiansen, G Mpourmpakis, and DG Vlachos. Density functional theory-computed mechanisms of ethylene and diethyl ether formation from ethanol on γ-al2o3 (100). *ACS Catalysis*, 3(9):1965–1975, 2013.

[107] Jeffrey J Warren, Tristan A Tronic, and James M Mayer. Thermochemistry of proton-coupled electron transfer reagents and its implications. *Chemical reviews*, 110(12):6961–7001, 2010.

[108] RL Dekock and HB Gray. *Chemical Structure and Bonding.* University Science Books, 1989.

[109] Roald Hoffmann. *Solids and Surfaces: a Chemists View of Bonding in Extended Structures.* Wiley-VCH, 2002.

[110] Ralph G Pearson. Hard and soft acids and bases. *Journal of the American Chemical society*, 85(22):3533–3539, 1963.

[111] Aliaksandr V Krukau, Oleg A Vydrov, Artur F Izmaylov, and Gustavo E Scuseria. Influence of the exchange screening parameter on the performance of screened hybrid functionals. *The Journal of chemical physics*, 125(22):224106–224110, 2006.

[112] A Nilsson, LGM Pettersson, Bjørk Hammer, T Bligaard, Claus H Christensen, and Jens Kehlet Nørskov. The electronic structure effect in heterogeneous catalysis. *Catalysis Letters*, 100(3-4):111–114, 2005.

[113] M Haghighatlari, CY Shih, and J Hachmann. Thinking globally, acting locally: On the issue of training set imbalance and the case for local machine learning models in chemistry. *ChemRxiv*, (v1):1–10, 2019.

[114] Yu-Kang Tu, David Gunnell, and Mark S Gilthorpe. Simpson's paradox, lord's paradox, and suppression effects are the same phenomenon–the reversal paradox. *Emerging themes in epidemiology*, 5(1):1–9, 2008.

[115] Nitin A Kaskhedikar and Joachim Maier. Lithium storage in carbon nanostructures. *Advanced Materials*, 21(25-26):2664–2680, 2009.

[116] HR Shanks, PH Sidles, and GC Danielson. Electrical properties of the tungsten bronzes. *Advances in Chemistry*, 39(22):237–245, 1963.

[117] Dafni Chatzikyriakou, Natacha Krins, Bernard Gilbert, Pierre Colson, Jennifer Dewalque, Jessica Denayer, Rudi Cloots, and Catherine Henrist. Mesoporous amorphous tungsten oxide electrochromic films: a raman analysis of their good switching behavior. *Electrochimica Acta*, 137:75–82, 2014.

[118] G Leftheriotis, S Papaefthimiou, P Yianoulis, and A Siokou. Effect of the tungsten oxidation states in the thermal coloration and bleaching of amorphous wo3 films. *Thin solid films*, 384(2):298–306, 2001.

[119] Mogalahalli V Reddy, GV Subba Rao, and BVR Chowdari. Metal oxides and oxysalts as anode materials for Li ion batteries. *Chemical reviews*, 113(7):5364–5457, 2013.

[120] Carl M Lampert. Electrochromic materials and devices for energy efficient windows. *Solar Energy Materials*, 11(1-2):1–27, 1984.

[121] Evan V Miu, James R McKone, and Giannis Mpourmpakis. The sensitivity of metal oxide electrocatalysis to bulk hydrogen intercalation: Hydrogen evolution on tungsten oxide. *Journal of the American Chemical Society*, 144(14):6420–6433, 2022.

[122] Ya You and Arumugam Manthiram. Progress in high-voltage cathode materials for rechargeable sodium-ion batteries. *Advanced Energy Materials*, 8(2):1701785, 2018.

[123] Jan N Reimers and JR Dahn. Electrochemical and in situ x-ray diffraction studies of lithium intercalation in Li_xCoO_2. *Journal of the Electrochemical Society*, 139(8):2091, 1992.

[124] C Guery, C Choquet, F Dujeancourt, JM Tarascon, and JC Lassegues. Infrared and x-ray studies of hydrogen intercalation in different tungsten trioxides and tungsten trioxide hydrates. *Journal of Solid State Electrochemistry*, 1(3):199–207, 1997.

[125] Gopalakrishnan Sai Gautam, Pieremanuele Canepa, Aziz Abdellahi, Alexander Urban, Rahul Malik, and Gerbrand Ceder. The intercalation phase diagram of Mg in V_2O_5 from first-principles. *Chemistry of Materials*, 27(10):3733–3742, 2015.

[126] Dipan Kundu, Brian D Adams, Victor Duffort, Shahrzad Hosseini Vajargah, and Linda F Nazar. A high-capacity and long-life aqueous rechargeable zinc battery using a metal oxide intercalation cathode. *Nature Energy*, 1(10):1–8, 2016.

[127] Zhi-Jian Zhao, Sihang Liu, Shenjun Zha, Dongfang Cheng, Felix Studt, Graeme Henkelman, and Jinlong Gong. Theory-guided design of catalytic materials using scaling relationships and reactivity descriptors. *Nature Reviews Materials*, 4(12):792–804, 2019.

[128] Michael G Taylor, Natalie Austin, Chrysanthos E Gounaris, and Giannis Mpourmpakis. Catalyst design based on morphology-and environment-dependent adsorption on metal nanoparticles. *ACS Catalysis*, 5(11):6296–6301, 2015.

[129] Giannis Mpourmpakis, Antonis N Andriotis, and Dionisios G Vlachos. Identification of descriptors for the CO interaction with metal nanoparticles. *Nano letters*, 10(3):1041–1045, 2010.

[130] Federico Calle-Vallejo, José I Martínez, Juan M García-Lastra, Philippe Sautet, and David Loffreda. Fast prediction of adsorption properties for platinum nanocatalysts with generalized coordination numbers. *Angewandte Chemie International Edition*, 53(32):8316–8319, 2014.

[131] Victor Fung, Franklin Feng Tao, and D Jiang. General structure–reactivity relationship for oxygen on transition-metal oxides. *The Journal of Physical Chemistry Letters*, 8(10):2206–2211, 2017.

[132] Xianfeng Ma and Hongliang Xin. Orbitalwise coordination number for predicting adsorption properties of metal nanocatalysts. *Physical review letters*, 118(3):036101, 2017.

[133] Tian Xie and Jeffrey C Grossman. Crystal graph convolutional neural networks for an accurate and interpretable prediction of material properties. *Physical review letters*, 120(14):145301, 2018.

[134] Oliver T Unke and Markus Meuwly. Physnet: A neural network for predicting energies, forces, dipole moments, and partial charges. *Journal of chemical theory and computation*, 15(6):3678–3693, 2019.

[135] Johannes Gasteiger, Florian Becker, and Stephan Günnemann. Gemnet: Universal directional graph neural networks for molecules. *Advances in Neural Information Processing Systems*, 34:6790–6802, 2021.

[136] Fan RK Chung. *Spectral graph theory*, volume 92. American Mathematical Soc., 1997.

[137] Miroslav Fiedler. Laplacian of graphs and algebraic connectivity. *Banach Center Publications*, 1(25):57–70, 1989.

[138] Fan RK Chung. Laplacians of graphs and cheeger's inequalities. *Combinatorics, Paul Erdos is Eighty*, 2(157-172):13–2, 1996.

[139] Jianping Liu and Bolian Liu. A laplacian-energy-like invariant of a graph. *Match-Communications in Mathematical and in Computer Chemistry*, 59(2):355–372, 2008.

[140] Pavlo Kostestkyy, Jingye Yu, Raymond J Gorte, and Giannis Mpourmpakis. Structure–activity relationships on metal-oxides: alcohol dehydration. *Catalysis Science & Technology*, 4(11):3861–3869, 2014.

[141] USEIA. Annual energy outlook 2019. Technical report, US Energy Information Administration, 2019.

[142] A Boulamanti and JA Moya. Energy efficiency and ghg emissions: Prospective scenarios for the chemical and petrochemical industry. Technical report, Joint Research Centre, European Commission, 2017.

[143] Alireza Aslani and Kau-Fui V Wong. Analysis of renewable energy development to power generation in the united states. *Renewable Energy*, 63:153–161, 2014.

[144] Mark Z Jacobson, Mark A Delucchi, Guillaume Bazouin, Zack AF Bauer, Christa C Heavey, Emma Fisher, Sean B Morris, Diniana JY Piekutowski, Taylor A Vencill, and Tim W Yeskoo. 100% clean and renewable wind, water, and sunlight (wws) all-sector energy roadmaps for the 50 united states. *Energy & Environmental Science*, 8(7):2093–2117, 2015.

[145] Nancy M Haegel, Harry Atwater, Teresa Barnes, Christian Breyer, Anthony Burrell, Yet-Ming Chiang, Stefaan De Wolf, Bernhard Dimmler, David Feldman, Stefan Glunz, et al. Terawatt-scale photovoltaics: Transform global energy. *Science*, 364(6443):836–838, 2019.

[146] Michael J Orella, Yuriy Roman-Leshkov, and Fikile R Brushett. Emerging opportunities for electrochemical processing to enable sustainable chemical manufacturing. *Current opinion in chemical engineering*, 20:159–167, 2018.

[147] Gerardine G Botte. Electrochemical manufacturing in the chemical industry. *The Electrochemical Society Interface*, 23(3):49–55, 2014.

[148] Zachary J Schiffer and Karthish Manthiram. Electrification and decarbonization of the chemical industry. *Joule*, 1(1):10–14, 2017.

[149] CG Vayenas, S Bebelis, and S Neophytides. Non-faradaic electrochemical modification of catalytic activity. *The Journal of Physical Chemistry*, 92(18):5083–5085, 1988.

[150] Costas G Vayenas. Promotion, electrochemical promotion and metal–support interactions: their common features. *Catalysis letters*, 143(11):1085–1097, 2013.

[151] Costas G Vayenas, S Bebelis, IV Yentekakis, and H-G Lintz. Non-faradaic electrochemical modification of catalytic activity: a status report. *Catalysis today*, 11(3):303–438, 1992.

[152] CG Vayenas, S Ladas, S Bebelis, IV Yentekakis, S Neophytides, Jiang Yi, Ch Karavasilis, and C Pliangos. Electrochemical promotion in catalysis: non-faradaic electro-

chemical modification of catalytic activity. *Electrochimica Acta*, 39(11-12):1849–1855, 1994.

[153] Constantinos G Vayenas and Symeon Bebelis. Electrochemical promotion of heterogeneous catalysis. *Catalysis Today*, 51(3-4):581–594, 1999.

[154] J Nicole, D Tsiplakides, C Pliangos, XE Verykios, Ch Comninellis, and CG Vayenas. Electrochemical promotion and metal–support interactions. *Journal of Catalysis*, 204(1):23–34, 2001.

[155] Ian S Metcalfe. Electrochemical promotion of catalysis: I: Thermodynamic considerations. *Journal of Catalysis*, 199(2):247–258, 2001.

[156] A Katsaounis. Recent developments and trends in the electrochemical promotion of catalysis (epoc). *Journal of applied electrochemistry*, 40(5):885–902, 2010.

[157] Jean Sanabria-Chinchilla, Koichiro Asazawa, Tomokazu Sakamoto, Koji Yamada, Hirohisa Tanaka, and Peter Strasser. Noble metal-free hydrazine fuel cell catalysts: Epoc effect in competing chemical and electrochemical reaction pathways. *Journal of the American Chemical Society*, 133(14):5425–5431, 2011.

[158] Philippe Vernoux, Leonardo Lizarraga, Mihalis N Tsampas, Foteini M Sapountzi, Antonio De Lucas-Consuegra, Jose-Luis Valverde, Stamatios Souentie, Costas G Vayenas, Dimitris Tsiplakides, Stella Balomenou, et al. Ionically conducting ceramics as active catalyst supports. *Chemical reviews*, 113(10):8192–8260, 2013.

[159] SH Morejudo, R Zanón, S Escolástico, I Yuste-Tirados, H Malerød-Fjeld, PK Vestre, WG Coors, A Martínez, T Norby, JM Serra, et al. Direct conversion of methane to aromatics in a catalytic co-ionic membrane reactor. *Science*, 353(6299):563–566, 2016.

[160] Harald Malerød-Fjeld, Daniel Clark, Irene Yuste-Tirados, Raquel Zanón, David Catalán-Martinez, Dustin Beeaff, Selene H Morejudo, Per K Vestre, Truls Norby, Reidar Haugsrud, et al. Thermo-electrochemical production of compressed hydrogen from methane with near-zero energy loss. *Nature Energy*, 2(12):923, 2017.

[161] N Itoh, WC Xu, S Hara, and K Sakaki. Electrochemical coupling of benzene hydrogenation and water electrolysis. *Catalysis today*, 56(1-3):307–314, 2000.

[162] Rebecca S Sherbo, Aiko Kurimoto, Christopher M Brown, and Curtis P Berlinguette. Efficient electrocatalytic hydrogenation with a palladium membrane reactor. *Journal of the American Chemical Society*, 141:7815–7821, 2019.

[163] Neil M Wilson and David W Flaherty. Mechanism for the direct synthesis of h2o2 on pd clusters: heterolytic reaction pathways at the liquid–solid interface. *Journal of the American Chemical Society*, 138(2):574–586, 2015.

[164] PG Dickens and MS Whittingham. The tungsten bronzes and related compounds. *Quarterly Reviews, Chemical Society*, 22(1):30–44, 1968.

[165] Zheng Chen, Yiting Peng, Fang Liu, Zaiyuan Le, Jian Zhu, Gurong Shen, Dieqing Zhang, Meicheng Wen, Shuning Xiao, Chi-Ping Liu, et al. Hierarchical nanostructured wo3 with biomimetic proton channels and mixed ionic-electronic conductivity for electrochemical energy storage. *Nano letters*, 15(10):6802–6808, 2015.

[166] Yumi Tanaka, Masaru Miyayama, Mitsuhiro Hibino, and Tetsuichi Kudo. Preparation and proton conductivity of wo3· 2h2o/epoxy composite films. *Solid state ionics*, 171(1-2):33–39, 2004.

[167] S Khoobiar. Particle to particle migration of hydrogen atoms on platinum—alumina catalysts from particle to neighboring particles. *The Journal of Physical Chemistry*, 68(2):411–412, 1964.

[168] RB Levy and M Boudart. The kinetics and mechanism of spillover. *Journal of Catalysis*, 32(2):304–314, 1974.

[169] Paul A Sermon and Geoffrey C Bond. Studies of hydrogen spillover. part 1.—study of the rate, extent and products of hydrogen spillover from platinum to the trioxides of tungsten and molybdenum. *Journal of the Chemical Society, Faraday Transactions 1: Physical Chemistry in Condensed Phases*, 72:730–744, 1976.

[170] PA Sermon and GC Bond. Hydrogen spillover. *Catalysis Reviews*, 8(1):211–239, 1974.

[171] Ulf Roland, Thomas Braunschweig, and Frank Roessner. On the nature of spilt-over hydrogen. *Journal of Molecular Catalysis A: Chemical*, 127(1-3):61–84, 1997.

[172] Roel Prins. Hydrogen spillover. facts and fiction. *Chemical reviews*, 112(5):2714–2738, 2012.

[173] Paul A Sermon and Geoffrey C Bond. Studies of hydrogen spillover. part 4.—factors affecting hydrogen spillover and its reversal. *Journal of the Chemical Society, Faraday Transactions 1: Physical Chemistry in Condensed Phases*, 76:889–900, 1980.

[174] C Hoang-Van and O Zegaoui. Studies of high surface area pt/moo3 and pt/wo3 catalysts for selective hydrogenation reactions. ii. reactions of acrolein and allyl alcohol. *Applied Catalysis A: General*, 164(1-2):91–103, 1997.

[175] Tadahiro Kurosaka, Hideyuki Maruyama, Ikuya Naribayashi, and Yoshiyuki Sasaki. Production of 1, 3-propanediol by hydrogenolysis of glycerol catalyzed by pt/wo3/zro2. *Catalysis Communications*, 9(6):1360–1363, 2008.

[176] Xiao-Lin Li, Tian-Jun Lou, Xiao-Ming Sun, and Ya-Dong Li. Highly sensitive wo3 hollow-sphere gas sensors. *Inorganic chemistry*, 43(17):5442–5449, 2004.

[177] Shrisudersan Jayaraman, Thomas F Jaramillo, Sung-Hyeon Baeck, and Eric W McFarland. Synthesis and characterization of pt- wo3 as methanol oxidation catalysts for fuel cells. *The Journal of Physical Chemistry B*, 109(48):22958–22966, 2005.

[178] Tadeusz Borowiecki and Andrzej Gołcebiowski. Influence of molybdenum and tungsten additives on the properties of nickel steam reforming catalysts. *Catalysis letters*, 25(3-4):309–313, 1994.

[179] Claes G Granqvist. Electrochromic tungsten oxide films: review of progress 1993–1998. *Solar Energy Materials and Solar Cells*, 60(3):201–262, 2000.

[180] Ken-ichi Machida and Michio Enyo. Structural and electrochromic properties of tungsten and molybdenum trioxide electrodes in acidic media. *Journal of the Electrochemical Society*, 137(4):1169–1175, 1990.

[181] Bing Yan, Ryan P Bisbey, Alexander Alabugin, and Yogesh Surendranath. Mixed electron-proton conductors enable spatial separation of bond activation and charge transfer in electrocatalysis. *Journal of the American Chemical Society*, 141:11115–11122, 2019.

[182] Abraham Wolcott, Tev R Kuykendall, Wei Chen, Shaowei Chen, and Jin Z Zhang. Synthesis and characterization of ultrathin wo3 nanodisks utilizing long-chain poly (ethylene glycol). *The Journal of Physical Chemistry B*, 110(50):25288–25296, 2006.

[183] PM Woodward, AW Sleight, and T Vogt. Structure refinement of triclinic tungsten trioxide. *Journal of Physics and Chemistry of Solids*, 56(10):1305–1315, 1995.

[184] C Guery, C Choquet, F Dujeancourt, JM Tarascon, and JC Lassegues. Infrared and x-ray studies of hydrogen intercalation in different tungsten trioxides and tungsten trioxide hydrates. *Journal of Solid State Electrochemistry*, 1(3):199–207, 1997.

[185] Mino Green, WC Smith, and JA Weiner. A thin film electrochromic display based on the tungsten bronzes. *Thin Solid Films*, 38(1):89–100, 1976.

[186] WC Dautremont-Smith, Mino Green, and KS Kang. Optical and electrical properties of thin films of wo3 electrochemically coloured. In *International Symposium on Solid Ionic and Ionic-Electronic Conductors*, pages 751–759. Elsevier, 1977.

[187] James B Mitchell, William C Lo, Arda Genc, James LeBeau, and Veronica Augustyn. Transition from battery to pseudocapacitor behavior via structural water in tungsten oxide. *Chemistry of Materials*, 29(9):3928–3937, 2017.

[188] Todd M McEvoy, Keith J Stevenson, Joseph T Hupp, and Xiaojun Dang. Electrochemical preparation of molybdenum trioxide thin films: Effect of sintering on electrochromic and electroinsertion properties. *Langmuir*, 19(10):4316–4326, 2003.

[189] W Curtis Conner Jr and John L Falconer. Spillover in heterogeneous catalysis. *Chemical reviews*, 95(3):759–788, 1995.

[190] JH Simpson and HY Carr. Diffusion and nuclear spin relaxation in water. *Physical Review*, 111(5):1201, 1958.

[191] O Bohnke, M Rezrazi, B Vuillemin, Cl Bohnké, PA Gillet, and C Rousselot. "in situ" optical and electrochemical characterization of electrochromic phenomena into tungsten trioxide thin films. *Solar energy materials and solar cells*, 25(3-4):361–374, 1992.

[192] M Stanley Whittingham. Hydrogen motion in oxides: from insulators to bronzes. *Solid State Ionics*, 168(3-4):255–263, 2004.

[193] YM Li, M Hibino, M Miyayania, and T Kudo. Proton conductivity of tungsten trioxide hydrates at intermediate temperature. *Solid State Ionics*, 134(3-4):271–279, 2000.

[194] Jacques C Védrine. Heterogeneous catalysis on metal oxides. *Catalysts*, 7(11):341, 2017.

[195] Israel E Wachs. Recent conceptual advances in the catalysis science of mixed metal oxide catalytic materials. *Catalysis Today*, 100(1-2):79–94, 2005.

[196] Yinlong Zhu, Qian Lin, Yijun Zhong, Hassan A Tahini, Zongping Shao, and Huanting Wang. Metal oxide-based materials as an emerging family of hydrogen evolution electrocatalysts. *Energy & Environmental Science*, 13(10):3361–3392, 2020.

[197] Yihong Chen and Matthew W Kanan. Tin oxide dependence of the CO_2 reduction efficiency on tin electrodes and enhanced activity for tin/tin oxide thin-film catalysts. *Journal of the American Chemical Society*, 134(4):1986–1989, 2012.

[198] Minh Le, Maoming Ren, Ziyu Zhang, Phillip T Sprunger, Richard L Kurtz, and John C Flake. Electrochemical reduction of CO_2 to CH_3OH at copper oxide surfaces. *Journal of the Electrochemical Society*, 158(5):E45, 2011.

[199] Lena Trotochaud, James K Ranney, Kerisha N Williams, and Shannon W Boettcher. Solution-cast metal oxide thin film electrocatalysts for oxygen evolution. *Journal of the American Chemical Society*, 134(41):17253–17261, 2012.

[200] Dandan Gao, Rongji Liu, Johannes Biskupek, Ute Kaiser, Yu-Fei Song, and Carsten Streb. Modular design of noble-metal-free mixed metal oxide electrocatalysts for complete water splitting. *Angewandte Chemie International Edition*, 58(14):4644–4648, 2019.

[201] Liang Zeng, Zhuo Cheng, Jonathan A Fan, Liang-Shih Fan, and Jinlong Gong. Metal oxide redox chemistry for chemical looping processes. *Nature Reviews Chemistry*, 2(11):349–364, 2018.

[202] Gaurav Assat, Dominique Foix, Charles Delacourt, Antonella Iadecola, Rémi Dedryvère, and Jean-Marie Tarascon. Fundamental interplay between anionic/cationic redox governing the kinetics and thermodynamics of lithium-rich cathodes. *Nature communications*, 8(1):1–12, 2017.

[203] JJ Fripiat and X Lin. Hydrogen intercalation within transition metal oxides: Entropy, enthalpy, and charge transfer. *The Journal of Physical Chemistry*, 96(3):1437–1444, 1992.

[204] WC Dautremont-Smith. Transition metal oxide electrochromic materials and displays: A review: Part 1: Oxides with cathodic coloration. *Displays*, 3(1):3–22, 1982.

[205] Nevill Mott. *Metal-insulator transitions*. CRC Press, 2004.

[206] Evan V Miu and James R McKone. Comparisons of WO_3 reduction to H_xWO_3 under thermochemical and electrochemical control. *Journal of Materials Chemistry A*, 7(41):23756–23761, 2019.

[207] James B Mitchell, William C Lo, Arda Genc, James LeBeau, and Veronica Augustyn. Transition from battery to pseudocapacitor behavior via structural water in tungsten oxide. *Chemistry of Materials*, 29(9):3928–3937, 2017.

[208] Dong-Dong Xu, Xing Deng, Yi-Feng Zhao, Ru-Ru Ma, Ni Zhong, Rong Huang, Hui Peng, Ping-Hua Xiang, and Chun-Gang Duan. Hydrogenation dynamics of electrically controlled metal–insulator transition in proton-gated transparent and flexible WO_3 transistors. *Advanced Functional Materials*, 29(34):1902497, 2019.

[209] Sang-Mun Jung, Su-Won Yun, Jun-Hyuk Kim, Sang-Hoon You, Jinheon Park, Seong-gyu Lee, Seo Hyoung Chang, Seung Chul Chae, Sang Hoon Joo, Yousung Jung, et al. Selective electrocatalysis imparted by metal–insulator transition for durability enhancement of automotive fuel cells. *Nature Catalysis*, 3(8):639–648, 2020.

[210] Bjørk Hammer and Jens K Nørskov. Why gold is the noblest of all the metals. *Nature*, 376(6537):238–240, 1995.

[211] Yu Hang Li, Peng Fei Liu, Lin Feng Pan, Hai Feng Wang, Zhen Zhong Yang, Li Rong Zheng, P Hu, Hui Jun Zhao, Lin Gu, and Hua Gui Yang. Local atomic structure modulations activate metal oxide as electrocatalyst for hydrogen evolution in acidic water. *Nature communications*, 6(1):1–7, 2015.

[212] Gianfranco Pacchioni. Oxygen vacancy: the invisible agent on oxide surfaces. *ChemPhysChem*, 4(10):1041–1047, 2003.

[213] Hongjie Liu, Hao Fu, Yuchang Liu, Xiyong Chen, Kefu Yu, and Liwei Wang. Synthesis, characterization and utilization of oxygen vacancy contained metal oxide semiconductors for energy and environmental catalysis. *Chemosphere*, 272:129534, 2021.

[214] James B Mitchell, Natalie R Geise, Alisa R Paterson, Naresh C Osti, Yangyunli Sun, Simon Fleischmann, Rui Zhang, Louis A Madsen, Michael F Toney, De-en Jiang, et al.

Confined interlayer water promotes structural stability for high-rate electrochemical proton intercalation in tungsten oxide hydrates. *ACS Energy Letters*, 4(12):2805–2812, 2019.

[215] Evan V Miu, Giannis Mpourmpakis, and James R McKone. Predicting the energetics of hydrogen intercalation in metal oxides using acid–base properties. *ACS Applied Materials & Interfaces*, 12(40):44658–44670, 2020.

[216] Ebrahim Tayyebi, Javed Hussain, Younes Abghoui, and Egill Skúlason. Trends of electrochemical CO_2 reduction reaction on transition metal oxide catalysts. *The Journal of Physical Chemistry C*, 122(18):10078–10087, 2018.

[217] Árni B H́oskuldsson, Younes Abghoui, Anna B Gunnarsdottir, and Egill Skúlason. Computational screening of rutile oxides for electrochemical ammonia formation. *ACS Sustainable Chemistry & Engineering*, 5(11):10327–10333, 2017.

[218] Tingting Zheng, Wei Sang, Zhihai He, Qiushi Wei, Bowen Chen, Hongliang Li, Cong Cao, Ruijie Huang, Xupeng Yan, Bicai Pan, et al. Conductive tungsten oxide nanosheets for highly efficient hydrogen evolution. *Nano letters*, 17(12):7968–7973, 2017.

[219] Guoqing Li, Du Zhang, Yifei Yu, Shengyang Huang, Weitao Yang, and Linyou Cao. Activating MoS_2 for pH-universal hydrogen evolution catalysis. *Journal of the American Chemical Society*, 139(45):16194–16200, 2017.

[220] Guangxia Wang, Jinyang Liu, Yongming Sui, Ming Wang, Liang Qiao, Fei Du, and Bo Zou. Palladium structure engineering induced by electrochemical H intercalation boosts hydrogen evolution catalysis. *Journal of Materials Chemistry A*, 7(24):14876–14881, 2019.

[221] Graeme Henkelman, Blas P Uberuaga, and Hannes Jónsson. A climbing image nudged elastic band method for finding saddle points and minimum energy paths. *The Journal of chemical physics*, 113(22):9901–9904, 2000.

[222] Andreas Heyden, Alexis T Bell, and Frerich J Keil. Efficient methods for finding transition states in chemical reactions: Comparison of improved dimer method and partitioned rational function optimization method. *The Journal of chemical physics*, 123(22):224101, 2005.

[223] Ask Hjorth Larsen, Jens Jørgen Mortensen, Jakob Blomqvist, Ivano E Castelli, Rune Christensen, Marcin Dułak, Jesper Friis, Michael N Groves, Bjørk Hammer, Cory Hargus, Eric D Hermes, Paul C Jennings, Peter Bjerre Jensen, James Kermode, John R Kitchin, Esben Leonhard Kolsbjerg, Joseph Kubal, Kristen Kaasbjerg, Steen Lysgaard, Jón Bergmann Maronsson, Tristan Maxson, Thomas Olsen, Lars Pastewka, Andrew Peterson, Carsten Rostgaard, Jakob Schiøtz, Ole Schütt, Mikkel Strange, Kristian S Thygesen, Tejs Vegge, Lasse Vilhelmsen, Michael Walter, Zhenhua Zeng, and Karsten W Jacobsen. The atomic simulation environment—a python library for working with atoms. *Journal of Physics: Condensed Matter*, 29(27):273002, 2017.

[224] Yongjie Xi, Qingfan Zhang, and Hansong Cheng. Mechanism of hydrogen spillover on WO_3 (001) and formation of H_xWO_3 (x= 0.125, 0.25, 0.375, and 0.5). *The Journal of Physical Chemistry C*, 118(1):494–501, 2014.

[225] PG Dickens, JH Moore, and DJ Neild. Thermochemistry of hydrogen tungsten bronze phases H_xWO_3. *Journal of Solid State Chemistry*, 7(2):241–244, 1973.

[226] Kiran Mathew, VS Chaitanya Kolluru, Srinidhi Mula, Stephan N Steinmann, and Richard G Hennig. Implicit self-consistent electrolyte model in plane-wave density-functional theory. *The Journal of chemical physics*, 151(23):234101, 2019.

[227] Deniz Gunceler, Kendra Letchworth-Weaver, Ravishankar Sundararaman, Kathleen A Schwarz, and TA Arias. The importance of nonlinear fluid response in joint density-functional theory studies of battery systems. *Modelling and Simulation in Materials Science and Engineering*, 21(7):074005, 2013.

[228] Stephan N Steinmann, Carine Michel, Renate Schwiedernoch, and Philippe Sautet. Impacts of electrode potentials and solvents on the electroreduction of CO_2: a comparison of theoretical approaches. *Physical Chemistry Chemical Physics*, 17(21):13949–13963, 2015.

[229] Joseph A Gauthier, Stefan Ringe, Colin F Dickens, Alejandro J Garza, Alexis T Bell, Martin Head-Gordon, Jens K Nørskov, and Karen Chan. Challenges in modeling electrochemical reaction energetics with polarizable continuum models. *ACS Catalysis*, 9(2):920–931, 2018.

[230] Sergio Trasatti et al. The absolute electrode potential: an explanatory note (recommendations 1986). *Pure Appl. Chem*, 58(7):955–966, 1986.

[231] Maxime Van den Bossche, Egill Skúlason, Christoph Rose-Petruck, and Hannes Jónsson. Assessment of constant-potential implicit solvation calculations of electro-

chemical energy barriers for H_2 evolution on Pt. *The Journal of Physical Chemistry C*, 123(7):4116–4124, 2019.

[232] Georg Kastlunger, Per Lindgren, and Andrew A Peterson. Controlled-potential simulation of elementary electrochemical reactions: Proton discharge on metal surfaces. *The Journal of Physical Chemistry C*, 122(24):12771–12781, 2018.

[233] Ravishankar Sundararaman, William A Goddard III, and Tomas A Arias. Grand canonical electronic density-functional theory: Algorithms and applications to electrochemistry. *The Journal of chemical physics*, 146(11):114104, 2017.

[234] Abraham Wolcott, Tev R Kuykendall, Wei Chen, Shaowei Chen, and Jin Z Zhang. Synthesis and characterization of ultrathin WO_3 nanodisks utilizing long-chain poly (ethylene glycol). *The Journal of Physical Chemistry B*, 110(50):25288–25296, 2006.

[235] Allen J Bard, Larry R Faulkner, et al. *Electrochemical methods: Fundamentals and applications*, volume 2. Wiley New York, 2001.

[236] Jan C Myland and Keith B Oldham. Uncompensated resistance. 1. the effect of cell geometry. *Analytical chemistry*, 72(17):3972–3980, 2000.

[237] JOM Bockris and EC Potter. The mechanism of the cathodic hydrogen evolution reaction. *Journal of The Electrochemical Society*, 99(4):169, 1952.

[238] Tatsuya Shinagawa, Angel T Garcia-Esparza, and Kazuhiro Takanabe. Insight on tafel slopes from a microkinetic analysis of aqueous electrocatalysis for energy conversion. *Scientific reports*, 5(1):1–21, 2015.

[239] Wolfgang Schmickler and Rolando Guidelli. The partial charge transfer. *Electrochimica Acta*, 127:489–505, 2014.

[240] Aimin Ge, Georg Kastlunger, Jinhui Meng, Per Lindgren, Jia Song, Qiliang Liu, Alexander Zaslavsky, Tianquan Lian, and Andrew A Peterson. On the coupling of electron transfer to proton transfer at electrified interfaces. *Journal of the American Chemical Society*, 142(27):11829–11834, 2020.

[241] Leanne D Chen, Michal Bajdich, J Mark P Martirez, Caroline M Krauter, Joseph A Gauthier, Emily A Carter, Alan C Luntz, Karen Chan, and Jens K Nørskov. Understanding the apparent fractional charge of protons in the aqueous electrochemical double layer. *Nature communications*, 9(1):1–8, 2018.

[242] Joseph A Gauthier, Colin F Dickens, Stefan Ringe, and Karen Chan. Practical considerations for continuum models applied to surface electrochemistry. *ChemPhysChem*, 20(22):3074–3080, 2019.

[243] Haochen Zhang, William A Goddard, Qi Lu, and Mu-Jeng Cheng. The importance of grand-canonical quantum mechanical methods to describe the effect of electrode potential on the stability of intermediates involved in both electrochemical CO_2 reduction and hydrogen evolution. *Physical Chemistry Chemical Physics*, 20(4):2549–2557, 2018.

[244] JW Schultze and KJ Vetter. Experimental determination and interpretation of the electrosorption valency γ. *Journal of Electroanalytical Chemistry and Interfacial Electrochemistry*, 44(1):63–81, 1973.

[245] Rolando Guidelli, Richard G Compton, Juan M Feliu, Eliezer Gileadi, Jacek Lipkowski, Wolfgang Schmickler, and Sergio Trasatti. Defining the transfer coefficient in electrochemistry: An assessment (iupac technical report). *Pure and Applied Chemistry*, 86(2):245–258, 2014.

[246] DA Harrington and BE Conway. Kinetic theory of the open-circuit potential decay method for evaluation of behaviour of adsorbed intermediates: Analysis for the case of the h2 evolution reaction. *Journal of electroanalytical chemistry and interfacial electrochemistry*, 221(1-2):1–21, 1987.

[247] Aditya M Limaye, Joy S Zeng, Adam P Willard, and Karthish Manthiram. Bayesian data analysis reveals no preference for cardinal tafel slopes in CO_2 reduction electrocatalysis. *Nature communications*, 12(1):1–10, 2021.

[248] M Digne, P Sautet, P Raybaud, P Euzen, and H Toulhoat. Hydroxyl groups on γ-alumina surfaces: a DFT study. *Journal of Catalysis*, 211(1):1–5, 2002.

[249] Daniel J Aschaffenburg, Seiji Kawasaki, Chaitanya Das Pemmaraju, and Tanja Cuk. Accuracy in resolving the first hydration layer on a transition-metal oxide surface: experiment (AP−XPS) and theory. *The Journal of Physical Chemistry C*, 124(39):21407–21417, 2020.

[250] Oskar Glemser and Hubert Sauer. Die zusammensetzung von wolframblau. *Zeitschrift für anorganische Chemie*, 252(3-4):160–163, 1943.

[251] James B Mitchell, William C Lo, Arda Genc, James LeBeau, and Veronica Augustyn. Transition from battery to pseudocapacitor behavior via structural water in tungsten oxide. *Chemistry of Materials*, 29(9):3928–3937, 2017.

[252] James B Mitchell, Natalie R Geise, Alisa R Paterson, Naresh C Osti, Yangyunli Sun, Simon Fleischmann, Rui Zhang, Louis A Madsen, Michael F Toney, De-en Jiang, et al. Confined interlayer water promotes structural stability for high-rate electrochemical proton intercalation in tungsten oxide hydrates. *ACS Energy Letters*, 4(12):2805–2812, 2019.

[253] James B Gerken, Yutong Q Pang, Markus B Lauber, and Shannon S Stahl. Structural effects on the ph-dependent redox properties of organic nitroxyls: pourbaix diagrams for tempo, abno, and three tempo analogs. *The Journal of organic chemistry*, 83(14):7323–7330, 2017.

[254] Rishi G Agarwal, Scott C Coste, Benjamin D Groff, Abigail M Heuer, Hyunho Noh, Giovanny A Parada, Catherine F Wise, Eva M Nichols, Jeffrey J Warren, and James M Mayer. Free energies of proton-coupled electron transfer reagents and their applications. *Chemical reviews*, 122(1):1–49, 2021.

[255] Judith R Fish, Steven G Swarts, Michael D Sevilla, and Tadeusz Malinski. Electrochemistry and spectroelectrochemistry of nitroxyl free radicals. *The Journal of Physical Chemistry*, 92(13):3745–3751, 1988.

[256] Bing Yan, Ryan P Bisbey, Alexander Alabugin, and Yogesh Surendranath. Mixed electron–proton conductors enable spatial separation of bond activation and charge transfer in electrocatalysis. *Journal of the American Chemical Society*, 141(28):11115–11122, 2019.

[257] Rebecca S Sherbo, Aiko Kurimoto, Christopher M Brown, and Curtis P Berlinguette. Efficient electrocatalytic hydrogenation with a palladium membrane reactor. *Journal of the American Chemical Society*, 141(19):7815–7821, 2019.

[258] Liuchuan Tong, Qing Chen, Andrew A Wong, Rafael Gómez-Bombarelli, Alán Aspuru-Guzik, Roy G Gordon, and Michael J Aziz. Uv-vis spectrophotometry of quinone flow battery electrolyte for in situ monitoring and improved electrochemical modeling of potential and quinhydrone formation. *Physical Chemistry Chemical Physics*, 19(47):31684–31691, 2017.

[259] National Institute of Standards and Technology.

[260] Paul A Sermon and Geoffrey C Bond. Studies of hydrogen spillover. part 4.—factors affecting hydrogen spillover and its reversal. *Journal of the Chemical Society, Faraday Transactions 1: Physical Chemistry in Condensed Phases*, 76:889–900, 1980.

[261] Evan V Miu and James R McKone. Comparisons of wo 3 reduction to h x wo 3 under thermochemical and electrochemical control. *Journal of Materials Chemistry A*, 7(41):23756–23761, 2019.

[262] James B Gerken and Shannon S Stahl. High-potential electrocatalytic o2 reduction with nitroxyl/no x mediators: Implications for fuel cells and aerobic oxidation catalysis. *ACS Central Science*, 1(5):234–243, 2015.

[263] Joachim Paier, Martijn Marsman, K Hummer, Georg Kresse, Iann C Gerber, and János G Ángyán. Screened hybrid density functionals applied to solids. *The Journal of chemical physics*, 124(15):154709, 2006.

[264] Xiang Leng, Juan Pereiro, Jure Strle, G Dubuis, AT Bollinger, A Gozar, J Wu, N Litombe, C Panagopoulos, D Pavuna, et al. Insulator to metal transition in wo3 induced by electrolyte gating. *npj Quantum Materials*, 2(1):1–7, 2017.

[265] Taejong Paik, Matteo Cargnello, Thomas R Gordon, Sen Zhang, Hongseok Yun, Jennifer D Lee, Ho Young Woo, Soong Ju Oh, Cherie R Kagan, Paolo Fornasiero, et al. Photocatalytic hydrogen evolution from substoichiometric colloidal wo3–x nanowires. *ACS Energy Letters*, 3(8):1904–1910, 2018.

[266] Beatriz Cordero, Verónica Gómez, Ana E Platero-Prats, Marc Revés, Jorge Echeverría, Eduard Cremades, Flavia Barragán, and Santiago Alvarez. Covalent radii revisited. *Dalton Transactions*, (21):2832–2838, 2008.

[267] Georg Kresse and Jürgen Furthmüller. Efficient iterative schemes for ab initio total-energy calculations using a plane-wave basis set. *Physical review B*, 54(16):11169, 1996.

[268] John P Perdew, Kieron Burke, and Matthias Ernzerhof. Generalized gradient approximation made simple. *Physical review letters*, 77(18):3865, 1996.

[269] Stefan Grimme, Jens Antony, Stephan Ehrlich, and Helge Krieg. A consistent and accurate ab initio parametrization of density functional dispersion correction (dft-d) for the 94 elements H-Pu. *The Journal of chemical physics*, 132(15):154104, 2010.

[270] Stefan Grimme, Stephan Ehrlich, and Lars Goerigk. Effect of the damping function in dispersion corrected density functional theory. *Journal of computational chemistry*, 32(7):1456–1465, 2011.

[271] Peter E Blöchl, Ove Jepsen, and Ole Krogh Andersen. Improved tetrahedron method for brillouin-zone integrations. *Physical Review B*, 49(23):16223, 1994.

[272] F. Pedregosa, G. Varoquaux, A. Gramfort, V. Michel, B. Thirion, O. Grisel, M. Blondel, P. Prettenhofer, R. Weiss, V. Dubourg, J. Vanderplas, A. Passos, D. Cournapeau, M. Brucher, M. Perrot, and E. Duchesnay. Scikit-learn: Machine learning in Python. *Journal of Machine Learning Research*, 12:2825–2830, 2011.

[273] The pandas development team. pandas-dev/pandas: Pandas, February 2020.

[274] In-Kwon Yeo and Richard A Johnson. A new family of power transformations to improve normality or symmetry. *Biometrika*, 87(4):954–959, 2000.

[275] The Tensorflow development team. TensorFlow: Large-scale machine learning on heterogeneous systems, 2015. Software available from tensorflow.org.

[276] François Chollet et al. Keras. `https://keras.io`, 2015.

[277] Diederik P Kingma and Jimmy Ba. Adam: A method for stochastic optimization. *arXiv preprint arXiv:1412.6980*, 2014.

[278] K Bange. Colouration of tungsten oxide films: A model for optically active coatings. *Solar Energy Materials and Solar Cells*, 58(1):1, 1999.

[279] B Vuillemin and O Bohnke. Kinetics study and modelling of the electrochromic phenomenon in amorphous tungsten trioxide thin films in acid and lithium electrolytes. *Solid State Ionics*, 68(3-4):257–267, 1994.

[280] James M Mayer. Proton-coupled electron transfer: a reaction chemist's view. *Annu. Rev. Phys. Chem.*, 55:363–390, 2004.